

# Computational studies of membrane-active antimicrobial peptides and comparison with NMR data

Zur Erlangung des akademischen Grades eines  
Doktors der Naturwissenschaften  
(Dr. rer. nat.)

Fakultät für Chemie und Biowissenschaften  
Karlsruher Institut für Technologie (KIT) - Universitätsbereich  
genehmigte

Dissertation

von  
Dipl.-Phys. Sabine Reißer  
aus  
Leimen

Dekan: Prof. Dr. Peter Roesky  
Referentin: Prof. Dr. Anne Ulrich  
Korreferent: Prof. Dr. Marcus Elstner  
Tag der mündlichen Prüfung: 15.12.2014



Ich erkläre hiermit, dass ich die vorliegende Arbeit selbständig verfasst und keine anderen als die angegebenen Quellen und Hilfsmittel verwendet, sowie die Satzung des Karlsruher Instituts für Technologie zur Sicherung guter wissenschaftlicher Praxis beachtet habe.

Sabine Reißer

05.11.2014



## Danksagung / Acknowledgements

Ich danke Prof. Anne Ulrich für die spontane Aufnahme als Doktorandin, das große mir bei zahllosen Anlässen entgegengebrachte Vertrauen, ihr unermüdliches Interesse und die motivierenden Gespräche und Diskussionen.

Ich danke Prof. Marcus Elstner für die Aufnahme in seinen Arbeitskreis, die Bereitstellung aller für meine Arbeit notwendigen Infrastruktur und seinen Einsatz in Bezug auf meine Zwischenfinanzierung nach der Promotion.

Herzlichen Dank an Dr. Thomas Steinbrecher für die Betreuung während der ersten Hälfte meiner Promotionszeit, fruchtbare Diskussionen und Anregungen, Vertrauen und Förderung.

Thanks to Dr. Erik Strandberg and Dr. Sergii Afonin for their advise, feedback and countless discussions regarding the projects presented in this work, and their intense correction reading of this thesis.

Many thanks to Prof. Alan Mark from the University of Queensland, for the possibility to spend four months in his lab, productive discussions, an inspiring work environment and a great time.

Thanks to Dr. David Poger for his friendly and productive supervision during my stay in Brisbane.

Ich danke dem Karlsruhe House of Young Scientists (KHYS) für die Finanzierung meines viermonatigen Projektaufenthaltes in Brisbane, Australien.

Vielen Dank an meinen Bürokollegen Dr. Tino Wolter, ohne den die ganze Promotion nur halb so spaßig gewesen wäre.

Danke an alle Mitglieder der Arbeitsgruppen Ulrich und Elstner. Es hat mir großen Spaß gemacht, mit euch zusammenzuarbeiten.

Ich danke allen Menschen, die im Internet ihr Wissen in Foren, Mailinglisten oder Blogs teilen. Ohne sie wäre diese Arbeit unmöglich gewesen oder hätte zumindest wesentlich länger gedauert.

Ich danke meinen Eltern für ihre ununterbrochene Förderung und Unterstützung, bei allem was ich tue.

Meinem Freund Andreas Kosmider danke ich für seinen unbeirraren Optimismus, seine konstante Unterstützung und Motivation.



## Zusammenfassung

In dieser Arbeit wurden verschiedene Computer-basierte Methoden verwendet, um die Wechselwirkung zwischen antimikrobiellen Peptiden und Phospholipid-Membranen zu studieren, und so eine bessere Interpretation der Ergebnisse aus Festkörper-Kernspinresonanzspektroskopie-Messungen in orientierten Doppellipidschichten zu ermöglichen.

In Kapitel 4 wurden freie MD-Simulationen von  $\alpha$ -helikalen Peptiden in DMPC-Membranen durchgeführt, um die Orientierung und die Struktur der Peptide in der Membran zu bestimmen und mit experimentellen Ergebnissen zu vergleichen. Durch die Simulationen konnten die Orientierungen, die aus Festkörper-NMR-Daten errechnet wurden, qualitativ reproduziert werden. Aus den Simulationen wurden wichtige strukturelle Parameter berechnet, die die Orientierung der Seitenketten in Bezug auf die helikale Achse definieren und die für die Interpretation der Festkörper-NMR-Daten notwendig sind.

In Kapitel 5 wird ein neuer, drei-dimensionaler Hydrophobes-Moment-Vektor (HM-Vektor) definiert. Mit dieser Methode wird aus dem elektrostatischen Potential auf der Moleküloberfläche ein Vektor berechnet, der von den polaren Teilen der Oberfläche weg, hin zu den hydrophoben Teilen zeigt. Dieser Vektor kann eine Orientierung eines amphiphilen Peptids in der Membran vorhersagen. Da auch andere Orientierungen im Experiment und in Simulationen vorkommen, wird angenommen, dass die Wechselwirkungen mit den geladenen Lipid-Kopfgruppen der Membran und/oder andere Faktoren die Peptide davon abhalten, die geneigte Orientierung einzunehmen.

Kapitel 6 beinhaltet eine Simulationsstudie von lichtschtbaren Analoga des zyklischen Peptids Gramacidin S (GS). Die lichtschtbaren Fragmente wurden parametrisiert und an verschiedenen Stellen in GS eingesetzt. Die Strukturen dieser Analoga wurden durch Simulationen in isotroper Lösung, bzw. im membrangebundenen Zustand aufgeklärt. Das Einsetzen der lichtschtbaren Fragmente führte zu einer starken Abnahme der intra-molekularen Wasserstoffbrücken. Verschiedene physiko-chemische Eigenschaften wurden berechnet und mit experimentellen Daten verglichen.

In Kapitel 7 wurden verschiedene Fluor-Aminosäuren parametrisiert und als Markierungen an den Positionen 9, 10, 13 und 14 in das antimikrobielle Peptid PGLa eingesetzt, indem die dort natürlich vorkommenden Aminosäuren ersetzt wurden. Wie in Kapitel 4 wurden strukturelle Parameter aus Energie-minimierten und membrangebundenen Strukturen berechnet, die die Orientierung der Fluor-Seitenketten im Bezug auf die helikale Achse definieren. Diese Parameter sind wichtig für die Interpretation von  $^{19}\text{F}$  Festkörper-NMR-Daten und auch für den Entwurf neuer Markierungen. Außerdem wurde in den Membransimulationen eine mögliche Störung der helikalen Struktur durch die  $^{19}\text{F}$ -Markierung abgeschätzt.



# Contents

<b>1</b>	<b>Introduction</b>	<b>1</b>
1.1	Antibiotics and antimicrobial peptides . . . . .	1
1.2	Peptides studied in this work . . . . .	5
1.2.1	PGLa . . . . .	5
1.2.2	Magainin 2 . . . . .	7
1.2.3	Temporin A . . . . .	7
1.2.4	Gramicidin S . . . . .	8
1.2.5	BP100 . . . . .	10
1.2.6	MSI-103 . . . . .	10
1.2.7	KIA14 . . . . .	10
<b>2</b>	<b>Theory</b>	<b>11</b>
2.1	Molecular dynamics simulations . . . . .	11
2.1.1	Bonded interactions . . . . .	11
2.1.2	Nonbonded interactions . . . . .	12
2.1.3	Propagation of the system . . . . .	13
2.2	Nuclear magnetic resonance spectroscopy . . . . .	13
2.2.1	$^2\text{H}$ NMR . . . . .	14
2.2.2	$^{19}\text{F}$ NMR . . . . .	15
<b>3</b>	<b>Methods</b>	<b>17</b>
3.1	Simulations . . . . .	17
3.1.1	Membrane simulations . . . . .	17
3.2	Helicity calculation . . . . .	18
3.3	Calculation of the peptide orientation . . . . .	18
3.4	Calculation of structural parameters from the simulations . . . . .	21
3.5	Calculation of NMR splittings from the simulations . . . . .	25

---

<b>4</b>	<b>Simulations of helical peptides in a DMPC membrane and comparison with NMR data</b>	<b>27</b>
4.1	Introduction . . . . .	27
4.2	Methods . . . . .	28
4.2.1	Simulations . . . . .	28
4.3	Results . . . . .	28
4.3.1	PGLa . . . . .	28
4.3.2	MSI-103 . . . . .	31
4.3.3	KIA14 . . . . .	34
4.3.4	Magainin 2 . . . . .	37
4.3.5	Calculated fit parameters . . . . .	39
4.3.6	RMSD analysis . . . . .	39
4.3.7	Analysis of the standard deviations of $\Delta\nu_q$ . . . . .	40
4.4	Discussion . . . . .	43
<b>5</b>	<b>3D hydrophobic moment vectors as a tool to characterize the surface polarity of amphiphilic peptides</b>	<b>45</b>
5.1	Introduction . . . . .	45
5.2	Methods . . . . .	46
5.2.1	Simulations . . . . .	46
5.2.2	Hydrophobic moment calculation . . . . .	47
5.3	Results . . . . .	49
5.3.1	Model charge distributions . . . . .	49
5.3.2	Peptide studies . . . . .	51
5.3.3	Results summary . . . . .	61
5.4	Discussion . . . . .	62
5.5	3D HM vector web application . . . . .	63
<b>6</b>	<b>Simulations of photoswitchable analogs of the antimicrobial peptide gramicidin S</b>	<b>65</b>
6.1	Introduction . . . . .	65
6.2	Methods . . . . .	66
6.2.1	Parametrization and model building . . . . .	66
6.2.2	Simulations . . . . .	67
6.3	Results . . . . .	70
6.3.1	Simulations in MeOH . . . . .	70
6.3.2	Simulations in a DMPC membrane . . . . .	74

---

6.3.3	Correlation with the experiment . . . . .	80
6.4	Discussion . . . . .	85
<b>7</b>	<b>Calculation of structural parameters for fluorine labelled helical peptides</b>	<b>87</b>
7.1	Introduction . . . . .	87
7.2	Methods . . . . .	88
7.2.1	Parametrization and model building . . . . .	88
7.2.2	Simulations . . . . .	88
7.2.3	Helicity calculation . . . . .	90
7.3	Results . . . . .	90
7.3.1	Energy minimization . . . . .	90
7.3.2	Membrane simulations . . . . .	94
7.4	Discussion . . . . .	100
<b>8</b>	<b>Summary</b>	<b>101</b>
	<b>Bibliography</b>	<b>103</b>
<b>A</b>	<b>Membrane simulations of helical peptides</b>	<b>119</b>
<b>B</b>	<b>3D hydrophobic moment vectors</b>	<b>133</b>
<b>C</b>	<b>Photoswitchable analogs of gramicidin S</b>	<b>137</b>
<b>D</b>	<b>Fluorine amino acids</b>	<b>141</b>



## Abbreviations

**2D** two-dimensional.

**3D** three-dimensional.

**Ala-d<sub>3</sub>** threefold deuterated alanine.

**AMP** antimicrobial peptide.

**BGR** (2R)-2-amino-2-[3-(trifluoromethyl)bicyclo[1.1.1]pentan-1-yl]acetic acid.

**BGS** (2S)-2-amino-2-[3-(trifluoromethyl)bicyclo[1.1.1]pentan-1-yl]acetic acid, also known as CF<sub>3</sub>-Bpg.

**BP100** peptide with sequence KKLFFKKILKYL-NH<sub>2</sub>.

**C** carbon.

**CBR** trans-1-amino-3-(trifluoromethyl)-cyclobutane-1-carboxylic acid.

**CBS** cis-1-amino-3-(trifluoromethyl)-cyclobutane-1-carboxylic acid.

**CD** circular dichroism.

**CF<sub>3</sub>-Bpg** (2S)-2-amino-2-[3-(trifluoromethyl)bicyclo[1.1.1]pentan-1-yl]acetic acid.

**CF<sub>3</sub>-Phg** (2S)-amino[4-(trifluoromethyl)phenyl]acetic acid.

**CPR** (1s,2s)-1-amino-2-(trifluoromethyl)-cyclopropane-1-carboxylic acid.

**CPS** (1s,2r)-1-amino-2-(trifluoromethyl)-cyclopropane-1-carboxylic acid.

**CRR** (1r,2r)-1-amino-2-(trifluoromethyl)-cyclopropane-1-carboxylic acid.

**CRS** (1r,2s)-1-amino-2-(trifluoromethyl)-cyclopropane-1-carboxylic acid.

**DLPC** dilauroylphosphatidylcholine.

**DMPC** dimyristoylphosphatidylcholine.

**DMPG** dimyristoylphosphatidylglycerol.

**DMSO** dimethylsulfoxide.

**DOPC** dioleoylphosphatidylcholine.

**ESP** electrostatic potential.

**FAA** fluorine amino acid.

**FP\_SC1** GS analog, where <sup>D</sup>Phe-Pro is replaced with SC1.

**FP\_SC2** GS analog, where <sup>D</sup>Phe-Pro is replaced with SC2.

**FP\_SWO** GS analog, where <sup>D</sup>Phe-Pro is replaced with SWO.

**GS** peptide gramicidin S, sequence *cyclo*(VOL-<sup>D</sup>F-P)<sub>2</sub>.

**HM** hydrophobic moment.

**HSR** cis-1-amino-3-hydroxy-3-(trifluoromethyl)-cyclobutane-1-carboxylic acid.

**HSS** trans-1-amino-3-hydroxy-3-(trifluoromethyl)-cyclobutane-1-carboxylic acid.

**KIA14** peptide with sequence KIAGKIAKIA GKIA-NH<sub>2</sub>.

**LF\_SC1** GS analog, where Leu-<sup>D</sup>Phe is replaced with SC1.

**LF\_SC2** GS analog, where Leu-<sup>D</sup>Phe is replaced with SC2.

**LF\_SWO** GS analog, where Leu-<sup>D</sup>Phe is replaced with SWO.

**Mag2** peptide magainin 2, sequence GIGKFLHSAK KFGKAFVGEI MNS.

**MD** molecular dynamics.

**MeOH** methanol.

**MIC** minimal inhibitory concentration.

**MID** membrane insertion depth.

**MSI-103** peptide with sequence KIAGKIAKIA GKIAKIAGKI A-NH<sub>2</sub>.

**N** nitrogen.

**NMR** nuclear magnetic resonance.

**O** oxygen.

**PB** Poisson-Boltzmann.

**PFR** (1s,2r)-1-amino-2[4-(trifluoromethyl)phenyl]-cyclopropane-1-carboxylic acid.

**PFS** (1s,2s)-1-amino-2[4-(trifluoromethyl)phenyl]-cyclopropane-1-carboxylic acid.

**PGLa** peptide peptidyl-glycine-leucine-carboxamide, sequence GMASKAGAIA GKI-AKVALKA L-NH<sub>2</sub>.

**PGR** (2R)-amino[4-(trifluoromethyl)phenyl]acetic acid.

**PGS** (2S)-amino[4-(trifluoromethyl)phenyl]acetic acid, also known as CF<sub>3</sub>-Phg.

**PME** Particle-Mesh Ewald.

**POPC** 1-palmitoyl-2-oleoyl-phosphatidylcholine.

**POPG** 1-palmitoyl-2-oleoyl-phosphatidylglycerol.

**PRR** (1r,2s)-1-amino-2[4-(trifluoromethyl)phenyl]-cyclopropane-1-carboxylic acid.

**PRS** (1r,2r)-1-amino-2[4-(trifluoromethyl)phenyl]-cyclopropane-1-carboxylic acid.

**PV\_SC1** GS analog, where Pro-Val is replaced with SC1.

**PV\_SC2** GS analog, where Pro-Val is replaced with SC2.

**PV\_SWO** GS analog, where Pro-Val is replaced with SWO.

**RESP** restrained electrostatic potential.

**RMSD** root mean square deviation.

**RMSF** root mean square fluctuation.

**RP-HPLC** reverse-phase high-performance liquid chromatography.

**SC1** diarylethene-based photoswitch in 'ring closed' state, (S,S)-diastereomer.

**SC2** diarylethene-based photoswitch in 'ring closed' state, (R,R)-diastereomer.

**SEM** scanning electron microscopy.

**SES** solvent excluded surface.

**SSNMR** solid-state nuclear magnetic resonance.

**SWO** diarylethene-based photoswitch in 'ring open' state.

**TEM** transmission electron microscopy.

**TempA** peptide temporin A, sequence FLPLIGRVLSGIL-NH<sub>2</sub>.

Amino acid sequences are given in the standard one-letter or three-letter code. O (Orn) stands for ornithine, <sup>D</sup>F (<sup>D</sup>Phe) for D-phenylalanine.

# 1. Introduction

## 1.1 Antibiotics and antimicrobial peptides

In World War II, the mass production of penicillin [1] made it possible to use it widely for the treatment of infected wounds, reducing greatly the number of amputations and deaths caused by bacterial infections. The discovery of the antibiotic penicillin was published in 1929 by Fleming, he isolated it from the mold *Penicillium*, and showed that it caused lysis of staphylococcal colonies [2]. The structure of penicillin was solved 20 years later by the Nobel prize winner Dorothy Hodgkin, using X-ray analysis [3]. Again almost 20 years later, in 1965, the mechanism of action was proposed to be an inhibition of the cell wall synthesis [4], which was confirmed in 1979 [5]. Penicillin binds to the D-alanine-transpeptidase, which is an enzyme responsible for the formation of peptidoglycan cross-links in the cell wall of Gram-positive bacteria. The binding of penicillin inhibits this enzyme and causes lysis of the cellular membrane. Thus, penicillin is historically the first member of the class of  $\beta$ -lactam antibiotics.

In 1940, some years before the introduction of penicillin as a therapeutic agent, however, a bacterial penicillinase was identified [6] in *Escherichia coli* (*E. coli*), an enzyme which was capable to destroy penicillin. Until 2010, up to 1000 resistance-related  $\beta$ -lactamases have been identified [7], which render  $\beta$ -lactam antibiotics ineffective. Additionally, the short reproduction times and horizontal gene transfer of bacteria constantly lead to the emergence of novel resistant strains of bacteria which have genetically altered binding sites [8]. In these bacteria, the antibiotic compounds cannot bind to their binding site (the transpeptidase for penicillin) and are thus inefficient. The mutation of binding sites is a powerful resistance mechanism also against macrolides, which bind to the peptide exit tunnel of the ribosome, thereby inhibiting peptide synthesis [9].

Within the last 60 years, when antibiotics were therapeutically used against various types of infections, also the antibiotic resistance has drastically grown. One of the causes is the systemic prophylactic use of antibiotics, even when not required or

actually useless (e.g. because the disease is caused by a viral infection). The second cause is the prophylactic application of antibiotics in animal husbandry, which was identified as a problem already in 1958 [10].

In 2014, the World Health Organization published a report on antimicrobial resistance, where they issued a warning of a currently emerging post-antibiotic era, when already common infections and minor injuries start killing again [11].

For these reasons, many new compounds are needed, which has rendered a new class of antibiotic agents increasingly interesting within the last 20 years: the antimicrobial peptides (AMPs), also known as host defense peptides. In contrast to 'conventional' antibiotics, they do not target a specific site on a protein or ribosome, but act directly on the bacterial cell membrane [12]. It is therefore less likely for bacteria to develop resistances against AMPs.

The first AMP was Gramicidin A, discovered by Dubos and published in 1941 [13]. Gramicidin A was isolated from *Bacillus brevis* and bactericidal against Gram-positive bacteria. Until 2014, a few tens of thousands AMPs, natural and synthetic ones, have been discovered. Naturally occurring AMPs are produced by all organisms, be it unicellular microorganisms or bigger organisms like plants, insects, anurans or mammals. Secretions from frog skin, for example, contain more than 300 different AMPs [14, 15].

AMPs are polypeptides and range from 10 to 50 amino acids [16]. They are generally cationic, which allows them to bind to the negatively charged phospholipids of bacterial membranes by electrostatic attraction [17]. Generally, helical AMPs are unstructured in solution and fold once bound to the membrane. Typically, five types of AMPs can be distinguished based on their secondary structure in the membrane-bound state:  $\beta$ -sheet,  $\alpha$ -helix, non-structured, cyclic and mixed. The AMPs studied in this work are all  $\alpha$ -helical except for the cyclic  $\beta$ -sheet-folded gramicidin S (GS). Figure 1.1 describes some postulated mechanisms of action between AMPs and phospholipid membranes. The membrane bound structure is generally amphiphilic, such that hydrophobic side chains are located on one side of the peptide, and hydrophilic side chains on the opposite side of the peptide [18]. This amphiphilicity allows the peptides to embed into the phospholipid bilayer in such a way that their hydrophobic face points towards the membrane core, while the polar or charged side chains point towards the water phase [19, 20].

One postulated mode of action is the pore formation, where peptides start to insert vertically into the membrane and oligomerize to pores, once the concentration of peptides on the membrane surface is high enough [20]. In this trans-membrane

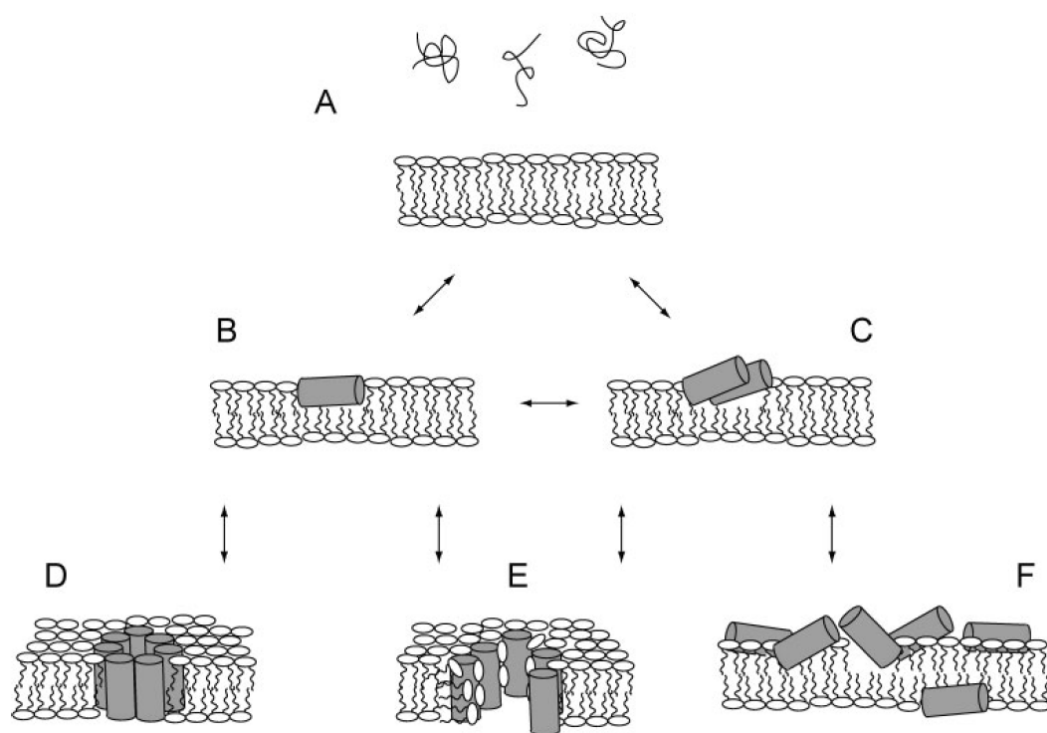


Figure 1.1: Postulated mechanisms of action of AMPs. A: Peptides are unstructured in solution. B: Once bound to the membrane, the peptides fold to an amphiphilic conformation. C: Peptides dimerize or form higher oligomers, while still lying flat on the membrane surface. D, E and F: Insertion into the membrane at high peptide concentrations, forming a barrel-stave pore (D), a toroidal pore (E), where the lipid head groups relocate such that they cover the entire surface of the pore, or where they permeabilize the membrane via the 'carpet' mechanism (F). Figure from [16].

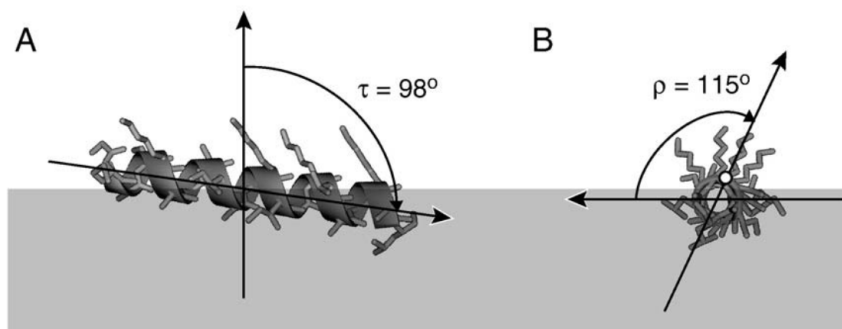


Figure 1.2: 'Definitions of the orientational angles. A: The tilt angle  $\tau$  is the angle between the membrane normal and the helix long axis, which is defined to point from the N- to the C-terminus. B: The azimuthal rotation angle  $\rho$  is defined as a right-handed rotation around the helix long axis, with  $0^\circ$  defined to place the vector from the helix axis to the  $C_\alpha$  atom of position 12 (marked with a white circle) parallel to the membrane plane.' [41]

orientation the hydrophobic side chains are postulated to face towards the hydrophobic membrane core, while the hydrophilic side chains point towards the hydrophilic interior of the pore [12]. Another possibility is the disturbance of the membrane via the so-called 'carpet' model, whereby the membrane is permeabilized without the need of pore formation [21].

Unfortunately, AMPs can generally act in a similar way towards the membrane of erythrocytes, in whose membranes phospholipids with zwitterionic head groups are more abundant, and can cause hemolysis [22–24]. Recent studies also showed that the use of AMPs can stimulate the growth of biofilms, thereby enhancing the risk of persistent infections [25].

These side effects and the lack of a detailed physico-chemical understanding of the underlying mechanisms of action still prevent AMPs to be used against bacterial infections. Solid-state nuclear magnetic resonance (SSNMR) measurements in oriented phospholipid bilayers [26–30] and circular dichroism (CD) spectroscopy [31–37] provide important structural and dynamic information, which helps in the understanding of the behaviour on AMPs. This is typically described in an internal coordinate system defined by the helix tilt angle, azimuthal rotation angle, insertion depth, and information on whole-body dynamics (Figure 1.2) [20, 27, 38–40]. However, these results are averages, giving a time-averaged picture over milliseconds to seconds and a big ensemble of peptides in possibly different conformations.

In recent years, both coarse-grained and all-atom molecular dynamics (MD) simulations have been used to reproduce and predict the geometry of peptide-membrane assemblies [42–47]. With simulations, it is possible to get an insight on the femtosecond timescale and at atomic resolution. Even though MD simulations are generally

not yet capable of covering experimental time scales due to hardware constraints, they are a useful and inexpensive tool to investigate peptide-membrane interactions.

This thesis is devoted to the development of computational tools and MD simulations, which help in the interpretation and prediction of SSNMR data.

In Chapter 4, four helical AMPs have been simulated in a dimyristoylphosphatidylcholine (DMPC) membrane. Their orientation and structure has been analyzed and compared with the experimental SSNMR data, to get systematic information about the validity of the simulations, and to draw conclusions concerning the interpretation of experimental data. Chapter 5 introduces a computational tool which was developed to predict the membrane-inserted orientations of amphiphilic peptides directly from their structure. An extensive study of photo-switchable analogs of GS is presented in Chapter 6, which helps in the understanding of the molecular basis of the photoregulation. Finally, Chapter 7 presents the results of a computational study of fluorine-based SSNMR labels, which are already used or considered for the determination of orientational constraints for membrane-active peptide. Here, important geometric parameters were calculated and the potential disturbance of the labels in the natural peptide structure was evaluated.

## 1.2 Peptides studied in this work

The following seven peptides, and photoswitchable analogs of GS, were studied in this work.

### 1.2.1 PGLa

In 1985, the AMP peptidyl-glycine-leucine-carboxyamide (PGLa) (charge +5, GMASK-AGAIA GKIAKVALKA L-NH<sub>2</sub>) was identified in the skin secretion of *X. laevis*, after being predicted from the nucleotide sequence [48].

Atomic force microscopy studies showed, that *E. coli* treated with PGLa caused the loss of surface stiffness and finally the total cell rupture. It was suggested that PGLa interacts with the outer membrane by displacing Mg<sup>2+</sup> ions from lipopolysaccharides, inserting itself into the bilayer [49]. Similar results were obtained from scanning electron microscopy (SEM) and transmission electron microscopy (TEM) experiments on Gram-negative and Gram-positive bacteria treated with PGLa [50]. Here, shortening and swelling of the *E. coli* bacteria, as well as the formation of 'blisters and bubbles' could be observed.

PGLa was shown to be helical between residues 6 and 21 using solid-state <sup>15</sup>N

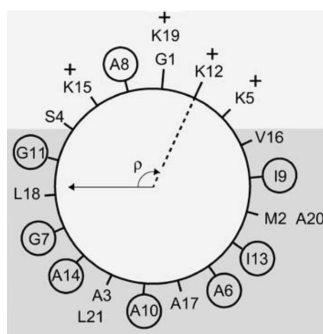


Figure 1.3: Sequence of PGLa, in the projection on the Edmundson helical wheel, showing an amphipathic  $\alpha$ -helix. All charged side chains and the charged amino-terminus are in the upper region of the helical wheel (light grey), while all hydrophobic amino acids are in the lower part (dark grey). Figure from [52].

SSNMR, and to lie flat in oriented bilayers [51]. The distribution of the side chains on the helical wheel in Figure 1.3 shows, that it is an amphipathic  $\alpha$ -helix. The membrane-aligned orientation was confirmed by studies with  $^{19}\text{F}$  labeled peptides at a low peptide:lipid concentration of 1:200 in a DMPC bilayer, in native biomembranes of the Gram-positive bacterium *Micrococcus luteus* and human erythrocytes [53]. The azimuthal rotation angle of the helical axis was also defined, resulting in an orientation where the charged side chains point towards the aqueous side, as expected [54].

At higher peptide:lipid concentrations of  $\geq 1:80$  molar ratio, a tilted state with a tilt angle of  $\sim 120^\circ$  against the membrane normal was observed with  $^{19}\text{F}$  SSNMR, where the carboxy-terminus pointed towards the bilayer interior [19]. Qualitatively the same orientations were observed with potentially less disturbing  $^2\text{H}$  SSNMR labels [52]. Here the tilt angle at a concentration of 1:50 was measured to be  $\sim 125^\circ$ . It was shown that even at very high peptide:lipid ratios of 1:35, PGLa did not fully insert into the membrane, but remained in this tilted state. In DMPC vesicles at a peptide:lipid ratio of 1:50, an intermediate state was observed, suggesting a rapid exchange between the surface-aligned and the tilted state, or between a bound and a non-bound state. It was shown that this equilibrium was sensitive to the peptide concentration, the lipid composition and the sample hydration [55]. With  $^{19}\text{F}$  SSNMR measurements below the lipid phase transition, a fully inserted state could be detected, at a peptide:lipid ratio of 1:50 in a DMPC/dimyristoylphosphatidylglycerol (DMPG) mixture (3:1 mol:mol) [56] (Figure 1.4).

Also based on  $^2\text{H}$  SSNMR, it was shown that in a 1:1 mixture with magainin 2 (Mag2), PGLa inserts almost vertically into the membrane, at tilt angle of  $\sim 158^\circ$

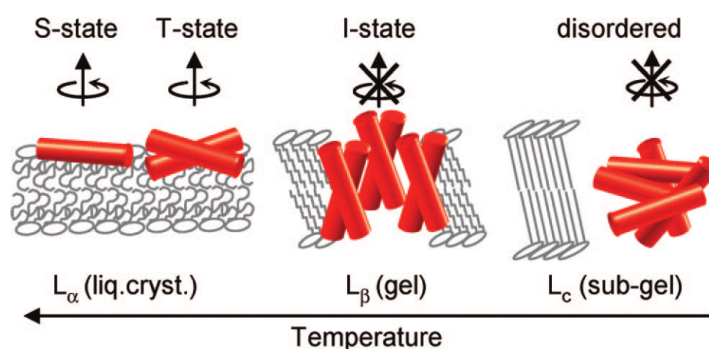


Figure 1.4: The different postulated states of PGLa in a phospholipid membrane. In the liquid crystalline phase, a surface-aligned state (S-state) and a tilted state (T-state) could be observed, the latter might be result of a dimerization. In the gel-phase, a state was found where PGLa was almost vertically inserted (I-state). At temperature below the gel-phase, no defined orientation could be observed. Figure from [56].

[41, 57, 58]. Recently, it was shown that the tilt angles of PGLa and Mag2 alone or in a mixture depend strongly on the lipid composition [59].

Computational studies investigated a possible dimer formation in the tilted state [60]. Although a preformed antiparallel dimer was stable throughout the simulations, the tilt angles of the two peptides were much too low with  $103^\circ$  resp.  $107^\circ$  in two different force fields, compared to  $\sim 125^\circ$  found in SSNMR studies.

### 1.2.2 Magainin 2

The helical magainin 2 (Mag2) is a member of the magainin family of AMPs, found in *Xenopus laevis* (*X. laevis*), like PGLa. It is 23 amino acids long with the following sequence: GIGKFLHSAK KFGKAFVGEI MNS. It displays antibiotic activity against numerous Gram-negative and Gram-positive bacteria, but was found to be only moderately hemolytic [61].

In  $^2\text{H}$  SSNMR measurements it was shown that PGLa and Mag2 work synergistically in the membrane, since the presence of Mag2 enables PGLa to insert vertically into the membrane [41, 57, 58]. Recently it was shown, that this synergistic trans-membrane insertion depends on the lipid composition [59], whereas Mag2 is generally in a surface aligned state or slightly tilted, while the tilt angle of PGLa changes drastically from case to case.

### 1.2.3 Temporin A

The small 13 amino acid long,  $\alpha$ -helical AMP temporin A (TempA) belongs to the group of temporins, isolated from the skin of the European red frog *Rana temporaria*

(*R. temporaria*). Its amino acid sequence is FLPLIGRVLSGIL-NH<sub>2</sub>. It is active against Gram-negative and Gram-positive bacteria, without any evidence for hemolysis [62]. Especially, TempA is active against the dangerous methicillin-resistant strain of *Staphylococcus aureus* (MRSA) [63] and certain tapeworm parasites [64]. It was shown by <sup>19</sup>F SSNMR that in DMPC bilayers at peptide:lipid ratios of 1:50 and 1:20, TempA is tilted at an angle of 135° with respect to the membrane normal [65].

#### 1.2.4 Gramicidin S

GS was discovered in 1942 in the soil bacterium *Aneurinibacillus migulanus* (earlier known as *Bacillus brevis*) [66,67]. It was shown to be antimicrobially active against various bacterial strains, both Gram-negative and Gram-positive bacteria. In more recent studies in *E. coli*, a disruption of the permeability barrier of outer membrane was observed, followed by an efflux of K<sup>+</sup> ions [68]. Dormant spores of *Bacillus subtilis* (*B. subtilis*) were inhibited in their germination and growth by treatment with GS. The damage could be located not only to the outer membrane-spore coat complex, but also to the inner membrane surrounding the spore protoplast [69].

A study using TEM and SEM visualized the irritating effect, which GS has on bacterial membranes, showing 'blisters' and 'bubbles', and interactions with the inner membrane of Gram-negative bacteria [50]. Hemolysis studies showed that GS permeabilizes also the membranes of erythrocytes, producing small membrane lesions which result in the release of hemoglobin [70] and of membrane fragments [71].

GS is a cyclic, non-ribosomal decapeptide with the sequence *cyclo*(Val-Orn-Leu-<sup>D</sup>Phe-Pro)<sub>2</sub> (Orn stands for ornithine, <sup>D</sup>Phe for D-phenylalanine), which was published in 1947, elucidated by paper chromatography [72]. In 1957, Dorothy Hodgkin proposed that GS is structured in a cyclic, C<sub>2</sub>-symmetric β-sheet, connected by 4 intra-molecular hydrogen bonds (H-bonds) [73], which was later confirmed by SS-NMR measurements [74].

In the first computational work from 1984, a minimum-energy conformation was found [75] with additional side chain H-bonds from the Orn side chain to the carboxy-oxygen of the following <sup>D</sup>Phe. In the first MD study, GS was simulated for 5 ns in a dimethylsulfoxide (DMSO) solution [76]. In this study, one of two Orn side chains was involved in a H-bond with the following <sup>D</sup>Phe. The same group performed the first MD study in a DMPC membrane [77]. In the 6.5 ns simulation, GS maintained the preformed orientation, pointing its Orn side chains towards the water region and its hydrophobic side towards the membrane interior. In the membrane simulations, again two side chain H-bonds from Orn to <sup>D</sup>Phe were visible.

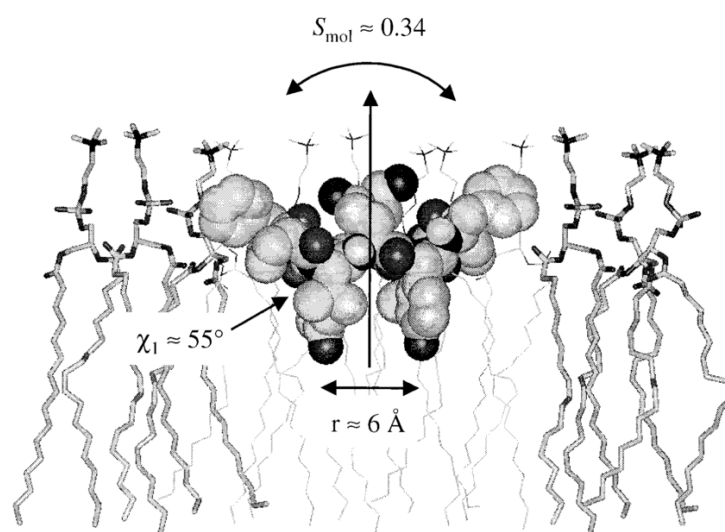


Figure 1.5: GS, as it is oriented in a phospholipid bilayer at low concentration. The charged Orn side chains reach towards the water phase, while the hydrophobic side chains point towards the hydrophobic membrane core. Figure from [78].

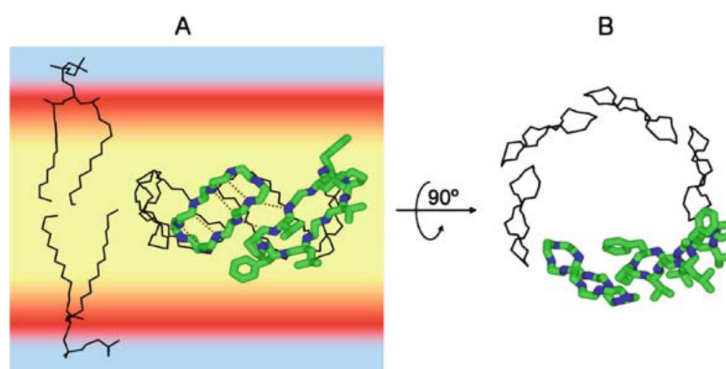


Figure 1.6: Putative model of a GS pore, based on a multinuclear SSNMR study which showed GS in an upright, membrane-spanning orientation. Figure from [80].

$^{19}\text{F}$  SSNMR studies in a DMPC bilayer at a peptide:lipid ratio of  $\geq 1:80$  showed an orientation where the symmetry axis of the peptide was aligned with the membrane normal, in both the gel-phase and the liquid-crystalline phase [78]. In the liquid-crystalline phase, a high mobility was observed (Figure 1.5).

The possibility of transmembrane pores formed by GS was investigated via crystallization experiments [79] and  $^{19}\text{F}$  SSNMR, combined with  $^{15}\text{N}$  SSNMR. In the SSNMR experiments, a flip into an upright orientation could be observed at a peptide:lipid ratio of  $\geq 1:40$ , which resulted in the postulation of an oligomeric  $\beta$ -barrel pore, stabilized by intermolecular H-bonds (Figure 1.6). It was shown that pore formation was favoured in thin membranes with short-chain lipids, while the upright orientation could not be observed in long-chain lipids.

### 1.2.5 BP100

The short designer-made undecapeptide BP100 (sequence KKLFFKKILKYL-NH<sub>2</sub>) was optimized by a combinatorial approach to be active against phytopathogenic Gram-negative bacteria [23] and *E. coli* [81], while having low hemolytic activity.

Using CD spectroscopy, it was shown that the peptide folds as a stable  $\alpha$ -helix in the presence of DMPC/DMPG vesicles and lies qualitatively flat in the membrane. While <sup>15</sup>N SSNMR also showed a surface aligned state at different peptide:lipid concentrations, the analysis via <sup>19</sup>F labels showed, that the best fit of the measured splittings resulted in a much more tilted state with a tilt angle of 156° with respect to the membrane normal. However, the possible range of fits with the experimental data allows a broad spectrum with tilt angles from 110° to 160°. Together with the results from <sup>15</sup>N SSNMR and CD spectroscopy, the authors concluded a surface-aligned orientation with a tilt angle of ~110° [21].

### 1.2.6 MSI-103

The designer-made antibiotic MSI-103, whose sequence (KIAGKIA)<sub>3</sub>-NH<sub>2</sub> was derived from PGLa, is an  $\alpha$ -helical, amphiphilic peptide. Like its parent peptide PGLa, it is active against Gram-negative and Gram-positive bacteria and also causes hemolysis [82]. <sup>2</sup>H SSNMR data showed that the peptide lies flat in a DMPC membrane at low peptide:lipid ratio of 1:200 and is more tilted at a higher peptide:lipid ratio of 1:50 [31]. The observed orientations are very similar to the ones observed for PGLa at equal experimental settings. In a recent study it was shown, that the membrane-inserted orientation depends on the lipid curvature [59].

### 1.2.7 KIA14

KIA14 is a short designer-made peptide with the sequence (KIAGKIA)<sub>2</sub>-NH<sub>2</sub>. It has the same subsequence (KIAGKIA) as MSI-103 and assumes a generally  $\alpha$ -helical structure. CD spectroscopy and <sup>2</sup>H SSNMR measurements showed that KIA14 is helical from positions 4-14 and is oriented in a surface-aligned state. It is part of a systematic study of peptides with the repeated sequence motif KIAGKIA (publications underway in the group of Anne S. Ulrich at KIT).

## 2. Theory

### 2.1 Molecular dynamics simulations

In MD simulations, all atoms of a simulated system are treated as classical particles. This means, that the electrons are not treated explicitly, but the atoms have constant partial charges, derived from *ab initio* calculations or considerations of thermodynamic properties of the system.

The atoms are grouped into so-called 'atom types', which are defined by their chemical environment. For example, there are different atom types for a carbon in a carbonyl, an aromatic ring or an aliphatic group.

#### 2.1.1 Bonded interactions

For each pair of atom types, a bond potential is defined. Generally, a harmonic potential is used to describe bonds, shown in Equation 2.1. This avoids bond dissociation, which would result in the necessity to recalculate atomic charges. The potential  $V_b$  depends on the distance between the two atoms  $r_{ij}$  and is characterised by an equilibrium distance  $b_{ij}$  and a force constant  $k_{ij}^b$ , both of which are specific for the pair of atom types  $i$  and  $j$ :

$$V_b(r_{ij}) = \frac{1}{2}k_{ij}^b(r_{ij} - b_{ij})^2. \quad (2.1)$$

The angular vibrations between two connected bonds  $ij$  and  $jk$  (e.g. for water), are also defined by a harmonic potential, specific for the atom types  $i$ ,  $j$  and  $k$ :

$$V_a(\theta_{ijk}) = \frac{1}{2}k_{ijk}^\theta(\theta_{ijk} - \theta_{ijk}^0)^2. \quad (2.2)$$

Here, the potential depends on the angle between the two bonds  $\theta_{ijk}$  and is characterised by the equilibrium angle  $\theta_{ijk}^0$  and the force constant  $k_{ijk}^\theta$ .

In the model used in this work for the description of the phospholipid bilayer,

SLIPDS [83], this potential is extended with a harmonic correction term on the distance between atoms  $i$  and  $k$ , resulting in a Urey-Bradley potential [84]:

$$V_a(\theta_{ijk}) = \frac{1}{2}k_{ijk}^\theta(\theta_{ijk} - \theta_{ijk}^0)^2 + \frac{1}{2}k_{ijk}^{UB}(r_{ik} - r_{ik}^0), \quad (2.3)$$

The dihedral potential which describes the rotation around the bond  $jk$ , when the four atoms  $i, j, k$  and  $l$  are connected in the three bonds  $ij, jk$ , and  $kl$ , is a sum of periodic functions of the type

$$V_d(\phi_{ijkl}) = k_{\phi_{ijkl}}(1 + \cos(n\phi_{ijkl} - \phi_s)), \quad (2.4)$$

where  $\phi_{ijkl}$  is the dihedral angle between the bonds  $ij$  and  $kl$  in the projection along the  $jk$  bond,  $n$  the periodicity,  $\phi_s$  the phase shift and  $2k_{\phi_{ijkl}}$  the maximal energetic barrier. This is called a proper dihedral potential.

Planar molecules are kept planar with a harmonic improper dihedral potential

$$V_{id}(\xi_{ijkl}) = \frac{1}{2}k_{xi}(\xi_{ijkl} - \xi_0)^2, \quad (2.5)$$

where  $\xi_{ijkl}$  is the angle between the planes  $ijk$  and  $jkl$ ,  $k_{xi}$  the force constant and  $\xi_0$  the equilibrium angle.

### 2.1.2 Nonbonded interactions

Van-der-Waals interactions between two atoms  $i$  and  $j$  are described by a Lennard-Jones potential:

$$V_{LJ}(r_{ij}) = 4\epsilon_{ij} \left( \left( \frac{\sigma_{ij}}{r_{ij}} \right)^{12} - \left( \frac{\sigma_{ij}}{r_{ij}} \right)^6 \right), \quad (2.6)$$

Here, each atom type has two Lennard-Jones parameters  $\epsilon_i$  and  $\sigma_i$ . For a potential between two atoms, these parameters are averaged following the combination rules:  $\epsilon_{ij} = \sqrt{\epsilon_i \cdot \epsilon_j}$  and  $\sigma_{ij} = \frac{1}{2}(\sigma_i + \sigma_j)$ .  $-\epsilon_{ij}$  is the depth of the potential minimum,  $\sigma_{ij}$  is the zero crossing point of the potential.

Electrostatic interactions are treated by Particle-Mesh Ewald (PME), where the long-range part of the interaction is computed exclusively in Fourier space based on Gaussian charge distributions, and for the short-range interactions an additional real-space sum is computed. The exact calculation is too complex for this scope and can be looked up in [85].

### 2.1.3 Propagation of the system

The initial structure of a given simulation system is defined by the coordinates  $\mathbf{r}_i$  and velocities  $\mathbf{v}_i$  of all particles  $i$ . The new coordinates and velocities after a timestep  $\Delta t$  (in this work,  $\Delta t = 2$  fs) are calculated via the *leap-frog* algorithm [86] based on the old coordinates at time  $t$  and the velocities at time  $t - \frac{1}{2}\Delta t$ , and on the force  $\mathbf{F}_i(t)$  determined by the positions at time  $t$  [87]:

$$\mathbf{v}_i(t + \frac{1}{2}\Delta t) = \mathbf{v}_i(t - \frac{1}{2}\Delta t) + \frac{\Delta t}{m} \mathbf{F}_i(t) \quad (2.7)$$

$$\mathbf{r}_i(t + \Delta t) = \mathbf{r}_i(t) + \Delta t \cdot \mathbf{v}_i(t + \frac{1}{2}\Delta t) \quad (2.8)$$

The force  $\mathbf{F}_i$  is the negative derivative of the total potential  $V_{tot}$ , which is the sum of the potentials described above, by the coordinates of particle  $i$ :

$$\mathbf{F}_i = -\frac{\partial V_{tot}}{\partial \mathbf{x}_i} \quad (2.9)$$

## 2.2 Nuclear magnetic resonance spectroscopy

Protons and neutrons, the constituents of the nuclei of atoms or nucleons, both have an intrinsic angular momentum or spin with value  $1/2$ . Being combined to a nucleus, the spins and orbital angular momenta of the nucleons combine to the total spin of the nucleus. Even numbers of nucleons result in an integer spin, otherwise the spin is half-integral. If both the number of protons and the number of neutrons are even, the nucleus spin is zero.

The magnetic moment of a nucleus is

$$\boldsymbol{\mu} = \gamma \mathbf{s} \quad (2.10)$$

where  $\mathbf{s}$  is the nuclear spin and  $\gamma$  is the gyromagnetic constant which is characteristic for every nuclide, i.e. for every possible combination of protons and neutrons in atomic nuclei.

The orientation of a non-zero magnetic moment is constrained by quantum mechanics. There are  $2s+1$  possible orientations, e.g. a hydrogen nucleus with  $s = \frac{1}{2}$  has two orientations with  $m_s = \frac{1}{2}$  and  $m_s = -\frac{1}{2}$ , whereas a deuterium nucleus with  $s = 1$  has three orientations with  $m_s = [-1, 0, 1]$ .

While these orientation states are energetically degenerate without an exterior

magnetic field, they have different energies in the presence of an exterior magnetic field  $B_0$ . The energy difference between neighboring levels or 'coupling' is

$$\Delta E = \hbar\gamma B_0 = -\hbar\omega_0 \quad (2.11)$$

with the resonance or 'Larmor' frequency  $\omega_0$ . The nuclear magnetic resonance (NMR) sensitivities of the nuclei depend on their gyromagnetic ratio  $\gamma$  like  $\propto \gamma^3$ . In this work, the simulation results have been compared with experimental results from  $^2\text{H}$  NMR ( $\gamma/2\pi = 6.53$  MHz/T) and  $^{19}\text{F}$  NMR ( $\gamma/2\pi = 40.03$  MHz/T) [26].

### 2.2.1 $^2\text{H}$ NMR

#### Electric quadrupole coupling

All nuclei with a spin  $s > 1/2$ , like  $^2\text{H}$  with  $s = 1$ , have an electric quadrupole moment and interact with the electric field gradient of the environment [88]. This 'electric quadrupole coupling' causes a shift of the energy levels described above. For  $^2\text{H}$  this means, that  $\Delta E$  between the first and the second energy level is lower than  $\Delta E$  between the second and the third energy level, leading to two different resonance frequencies and thus NMR signals. The difference between the two signals is called 'splitting' and is defined as

$$\Delta\nu_q = S_{mol} \cdot K \cdot \frac{1}{2}(3 \cos^2 \vartheta - 1) \quad (2.12)$$

Here,  $\vartheta$  is the angle between the major principal axis of the electric field gradient tensor and the magnetic field [89].  $K$  is a constant defined by

$$K = \frac{3}{2} \frac{e^2 Q q}{h} \quad (2.13)$$

and includes the quadrupolar coupling constant  $\frac{e^2 Q q}{h}$ , which is specific for a given isotope.

For a completely static C- $^2\text{H}$  bond,  $K \approx 250$  kHz [89]. However, in the  $^2\text{H}$  NMR studies mentioned in this work, the hydrogen atoms in the methyl group of Ala are replaced with  $^2\text{H}$ . Due to the rapid rotation of the methyl group, the major principal axis of the electric field gradient tensor is equivalent to the direction of the  $\text{C}_\alpha\text{-C}_\beta$  bond. The fast rotation of the methyl group leads to a reduction of the splittings  $\Delta\nu_q$  by a factor of 1/3. Thus, a value of  $K = 84$  kHz is used in these studies [90].

$S_{mol}$  is a constant between 0 and 1, to account for the motional averaging of the complete peptide, which also causes a reduction of the splittings. For  $S_{mol}=1$ , the

molecule is very rigid (although there might be a rotation about the  $z$ -axis), for  $S_{\text{mol}}=0$ , the molecule is tumbling fast and isotropically. From the NMR measurements, the magnitude, but not the sign of  $\Delta\nu_q$  is accessible.

### 2.2.2 $^{19}\text{F}$ NMR

Due to its 6 times higher gyromagnetic ratio, the NMR sensitivity of the  $^{19}\text{F}$  nucleus is two orders of magnitude higher than that of the  $^2\text{H}$  nucleus, while having 100% natural abundance. At the same time, fluorine participates rarely in biological processes. The high sensitivity and the absence of background signals allow the use of small amounts of labeled material and shorter measuring times. For these reasons, fluorine NMR has become an important tool in the elucidation of molecular structures within the past years [26].

#### Dipolar coupling

The homonuclear dipolar coupling between two nuclei with spin  $s = 1/2$  like in the case of  $^{19}\text{F}$  leads to splittings which are defined by

$$\Delta\nu_d = S_{\text{mol}} \cdot K \cdot \frac{1}{2}(3 \cos^2 \vartheta - 1), \quad (2.14)$$

Here  $\vartheta$  is the angle between the F–F directional vector and the magnetic field. In the case of a fast rotating  $\text{CF}_3$  group,  $\vartheta$  is the angle between the C– $\text{CF}_3$  bond and the magnetic field.

K is

$$K = 3\hbar\gamma_F^2 \frac{\mu_0}{4\pi} \frac{1}{r^3}, \quad (2.15)$$

with  $\gamma_F$ , the gyromagnetic ratio for  $^{19}\text{F}$  mentioned above, the magnetic constant  $\mu_0$  and the F–F distance  $r$ .

The averaging of the fast rotational motion of the  $\text{CF}_3$  group leads to an additional factor  $1/2$ , which results in a value of  $K = 17.0$  kHz [91].  $S_{\text{mol}}$  is defined as above.

Here, the sign of  $\Delta\nu_d$  can also be determined, from the chemical shift of the signal [54].



## 3. Methods

### 3.1 Simulations

All MD simulations were conducted using the molecular simulation package GRO-MACS 4.5.5 [92] with a time step of 2 fs and the PME method [85] for long range electrostatics with a cut-off radius of 1.4 nm (1.2 nm in Chapter 6) and constraints on all bonds, using the LINCS algorithm [93]. Production simulations used for statistical evaluation were conducted with a *Nosé-Hoover* thermostat [94] and a *Parrinello-Rahman* [95] barostat, unless otherwise stated. For the membrane simulations, semiisotropic pressure coupling was used.

#### 3.1.1 Membrane simulations

Simulations were conducted in a DMPC bilayer solvated in TIP3P water [96] and neutralized with chloride ions. The numbers of the lipids and water molecules is stated in the individual chapters. The SLIPID force field was used for the lipids [83], and the AMBER99SB-ILDN [97] force field for everything else, unless otherwise stated.

The helical peptides were initially modeled as ideal  $\alpha$ -helices using the *xleap* tool from the AmberTools modelling suite [98]. The modelling of starting structures for the GS peptidomimetics in Chapter 6 is described there.

The peptide-membrane complexes were constructed by conducting unrestrained membrane binding simulations of 10-20 ns length, placing the peptide molecules parallel to pre-equilibrated lipid bilayers at distances of  $\sim 2$  nm, at an elevated temperature of 480 K (respectively 400 K in Chapter 6), to speed up insertion (simulation protocol from [60]). During the high temperature insertion, H-bonds in the helical peptides were restrained using distance restraints of 1000 kJ/(mol nm<sup>2</sup>) to prevent unfolding. After cooling down to 303 K (respectively 308 K in the simulations of BP100 and TempA in Chapter 5), a short equilibration run of 500 ps with position restraints of 1000 kJ/(mol nm<sup>2</sup>) on the membrane-inserted peptides was performed to

allow temperature and volume to stabilize. Then, the systems were simulated without any restraints at 303 K for several hundred nanoseconds in the NPT ensemble (constant pressure  $P$ , temperature  $T$  and number of particles  $N$ ).

### 3.2 Helicity calculation

The helicity  $H_i$  was determined for each residue  $i$  based on the dihedral angles  $\Psi$  ( $N_i, C_{\alpha, i}, C_i, N_{i+1}$ ) and  $\Phi$  ( $C_{i-1}, N_i, C_{\alpha, i}, C_i$ ):

$$H_i = \frac{1}{N_{\text{timesteps}}} \sum^{N_{\text{timesteps}}} h_i \quad (3.1)$$

$$h_i = \begin{cases} 1, & \text{if } (\Psi_0 - 30^\circ) < \Psi_i < (\Psi_0 + 30^\circ) \\ & \text{and } (\Phi_0 - 30^\circ) < \Phi_i < (\Phi_0 + 30^\circ), \\ 0, & \text{otherwise} \end{cases} \quad (3.2)$$

A residue is counted as helical at a specific snapshot, if  $\Psi$  and  $\Phi$  are within  $30^\circ$  around their ideal values  $\Psi_0 = -47^\circ$  and  $\Phi_0 = -57^\circ$ . This means, a residue is 100% helical if the condition in Equation 3.2 is fulfilled for all evaluated time steps.

### 3.3 Calculation of the peptide orientation

The tilt angle  $\tau$  is the angle between the helical axis defined from the amino-terminus to the carboxy-terminus and the membrane normal, see Figure 3.1A. If  $\tau$  is  $90^\circ$ , the peptide lies flat in the membrane. The azimuthal rotation angle  $\rho$  is the rotation angle of the  $C_\alpha$ -atom of the 12th residue about the helical axis (Figure 3.1D). If  $\rho$  is  $90^\circ$ , the  $C_\alpha$  of the 12th residue is on top of the helix, pointing directly towards the water phase, if its  $0^\circ$  or  $180^\circ$ , it is on the side of the helix. Average values for the angles  $\tau$  and  $\rho$  and some information about dynamics can be obtained from NMR splittings.

The splitting  $\Delta\nu_q$ , which is the difference between two peaks of an NMR spectrum, is directly related to the angle  $\vartheta$  between an NMR-labeled bond (in  $^2\text{H-NMR}$  the  $C_\alpha$ - $C_\beta$  bond) and the external magnetic field  $\mathbf{B}_0$ :

$$\Delta\nu_q = K \langle (3 \cos^2 \vartheta - 1) \rangle \quad (3.3)$$

Here,  $K$  is a constant and  $\langle \rangle$  indicates a time average. In order to calculate the orientational angles  $\tau$  and  $\rho$  from these splittings, one has to know the orientation of the labeled bond with respect to the helical axis. This orientation is defined by the

angles  $\alpha$  and  $\beta$ .  $\beta$  is the angle between the  $C_\alpha$ - $C_\beta$  bond and the helical axis (Figure 3.1B). For  $^{19}\text{F}$  NMR, however,  $\beta$  is defined as the angle between the  $C$ - $\text{CF}_3$  bond (the 'director') and the helical axis, which depending on the labelled amino acid can have very different values.  $\alpha$  is the angle between the connection of the helical axis with a  $C_\alpha$  atom and the  $C_\alpha$ - $C_\beta$  bond, respectively the director in  $^{19}\text{F}$  NMR, in the projection onto the plane perpendicular to the helical axis (Figure 3.1D).

The splitting  $\Delta\nu_q$  can then be written as a function of the angles  $\tau$  and  $\rho$ ,  $\alpha$  and  $\beta$ , and the helix pitch  $\theta$ :

$$\Delta\nu_q = K \cdot S_{mol} \cdot (3 \cos^2 \beta (\cos \tau - \sin \tau \cos \delta^i \tan \beta)^2 - 1) \quad (3.4)$$

$$\delta^i = \rho + \alpha + (i - 12) \cdot \theta \quad (3.5)$$

Here,  $i$  is the number of the labeled residue, starting from the amino-terminus.  $S_{mol}$  is a constant between 0 and 1 to account for the motional averaging. For  $S_{mol}=1$ , the molecule is very rigid (although there might be a rotation about the z-axis), for  $S_{mol}=0$ , the molecule is tumbling isotropically.  $\theta$  is the helix pitch, which is the angle between two subsequent residues (Figure 3.1D).  $\theta$  is  $100^\circ$  for an ideal  $\alpha$ -helix.

The splittings of at least four labeled positions are needed to define the orientational angles  $\tau$  and  $\rho$  unambiguously.

In the fitting procedure, constant values for the angles  $\alpha$  and  $\beta$  are used, which have been derived from a structural model [54]. For  $^2\text{H}$  NMR,  $\alpha = 53.2^\circ$ , and  $\beta = 121.1^\circ$  are used, and  $\theta = 100^\circ$  for all  $\alpha$ -helical peptides [52]. For  $^{19}\text{F}$ -labeled residues,  $\alpha = 47.0^\circ$ , and  $\beta = 110.0^\circ$ , and  $\theta = 100^\circ$  are used [99], or the same as for  $^2\text{H}$  NMR.

A computer program is used to calculate  $\Delta\nu_q$  for different values of  $\tau$ ,  $\rho$  and  $S_{mol}$  using equation 3.4 and 3.5.

For each triplet of  $\tau$ ,  $\rho$  and  $S_{mol}$ , the difference between the calculated and the measured splittings is evaluated for all labelled residues. The best fit is the  $\tau$ ,  $\rho$ ,  $S_{mol}$  triplet which has the lowest root mean square deviation (RMSD) of measured and calculated values.

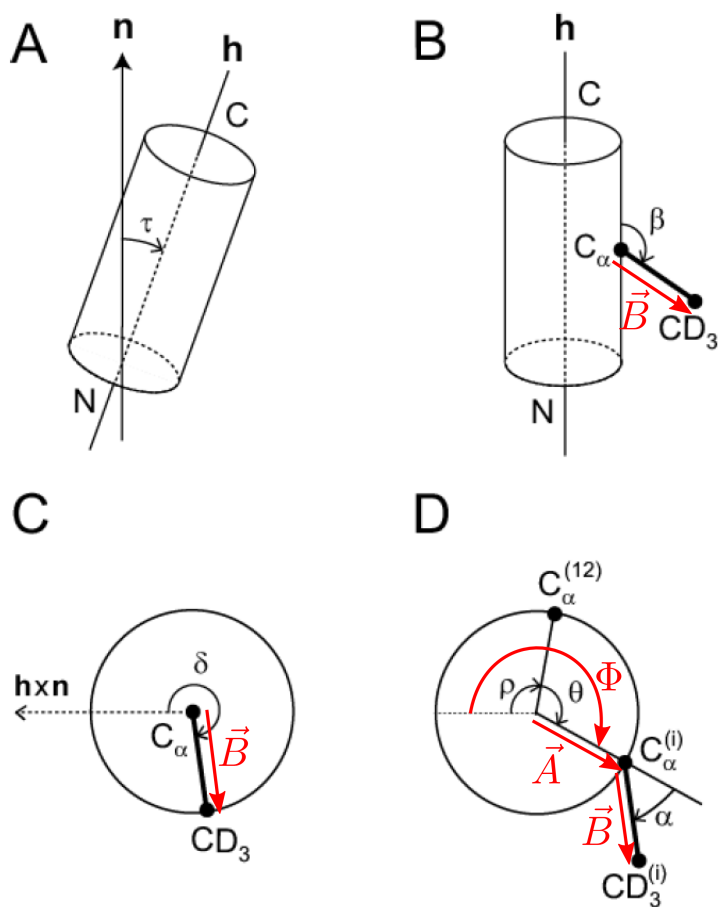


Figure 3.1: Definition of angles and vectors determining the orientation and geometry of the peptides, original figure from [20] Supplementary Material

### 3.4 Calculation of structural parameters from the simulations

In order to check if the angles  $\alpha$ ,  $\beta$  and  $\theta$ , which are used to define the orientation of the labeled bond with respect to the helical axis, are valid, these angles have been extracted from the MD simulations. Additionally, the angles  $\tau$  and  $\rho$  have been calculated directly from the simulation trajectories, without calculating the splittings  $\Delta\nu_q$  first. For these calculations, only the helical part of the peptide, as defined in Chapter 3.2, has been taken into account.

In the simulations, the z-axis always corresponds to the membrane normal, and the membrane lies in the xy-plane.

To calculate the angles, firstly three vectors have been defined:

- The helix axis vector  $\mathbf{h}$ : the heavy backbone atoms of the helical part of the peptide (N, C $_{\alpha}$ , C, O) are divided into two equally sized parts (or differing by one atom, if the number of atoms is odd), an amino-terminal and a carboxy-terminal part. For each part the center of mass is calculated for each frame,  $\overrightarrow{COM_{MC(N)}}$  and  $\overrightarrow{COM_{MC(C)}}$ . The vector  $\mathbf{h}$  is then defined by the difference between the two vectors:

$$\vec{h} = \overrightarrow{COM_{MC(C)}} - \overrightarrow{COM_{MC(N)}} \quad (3.6)$$

- The vector  $\mathbf{B}_i$  from C $_{\alpha}$  to C $_{\beta}$  of residue  $i$  (Figure 3.1B, C and D): it can be obtained from the coordinates of the C $_{\alpha}$  and C $_{\beta}$  atoms in each frame (for a glycine residue the hydrogen atom on the C $_{\alpha}$ , corresponding to the position of C $_{\beta}$  in L-Ala is used):

$$\vec{B}_i = \vec{C}_{\beta,i} - \vec{C}_{\alpha,i} \quad (3.7)$$

- The vector  $\mathbf{A}_i$  between the center of the helix and the C $_{\alpha}$  atom of residue  $i$ : the center of the helix is calculated as the center of mass of the heavy backbone atoms of the helical part of the peptide. This vector will be used in its projection onto the plane perpendicular to the helical axis (Figure 3.1D).

$$\vec{A}_i = \vec{C}_{\alpha,i} - \overrightarrow{COM_{MC}} \quad (3.8)$$

The angle  $\beta$  between the helical axis and the C $_{\alpha}$ -C $_{\beta}$  bond is then simply the angle

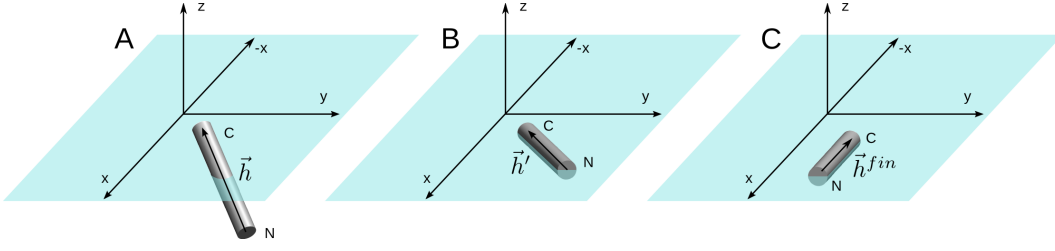


Figure 3.2: Steps of the rotation procedure to obtain the helix vector oriented parallel to the x-axis. A: initial orientation of the helix axis. B: after rotation of the helix axis into the xy plane. C: after rotation of the helix axis about the z-axis, in order to be parallel with the x-axis, the final vector  $\mathbf{h}^{fin}$  pointing towards the negative end.

between  $\mathbf{h}$  and  $\mathbf{B}$ :

$$\beta = \arccos \left( \frac{\mathbf{h} \cdot \mathbf{B}}{|\mathbf{h}| \cdot |\mathbf{B}|} \right) \quad (3.9)$$

$\tau$  is the angle between the helical axis vector  $\mathbf{h}$  and the membrane normal, which is the z-direction in the simulations:

$$\tau = \arccos \left( \frac{h_z}{|\mathbf{h}|} \right) \quad (3.10)$$

The angles  $\alpha$ ,  $\beta$  and  $\theta$  are calculated from the projection of the vectors  $\mathbf{A}$  and  $\mathbf{B}$  onto the plane perpendicular to the helix axis.

Therefore, rotation matrices are used to rotate the helix vector  $\mathbf{h}$  parallel to the x-axis. First, the helix vector will be rotated in order to lie within the xy plane. Then, a second rotation about the z-axis will rotate the helix vector to be parallel to the x-axis. The different steps of the procedure are visualized in Figure 3.2. Thus, the plane orthogonal to the helix axis is equivalent with the yz plane and the angles can be calculated by omission of the x components of the vectors.

We define a unit vector  $\mathbf{u}$  perpendicular to  $\mathbf{h}$  and in the xy plane, which we use to rotate  $\mathbf{h}$  into the xy plane:

$$\mathbf{u} = \begin{pmatrix} \frac{h_y}{\sqrt{h_x^2 + h_y^2}} \\ \frac{-h_x}{\sqrt{h_x^2 + h_y^2}} \\ 0 \end{pmatrix} \quad (3.11)$$

The matrix for a rotation by an angle  $\psi$  about an axis in the direction of  $\mathbf{u}$  is

$$R_{\mathbf{u}}(\psi) = \begin{pmatrix} u_x^2 (1 - \cos \psi) + \cos \psi & u_x u_y (1 - \cos \psi) - u_z \sin \psi & u_x u_z (1 - \cos \psi) + u_y \sin \psi \\ u_y u_x (1 - \cos \psi) + u_z \sin \psi & u_y^2 (1 - \cos \psi) + \cos \psi & u_y u_z (1 - \cos \psi) - u_x \sin \psi \\ u_z u_x (1 - \cos \psi) - u_y \sin \psi & u_z u_y (1 - \cos \psi) + u_x \sin \psi & u_z^2 (1 - \cos \psi) + \cos \psi \end{pmatrix} \quad (3.12)$$

The rotated vector  $\mathbf{h}'$  in the xy plane is

$$\mathbf{h}' = R_{\mathbf{u}}(\psi) \cdot \mathbf{h} \quad (3.13)$$

$$\psi = \tau - 90^\circ \quad (3.14)$$

where the tilt angle  $\tau$  is the angle between the helix axis and the membrane normal.

Now the vector  $\mathbf{h}'$  is rotated by an angle  $\xi$  about the z-axis, in order to be parallel to the x axis, such that the final helical axis vector  $\mathbf{h}^{fin}$  points along the negative x-axis. The angle  $\xi$  is

$$\xi = \arccos\left(\frac{-h'_x}{\sqrt{h_x'^2 + h_y'^2}}\right) \quad (3.15)$$

The matrix for a rotation by an angle  $\xi$  about the z-axis is

$$R_z(\xi) = \begin{pmatrix} \cos \xi & -\sin \xi & 0 \\ \sin \xi & \cos \xi & 0 \\ 0 & 0 & 1 \end{pmatrix} \quad (3.16)$$

The final vector  $\mathbf{h}^{fin}$ , which is parallel to the x axis, is then

$$\mathbf{h}^{fin} = R_z(\xi) \cdot \mathbf{h}' \quad (3.17)$$

The two rotations by the angles  $\xi$  and  $\psi$  are performed in the same way for the vectors  $\mathbf{A}$  and  $\mathbf{B}$ , leading to the final vectors  $\mathbf{A}^{fin}$  and  $\mathbf{B}^{fin}$ , see Figure 3.3.

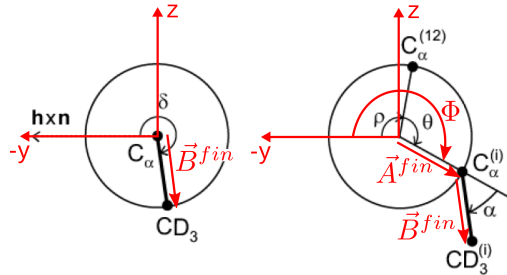


Figure 3.3: Definition of angles and vectors after rotation of the helical axis onto the negative x axis (original figure from [20] Supplementary Material)

Now, the angle  $\phi_i$  is calculated between the negative y axis representing the

membrane plane and the connection from the helix axis to the C $_{\alpha}$  of residue  $i$ ,  $\mathbf{A}_i^{fin}$ :

$$\phi'_i = \arccos \left( \frac{-A_{i,y}^{fin}}{\sqrt{(A_{i,y}^{fin})^2 + (A_{i,z}^{fin})^2}} \right) \quad (3.18)$$

$$\phi_i = \begin{cases} \phi'_i, & \text{if } A_{i,z}^{fin} \geq 0, \\ 360 - \phi'_i, & \text{if } A_{i,z}^{fin} < 0. \end{cases} \quad (3.19)$$

Equation 3.19 is needed, because the cosine function is symmetric around zero. Without Equation 3.19,  $\phi_i$  would be independent of the sign of  $A_{i,z}^{fin}$ .

The azimuthal rotation angle  $\rho$  between the membrane plane and the C $_{\alpha}$  of the 12th residue is now calculated as average of the  $\phi_i$ , translated to position 12. Modulo (%) 360 is needed to subtract multiples of 360°, to get a value between 0 and 360°.

$$\rho = \frac{1}{N+1} \sum_{i=first}^{first+N} (\phi_i + (12-i) \cdot 100^\circ) \% 360, \quad (3.20)$$

where the sum goes from the first to the last residue in the helical part of the peptide.

The angle  $\theta_{i,i+1}$  between two subsequent residues  $i$  and  $i+1$  is then

$$\theta'_{i,i+1} = \phi_{i+1} - \phi_i \quad (3.21)$$

$$\theta_{i,i+1} = \begin{cases} \theta'_{i,i+1}, & \text{if } \theta'_{i,i+1} \geq 0, \\ \theta'_{i,i+1} + 360, & \text{if } \theta'_{i,i+1} < 0. \end{cases} \quad (3.22)$$

The angle  $\delta_i$  between the membrane plane, represented by the negative y axis, and the C $_{\alpha}$ -C $_{\beta}$  bond of residue  $i$ , represented by the vector  $\mathbf{B}_i$ , is

$$\delta'_i = \arccos \left( \frac{-B_{i,y}^{fin}}{\sqrt{B_{i,y}^{fin2} + B_{i,z}^{fin2}}} \right) \quad (3.23)$$

$$\delta_i = \begin{cases} \delta'_i, & \text{if } B_{i,z}^{fin} \geq 0, \\ 360 - \delta'_i, & \text{if } B_{i,z}^{fin} < 0. \end{cases} \quad (3.24)$$

The angle  $\alpha_i$  between the connection of the helical axis and the C $_{\alpha}$  atom of residue  $i$ ,  $\mathbf{A}_i$  and the C $_{\alpha}$ -C $_{\beta}$  bond,  $\mathbf{B}_i$ , is

$$\alpha_i = \delta_i - \phi_i \quad (3.25)$$

### 3.5 Calculation of NMR splittings from the simulations

For direct comparison with the experimental data, the splittings  $\Delta\nu_q$  are calculated from the MD simulations using equation 3.3. In order to do this, first the angle  $\vartheta_i$  between the  $C_\alpha$ - $C_\beta$  bond of residue  $i$  and the z-axis (representing the external magnetic field) has to be calculated:

$$\vartheta = \arccos\left(\frac{B_z}{|B|}\right) \quad (3.26)$$

The obtained splittings are then fitted following the same procedure as the experimental splittings, compare Section 3.3.



## 4. Simulations of helical peptides in a DMPC membrane and comparison with NMR data

### 4.1 Introduction

In various studies, it was shown that SSNMR can reveal the orientation of amphiphilic peptides in oriented phospholipid bilayers [19,27,31,52–54]. Special isotope-labelled amino acids are incorporated into the sequence of the peptide, and the resulting NMR signals provides information about the orientation of the label with respect to the exterior magnetic field, based on the relationships in Equations 3.3 to 3.4. With a sufficient amount of measurements with labels at different positions ( $\geq 4$ ), the orientation of the entire peptide in the membrane can be reconstructed (Chapter 3.3).

The model used for the calculation requires the constant parameters  $\alpha$ ,  $\beta$ , and  $\theta$ . These angles define the position of the label with respect to the helical axis of the peptides and are defined in Chapter 3.3. The values, which are used for these angles until now, have been derived from molecular model building.

Here, long MD simulations of four different amphiphilic peptides in a DMPC membrane were performed, and the angles  $\alpha$ ,  $\beta$ , and  $\theta$  were measured directly from the peptide structure during the simulation, in order to improve the model. The investigated peptides are PGLa and Mag2 from *X. laevis*, and the designer-made peptides MSI-103 and KIA14, which were derived from the sequence of PGLa. The overall orientation in the membrane environment and the helicity of the peptides were evaluated and compared with experimental data. Additionally, the splittings which would be expected from the peptide trajectory in a  $^2\text{H}$  NMR measurement were calculated, and fitted in the same way as the experimental splittings.

## 4.2 Methods

### 4.2.1 Simulations

Four helical antimicrobial and model peptides were simulated:

- the 21-mer PGLa from *X. laevis* (charge +5, GMASKAGAIA GKIAKVALKA L-NH<sub>2</sub>) [19,32,51–57,82,99,100], which we have studied extensively in the past
- the 21-mer MSI-103 whose sequence was derived from PGLa to obtain an ideal amphiphilic structure (charge +7, (KIAGKIA)<sub>3</sub>-NH<sub>2</sub>) [31]
- the 14-mer KIA14 with the same sub-sequence as MSI-103 (charge +5, (KIAGKIA)<sub>2</sub>-NH<sub>2</sub>)
- the 23-mer magainin 2 (Mag2), also from *X. laevis*, which acts synergistically together with PGLa (charge +3, GIGKFLHSAK KFGKAFVGEI MNS) [57]

Simulations were conducted in a DMPC bilayer consisting of 128 lipids with 4500-5700 TIP3P water molecules [96]. The SLIPID force field was used for the lipids [83], and the AMBER99SB-ILDN [97] force field for everything else. The membrane simulation protocol is described in Chapter 3.1.

The definition and calculation of the angles  $\alpha$ ,  $\beta$ ,  $\theta$  and  $\delta$  is described in Chapter 3.3 and the calculation of the helicity is described in Chapter 3.2.

## 4.3 Results

Each simulation of one microsecond has been divided into five parts of each 200 ns length. The first part, 0-200 ns, was omitted in the evaluation to allow for equilibration of the system. For each peptide, the helicity per residue and the angles  $\tau$ ,  $\rho$ ,  $\alpha$ ,  $\beta$  and  $\theta$  were calculated as averages over each of the four remaining intervals. Additionally, the <sup>2</sup>H NMR splittings were calculated from the simulations. The tables with all splittings,  $\alpha$ ,  $\beta$  and  $\theta$  can be found in Appendix A.

### 4.3.1 PGLa

The evaluation of the helicity for PGLa showed, that the peptide unravels at the C-terminus, starting from position 18 (Figure 4.1).

When looking at the different time intervals, each of 200 ns length, the unraveling is stronger in the inner intervals, and becomes less in the last interval. The region

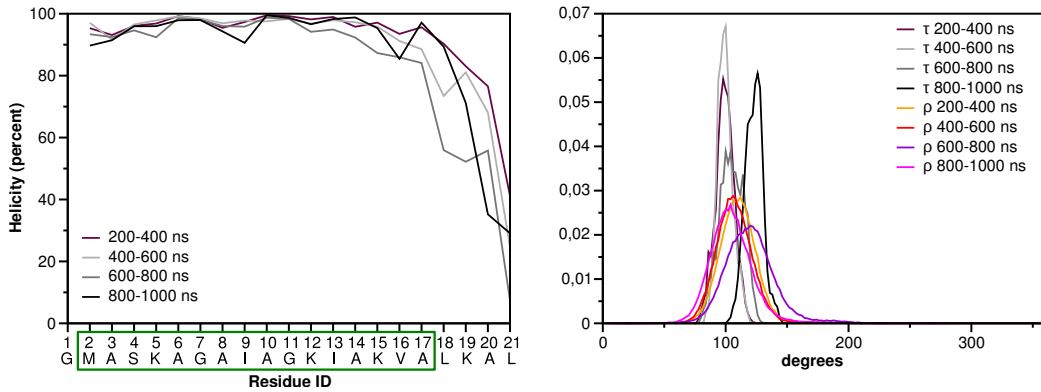


Figure 4.1: Helicity and orientation of **PGLa**. *Left*: helicity along the peptide sequence as percentage of time, for different time intervals. The highlighted region from position 2-17 is almost perfectly helical. *Right*: the helix tilt angle  $\tau$  against the membrane normal and azimuthal rotation angle  $\rho$  for the different time intervals of the simulation, measured for the helical part from position 2-17.

Table 4.1: Tilt angle  $\tau$  and azimuthal rotation angle  $\rho$  for PGLa, measured for the helical part from residue 2 to 17.

#	Time interval [ns]	$\tau \pm \sigma_\tau [^\circ]$	$\rho \pm \sigma_\rho [^\circ]$
1	200-400	$99 \pm 8$	$110 \pm 15$
2	400-600	$100 \pm 6$	$107 \pm 16$
3	600-800	$105 \pm 10$	$120 \pm 20$
4	800-1000	$123 \pm 7$	$105 \pm 17$
	Average	$107 \pm 12$	$110 \pm 18$

from residues 2-17 is almost fully helical. Therefore the angles which have been calculated for an ideal helix refer to this region (Table 4.1).

The tilt angle  $\tau$  is  $99/100^\circ$  in the intervals 1 and 2. Here, the peptide lies flat in the membrane surface. The last interval shows a tilted state with a tilt angle of  $123^\circ$ , where the C-terminus makes contacts with the head groups of the opposite leaflet of the bilayer. The third interval shows an intermediate orientation between these two states with a tilt angle of  $105^\circ$ . The development of  $\tau$  over the course of the whole simulation is shown in Appendix Figure A.1.

The azimuthal rotation angle  $\rho$  is always between  $105^\circ$  and  $120^\circ$ . This signifies that the 12th residue, a charged Lys, points up into the water phase, as expected.

For each interval, the splittings which would be expected from an  $^2\text{H}$  NMR measurement have been calculated. The complete list is shown in Appendix Table A.2. The splittings have been fitted to ideal helices. The best fit for the average splittings from the first two intervals are shown in Figure 4.2 together with the  $^2\text{H}$  NMR data published previously [41]. Also, the best fits for the individual intervals are listed here.

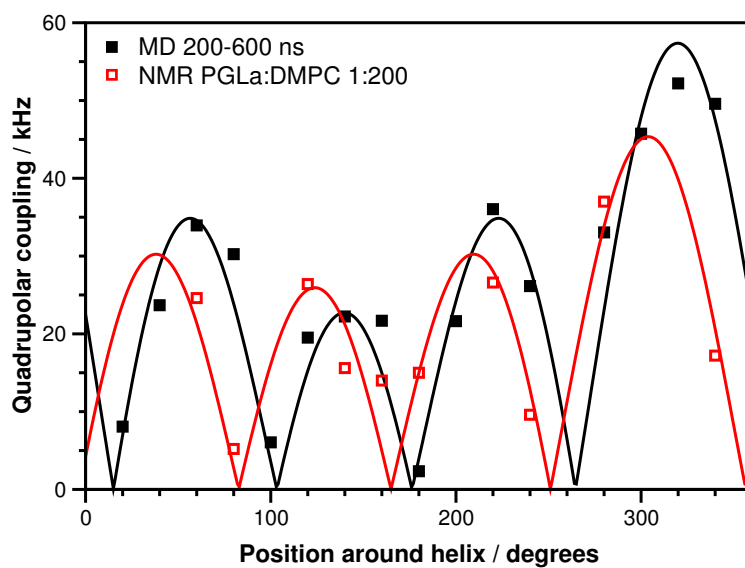


Figure 4.2: Best fits for the splittings averaged over intervals #1 and #2, and the data from  $^2\text{H}$  NMR, measured for a PGLa:DMPC ratio of 1:200. The table below shows the best fit parameters for these, for the individual intervals, and the complete evaluated time from 200-1000 ns. The values in bold correspond to the curves in the Figure.

Curve	positions	$\tau$ [°]	$\rho$ [°]	$S_{\text{mol}}$	RMSD [kHz]
200-400 ns	2-17	100	99	0.84	4.4
400-600 ns	2-17	101	95	0.83	4.3
<b>200-600 ns</b>	<b>2-17</b>	<b>101</b>	<b>97</b>	<b>0.83</b>	<b>4.3</b>
600-800 ns	2-17	107	107	0.79	3.5
200-1000 ns	2-17	108	99	0.79	3.4
<b>PGLa:DMPC 1:200</b>	<b>6-11, 13, 14, 16, 17</b>	<b>97</b>	<b>113</b>	<b>0.72</b>	<b>4.1</b>

The shape of the curve is defined by the tilt angle  $\tau$  and the shift on the x-axis is defined by the azimuthal rotation angle  $\rho$ . The curve is scaled by  $S_{\text{mol}}$ . The splittings from intervals 1 and 2 are very similar and give almost the same fit. The fit for interval 3 reflects the intermediate orientation mentioned above. The values for the tilt angle  $\tau$  are very close to the ones calculated directly from the coordinates. They differ by maximally  $2^\circ$ . The  $\rho$  values, however, are  $11\text{-}13^\circ$  lower than the ones calculated directly and shown in Table 4.1.

When comparing the splittings obtained from the simulations with those measured from  $^2\text{H}$  NMR experiments, they are often very different. From the curves in Figure 4.2 it can be seen that the largest difference is due to the shift of the curves on the x-axis by  $16^\circ$ , due to the different  $\rho$  angle. Another effect is the scaling, in the simulations  $S_{\text{mol}}$  is 0.83 opposed to 0.72 in the experiment. The shape of the curve is also different because of the small difference in  $\tau$ , which becomes clear in the change of the relative intensities between  $60^\circ$  and  $140^\circ$  on the x-axis. The RMSD, which is a measure of how well the single points agree with the fitted curve, is similar for the simulation fit and the experimental fit.

Figure 4.3 shows the best fits for interval #4 and  $^2\text{H}$  NMR, measured for a PGLa:DMPC ratio of 1:50, where a tilted state is observed. The  $\tau$  calculated via the splittings is now  $5^\circ$  higher than the one calculated directly.  $\rho$  is  $12^\circ$  too low.

The two curves clearly resemble each other, but again the fit of the experimental data is shifted towards the left side of the x-axis, by an angle of  $18^\circ$ . Again, the  $S_{\text{mol}}$  indicates a lower mobility for the simulation than for the experiment. The quality of the fit is clearly higher for the experimental data, which is indicated by a lower RMSD of 1.7 kHz, while the quality of the fit based on the simulation splittings has decreased, as indicated by a higher RMSD of 5.4 kHz. This indicates a better agreement with the fitting model of an ideal  $\alpha$ -helix for the experimental than for the simulation data.

### 4.3.2 MSI-103

The designer-made MSI-103, whose sequence has been derived from PGLa, showed a behaviour similar to the latter. Also here, the helical region ends at position 18 (Figure 4.4).

On the N-terminus, where Gly and Met have been replaced with Lys and Ile, MSI-103 is less helical than PGLa. Residues 3-17 were identified as the helical region and used as a reference to calculate the orientational angles  $\tau$  and  $\rho$  (Table 4.2).

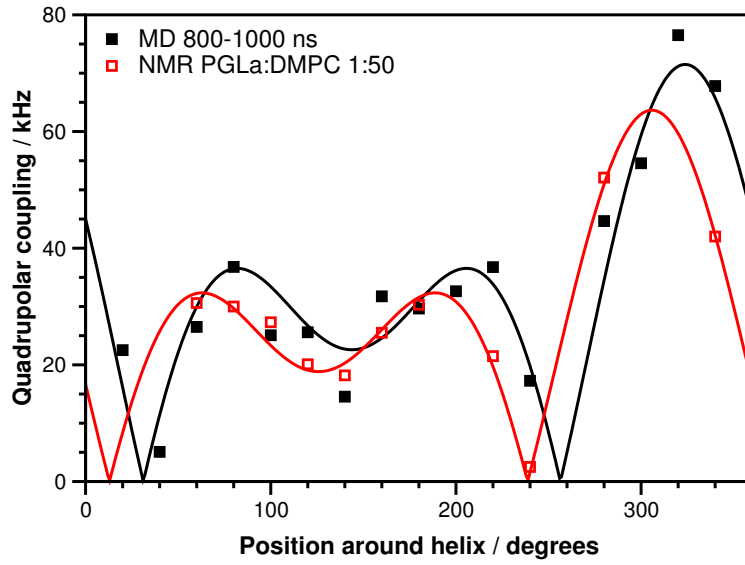


Figure 4.3: Best fit for the splittings from interval #4 and data from  $^2\text{H}$  NMR, measured for a PGLa:DMPC ratio of 1:50. The parameters for the best fit curve are:

Curve	positions	$\tau$ [°]	$\rho$ [°]	$S_{\text{mol}}$	RMSD [kHz]
800-1000 ns	2-17	128	93	0.87	5.4
PGLa:DMPC 1:50	6-11, 13, 14, 16, 17, 20	127	111	0.77	1.7

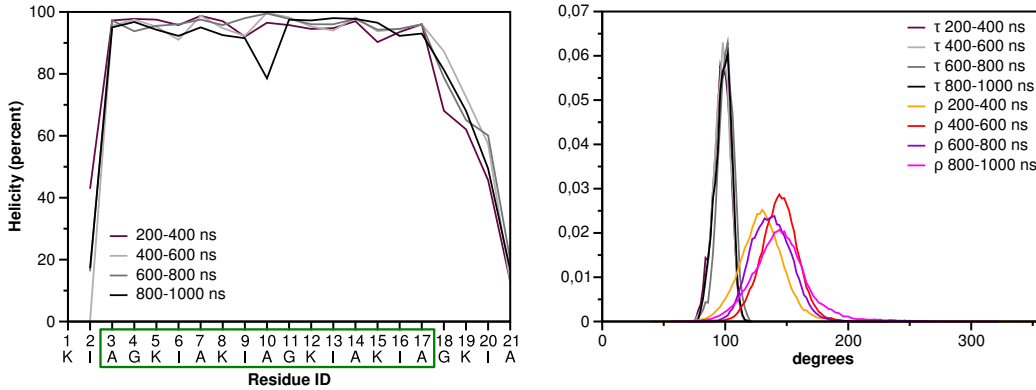


Figure 4.4: Helicity and orientation of **MSI-103**. *Left*: helicity along the peptide sequence as percentage of time. *Right*: the helix tilt angle  $\tau$  against the membrane normal and azimuthal rotation angle  $\rho$ , measured for the helical part from position 3-17.

Table 4.2: Tilt angle  $\tau$  and azimuthal rotation angle  $\rho$  for MSI-103, measured for the helical part from residue 3 to 17.

#	Time interval [ns]	$\tau \pm \sigma_\tau$ [°]	$\rho \pm \sigma_\rho$ [°]
1	200-400	$97 \pm 7$	$130 \pm 18$
2	400-600	$98 \pm 7$	$144 \pm 15$
3	600-800	$100 \pm 7$	$138 \pm 16$
4	800-1000	$98 \pm 7$	$145 \pm 24$
	Average	$98 \pm 7$	$139 \pm 19$

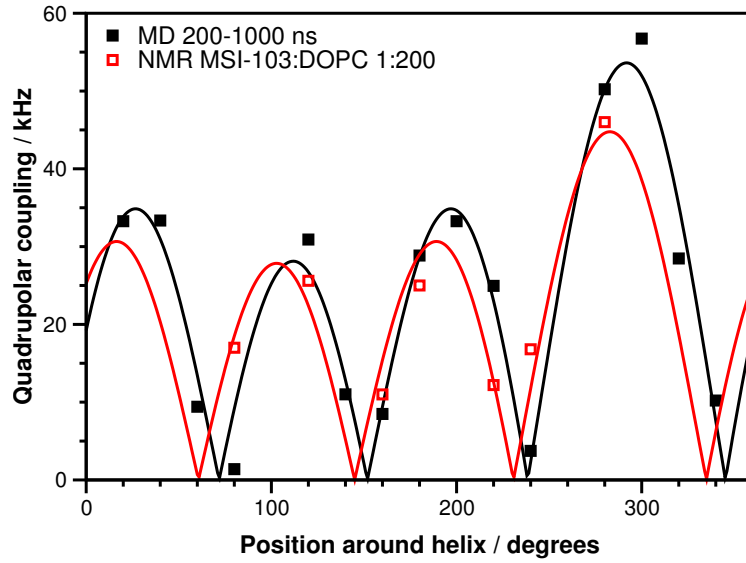


Figure 4.5: Best fits for the splittings averaged over intervals #1-4, and the data from  $^2\text{H}$  NMR, measured for a MSI-103:DOPC ratio of 1:200. The table below shows the best fit parameters for these and for the individual intervals, and the best fits from NMR data for measurements in DMPC at low peptide concentrations. The values in bold correspond to the curves in the Figure.

Curve	positions	$\tau$ [°]	$\rho$ [°]	$S_{\text{mol}}$	RMSD [kHz]
200-400 ns	3-17	97	116	0.85	6.3
400-600 ns	3-17	97	130	0.86	3.0
600-800 ns	3-17	100	124	0.87	2.6
800-1000 ns	3-17	98	130	0.81	4.9
<b>200-1000 ns</b>	<b>3-17</b>	<b>98</b>	<b>125</b>	<b>0.83</b>	<b>3.5</b>
MSI-103:DMPC 1:200	7, 9, 10, 11, 13, 14, 17	111	122	0.65	1.6
<b>MSI-103:DOPC 1:200</b>	<b>7, 9, 10, 11, 13, 14, 17</b>	<b>96</b>	<b>134</b>	<b>0.73</b>	<b>3.3</b>

All angles are very similar throughout the simulation, which can also be confirmed from the distributions in the right panel of Figure 4.4. The tilt angle  $\tau$  is on average  $98^\circ$  and close to that of PGLa in the intervals 1 and 2, which shows that also MSI-103 lies flat in the membrane surface. As above, the charged Lys residue at position 12 reaches towards the water phase at an average azimuthal rotation angle of  $139^\circ$ .

The splittings which were calculated for the helical part were fitted to an ideal helix. The fits were compared with the best fits from  $^2\text{H}$  NMR data [31] at different peptide:lipid ratios (Figure 4.5).

The best fits for the four simulation intervals have almost exactly the same tilt angle  $\tau$  as measured directly from the geometries, shown in Table 4.2. The  $\rho$  angles obtained from the fit are again lower, by  $14\text{-}16^\circ$ , when compared to the directly obtained values in Table 4.2.

When compared to the results from  $^2\text{H}$  NMR measurements in DMPC, the experimental data give generally a larger  $\tau$ , by  $\geq 10^\circ$  (Table in Figure 4.5 and [101]). In dioleoylphosphatidylcholine (DOPC) at a peptide:lipid ratio of 1:200, however,

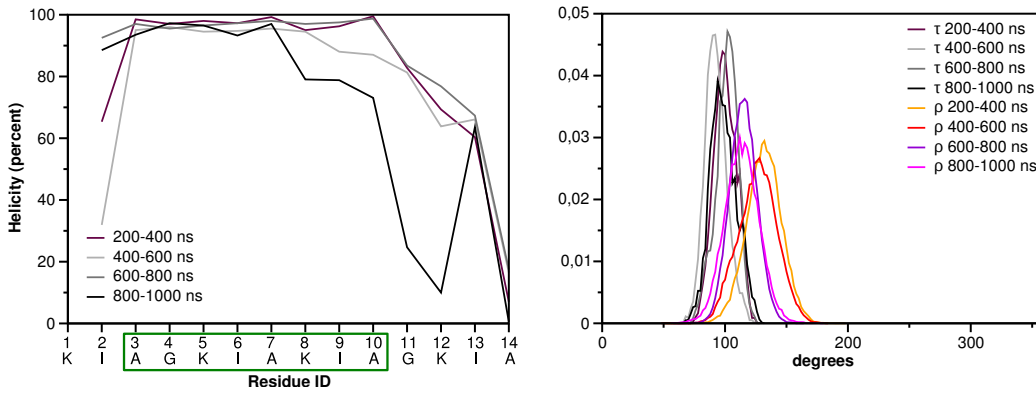


Figure 4.6: Helicity and orientation of **KIA14**. *Left*: helicity along the peptide sequence as percentage of time. *Right*: the helix tilt angle  $\tau$  against the membrane normal and azimuthal rotation angle  $\rho$ , measured for the helical part from position 3-10.

the NMR data show a state where the peptide is lying flat in the surface, as it was observed also in the simulation. Also here,  $\rho$  is larger than in the fit of the simulated splittings, by  $9^\circ$ .

The mobility of MSI-103, indicated by  $S_{\text{mol}}$ , is highest in the experiment with a low peptide:lipid ratio ( $S_{\text{mol}}(\text{MSI-103:DMPC } 1:200)=0.65$ ). The simulations show generally mobilities with values of  $S_{\text{mol}} \geq 0.8$ , similar to those of PGLa.

The quality of the fits based on the simulation splittings is very variable; the RMSD ranges from 2.6 to 6.3 kHz for the four different intervals. This can seem surprising, since the peptide is nearly perfectly helical in the range from positions 3-17, according to Figure 4.4. However, the peptide’s local structure is allowed to vary within a range of  $\Phi$  and  $\Psi$  angles and is still considered helical according to the definition in Section 3.2. A close look at the structural angles in Appendix Table A.2 shows some differences, and the calculated splittings change considerably between the single intervals.

For the experimental data, the fit in DMPC shows an intermediate state between the surface bound state and the tilted state observed above, and has a lower RMSDs than the fit in DOPC.

### 4.3.3 KIA14

The shorter peptide KIA14 is helical up to position 10. As observed for PGLa and MSI-103, the helicity is lost for the last four residues. Equally to MSI-103 which has the same sub-sequence (KIAGKIA), the helical part starts at position 3 (Figure 4.6).

While the angles  $\tau$  and  $\rho$  are more variable in intervals 1 and 2, they seem to converge to  $\tau \approx 100^\circ$  and  $\rho \approx 115^\circ$  in the last two intervals (Table 4.3). The average

Table 4.3: Tilt angle  $\tau$  and azimuthal rotation angle  $\rho$  for KIA14, measured for the helical part from residue 3 to 10.

#	Time interval [ns]	$\tau \pm \sigma_\tau [^\circ]$	$\rho \pm \sigma_\rho [^\circ]$
1	200-400	100 $\pm$ 9	132 $\pm$ 14
2	400-600	93 $\pm$ 9	127 $\pm$ 16
3	600-800	101 $\pm$ 9	115 $\pm$ 11
4	800-1000	99 $\pm$ 11	114 $\pm$ 14
	Average	98 $\pm$ 10	122 $\pm$ 16

tilt angle  $\tau$  is  $98^\circ$  and identical to that of MSI-103, while the average azimuthal rotation angle  $\rho$  is in average  $122^\circ$ ,  $17^\circ$  lower than for MSI-103. It should be noted that the position of the 12th residue itself has not been taken into account in the calculation of  $\rho$ , but it has been calculated only from the helical region (see Equation 3.20).

The tilt angles of the best fits for the splittings calculated for the helical region from position 3-10 are almost identical to the ones obtained directly from the atomic coordinates. The  $\rho$  angles obtained from the fit are again lower than those obtained directly from the coordinates, by  $14\text{-}15^\circ$ .

The best fits for the data from  $^2\text{H}$  NMR in DMPC and DOPC show roughly the same orientation. The tilt angle  $\tau$  generally agrees with the ones obtained from the simulation splittings. As observed also for PGLa, the curves obtained from the MD splittings are generally shifted to lower values of  $\rho$ . The  $\rho$  shift between the two fits shown in Figure 4.7 is  $16^\circ$ .

The  $S_{\text{mol}}$  values for the simulations again indicate a lower mobility than in the experiments with values  $\geq 0.84$ . The experimental value is 0.66.

For KIA14, the fits of the simulation data are much better than for the previous peptides, they have RMSD values between 1.4 and 2.5 kHz. The fits of the experimental data, however, have average RMSD values of 3-4 kHz.

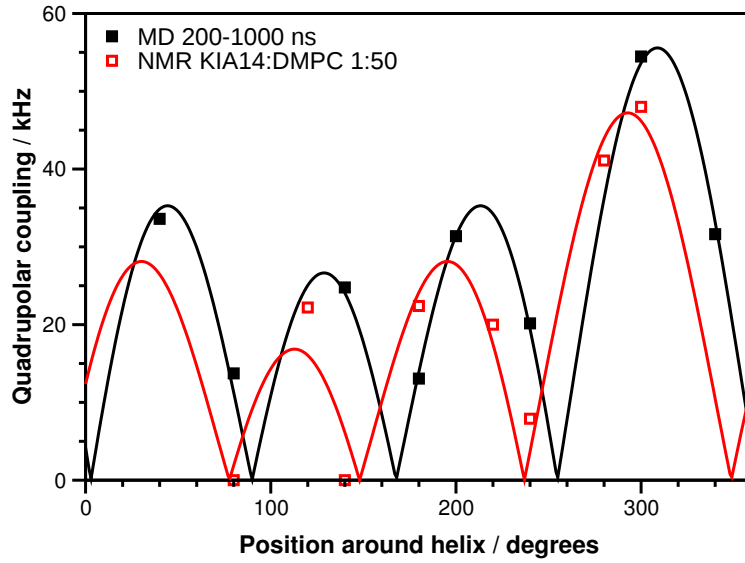


Figure 4.7: Best fits for the splittings averaged over intervals #1-4, and the data from  $^2\text{H}$  NMR, measured for a KIA14:DMPC ratio of 1:50. The table below shows the best fit parameters for these, for the individual intervals, and also the best fits from NMR data for measurements in dilauroylphosphatidylcholine (DLPC) and DOPC. The values in bold correspond to the curves in the Figure.

Curve	positions	$\tau$ [°]	$\rho$ [°]	$S_{\text{mol}}$	RMSD [kHz]
200-400 ns	3-10	101	118	0.85	1.9
400-600 ns	3-10	93	112	0.84	2.5
600-800 ns	3-10	103	101	0.90	1.4
800-1000 ns	3-10	99	100	0.87	1.4
<b>200-1000 ns</b>	<b>3-10</b>	<b>99</b>	<b>108</b>	<b>0.84</b>	<b>1.2</b>
<b>KIA14:DMPC 1:50</b>	<b>4, 6, 7, 9-11, 13, 14</b>	<b>102</b>	<b>124</b>	<b>0.67</b>	<b>3.8</b>
KIA14:DOPC 1:50	4, 6, 7, 9-11, 13, 14	99	128	0.66	2.9

### 4.3.4 Magainin 2

Mag2 starts to unfold at position 14. It seems that position 17 is responsible for the unfolding, since the helicity for this residue drops to zero. The orientation of the helical part from position 3 to 13 is very stable throughout the whole simulation (Figure 4.8).

The tilt angle  $\tau$  is on average  $97^\circ$ , the peptide lies flat in the membrane surface (Table 4.4). The average azimuthal rotation angle  $\rho$  of the 12th residue, a Phe, is  $187^\circ$ . It is at the side of the peptide, pointing slightly towards the membrane interior.

The best fits obtained from the calculated splittings of positions 3-13 and the best fits of data from  $^2\text{H}$  NMR measurements at different peptide:lipid ratios are shown in Figure 4.9. The tilt angles  $\tau$  obtained from the simulation splittings are generally  $3\text{-}4^\circ$  lower than those obtained directly from the coordinates. The  $\rho$  angles from the fits are again lower than those calculated directly, by  $9\text{-}11^\circ$ .

The best fits of the experimental data show roughly the same orientations. Only for the Mag2:DMPC:DMPG 2:75:25 measurement, the helix is actually tilted in the opposite direction. The N-terminus is apparently deeper inserted than the C-terminus. Interestingly,  $\rho$  is not generally shifted with respect to the MD data.

The  $S_{\text{mol}}$  values for the simulations are again generally higher than those from the experiments. They are all  $\geq 0.79$ . The values for the experimental fits are between 0.6 and 0.79.

The RMSD values for the fits range from 3.2 to 4.3 kHz for the simulation fits. For the measurements in a DMPC/DMPG mixture, the fits are better (RMSD=2.4 and 2.8 kHz), and worse for the measurement in POPC/POPG (RMSD=5.1 kHz).

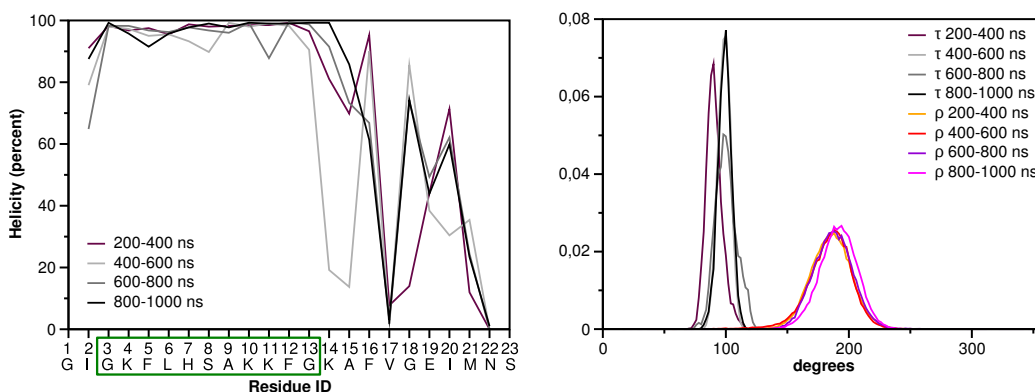


Figure 4.8: Helicity and orientation of **Mag2**. *Left*: helicity along the peptide sequence as percentage of time, for different time intervals. *Right*: the helix tilt angle  $\tau$  against the membrane normal and azimuthal rotation angle  $\rho$ , measured for the helical part from position 3-13.

Table 4.4: Tilt angle  $\tau$  and azimuthal rotation angle  $\rho$  for Mag2, measured for the helical part from residues 3 to 13.

#	Time interval [ns]	$\tau \pm \sigma_\tau [^\circ]$	$\rho \pm \sigma_\rho [^\circ]$
1	200-400	$91 \pm 7$	$186 \pm 16$
2	400-600	$99 \pm 5$	$184 \pm 18$
3	600-800	$100 \pm 9$	$187 \pm 16$
4	800-1000	$99 \pm 5$	$191 \pm 15$
	Average	$97 \pm 8$	$187 \pm 17$

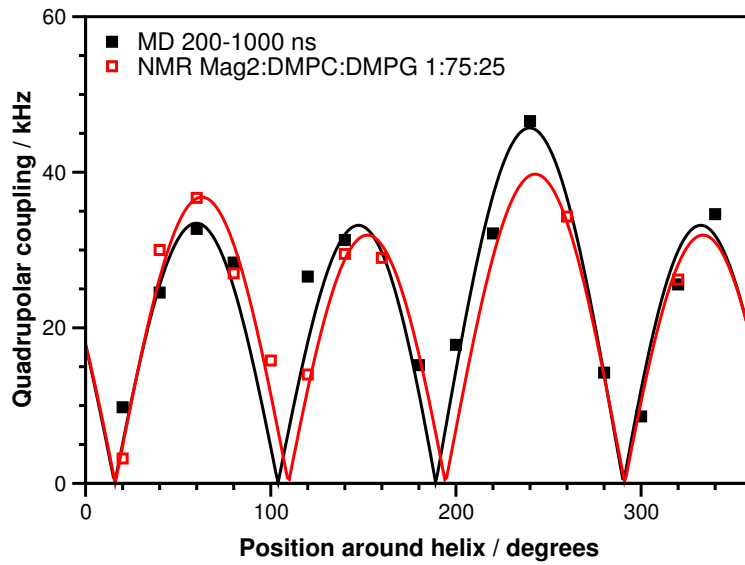


Figure 4.9: Best fits for the splittings averaged over intervals #1-4, and the data from  $^2\text{H}$  NMR, measured for a Mag2:DMPC:DMPG ratio of 1:75:25. The table below shows the best fit parameters for these, for the individual intervals and for NMR data from measurements at a different peptide:lipid concentration and within a 1-palmitoyl-2-oleoyl-phosphatidylcholine (POPC)/1-palmitoyl-2-oleoyl-phosphatidylglycerol (POPG) mixture. The values in bold correspond to the curves in the Figure.

Curve	positions	$\tau [^\circ]$	$\rho [^\circ]$	$S_{\text{mol}}$	RMSD [kHz]
200-400 ns	3-13	87	175	0.83	4.0
400-600 ns	3-13	96	175	0.83	4.3
600-800 ns	3-13	97	178	0.85	4.3
800-1000 ns	3-13	96(84)	181(1)	0.87	3.2
<b>200-1000 ns</b>	<b>3-13</b>	<b>94</b>	<b>177</b>	<b>0.79</b>	<b>3.7</b>
<b>Mag2:DMPC:DMPG 1:75:25</b>	<b>5, 6, 9, 12, 13, 15-18, 20</b>	<b>91</b>	<b>174</b>	<b>0.76</b>	<b>2.4</b>
Mag2:DMPC:DMPG 2:75:25	6, 9, 13, 15-17, 20	78(102)	189(9)	0.60	2.8
Mag2:POPC:POPG 2:90:10	5, 6, 9, 12, 13, 15-18, 20	90	171	0.79	5.1

Table 4.5: Average values for the fit parameters  $\alpha$ ,  $\beta$ ,  $\theta$ 

Peptide	$\alpha$ [°]	$\beta$ [°]	$\theta$ [°]	$\Delta\delta^a$	$\Delta\rho$ [°] <sup>b</sup>
PGLa	39.4 ±12.8	121.5 ±7.6	100.2 ±15.7	99.4 ± 14.3	11-13
MSI-103	38.9 ±13.5	120.9 ±9.0	99.9 ±18.1	99.6 ± 15.0	14-16
KIA14	39.0 ±9.3	121.7 ±6.0	98.4 ±7.3	99.1 ±13.2	14-15
Mag2	41.7 ±13.7	122.1 ±7.2	103.2 ±17.2	100.3 ±13.2	9-11

<sup>a</sup> Average difference between the  $\delta$  angles from Equation 3.5 for two subsequent residues  $i, i + 1$ .

<sup>b</sup> Difference between  $\rho$  calculated directly from the coordinates and  $\rho$  from the best fit of the splittings, fitted with  $\alpha = 53.2^\circ$ ,  $\beta = 121.1^\circ$ .

### 4.3.5 Calculated fit parameters

Table 4.5 shows the averages of the fit parameters  $\alpha$ ,  $\beta$  and  $\theta$ , calculated from the last 800 ns of the simulations. The averages for each of the four intervals are shown in Appendix Tables A.2 to A.5. The values for  $\beta$  are very close to the value used in the fits above ( $121.1^\circ$ ).  $\alpha$ , however, is generally between  $11^\circ$  and  $14^\circ$  lower than the value which was used for the fit ( $53.2^\circ$ ).

A different value for  $\alpha$  does not influence the RMSD which represents the quality of the fit, but only the resulting  $\rho$  angle. Repeating the fit with the average  $\alpha$  angles calculated from the single simulations would therefore result in  $\rho$  angles which are almost identical to the ones calculated directly.

Table 4.5 shows that the average helix pitch angle  $\theta$  varies from the ideal value of  $100^\circ$ . Mag2 shows the highest deviation with a value of  $103^\circ$ . However, the splitting  $\Delta\nu_q$  is calculated from  $\delta$ , which is the angle between the membrane plane and the  $C_\alpha$ - $C_\beta$  bond, projected onto the plane vertical to the helical axis. It contains a sum of  $\theta$  angles and  $\alpha$  (Equations 3.4 and 3.5). Therefore, the pitch  $\Delta\delta$  between two subsequent  $\delta$  angles has been calculated for each snapshot, the average values are shown in the fourth column of Table 4.5 (and in Appendix A). It shows that the deviation in the  $\theta$  angle is slightly compensated by a deviation in the  $\alpha$  angle or *vice versa*. For PGLa, MSI-103 and Mag2, the lower standard deviations show that  $\Delta\delta$  is fluctuating generally less than  $\theta$ .

### 4.3.6 RMSD analysis

Taking into account that the fits of the simulation data have been done on the splittings of the positions which are known to be helical, lower RMSD values would have been expected. Only for KIA14 the RMSD values are below 2 kHz. Especially intriguing is MSI-103, where the RMSD values range from 2.6 to 6.3 kHz for the different intervals.

Figure 4.10 shows the deviation of the measured splittings for MSI-103 with respect to the ideal fit curve, which is shown in Figure 4.5. The large RMSD of 6.3 kHz in interval #1 is mainly caused by positions 9 and 15, both on the polar part of the peptide, which deviate by  $\sim 13$  kHz from the fitted curve. In intervals #2 and #3, the deviations are smaller, leading to RMSD values of 3.0 kHz and 2.6 kHz. In interval #4, the deviations become larger again, leading to an RMSD value of 4.9 kHz.

The red values in Figure 4.10 are the splittings which are obtained when using the average values for  $\beta$ ,  $\tau$  and  $\delta$  which have been calculated from the trajectory for each single position. For intervals #1-3, this shows that the deviations are mainly caused by the deviations of the individual  $\beta$  and  $\delta$  for each residue from the ideal values. For interval #4, the red values deviate more from the black values in the first part of the helical region from position 2-11, and agree nicely in the remaining part. The orientations in intervals #2 and #4 are almost identical, when calculated directly from the coordinates, or via fit, but the dynamic factor  $S_{\text{mol}}$  varies from 0.86 (interval #2) to 0.81 (interval #4). Additionally, the  $\rho$  angle calculated from the coordinates (Table 4.2) in interval #4 has the highest standard deviation. Probably, special dynamics are responsible for the bad agreement of the measured splittings with the splittings calculated from the individual angles for each position. This is also confirmed by the analysis of the deviations for the other peptides, shown in Appendix Figures A.2 to A.4.

#### 4.3.7 Analysis of the standard deviations of $\Delta\nu_q$

When looking at the standard deviations of the splittings, averaged over the total evaluated time from 200-1000 ns of the simulations (listed in Appendix Table A.1), they range from  $\sim 8$  kHz up to 30 kHz. The standard deviations for splittings below -30 kHz are clearly the lowest. In Figure 4.11A, the standard deviations are shown with respect to the average splittings. The splittings close to the minimal splitting -42 kHz have the lowest standard deviations. Also the spread on the y-axis for a specific x-value is the smallest. For larger splittings, the range of possible standard deviations and thus angular distributions of  $\vartheta$  is also larger. Figure 4.11B shows the average  $\vartheta$  angles which correspond to the splittings  $\Delta\nu_q$ . Due to the relationship in Equation 3.3, there are many more possible  $\vartheta$  values in a small interval around  $\vartheta = 90^\circ$  which result in almost identical splittings, than for other values of  $\vartheta$ .

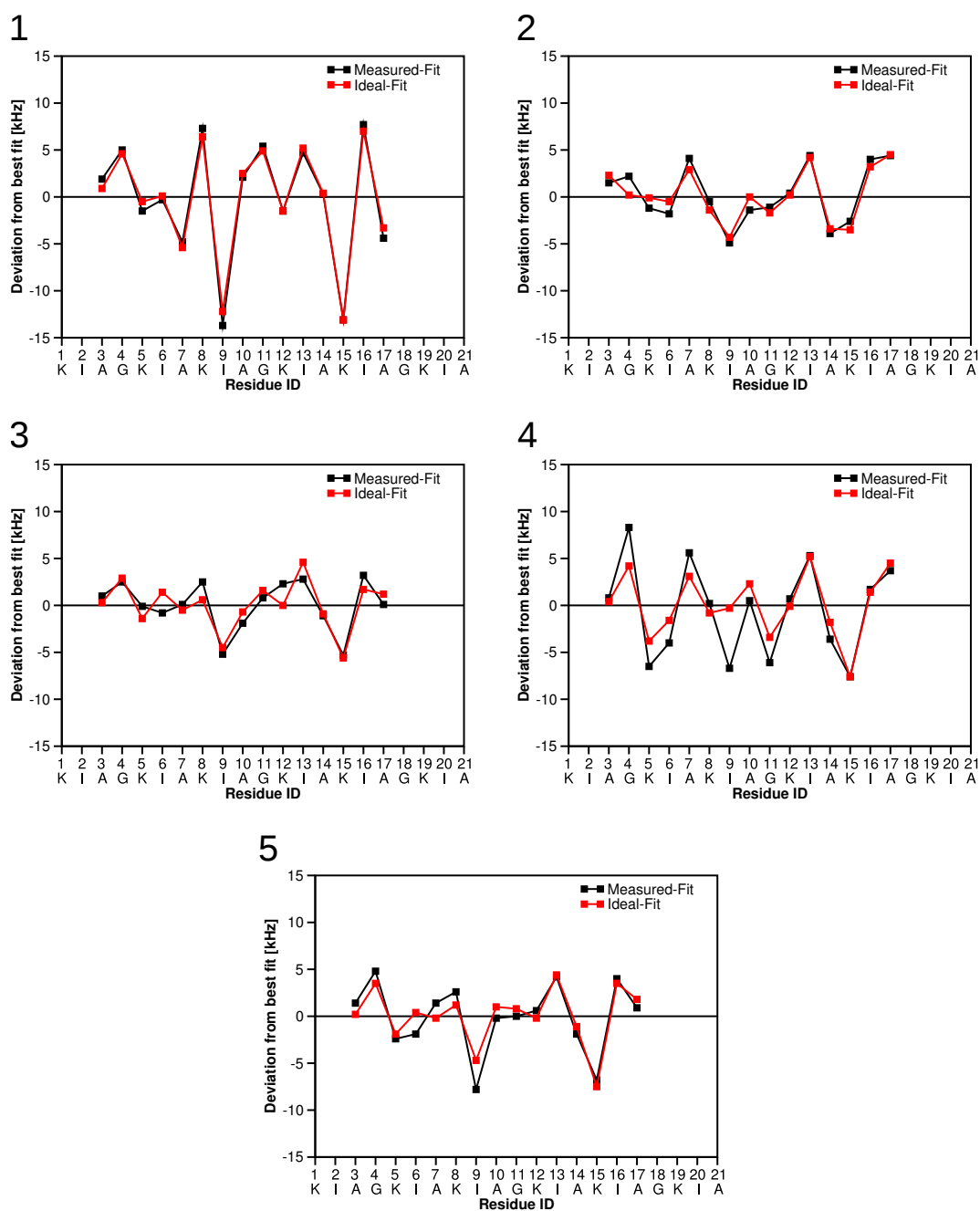


Figure 4.10: MSI-103, *black*: Deviation of measured splittings from ideal splitting at the same position, calculated from the best fit parameters, shown in Figure 4.5. *Red*: Deviation of the splittings calculated from the  $\alpha$ ,  $\beta$ ,  $\tau$ , and  $\delta$  values for each position, which were obtained from evaluation of the trajectories and which are shown in Appendix A, from the ideal splittings. 1-4 are the different intervals, each of 200 ns length, 1-4 or the different intervals, 5 are the values obtained for the complete evaluation period 200-1000 ns.

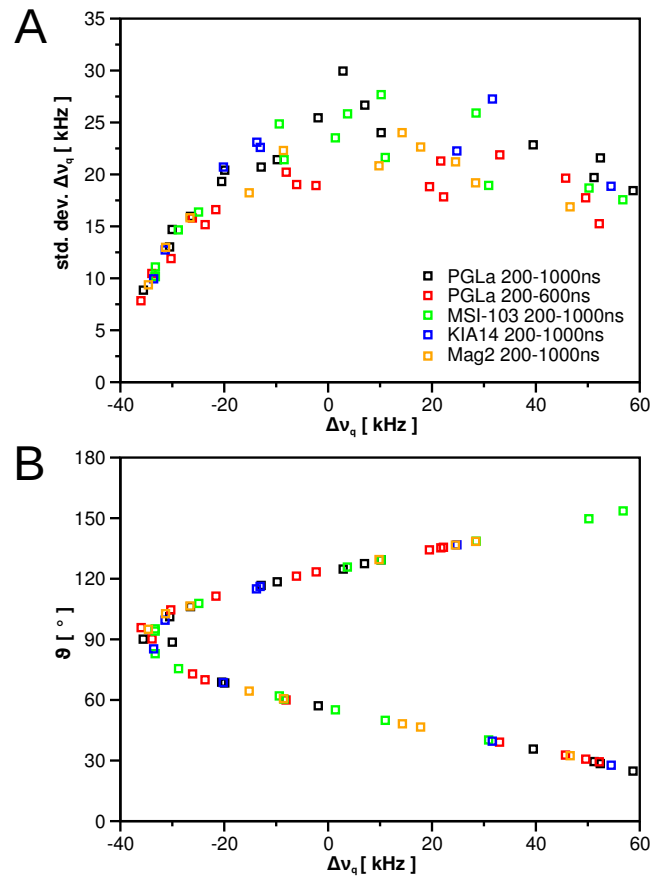


Figure 4.11: A: the standard deviations of the splittings with respect to the average splittings  $\Delta\nu_q$ , averaged over the time period given in the legend. B: the average  $\vartheta$  angles corresponding to the average splittings.

## 4.4 Discussion

The MD simulations cannot reproduce the splittings from the  $^2\text{H}$  NMR experiments. One of the reasons is the incomplete convergence of the peptide-membrane systems, which has been shown recently [47]. The helicity plots show that the secondary structure of the peptides is not fixed but evolving. Only longer simulations can show if this evolution is an intrinsic dynamic process or if it is part of a converging process.

For all simulations, the general peptide orientations could be successfully compared with experimental data. For PGLa, there is a drastic reorientation taking place within the last 300 ns of the simulation, leading to a state where the peptide is tilted into the membrane, connecting with the opposite leaflet. This tilted state agrees very well with the state measured by NMR at a higher peptide:lipid ratio of 1:50, which has been postulated to be dimeric [60,80]. The simulations show that this state is not necessarily dimeric, but can occur also for a monomer.

For MSI-103, the orientation matched better that of MSI-103 in a DOPC bilayer than in the simulated DMPC, which has an identical head group as DMPC, but longer aliphatic tails. In the NMR measurements with DMPC, an intermediate orientation between a surface aligned state and a state where the peptide is tilted into the membrane, was found. This can be due to a stronger self-assembly of MSI-103, which is seen already at a peptide:lipid ratio of 1:200 in the DMPC bilayer by oriented CD [32]. In DOPC, MSI-103 is likely monomeric, even at a high peptide:lipid ratio of 1:20 [101].

When comparing the fits of the simulation splittings for PGLa, MSI-103 and KIA14 with the experimental fits with a similar  $\tau$  angle, there is always a shift in the azimuthal rotation angle  $\rho$  between the fits based on the simulations and the experiments, using the same value of  $\alpha$ . The  $\rho$  angle obtained from the experiments is always larger than the one measured in the simulations. This shift is largest for PGLa and KIA14 with  $\sim 17^\circ$ , and smallest for MSI-103 with  $\sim 9^\circ$ . For PGLa, this has been observed earlier in [47,60]. Here the shift was  $\sim 18^\circ$ , obtained from simulations with a different force field (CHARMM). For Mag2 there is no significant  $\rho$  shift. Here, also the agreement between the splittings obtained from the simulation and from the experiment is the best. All three peptides PGLa, MSI-103 and KIA14 have amidated carboxy-termini, opposed to Mag2. Also, they all have similar sequences, with only Lys as charged residues. Possibly, the description of the amide group or Lys in the force fields is responsible for the  $\rho$  shift.

The dynamic factor  $S_{\text{mol}}$  is generally higher in the fits of the simulations than of

the experiments, indicating a lower mobility in the simulations. However, the fits which have been done on the splittings, averaged over intervals #1-4, show lower  $S_{\text{mol}}$  values and lower RMSDs than the averaged  $S_{\text{mol}}$  and averaged RMSDs of #intervals 1-4. This indicates that deviations from the ideal helical structure also average out in the course of the simulation, leading both to better fits and  $S_{\text{mol}}$  values closer to the experiment.

High RMSD values, when fitting the splittings to an ideal helix, do not necessarily mean that the evaluated positions are nonhelical. There might as well be local deviations from the ideal angles, due to steric or dynamic reasons.

Experimentally measured splittings  $\Delta\nu_q$  with values between 35 and 40 kHz should be considered with care. In  $^2\text{H}$  NMR, the sign of the splitting cannot be obtained. If the sign can be reconstructed due to physico-chemical considerations, the value of the splitting might be more reliable when it has a negative sign, since this implies an orientation of the director of  $90^\circ$  with respect to the membrane normal, where small deviations of  $\vartheta$  have only small effects on the splitting. If the splitting is around +40 kHz, it is more sensitive to small changes in the peptide structure and orientation.

## 5. 3D hydrophobic moment vectors as a tool to characterize the surface polarity of amphiphilic peptides<sup>1</sup>

### 5.1 Introduction

Understanding the mechanism of interaction between amphiphilic peptides and membranes is a central goal of many investigations on antimicrobial agents, cell penetrating carriers, and of peripheral membrane proteins in general [42, 60, 102–108]. Membrane binding is the first step, for example, in the formation of peptidic transmembrane pores, and further transitions between surface-bound and inserted structures are often of functional significance [50, 57, 81, 109].

In this work, we have defined and utilized three-dimensional (3D) hydrophobic moment (HM) vectors as a new tool to predict peptide-bilayer binding geometries.

This 3D approach extends the idea of molecular hydrophobicity potentials (MHP), which are based on heuristic [110] or experimental [111–115] definitions of the hydrophobicity for whole residues [112], molecular fragments or individual atoms [116]. Tools like MPEx [117] use these hydrophobicity scales to calculate water-bilayer transfer energies for small peptides. The first concept of a HM for individual protein helices was presented in 1982 by Eisenberg et al. [118, 119]. Based on the experimentally determined amino acid side chain hydrophobicities [119], a two-dimensional (2D) HM vector is calculated that represents the distribution of hydrophobic and hydrophilic residues perpendicular to the helix axis. In this way, it is possible to categorize helical peptides according to their amphiphilicity, and to roughly predict their insertion geometry into a membrane. More recently, refined hydrophobicity scales have been developed [120], and the methodology is used regularly for the analysis of membrane proteins [121]. The Eisenberg definition of a 2D HM vector is useful for the qualitative description of peptide helices, but it is limited in applica-

---

<sup>1</sup>Parts of this Chapter have been published in: S. Reißer, E. Strandberg, T. Steinbrecher, and A. S. Ulrich; *Biophysical Journal*, 106(11):2385–2394, 2014

bility to structures close to ideal  $\alpha$ -helical geometry. Amphiphilic gradients along the helix axis cannot be taken into consideration either, because the calculation relies on a projection of the vector onto the plane of the helical wheel. Furthermore, the commonly used hydrophobicity scales have been determined with respect to the free energies of transferring isolated amino acid side chains from polar to non-polar environments [119]. They do not take into account the cooperativity between side chains (e.g. salt bridges), nor any conformational rearrangements within a whole peptide (e.g. upon membrane binding).

To establish a simple and generally applicable method to compute 3D HM vectors for arbitrary molecules, we combine structural data from MD simulations with the protocol outlined below. It is based on the electrostatic potential on the peptide surface, computed via Poisson-Boltzmann continuum electrostatics calculations. We will show for four representative peptides of different conformation, size and hydrophobicity that their 3D HM vectors align with the membrane normal. We have selected four different AMPs as a test set, namely the  $\alpha$ -helical peptides PGLa [19,32,51–57,82,99,100], BP100 [21] and TemporinA [62–64], and the cyclic  $\beta$ -pleated gramicidin S [66,67,78,80,122]. For the latter, the currently established methods to calculate a HM are not applicable.

## 5.2 Methods

### 5.2.1 Simulations

Four antimicrobial peptides were selected as model systems:

- the cyclic decapeptide gramicidin S (GS, charge +2, cyclo[VOL-<sup>D</sup>F-P]<sup>2</sup>, where O stands for ornithine) [66,67,78,80,122],
- the helical 21-mer PGLa (charge +5, GMASKAGAIA GKI<sup>A</sup>KVALKA L-NH<sub>2</sub>) [19,32,51–57,82,99,100], which we have studied extensively in the past,

and the two short helical peptides

- BP100 (charge +6, KKLFKKILKY L-NH<sub>2</sub>) [21] and
- temporin A (TempA, charge +2, FLPLIGRVLS GIL-NH<sub>2</sub>) [62–64].

Simulations were conducted in methanol (MeOH) or water for solvated conditions, and in a DMPC bilayer for the membrane-bound states. The water model was in all simulations TIP3P, and for MeOH AMBER99 parameters were used.

For the peptide/lipid systems, two different setups were used: GS and PGLa were simulated using the AMBER99SB-ILDN [97] force field with the SLIPID force field for the lipids [83], BP100 and TempA were simulated by cooperator Jakob Ulmschneider using CHARMM27 [123] for the peptide and water together with a CHARMM36 [124] membrane.

The starting conformation for GS was constructed using the *xleap* tool from the AmberTools modelling suite [98], based on dihedral angles obtained from a high-resolution liquid-state NMR structure [74]. PGLa as well as BP100 and TempA were modeled as ideal  $\alpha$ -helices, based on helicity measurements by CD spectroscopy [21, 54].

Unrestrained production simulations were conducted using a *Nosé-Hoover* thermostat [94] and *Parrinello-Rahman* barostat [95] for GS and PGLa, respectively a *V-rescale* thermostat and a *Berendsen* barostat [125] for BP100 and TempA, with semiisotropic pressure coupling in the case of lipid bilayer systems. Long range electrostatics were treated with PME combined with a 1.4 nm (GS, PGLa) or a 1.0 nm (BP100, TempA) direct space cut-off radius for van-der-Waals and Coulomb interactions.

GS was simulated for 600 ns at 303 K, embedded in a box of  $\sim 1000$  MeOH molecules, and for 650 ns in a lipid bilayer composed of 72 pre-equilibrated DMPC molecules that were solvated with  $\sim 2000$  TIP3P water molecules and chloride counter-ions.

PGLa was simulated for 600 ns at 303 K in solution in a box with  $\sim 6000$  water molecules and chloride counter-ions, and for 600 ns embedded in a pre-equilibrated bilayer composed of 100 DMPC lipid molecules that were solvated with  $\sim 3000$  TIP3P water molecules and chloride counter-ions.

BP100 was simulated for 574 ns at 308 K in a box of 58 DMPC molecules, solvated with  $\sim 2000$  water molecules, including chloride counter-ions.

TempA was simulated for 508 ns at 308 K in a box of 42 DMPC molecules and  $\sim 1300$  water molecules and chloride counter-ions to neutralize the system.

For the membrane simulations of GS and PGLa, two or three control simulations were performed, each of 400 ns length and following the same protocol but with slightly different starting positions of the peptides.

### 5.2.2 Hydrophobic moment calculation

The last 100 ns of each simulation were used to compute and analyse the hydrophobic moment, based on 100 structural snapshots collected at equidistant time steps of one

nanosecond. To determine the averaging procedure, we performed the calculation on one of the PGLa simulations also at a smaller time step of 50 ps to have 20 times more snapshots, and also over the last 300 ns instead of over the last 100 ns. All of these different datasets (100, 2000, 300, 6000 snapshots) gave almost the same average values for the HM vector, the maximal difference being 1.2% (see Table B.1). See also Figure B.1 for evolution of the different properties. Considering the fast fluctuations of the values and the considerable amount of calculation time needed (approx. one minute per snapshot), we find that a choice of 100 snapshots taken at a time step of 1 ns in 100 ns of equilibrated trajectory is justified.

Solvent and lipid molecules were removed, and continuum solvent calculations were set up for the peptides using *PARSE* radii [126] while atomic partial charges were kept from the force field.

For each structure the solvent accessible surface (as a set of discrete triangles) was calculated using NanoShaper [127]. The APBS [128] numerical Poisson-Boltzmann (PB) solver was used to compute the electrostatic potential  $V_e$  on every surface triangle vertex. The interior dielectric constant for the peptide solutes was set to 2.0 to account for electronic polarization effects. Solvent dielectric constants of 78.5 were used for an aqueous environment, 32.6 for MeOH solvation, and a value of 20.0 was used for the membrane-water interface as an interpolation between the polar aqueous and hydrophobic bilayer interior conditions. Based on the continuum electrostatic calculations, we define the resulting hydrophobic moment vector  $\boldsymbol{\mu}$  as

$$\boldsymbol{\mu} = \sum_{i=1}^n \sum_{j=1}^3 \left( \langle |V_e| \rangle - |V_e|_{ij} \right) \cdot \mathbf{r}_{ij} \quad (5.1)$$

The sum over  $i$  runs over all triangles, and the sum over  $j$  runs over the three corner points of each triangle.  $|V_e|_{ij}$  is the absolute value of the electric potential at the corner point labeled  $ij$ . All parts of the surface that have an absolute electric potential  $|V_e|$  greater than the average absolute potential are counted as negative or polar, while the parts with lower electric potential are counted as positive or unpolar. The average absolute potential  $\langle |V_e| \rangle$  is defined as

$$\langle |V_e| \rangle = \frac{1}{A_{tot}} \sum_{i=1}^n \sum_{j=1}^3 |V_e|_{ij} \cdot \frac{A_i}{3} \quad (5.2)$$

Due to the uneven spacing of the triangulated surface, the potential on each vertex is scaled by one third of the area of the surrounding triangles  $A_i$ . The whole sum

is then divided by the total surface area  $A_{tot}$ . The vector  $\mathbf{r}_{ij}$  in Equation 5.1 points towards the vertex  $ij$  and is defined as

$$\mathbf{r}_{ij} = \mathbf{x}_{ij} \cdot \frac{A_i}{3 \cdot A_{tot}}, \quad (5.3)$$

where  $\mathbf{x}_{ij}$  is the actual vertex vector. As above,  $\mathbf{x}_{ij}$  is scaled by one third of the surrounding triangle area. This way, we avoid an overestimation of highly curved parts of the surface that contain a lot of vertices.  $A_{tot}$  is simply the sum over all triangles:

$$A_{tot} = \sum_{i=1}^n A_i \quad (5.4)$$

We use absolute values for the electrostatic potential, since we aim to describe the differential distribution of polar and unpolar patches on the surface, effectively constructing a vector  $\boldsymbol{\mu}$  that points away from the most polar parts of the molecular surface. By using the difference between the absolute surface potential at each point and the average absolute surface potential,  $\boldsymbol{\mu}$  reflects the distribution of polar patches on the surface (not the total polarity of the molecule). If the electrostatic potential is given in  $\text{kT}/e$  and the vectors in  $\text{\AA}$ , the resulting hydrophobic moment vector has a unit of  $2.56 \cdot 10^{-12} \text{ Vm}$  at room temperature. Since this unit doesn't imply any physical meaning, we omit it in the following and give  $\boldsymbol{\mu}$  in multiples of  $\text{kT}\text{\AA}/e$ .

## 5.3 Results

### 5.3.1 Model charge distributions

To illustrate the principle and to help visualize the results obtained from HM calculations, we created a model system consisting of a hexagonal pseudo-molecule that is shaped like benzene, on which we placed varying charge distributions (Figure 5.1). In the initial form all partial charges were set to zero, and then various sets of one to four positive and/or negative charges of magnitude  $0.3e$  each were distributed around the ring.

Cases A and B in Figure 5.1 show the trivial situation of no charge or a single charge, resulting in no HM or one pointing away from the charge. Cases C, D, J and M show that symmetrical arrangements of charges cancel the HM, independent of the sign of these charges. For cases E and F, it can be observed that charges of opposite sign, placed closely together, compensate each other's effect to some extent, leading to a slightly smaller HM vector for F than for E. Cases B, E and G show that HM

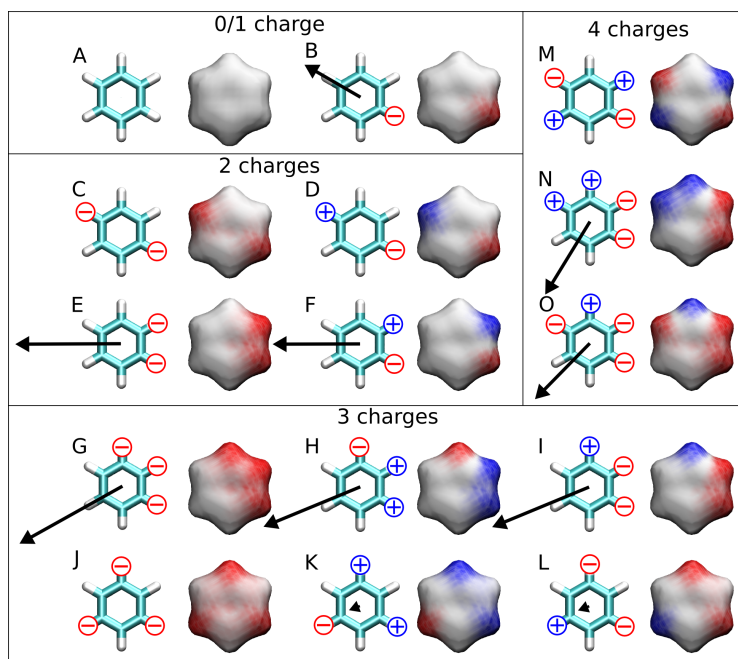


Figure 5.1: HM vectors and surface electrostatic potential for various model charge distributions on a hexagonal pseudo-molecule. The HM vectors consistently point towards the most nonpolar parts of the molecular surface, independent of the sign of the individual charges or the total molecular charge. The length of the arrow reflects the size of the HM. (Cases without an arrow indicate  $\mu = 0$ .)

vectors increase in length the more unbalanced the distribution of polar and nonpolar surface areas becomes. Cases H and K show the effect of neighbouring charges of opposite sign in more detail. For H, the vector is rotated slightly compared to G, and in K a small non-zero vector is found in contrast to J. Cases I and L (compared to H and K, respectively) show that reversing the sign of all charges does not influence the HM at all. Finally, cases N and O show that meaningful and comparable HM vectors can be obtained, even in highly charged molecules of different total molecular charge.

These examples show that the HM is a quantity independent of the total charge. It is similar in definition to the dipole moment, but is a different measure of the charge distribution. The vector represents the distribution of polar and nonpolar parts of a molecular surface, while taking into account solvation effects and partial charge compensation via salt bridges. Since the distribution of nonpolar surface patches is crucial in many areas of macromolecular interactions - from protein oligomerization to receptor-ligand recognition and peptide-bilayer binding - the HM vector serves as a useful descriptor of macromolecular shape-dependent properties.

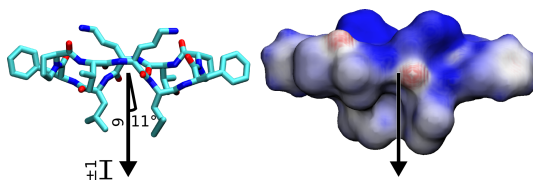


Figure 5.2: *Left*: Representative structure of GS in MeOH with its calculated HM vector. *Right*: Electrostatic potential on the solvent accessible surface of the same structure. The HM vector is pointing away from the surface region with high electrostatic potential.

### 5.3.2 Peptide studies

We calculated the HM, based on conformational ensembles from long MD simulations (several hundred ns), for four amphiphilic antimicrobial peptides.

#### Gramicidin S in solution

The cyclic peptide GS was simulated for 600 ns at 303 K, embedded in a cubic box of  $\sim 1000$  MeOH molecules (box side length ca. 4 nm). The peptide starting structure was obtained from high-resolution NMR data [74]. All-atom RMSD evolution (see Appendix Figure B.2) shows that a minor structural rearrangement takes place after 130 ns simulation time, upon which a stable conformational ensemble is obtained. Figure 5.2 gives the representative structure from a clustering analysis of the peptide, and the results of HM calculations based on the last 100 ns of the simulation data. The HM vector is aligned almost perfectly with the molecular C<sub>2</sub>-symmetry axis, as expected, and it points away from the charged Orn residues, passing in between the hydrophobic side chains of the four Val and Leu residues. When aligning all snapshots, the instantaneous HM vectors deviate from the time-averaged vector by  $11^\circ \pm 6^\circ$ , and the average length is  $9.3 \pm 0.9$ .

#### Gramicidin S in a membrane

Next, we calculated the HM for GS inserted into a lipid bilayer (see Figure 5.3), in order to compare these results with the isotropic solution (Figure 5.2) and to see how the HM vector aligns with respect to the membrane normal. Here, the snapshots were taken from the last 100 ns of a 650 ns long simulation in a bilayer composed of 72 pre-equilibrated DMPC molecules, solvated with  $\sim 2000$  TIP3P water molecules and chloride counter-ions. The RMSD evolution after embedding the peptide in the membrane shows small conformational rearrangements until ca. 250 ns of simulation time, after which a stable, converged structure is obtained (see Appendix Figure B.3). The peptide lies directly underneath the zwitterionic lipid head groups, point-

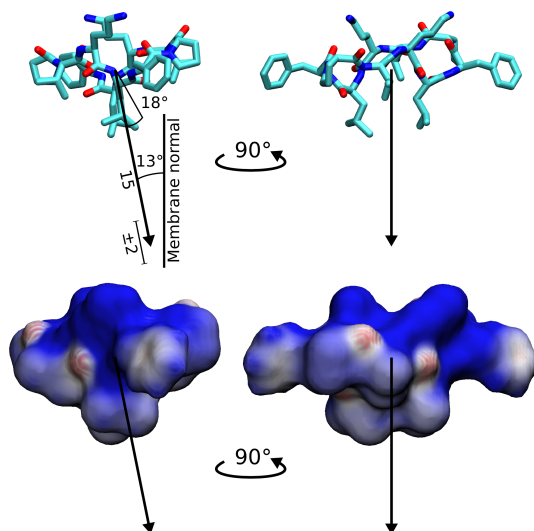


Figure 5.3: *Top*: Representative structure of GS embedded in a DMPC membrane (bilayer not shown, aligned horizontally) with its calculated HM vector. *Bottom*: Electrostatic potential on the solvent accessible surface. The HM vector is almost parallel to the membrane normal ( $13^\circ$ ).

ing its charged residues up towards the water. The average distance between the peptide backbone and the phosphorus atoms of the lipids is  $8.1 \text{ \AA}$ . All three control simulations show the same average orientation upon insertion into the membrane. The resulting orientation of the peptide in the membrane is in full agreement with the results from SSNMR measurements, in which the C2-symmetry axis tilt angle and the azimuthal rotation angle had been measured in an oriented DMPC sample with a peptide:lipid ratio of 1:80 [80].

The HM vector was calculated using an intermediate solvent dielectric constant of 20.0, to represent the conditions at the bilayer/water interface region.

HM analysis shows that the fluctuations of the vector are more pronounced than during the simulation in MeOH, with an average angle deviation with respect to the average HM vector of  $18^\circ \pm 10^\circ$ , and a standard deviation of the absolute length of  $\pm 2.0$  (Figure 5.3). Interestingly, the HM vector has become much longer by more than 50% to  $15.2 \pm 2.0$ . This increase in length is caused partly by the smaller dielectric constant used in the PB calculations (reducing solvent screening), but also by conformational changes of the peptide upon membrane binding. Exposing the molecule to a less polar environment leads to internal rearrangements that result in a more unequal distribution of polar and nonpolar surface residues. The charged Orn side chains now point up directly into the solvent region, while the  $^D\text{Phe}$  rings bend further down towards the hydrophobic bilayer core. Repeating the calculations of the HM vector with a dielectric constant of 32.6 yields an average HM vector length of 11.1, showing that structural rearrangements cause about 30% of the difference in

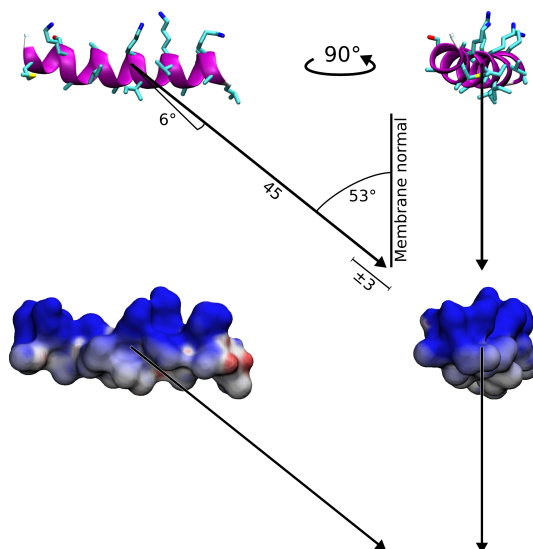


Figure 5.4: *Top*: Representative structure of PGLa in a DMPC membrane (bilayer not shown, aligned horizontally) with its calculated HM vector. *Bottom*: Electrostatic potential on the solvent accessible surface.

the HM vector lengths. The remaining 70% result from the lower dielectric constant and less well screened electrostatic potential on the molecular surface. The resulting combined forces constrain the surface-bound geometry of GS in the membrane and lead to a lengthening of the HM vector. The angle between the HM vector of the time-averaged peptide structure and the membrane normal is small with a value of only  $13^\circ$ , i.e. it points almost straight into the membrane core, as expected. For individual snapshots, the angle undergoes considerable fluctuations and measures on average  $29^\circ \pm 17^\circ$ , indicating that the small, surface-bound peptide behaves rather dynamically when embedded in the membrane. We also performed three control simulations, which gave similar results, summarized in Appendix Table B.2.

### PGLa in a membrane

For peptides that retain a predominantly helical structure in their membrane-bound state, we can compare the 3D HM vector defined above with the conventional 2D HM. The antimicrobial peptide PGLa, which contains 5 positively charged residues along one face of the  $\alpha$ -helix, was simulated for 600 ns at 303 K, embedded in a pre-equilibrated bilayer composed of 100 DMPC lipid molecules, solvated with  $\sim 3000$  TIP3P water molecules and chloride counter-ions. The RMSD evolution of the surface-bound peptide shows a stable structure with no significant conformational changes after 200 ns simulation time (see Appendix Figure B.4). PGLa maintains a completely helical fold in the unrestrained simulation, in good agreement with the

high helical content measured by CD experiments [54]. The helix lies stably in the membrane-water interface, the distance from the N-terminus to the average position of the phosphorus atoms is 4.7 Å, while the C-terminus is deeper embedded with an average distance of 11.2 Å. The peptide is pointing its charged Lys side chains up towards the water phase. The long axis is aligned flat on the membrane surface, at an average tilt angle of  $93^\circ \pm 7^\circ$  with respect to the membrane normal. This alignment is very close to the experimentally obtained  $95^\circ$  that was determined by SSNMR in oriented DMPC bilayers at a peptide-to-lipid molar ratio of 1:200 [41, 52, 54, 55].

The HM vector analysis was conducted over the last 100 ns of simulation time. The resulting HM vector and the corresponding electrostatic surface potential of the molecule are shown in Figure 5.4. The HM vector points away from the charged Lys residues, but the angle between the HM vector and the helix axis is only  $39^\circ \pm 5^\circ$ . This makes an important difference compared to the implicit value of  $90^\circ$  that is imposed by the conventional 2D HM analysis. Several reasons contribute to the pronounced inclination of the vector towards the C-terminus, including an unbalanced charge distribution along the peptide sequence, the additional charge at the uncapped N-terminus, and a large hydrophobic patch formed by a C-terminal Leu residue. At the same time, the HM vector of the time-averaged peptide structure is tilted quite far away from the membrane normal by  $53^\circ$ . Together with its tilt angle of  $39^\circ$  relative to the helix axis, the sum of  $92^\circ$  is consistent with a peptide helix aligned essentially perpendicular to the membrane normal, as described above and by SSNMR. The HM projection perpendicular to the helical axis aligns well with the membrane normal. The length of the vector is  $44.9 \pm 3.3$ , significantly larger than the value for GS above, which indicates that PGLa is not only highly charged, but has a very unequal polarity distribution along the helix. We also performed two control simulations, which gave very similar results (Appendix Table B.2).

When comparing the 3D HM vector obtained by our method with the original 2D HM definition by Eisenberg et al. [119], we find that the projection of the three-dimensional HM vector onto the plane orthogonal to the helix axis results in closely aligned vectors (within an angle of  $18^\circ$ , see Figure 5.5).

Notably, the new, 3D definition of the HM not only properly reproduces the unequal distribution of polar residues on the helical wheel of PGLa, but it also contains additional information about their distribution along the helix as well. Our HM calculations suggest that PGLa should have a tendency to insert the C-terminus more deeply into the hydrophobic core than the N-terminus, such that the HM aligns more closely with the membrane normal. Such a strongly tilted peptide orientation

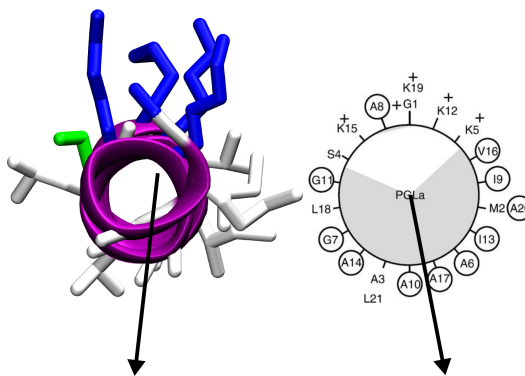


Figure 5.5: *Left*: Projection of the 3D HM vector from this work onto the helix cross section of PGLa. *Right*: Conventional 2D HM vector calculated according to Eisenberg [118]. (The vectors have been normalized.)

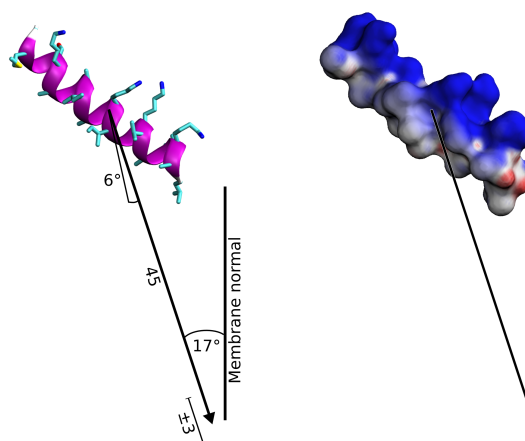


Figure 5.6: *Left*: Tilted state of PGLa as measured experimentally by SSNMR in DMPC membranes at a peptide:lipid ratio of 1:50 (79) (bilayer not shown, aligned horizontally), shown together with its HM vector calculated from MD simulations. *Right*: Electrostatic potential on the solvent accessible surface.

is not seen in our simulations, probably due to sampling constraints. The membrane-bound geometry observed here corresponds to the so-called "surface-state" obtained by SSNMR at a peptide:lipid ratio of 1:200 [41,52,54,55]. However, a second, distinct membrane-bound structure has been found for PGLa in NMR experiments at a higher peptide:lipid ratio of 1:50 [19,41,52,55]. In this so-called "tilted state", the helix axis is inclined at an angle of  $127^\circ$  with respect to the membrane normal. In this tilted orientation, our HM vector would be aligned almost parallel to the membrane normal (at  $17^\circ$ , as seen in Figure 5.6). It has been argued, based on the concentration-dependence [54,55] and on MD analysis [47,60], that the "tilted state" of PGLa may be accompanied by dimerization. The peptide obviously experiences different forces and different stabilizing interactions under different conditions, and it will adjust its geometry in the membrane according to the dominant influence. We

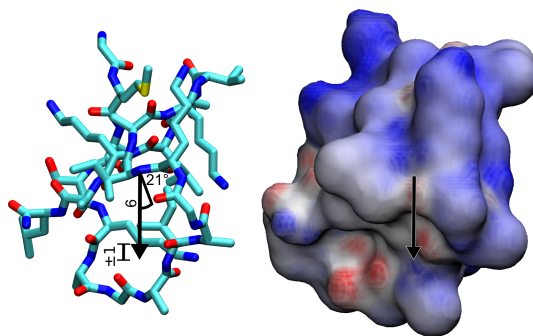


Figure 5.7: *Left*: Representative structure of largely unfolded PGLa in water with its calculated HM vector. *Right*: Electrostatic potential on the solvent-accessible surface.

may thus suggest that the HM vector represents one of these factors and contributes significantly to stabilizing the strongly tilted membrane-bound structure of PGLa that has been observed experimentally.

### PGLa in water

For GS, we have shown above that the HM vector becomes longer when the peptide binds to a membrane. In order to check whether this holds also for PGLa, the peptide was simulated for 600 ns, starting from an ideal helical structure, in a water box including counter-ions. However, the peptide quickly unfolded in the polar medium and collapsed into a compact state resembling an unstructured coil (see RMSD plot in Appendix Figure B.5). Here, the polar regions tend to point towards the surrounding solvent, while the hydrophobic residues are packed into the core. The HM vector is drastically reduced in this conformation, by almost 90% to an average length of  $5.5 \pm 1.2$  (see Figure 5.7). The HM calculation was performed both with a dielectric constant of 78.5 to represent water, and with a dielectric constant of 20.0 as above, to be able to distinguish between the contribution of the different dielectric environment and that of the conformational change. We find that about two thirds of the reduction of the HM can be attributed to the conformational change, and one third to the different dielectric constant used in the electrostatics calculations.

### BP100 in a membrane

The highly charged (+6) small helical peptide BP100 was simulated for 574 ns in a box with 58 lipid molecules and ~2000 water molecules. Throughout the simulation, the peptide is very mobile but maintains a stable orientation with a tilt angle  $\tau$  of  $120^\circ \pm 14^\circ$  against the membrane normal. The orientation of the peptide is in agreement with  $^{19}\text{F}$  NMR measurements, which determined an interval between  $110^\circ$

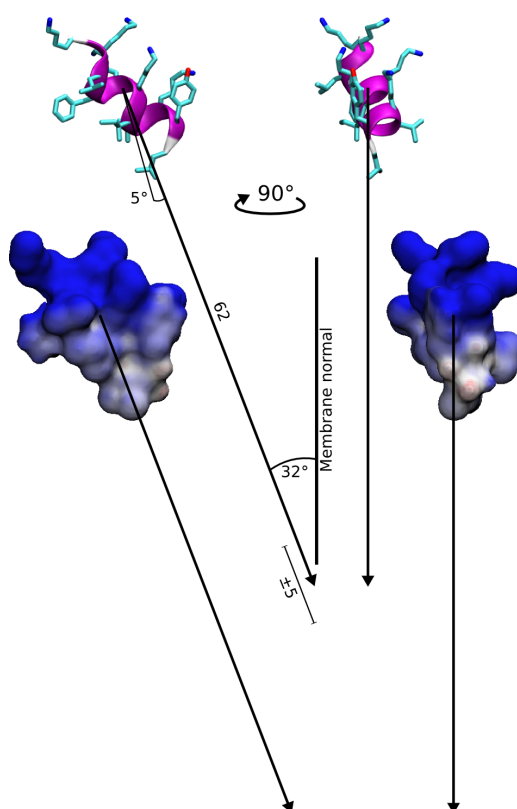


Figure 5.8: *Top*: Representative structure of BP100 in a DMPC membrane (bilayer not shown, aligned horizontally) with its calculated HM vector. *Bottom*: Electrostatic potential on the solvent accessible surface.

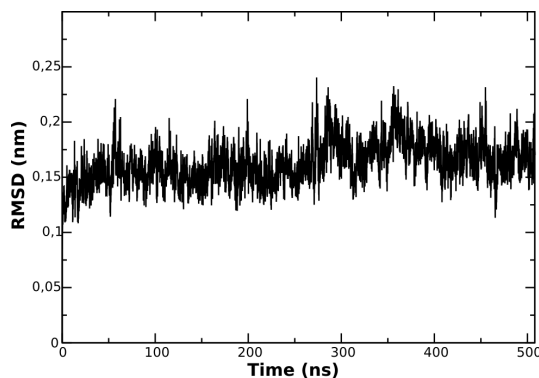


Figure 5.9: RMSD values calculated for TempA between the starting structure and every snapshot of the simulation. The values indicate a stable structure of the peptide throughout the simulation.

and  $160^\circ$  for  $\tau$  [21]. All the charged Lys residues reach into the membrane-water interface.

The HM vector calculated from the last 100 ns is closely aligned with the helical axis, at an angle of  $26^\circ \pm 4^\circ$  (Figure 5.8). Due to the asymmetric distribution of the six charges, the HM vector is extremely long with a length of 62. This leads to a comparably small angle between the membrane normal and the HM vector of  $32^\circ$ .

### Temporin A in a membrane

The 13 residue antimicrobial peptide TempA represents an amphiphilic helical peptide of low total charge (+2), in contrast to the more highly charged PGLa and BP100 discussed above. The membrane-embedded peptide was simulated for 508 ns in DMPC. The simulated box included 42 DMPC molecules and  $\sim 1300$  water molecules at 308 K. For this system, initially the last 100 ns of simulation time were analyzed, since the RMSD value indicated a converged, stable structure over the whole simulation (Figure 5.9). In this case, the asymmetric distribution of the two positive charges – an uncapped N-terminus and a central asparagine residue – lead to a HM vector tilted significantly towards the helix axis, at an angle of only  $31^\circ \pm 3^\circ$  degrees (Figure 5.10). Since the peptide lies nearly flat in the membrane, the angle between the membrane normal and the HM vector is around  $60^\circ$ , significantly higher than for the peptides studied above. Interestingly, when the entire simulation length for this system is analyzed (one HM calculation per ns), it becomes apparent that there are two stable membrane-bound states for TempA (Figure 5.11).

One persists from 0 to  $\sim 250$  ns simulation time and shows the peptide inserted almost vertically into the membrane at a tilt angle of  $152^\circ \pm 8^\circ$  (Figure 5.12, averaged over the first 200 ns), and the other from  $\sim 300$  ns to the end of the simulation at

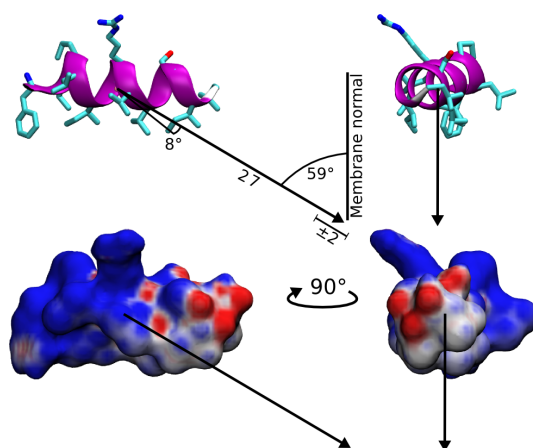


Figure 5.10: *Left*: Representative structure of TempA in a DMPC membrane (bilayer not shown, aligned horizontally) with its calculated HM vector and corresponding electrostatic potential on the solvent accessible surface, from the end of the simulation in the surface aligned state. *Right*: same structure, rotated by  $90^\circ$ .

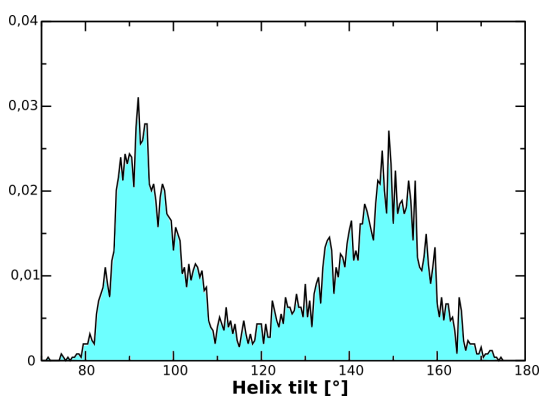


Figure 5.11: The distribution of helix tilt angles over the course of the whole simulation. There are two possible orientations - one with a tilt angle of  $\sim 92^\circ$ , and one with a tilt angle of  $\sim 152^\circ$ . The scale on the y-axis is such that the integral under the curve equals one.

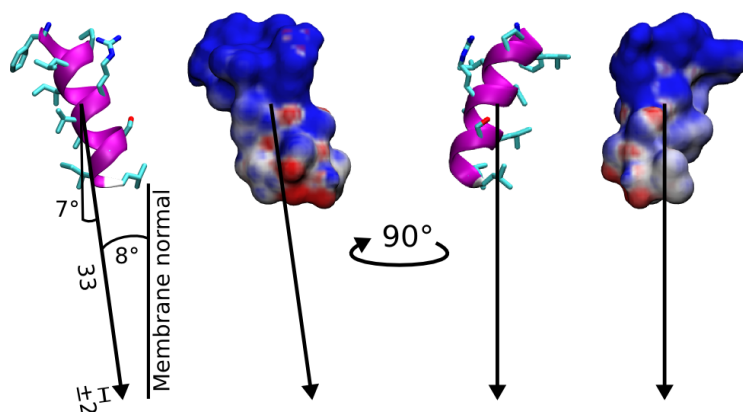


Figure 5.12: *Left*: Representative structure of TempA in a DMPC membrane (bilayer not shown, aligned horizontally) with its calculated HM vector and corresponding electrostatic potential on the solvent accessible surface, from the beginning of the simulation in the strongly tilted state. *Right*: same structure, rotated by  $90^\circ$ .

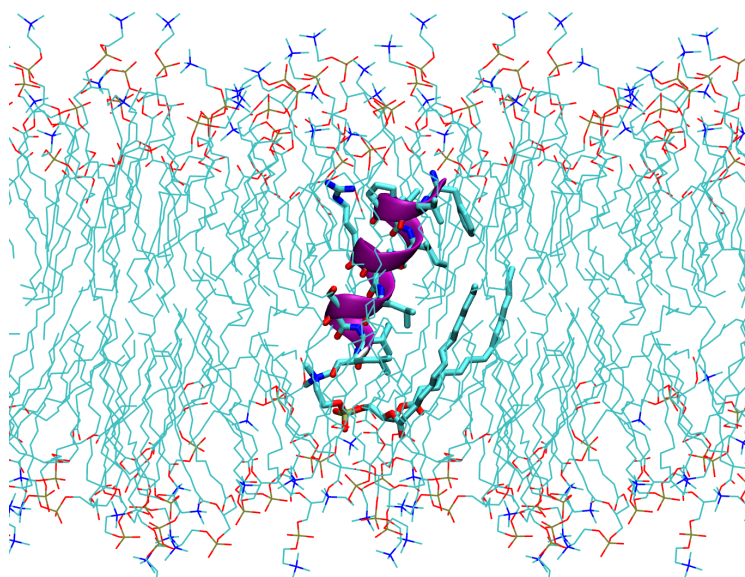


Figure 5.13: Snapshot from the first 200 ns of the simulation. The peptide stabilizes its upright orientation by electrostatic interaction between its negatively charged C-terminal backbone oxygens and the positively charged choline groups of the lipids. The distance between the oxygen of the 13th residue and the nitrogen atom of the choline group is  $\sim 3.5\text{\AA}$ .

508 ns, which shows a surface-aligned orientation of the peptide at a tilt angle of  $100^\circ \pm 7^\circ$  (averaged over the last 200 ns).

By evaluating the distance between the negatively charged C-terminal oxygen atoms of TempA and the choline groups of the lipids of the opposite membrane layer, it becomes clear that the upright position of the peptide is stabilized by electrostatic interaction between these two groups. Even though the peptide is too short to completely span the membrane, it is able to pull the flexible choline groups towards it, thus stabilizing its orientation (Figure 5.13).

Experimental data from  $^{19}\text{F}$  NMR revealed a tilt angle of  $\sim 128\text{--}135^\circ$ , depending on the peptide:lipid concentration [65]. Since this range lies almost exactly in the middle of the two orientations observed in the simulation, it might be possible that the experimentally measured values are a result of a superposition of these two states. However, longer simulations are necessary to find out if the highly tilted state observed at the beginning of the simulation is re-occurring, or an artefact from the start of the simulation.

The HM vector is nearly co-aligned with the membrane normal in the first case at an angle of only  $12^\circ \pm 6^\circ$ . The reorientation of the peptide which leads to a final angle between HM vector and membrane normal of  $60^\circ \pm 6^\circ$  is accompanied by a reduction in HM vector length of 18% from  $33 \pm 1$  to  $27 \pm 2$ .

Table 5.1: Summary of the HM vectors calculated for the last 100 ns of long MD simulations (for all peptides but TempA, for which it is explicitly stated). The value after a  $\pm$  sign is the standard deviation.

System	Average HM vector length (kTÅ/e) <sup>a</sup>	Average angle deviation from average HM vector (°) <sup>b</sup>	Average angle between HM vector and membrane normal (°) <sup>c</sup>	Angle between average HM vector and membrane normal (°) <sup>d</sup>
GS in MeOH	9.3 ± 0.9	11.1 ± 5.9	-	-
GS in membrane	15.2 ± 2.0	17.9 ± 9.5	28.8 ± 17.1	12.6
PGLa in water	5.5 ± 1.2	21.1 ± 13.0	-	-
PGLa in membrane	44.9 ± 3.3	5.7 ± 2.8	53.3 ± 6.6	53.2
BP100 in membrane	62.1 ± 4.8	5.4 ± 2.4	32.4 ± 13.4	30.6
TempA in membrane (0-200 ns)	33.0 ± 1.5	7.4 ± 3.1	12.4 ± 6.5	7.9
TempA in membrane (300-508 ns)	27.3 ± 2.3	7.9 ± 4.6	59.8 ± 6.4	59.4

<sup>a</sup>The average of the absolute values of all 100 vectors calculated from the snapshots.

<sup>b</sup>The average angular deviation between each snapshot vector and the average vector when all snapshot conformations have been optimally aligned. The relatively high standard deviations to these values show that the single frame vectors are not on a cone around the average vector (then they would have to be very small) but rather spread.

<sup>c</sup>The average of the angle between the HM vector and the membrane normal in each snapshot.

<sup>d</sup>The angle between the average HM vector after aligning all snapshots and the membrane normal. For GS, it is remarkably different from the value in column three. This shows that for the symmetrical GS, the HM vector is very flexible and averaging significantly decreases the single frame angular values.

### 5.3.3 Results summary

The HM vector properties for the different systems investigated here are summarized in Table 5.1.

We see that the time-dependent HM vector typically maintains a fairly constant length and orientation with respect to the peptide structure during any given simulation, but it can undergo considerable changes when the environmental conditions change, e.g. upon membrane embedding. The HM indicates a favourable orientation in which a peptide can bind to a lipid bilayer surface. However, the HM vector does not have to be aligned parallel with the membrane normal if the peptide in question contains an asymmetrical distribution of charged or non-polar residues along its sequence, or if other forces dominate the geometry of peptide insertion.

## 5.4 Discussion

The 3D HM vector as described in this work extends the classical 2D HM concept introduced by Eisenberg in several aspects: (i) It is applicable to arbitrary molecular structures, not only to regular conformations like  $\alpha$ -helices or  $\beta$ -sheets. Individual side chain rearrangements are taken into account as well as bent helices, partial unfolding, or unusual structures like the cyclic GS. (ii) Charge compensation caused by salt bridges or hydrogen bond formation is reflected in the resulting electrostatic potential on the molecular surface. (iii) Additionally, it is possible to perform MD simulations to calculate the HM time average over a realistic ensemble of highly dynamical peptide structures in fluid membranes.

The results obtained for the HM vectors of GS in solution and when bound to a DMPC bilayer agree very well with both chemical intuition and experimental data. We find that the peptide rearranges its flexible side chains, resulting in an elongated HM vector in the membrane-bound state. Also for BP100, the angle between the HM vector and the membrane normal is small and thus useful to predict its membrane-inserted orientation.

For PGLa, the HM vector points into the membrane at an oblique angle in our simulations, due to the uneven arrangement of polar residues along the helix. Interestingly, the HM vector does not align with the membrane normal in the present simulated orientation, but it would do so in another tilted alignment that has been experimentally observed at a different peptide:lipid ratio. We find that PGLa is not stable as a helix in aqueous solution, but it forms an amphiphilic helix upon binding to the membrane surface, in full agreement with experimental observation [54, 129]. This structural rearrangement produces a long HM vector only for the membrane-bound state.

For TempA, the two orientations seen in the simulation seem not to agree with experiment at the first glance, because neither tilt angle agrees with the one measured from  $^{19}\text{F}$  NMR experiments. But having the HM vector as a support to interpret this situation, the strongly tilted state with a HM vector closely aligned with the membrane normal seems very reasonable. Also the orientation where the peptide lies flat in the membrane is common as had been shown for PGLa in both experiment and simulation, despite the large angle between HM vector and membrane normal. This allows the interpretation that there are two meta-stable orientational states - one where the HM vector is closely aligned with the membrane normal, and one

where the peptide lies flat in the head group region of the membrane. The data measured by NMR could be the result of a quick interchange of these two states.

The 3D HM vector is a useful tool to classify the amphipathicity of peptides. It can predict which face of the peptide orients towards the membrane, even though it may not be sufficient to explain the exact alignment of the membrane-inserted monomer. There are several forces and possibly competing contributions that will determine the actual orientation of a peptide bound to a lipid bilayer. Regarding the HM vector, we expect that it has a stronger effect on shorter and thus more globular peptides (like GS, BP100, TempA) than on extended structures (like PGLa). Other, specific interactions between the lipid head groups and peptide side chains, such as hydrogen bonds, could play a role in preventing the peptide from taking on a position in which the HM vector would be perfectly aligned with the membrane normal. Also the overall dipole moment of the peptide (e.g. as intrinsically found along every helix axis) is of importance for determining the preferred geometry of insertion into charged as well as zwitterionic membranes. Furthermore, the spontaneous lipid curvature and bilayer thickness have been shown to have an effect on the orientation of inserted peptides [59, 101, 130–132].

## 5.5 3D HM vector web application

A web application has been developed and is available under <http://ibg.kit.edu/HM>. The HM vector can be calculated directly from the peptide sequence, in this case the peptide is modelled as ideal  $\alpha$ -helix. Different dielectric constants for the surrounding continuum and the properties of the amino- and the carboxy-terminus can be set before the calculation.

It is also possible to upload PDB structures of peptides, and calculate the HM vector for this structure.



## 6. Simulations of photoswitchable analogs of the antimicrobial peptide gramicidin S

### 6.1 Introduction

The cyclic decapeptide gramicidin S (GS) has been known for more than 70 years for its antimicrobial activity [66,67]. It is produced by the soil bacterium *Aneurinibacillus migullanus* (earlier known as *Bacillus brevis*), is highly active against a broad spectrum of microorganisms and has been extensively studied in the past [78,80,122]. Its mechanism of action is yet unclear, but based on the results of NMR [80] and crystallization studies [79], it was suggested that GS forms lytic pores in the membrane, which are stabilized by inter-molecular hydrogen bonds, keeping the GS monomers in an upright, membrane-spanning position. Figure 6.1 shows GS, which is known to be structured in a symmetrical antiparallel  $\beta$ -pleated conformation connected by two type-II'  $\beta$  turns. The two strands are connected by four intra-molecular hydrogen bonds between the aminocarboxylate moieties of the opposing Leu and Val residues.

GS is not only active against bacterial membranes, but also lyses membranes of red blood cells [24]. Until today, this strong side-effect prevents GS from being used as a systemic antibiotic against quickly evolving bacterial strains.

To improve the pharmaceutical properties of GS, several analogs of GS with an in-

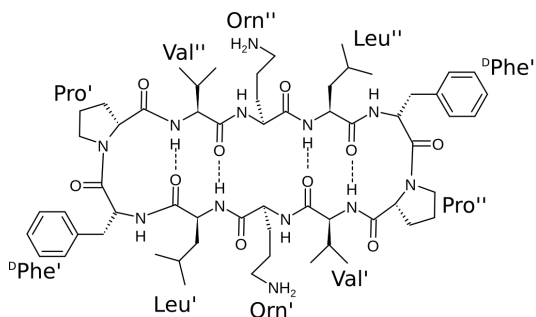


Figure 6.1: Sequence and residue nomenclature of the double-hairpin structure of gramicidin S with four stabilizing hydrogen bonds between Val and Leu residues. Residues are named with the standard 3-letter code; Orn - Ornithine, <sup>D</sup>Phe - D-Phenylalanine.

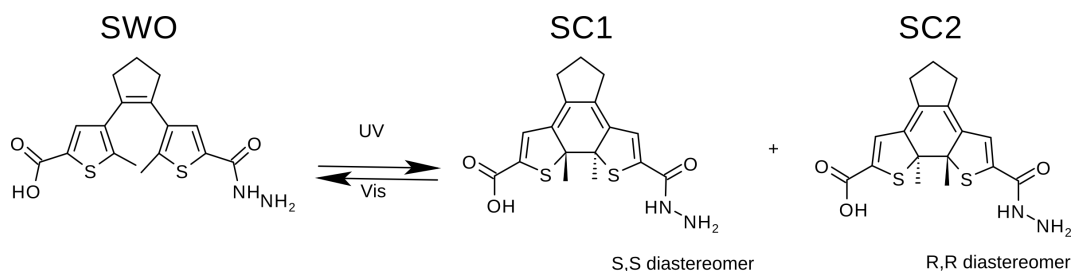


Figure 6.2: Light-induced photoconversion of the diarylethene-based photoswitch, showing its ring-open state (left) and the two possible ring-closed isomers (right).

incorporated diarylethene-based photoswitch (Figure 6.2) have been synthesized [24]. The sequences of the analogs are listed in Table 6.1. This building-block can be reversibly isomerized by irradiation with ultraviolet/visible light, leading to the formation/breaking of a C–C bond between two thiophene rings. The photoswitch can be changed from a flexible to a rigid conformation and *vice versa*, impairing thus a light-controlled element in the GS-based peptidomimetics.

It has been shown that indeed the antimicrobial and hemolytic activities of GS can be controlled by the incorporation of the photoswitch [24]. In this chapter, an extensive MD study is presented, which helps to explain the molecular basis of the photoregulation. Simulations have been performed in solution and in phospholipid membranes. The results are compared with experiments on the same molecules.

## 6.2 Methods

### 6.2.1 Parametrization and model building

The three possible conformations of the photoswitch - 'open' state (SWO), S,S 'closed' state (SC1) and R,R 'closed' state (SC2) - were constructed using *xleap* from the AmberTools package [98]. The photoswitch molecules were capped with an N-terminal aldehyde group and a C-terminal amide group to imitate peptide bonds on both sides. Geometries were then optimized and atomic charges were calculated from the electrostatic potential (ESP) obtained with the Hartree-Fock method using the basis set 6-31G\* [133] in the *Gaussian* quantum chemistry package [134].

Final charges were then obtained with *antechamber* [98] using the RESP methodology [135]. To use the molecules as fragments for the peptidomimetics, the capping groups were removed and the excess charges ( $\leq 0.03$  e) were redistributed equally on the two N-terminal nitrogen atoms and the C-terminal carbon (C) atom. Force field parameters were taken from GAFF [136].

The amino acid ornithine (Orn) was modeled based on the description of Lys in the

AMBER99SB force field [137]. Following the same protocol as above, charge distributions for butylammonium and propylammonium were calculated. Then, one methene group was removed from Lys and the AMBER99SB charges on the side chain were redistributed proportionally to the relation of butylammonium and propylammonium charges. <sup>D</sup>Phe was constructed in its correct geometry during model building, and parameters were taken from Phe (AMBER99SB).

GS was modeled based on experimentally measured dihedral angles [74]. Analogously to the experiment in [24], the photoswitch was inserted at three different positions, replacing Leu''-<sup>D</sup>Phe'', <sup>D</sup>Phe''-Pro'' and Pro''-Val' with the three possible photoswitch conformations. All molecules are listed in Table 6.1.

Table 6.1: GS and its photoswitchable analogs

#	Name	Sequence	Atoms
1	GS	<i>cyclo</i> (Orn'-Leu'- <sup>D</sup> Phe'-Pro'-Val''-Orn''-Leu''- <sup>D</sup> Phe''-Pro''-Val')	176
2	LF_SWO	<i>cyclo</i> (Orn'-Leu'- <sup>D</sup> Phe'-Pro'-Val''-Orn''-SWO-Pro''-Val')	176
3	LF_SC1	<i>cyclo</i> (Orn'-Leu'- <sup>D</sup> Phe'-Pro'-Val''-Orn''-SC1-Pro''-Val')	176
4	LF_SC2	<i>cyclo</i> (Orn'-Leu'- <sup>D</sup> Phe'-Pro'-Val''-Orn''-SC2-Pro''-Val')	176
5	FP_SWO	<i>cyclo</i> (Orn'-Leu'- <sup>D</sup> Phe'-Pro'-Val''-Orn''-Leu''-SWO-Val')	181
6	FP_SC1	<i>cyclo</i> (Orn'-Leu'- <sup>D</sup> Phe'-Pro'-Val''-Orn''-Leu''-SC1-Val')	181
7	FP_SC2	<i>cyclo</i> (Orn'-Leu'- <sup>D</sup> Phe'-Pro'-Val''-Orn''-Leu''-SC2-Val')	181
8	PV_SWO	<i>cyclo</i> (Orn'-Leu'- <sup>D</sup> Phe'-Pro'-Val''-Orn''-Leu''- <sup>D</sup> Phe''-SWO)	185
9	PV_SC1	<i>cyclo</i> (Orn'-Leu'- <sup>D</sup> Phe'-Pro'-Val''-Orn''-Leu''- <sup>D</sup> Phe''-SC1)	185
10	PV_SC2	<i>cyclo</i> (Orn'-Leu'- <sup>D</sup> Phe'-Pro'-Val''-Orn''-Leu''- <sup>D</sup> Phe''-SC2)	185

## 6.2.2 Simulations

The simulations were performed with the general settings and parameters described in Chapter 3.1, with a cut-off radius of 1.2 nm on long range electrostatics and van-der-Waals interactions. GS, the peptidomimetics and MeOH were simulated using the AMBER99SB force field [137].

### Simulation protocol in methanol

Each molecule was embedded into a box of ~1000 MeOH molecules with a density of ~825 kg/m<sup>3</sup> at 300 K. After 500 steps of energy minimization, the system was equilibrated at a constant volume in the NVT (N: number of atoms, V: volume, T: temperature) ensemble, while the temperature was controlled by a *V-rescale*

thermostat [138]. This equilibration was performed for 10 ps at 300 K with position restraints of 1000 kJ/(mol nm<sup>2</sup>) on GS and the analogs. Then, a 500 ps equilibration in the NPT (P: pressure) ensemble followed, where the temperature was controlled by a *Nosé-Hoover* thermostat [94] and the pressure by a *Parrinello-Rahman* barostat [95].

Molecules were then simulated for 10 ns with 3.5 Å distance restraints between the atoms potentially forming hydrogen bonds in GS: Leu:N-Val:O and Val:N-Leu:O. Four possible hydrogen bonds were stabilized in the analogs where <sup>D</sup>Phe''-Pro'' were replaced by the photoswitches (molecules 2, 3 and 4 from Table 6.1), and two hydrogen bonds for each of the remaining analogs. The distances were restrained with force constants of 600-1000 kJ/(mol nm<sup>2</sup>), using weaker restraints for atom pairs closest to the photoswitches.

Finally, each of the ten models was simulated for 1 μs in the NPT ensemble. Coordinates were saved every 50 ps. The last 700 ns were used for statistical evaluation.

### Simulation protocol in a membrane

For each of the ten models, four membrane simulations were performed, each one for the duration of 600 ns after the equilibration phase. As starting structures, the final conformations after the 10 ns equilibration in MeOH with distance restraints were used. The membrane insertion simulations were conducted at 400 K, following the protocol in Chapter 3.1, using a pre-equilibrated DMPC bilayer consisting of 72 lipids, solvated by ~3000 TIP3P water molecules.

Then, the system was simulated without any restraints for 600 ns at 303 K. All atomic coordinates were saved every 50 ps. The last 400 ns were used for statistical evaluation.

### Conformational flexibility

To obtain information about the flexibility of the different molecules, the GROMACS tool *g\_rmsf* was used to calculate the root mean square fluctuations (RMSFs) as an average over the whole molecule. The average structure of each molecule over the last 700 ns for the simulations in MeOH, respectively the last 400 ns for the membrane simulations, was taken as a reference for the calculation.

### Cluster analysis

To help visualizing the structures of GS and its analogs, the GROMACS tool *g\_cluster* was used to perform a cluster analysis. Here, a matrix of RMSDs between the

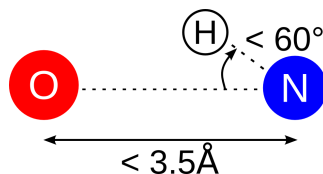


Figure 6.3: Hydrogen bond definition used in this work. The distance O–N has to be below 3.5 Å, the angle between O–N and N–H below 60°.

molecule coordinates of all saved snapshots from the last 700/400 ns (MeOH/DMPC) of the simulations was calculated. The single linkage algorithm [139] was used to obtain clusters of structural similarity.

### Hydrogen bonds

Hydrogen bonds within the 10 molecules were evaluated by measuring the distance between all possible oxygen (O) and nitrogen (N) pairs. A hydrogen bond was defined as follows (Figure 6.3): the distance for a pair of hydrogen-bonded atoms had to be below 3.5 Å. Additionally, the angle between O–N and N–H had to be below 60°. This criterion was evaluated for each snapshot for the last 700/400 ns (MeOH/DMPC) of the simulations. A specific hydrogen bond has the value 1, if the criterion is fulfilled for the complete time. Only hydrogen bonds with values of more than 0.1 (10%) were taken into account. Hydrogen bonds between adjacent residues were not counted.

### Molecular surfaces

The solvent excluded surface (SES) (Connolly-Richards surface [140]) of the molecules was calculated using NanoShaper [127] with a probe radius of 1.4 Å. It was calculated at a time interval of 1 ns during the last 700/400 ns (MeOH/DMPC) of the simulation.

### Hydrophobic moment vectors

The HM vectors for the molecules were calculated according to [141] (see Chapter 5). Dielectric constants were 32.6 for MeOH and 20.0 for the membrane-water interface. The electrostatic potential on the molecular surface was calculated with APBS [128]. HM vectors were calculated at a time interval of 1 ns during the last 700/400 ns (MeOH/DMPC) of the simulation.

### Electrostatics of solvation

APBS [128] was used to calculate the electrostatic component of the free energy of solvation. Two calculations were performed: first, the solvent dielectric constant  $\epsilon$  was set to 1.0 for vacuum. Then,  $\epsilon$  was set to 32.6 for MeOH, respectively to 20.0, to mimic the water/membrane interface in the membrane simulations.  $\epsilon$  for GS and its analogs was kept 2.0, to account for electronic polarization effects. The temperature was set to the simulation temperatures 300/303 K (MeOH/DMPC). The two energies obtained for the different  $\epsilon$  settings were subtracted from each other to obtain the solvation free energy. The calculations were performed at a time interval of 1 ns during the last 700/400 ns (MeOH/DMPC) of the simulations.

### Membrane insertion depth

For the membrane simulations, the membrane insertion depth (MID) of GS and its analogs were evaluated for the last 400 ns. The average z-coordinates (direction of the membrane normal) of the peptidic part and the photoswitch part were compared with the average z-coordinates of the phosphorus atoms of the bilayer leaflet where the molecules inserted. Only time steps were taken into account where the center of mass of the lipid was more than 1.5 Å away from the peptidomimetics, to get an average position independent of GS and its analogs. Positive values for the insertion depths mean that the peptidic/photoswitch part is below the average phosphorus position. The insertion depths were calculated for the last 400 ns at intervals of 50 ps.

## 6.3 Results

### 6.3.1 Simulations in MeOH

All simulations in MeOH started from a conformation where the postulated H-bonds from GS were stabilized during a 10 ns equilibration run. Nevertheless, all photoswitch analogs adapted quickly to less compact structures. Representative structures of the most dominant clusters (>78% of all structures from the last 700 ns) from a cluster analysis with an RMSD cut-off of 1.5 Å are shown in Figure 6.4. RMSF measurements averaged over all atoms (Table 6.2) showed that the conformations of the analogs are generally more flexible than GS, which has the lowest value with 0.13 nm. Generally, the analogs with the 'open' form of the photoswitch are more flexible than the 'closed' ones, which can be explained by additional degrees of free-

Table 6.2: RMSF values [nm] averaged over all atoms, from the simulations in MeOH. GS has the lowest value and thus the most rigid structure throughout the simulation.

<b>GS</b>	<b>LF SWO</b>	<b>LF SC1</b>	<b>LF SC2</b>	<b>FP SWO</b>	<b>FP SC1</b>	<b>FP SC2</b>	<b>PV SWO</b>	<b>PV SC1</b>	<b>PV SC2</b>
0.13	0.22	0.22	0.15	0.20	0.17	0.21	0.21	0.15	0.16

dom introduced by the ring opening. However, for the LF and the FP analogs, the two 'closed' states show a considerable mutual difference in their flexibility, while this difference is not present in the 'closed' PV analogs.

### Hydrogen bonds

The evaluation of H-bonds for the last 700 ns showed clearly, that initial H-bonds are lost by the introduction of the photoswitch (Figure 6.5). GS shows 8 H-bonds which persist between 40% and 100% of the simulation time. Here, the ones from Leu:N to Val:O are the strongest with 100%, the ones from Val:N to Leu:O are present for ~60% of the time. Additionally, the protonated Orn side chains form strong H-bonds with the backbone oxygen atoms of the two <sup>D</sup>Phe (~80%).

In the GS analogs, almost all H-bonds and the C2-symmetry are lost. The LF\_SC2 analog creates a strong (67%) H-bond between Val'':N and <sup>D</sup>Phe':O, which is also weakly present in LF\_SC1 (17%). It is the only H-bond in the peptidomimetics which was also observed in GS.

Of all analogs, the FP\_SWO analog has the highest amount of H-bonds, their sum is 1.2, opposed to 5.6 in GS. One of its Orns creates a strong bond with the backbone oxygen of the Orn on the opposite side (62%).

### Molecular surfaces

The averaged molecular surfaces of GS and its analogs are summarized in Figure 6.6. GS has clearly the smallest surface. The surface areas of the analogs increase from LF over FP to PV, the 'closed' photoswitch states being generally smaller than the 'open' states. The order of the size of the analogs is consistent with their number of atoms - LF: 176, FP: 181, PV: 185 (GS 176). From the LF-containing analogs, the 'closed' state SC2 has the lowest molecular surface. This could be explained by the strong H-bond between Val'':N and <sup>D</sup>Phe':O (Figure 6.5). However, FP\_SC1 and FP\_SC2 have a lower surface than the 'open' state, despite the higher amount of H-bonds for the latter.

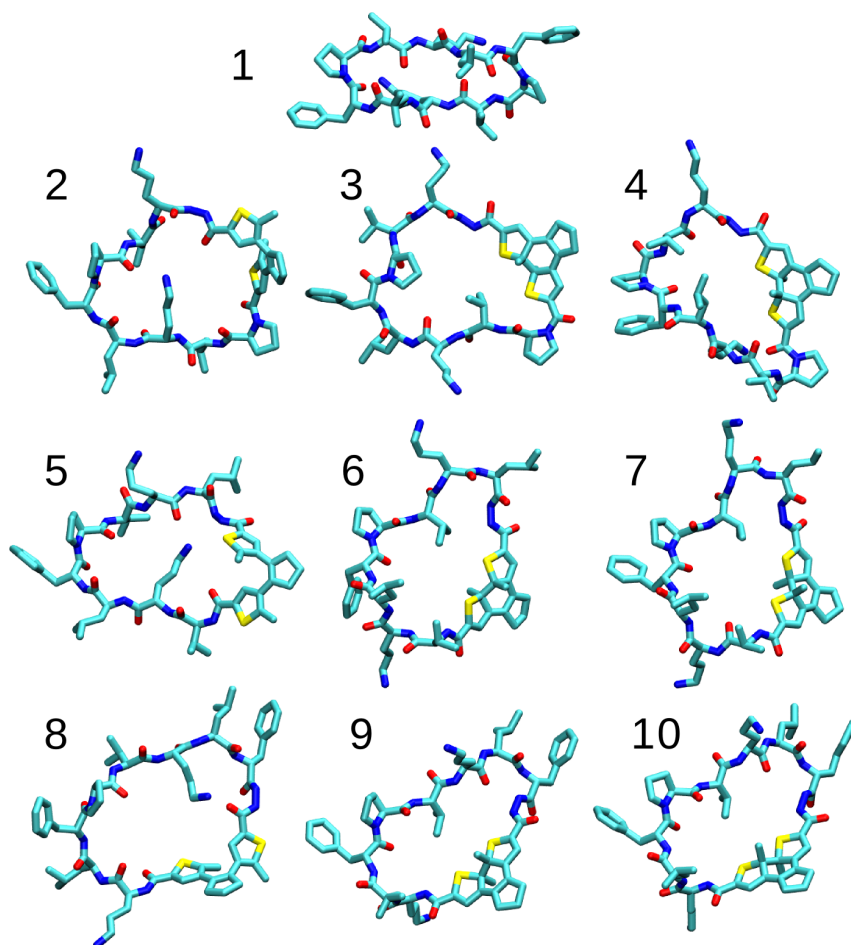


Figure 6.4: Representative structures of gramicidin S and its analogs in MeOH. 1: GS, 2: LF\_SWO, 3: LF\_SC1, 4: LF\_SC2. 5: FP\_SWO, 6: FP\_SC1, 7: FP\_SC2. 8: PV\_SWO, 9: PV\_SC1, 10: PV\_SC2.

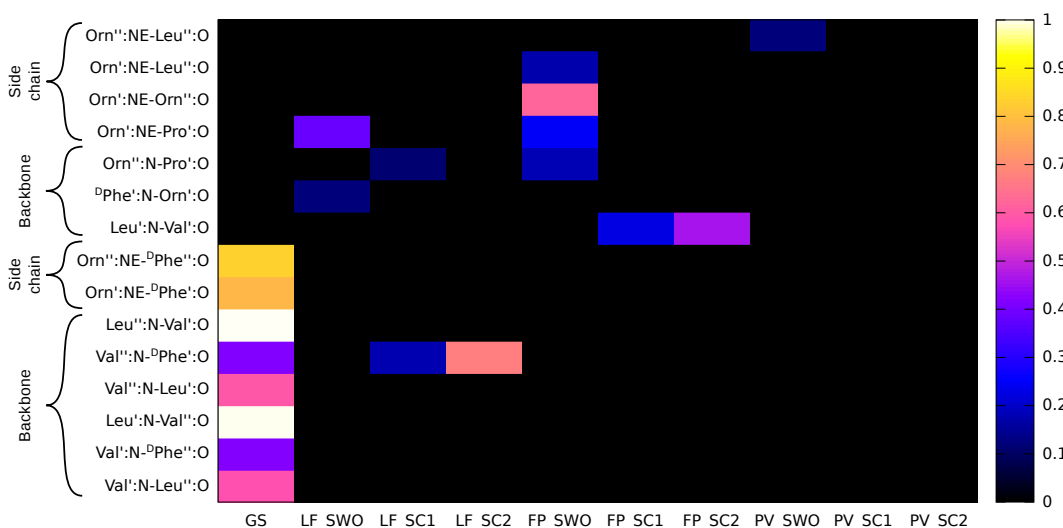


Figure 6.5: Hydrogen bonds for GS and its analogs in MeOH. The y-axis denotes the H-bond pair, nomenclature is analogous to Figure 6.1. O and N are backbone oxygens/nitrogens, NE is the nitrogen of the Orn side chains. The scale is explained in 6.2.

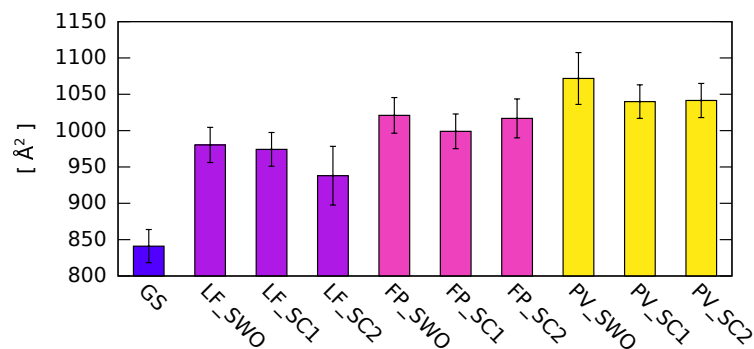


Figure 6.6: The average molecular surface calculated from 700 snapshots from the last 700 ns of the simulations in MeOH.

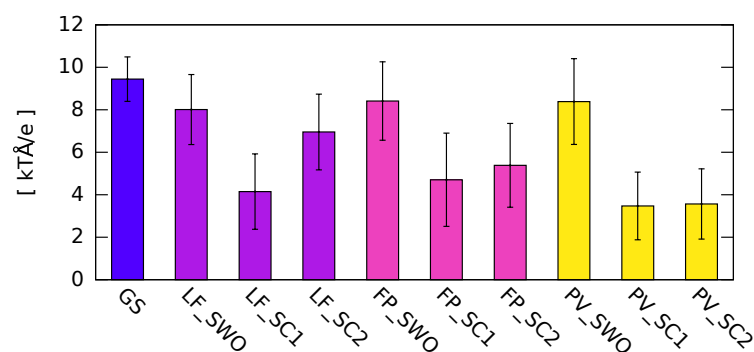


Figure 6.7: The average length of the HM vectors calculated for 700 snapshots from the last 700 ns of the simulations in MeOH.

### HM vectors

As seen from Figure 6.7, the HM vector is largest for GS. For the analogs in the 'open' state, it is of similar length, and generally lower in the cases with the 'closed' photoswitch conformations. All analogs show a higher standard deviation than GS, which shows again the increased flexibility of the molecules. The difference between 'open' and 'closed' states of the photoswitch is highest for the PV analogs.

### Electrostatics of solvation

The averaged electrostatic component of the free energy of solvation, shown in Figure 6.8 is lowest for GS, which has most of its polar groups paired in H-bonds. Of the other molecules, the LF analogs are again closest to GS. The FP and PV analogs show similar patterns, opposed to LF, where the two 'closed' conformations are clearly different. In all analogs, the 'open' forms have lower values than the 'closed' forms. The difference between 'open' and 'closed' states of the photoswitch is largest for the FP analogs. Interestingly, the values for the electrostatic component of the free energy of solvation are roughly proportional to  $1/\text{HM}$  (Figure 6.7).

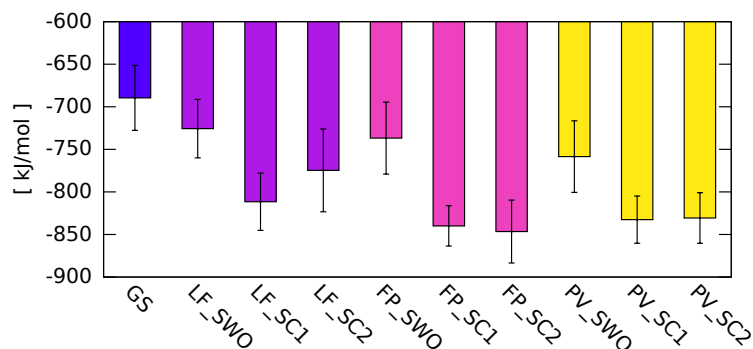


Figure 6.8: The average electrostatic component of the free energy of solvation, calculated from 700 snapshots from the last 700 ns of the simulations in MeOH.

### 6.3.2 Simulations in a DMPC membrane

For each of the 10 molecules (GS and 9 photoswitch-containing analogs), four simulations of 600 ns length have been performed. In each of them the RMSF, the molecular surface, the HM vector, the electrostatic component of the free energy of solvation and the insertion depth have been evaluated over the last 400 ns of simulation time. The complete data set for the 40 simulations can be found in the Appendix Table C.2 and Appendix Figure C.1. For the PV\_SC2 analogs, the molecules inserted into the bilayer in three out of four simulations. In one simulation, the peptide bound to the outside of the membrane by electrostatic attractions between the side chains and the head groups, but didn't insert into the core-head group interface (see insertion depths of all simulations in Appendix Table C.2).

The figures shown and discussed in this section contain the data from the one (out of four) simulation for each molecule, in which the molecule is in average inserted deepest into the membrane (Table 6.3).

While the average RMSF for GS hasn't changed when compared to the simulation in MeOH, almost all analogs show a decreased value and thus lower flexibility (Appendix Table C.2).

The structures of the molecules have dramatically changed upon membrane binding, which can be seen in Figure 6.9. Especially for the FP and PV analogs the hydrophobic side chains at the side opposite of the photoswitch tend to bend closer to the photoswitch.

#### Membrane insertion depths

GS inserted deepest into the membrane, with  $\sim 10$  Å below the average position of the phosphorus atoms. For the analogs, the average depth of the photoswitch and

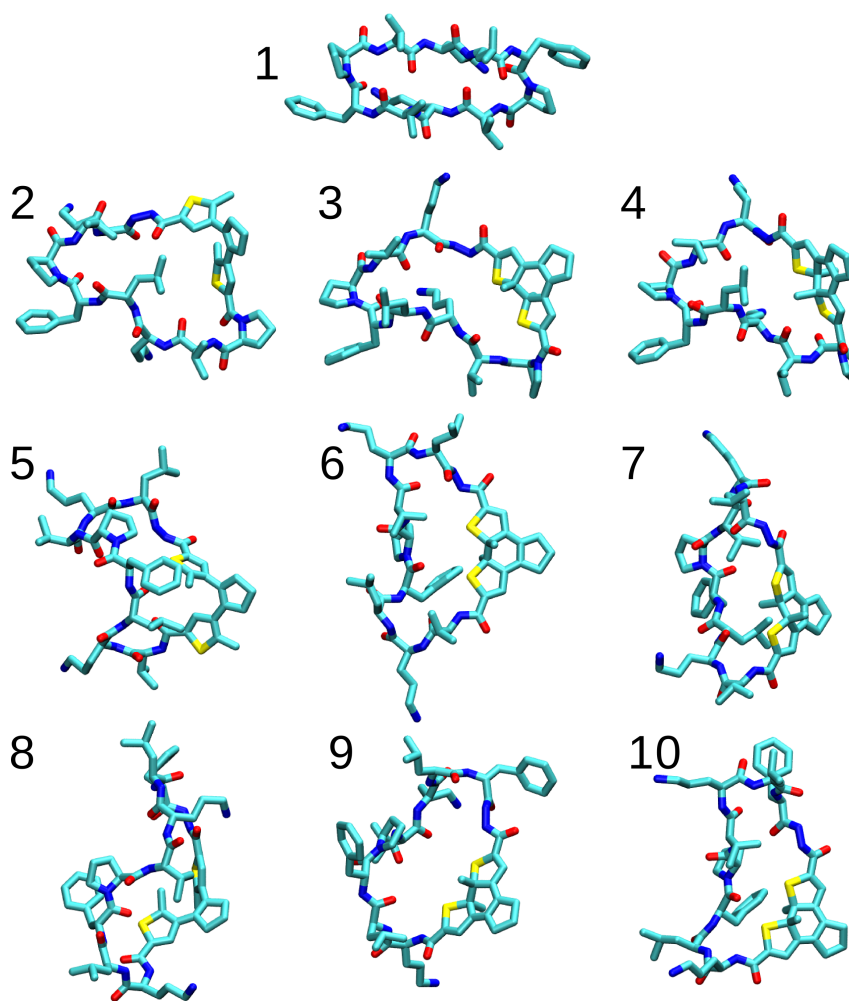


Figure 6.9: Representative structures of gramicidin S and its analogs in DMPC, from the simulations where the molecules inserted deepest into the membrane. 1: GS, 2: LF\_SWO, 3: LF\_SC1, 4: LF\_SC2. 5: FP\_SWO, 6: FP\_SC1, 7: FP\_SC2. 8: PV\_SWO, 9: PV\_SC1, 10: PV\_SC2.

Table 6.3: Insertion depths from the simulations where the molecules inserted deepest into the membrane.

Molecule	Sim. <sup>a</sup>	MID of peptidic part (Å) <sup>b</sup>	MID of photoswitch part(Å) <sup>b</sup>	MID of complete molecule (Å) <sup>b</sup>
GS	4	-	-	10.3 ± 2.0
LF_SWO	1	7.6 ± 2.9	9.2 ± 2.6	8.1 ± 2.6
LF_SC1	3	8.6 ± 2.1	7.1 ± 3.6	8.2 ± 2.3
LF_SC2	4	7.8 ± 2.1	9.2 ± 2.5	8.2 ± 2.0
FP_SWO	2	5.8 ± 2.0	11.2 ± 2.1	7.3 ± 2.0
FP_SC1	3	6.8 ± 2.1	6.9 ± 2.4	6.9 ± 2.0
FP_SC2	1	6.4 ± 2.3	11.1 ± 2.6	7.7 ± 2.3
PV_SWO	4	9.1 ± 2.0	8.4 ± 2.2	8.9 ± 2.0
PV_SC1	3	6.1 ± 2.1	10.0 ± 2.1	7.2 ± 2.0
PV_SC2	4	9.7 ± 1.8	8.6 ± 2.1	9.4 ± 1.7

<sup>a</sup>Simulation number. For each of the peptidomimetics, four membrane simulations were performed. The number indicates the simulation, where the molecule is on average inserted deepest into the membrane. The data for all simulations are shown in Appendix Table C.2.

<sup>b</sup>MID (membrane insertion depth) is the distance between the average z-coordinate of the phosphorus atoms of the lipids and the average z-coordinate of the peptide resp. the photoswitch.

the average depth of the peptidic part were measured separately (Appendix Table C.2). There is no clear general orientation of the photoswitch with respect to the rest of the peptide (Figure 6.10). The photoswitch apparently doesn't play the role of a membrane or a surface anchor. In some cases the photoswitch is inserted less into the membrane, in some cases deeper than the rest of the peptide. The analogs are in average between 6 and 9 Å below the average phosphorus position.

## Hydrogen bonds

The H-bond map shown in Figure 6.11 for the simulations with the deepest membrane insertion shows a very different picture compared to the observations in the MeOH simulations (Figure 6.5). The number of H-bonds has drastically increased, especially for the LF analogs which show now between 2 and 3 H-bonds, opposed to <1 in MeOH. Again, the LF analogs are the only analogs which have H-bond pairs which are also present in GS. The complete map for all simulations is shown in Appendix Figure C.1.

Interestingly, in two of the PV\_SC1 simulations (2 and 4), there is a H-bond between Leu<sup>''</sup>:N and Pro<sup>'</sup>:O, which forms one turn of a  $3_{10}$ -helix (Figure 6.12). In both these cases the photoswitch is oriented above the rest of the peptide with respect to the membrane surface plane.

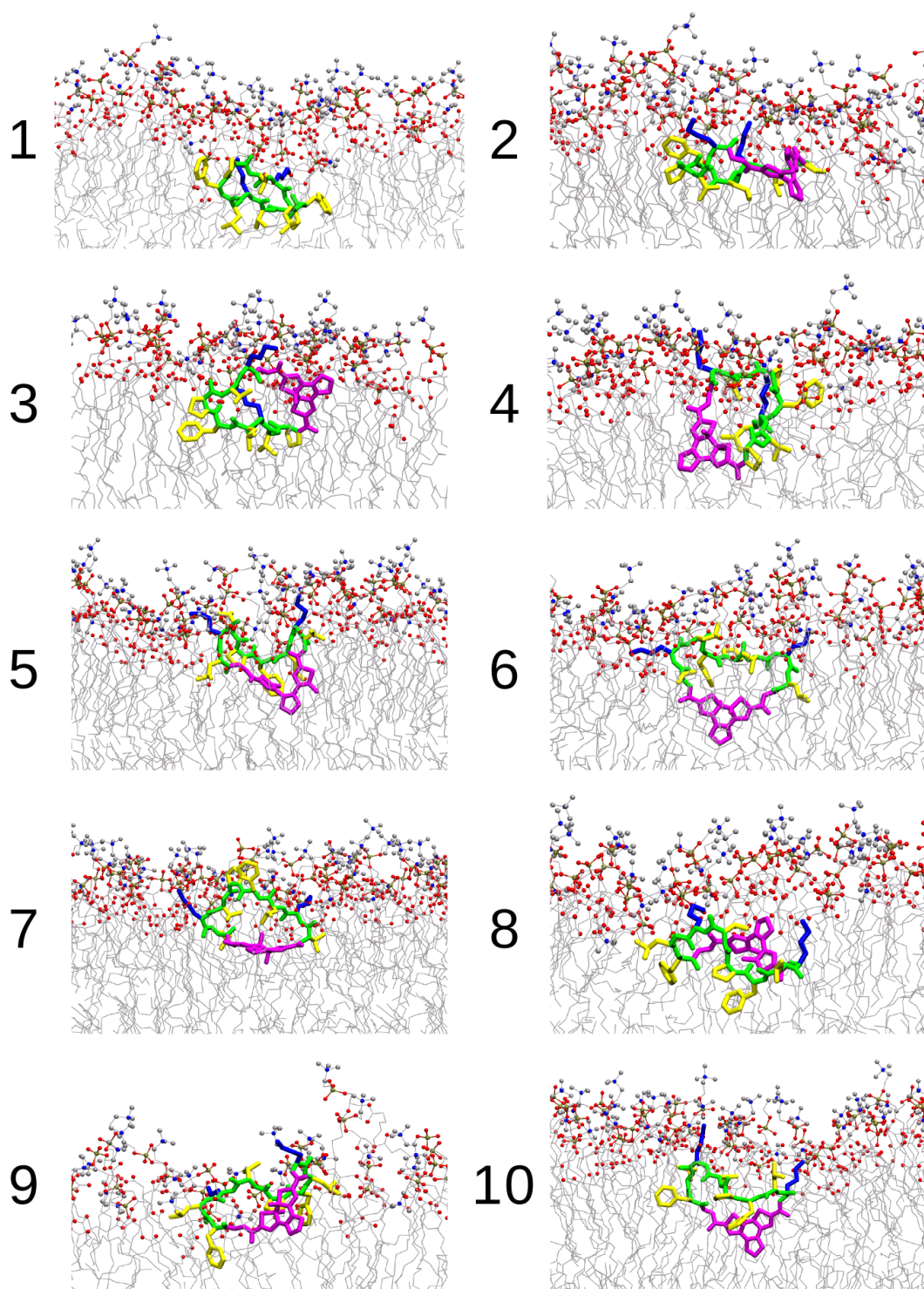


Figure 6.10: Representative structures from Figure 6.9 in the membrane environment. 1: GS, 2: LF\_SWO, 3: LF\_SC1, 4: LF\_SC2. 5: FP\_SWO, 6: FP\_SC1, 7: FP\_SC2. 8: PV\_SWO, 9: PV\_SC1, 10: PV\_SC2. *Magenta*: photoswitch, *yellow*: hydrophobic side chains (<sup>D</sup>Phe, Val, Leu, Pro), *blue*: Orn (charged), *green*: backbone.

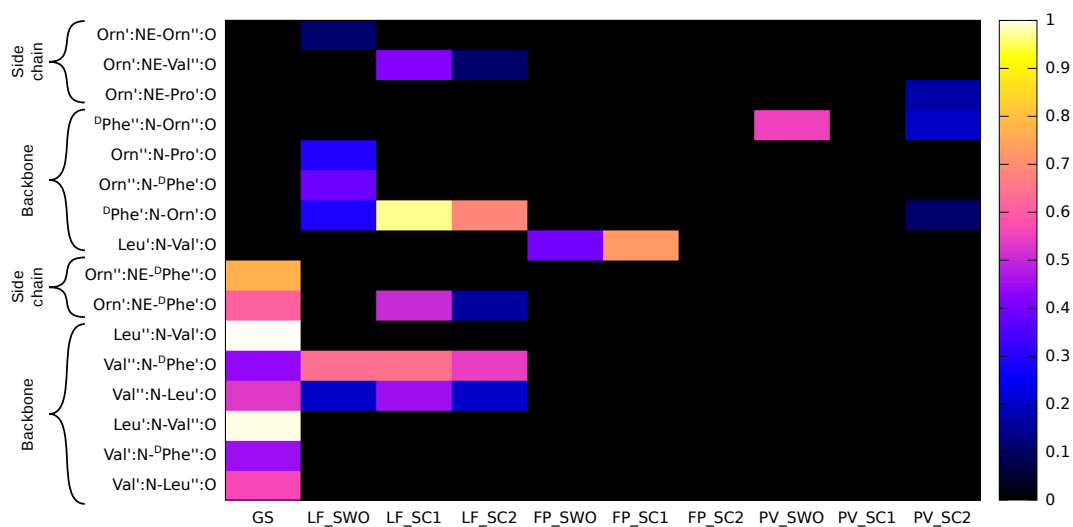


Figure 6.11: Hydrogen bonds for GS and its analogs in DMPC. The y-axis denotes the H-bond pair, nomenclature is analogous to Figure 6.1. O and N are backbone oxygens/nitrogens, NE is the nitrogen of the Orn side chains. (A complete map with H-bonds from all simulations can be found in Appendix Figure C.1.)

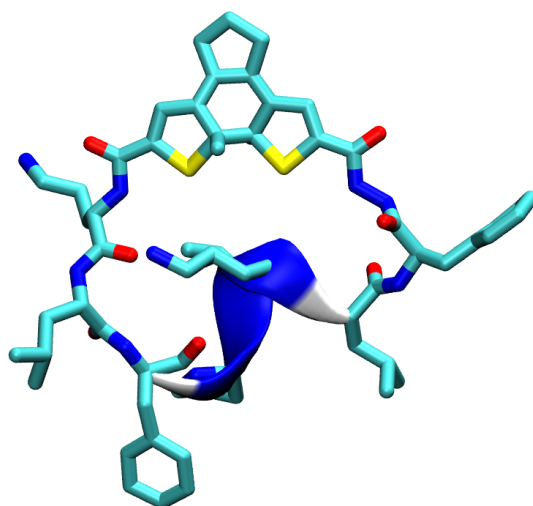


Figure 6.12: Representative structure for simulation #4 from PV\_SC1 in the membrane. In this and in simulation #2 there is a H-bond between 8Leu:N and 5Pro:O, which creates one turn of a  $3_{10}$ -helix.

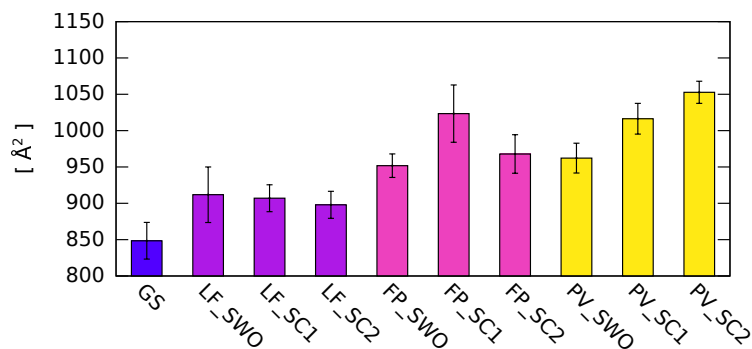


Figure 6.13: The average molecular surface calculated from 400 snapshots from the last 400 ns of the simulations in DMPC. Data are from the simulation with the deepest membrane insertion of each molecule.

### Molecular surfaces

Figure 6.13 shows, that except for GS, all of the peptidomimetics typically have a lower average molecular surface than in MeOH. In MeOH, the surface was generally slightly smaller for the molecules with a 'closed' photoswitch (Figure 6.6). Now, this is only the case for the LF analogs. For the FP and PV analogs, the surfaces of the SC1 and SC2 analogs are generally larger than that of the SWO analog. For both FP and PV, the surfaces of the two 'closed' states SC1 and SC2 are also considerably different from each other.

### HM vectors

In DMPC, the length of all HM vectors has increased, which is partly due to the lower dielectric constant of the medium ( $\epsilon=20.0$  for the water/membrane interface). Interestingly, some of the HM vectors are now larger than that of GS, suggesting a stronger repartitioning of polar and nonpolar parts of the molecules.

However, the average HM vector length is very different in the individual simulations, see Appendix Table C.2. While the GS HM vector changes within an interval of 0.6 between the four simulations, the difference between the largest and the shortest HM vector goes up to 8.1, for the PV\_SC1 analog simulations.

### Electrostatics of solvation

The electrostatic component of the free energy of solvation is the lowest for GS. For the peptidomimetics, the LF molecules are again closest to GS. Despite the difference between the two 'closed' states in Figure 6.15, all three conformations are very similar within the error margin. All FP and PV analogs have very similar, but higher values.

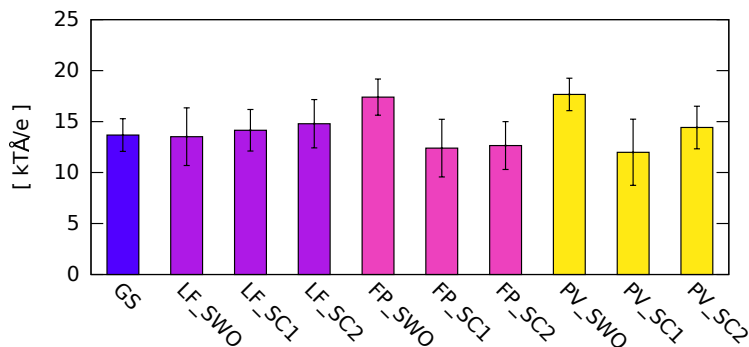


Figure 6.14: The average length of the HM vectors calculated for 400 snapshots from the last 400 ns of the simulations in DMPC. Data are from the simulation with the deepest membrane insertion of each molecule.

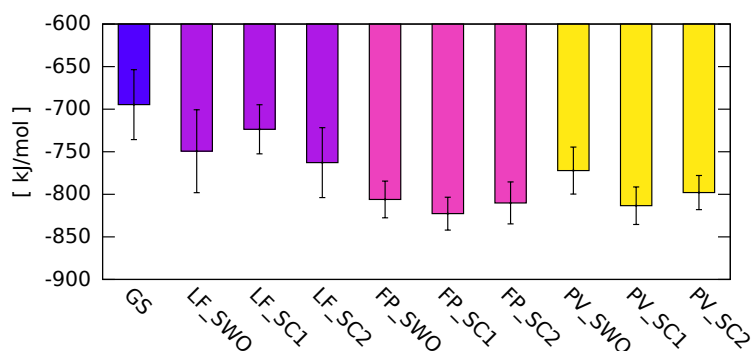


Figure 6.15: The average electrostatic component of the free energy of solvation, calculated from 400 snapshots from the last 400 ns of the simulations in DMPC. Data are from the simulation with the deepest membrane insertion of each molecule.

### 6.3.3 Correlation with the experiment

To correlate the MD-derived properties to experiments, all data which have been presented above and experimental data from [24] are summarized in radar plots for each molecule, shown in Figures 6.16 to 6.18. In these plots, each axis represents a different property.

Since the two 'closed' states (SC1 and SC2) cannot be distinguished in the experiment, the values for antimicrobial activity, hemolysis and reverse-phase high-performance liquid chromatography (RP-HPLC) retention times are identical in the plots for the two 'closed' states.

Figures 6.16 to 6.18 show the data from the simulations in MeOH. The GS plot has a unique shape. The plots for the analogs in the 'open' state resemble each other clearly. Only the LF\_SWO analog shows a reduced hemolytic activity, when compared to FP\_SWO and PV\_SWO, which demonstrate almost equally high activity. The two 'closed' states resemble each other clearly for the FP and PV analogs, while

there is a considerable difference between LF\_SC1 and LF\_SC2, which is caused mainly by the different HM vectors.

The LF analogs show the best 'switching' of the antimicrobial and the hemolytic activity. The analogs with the 'closed' photoswitch, LF\_SC1 and LF\_SC2, have no measurable antimicrobial or hemolytic activity, opposed to FP\_SC1, FP\_SC2, PV\_SC1 and PV\_SC2, which still act in these ways, even though to a decreased extent.

When comparing all plots, the retention times show a correlation to the biological activity. High retention times occur together with high hemolytic and antimicrobial activities and vice versa. In general, the antimicrobial activity is always higher than the hemolytic effect, which might be caused by the the decreased electrostatic attraction of the zwitterionic head groups of the erythrocytal membrane opposed to the negatively charged bacterial membrane.

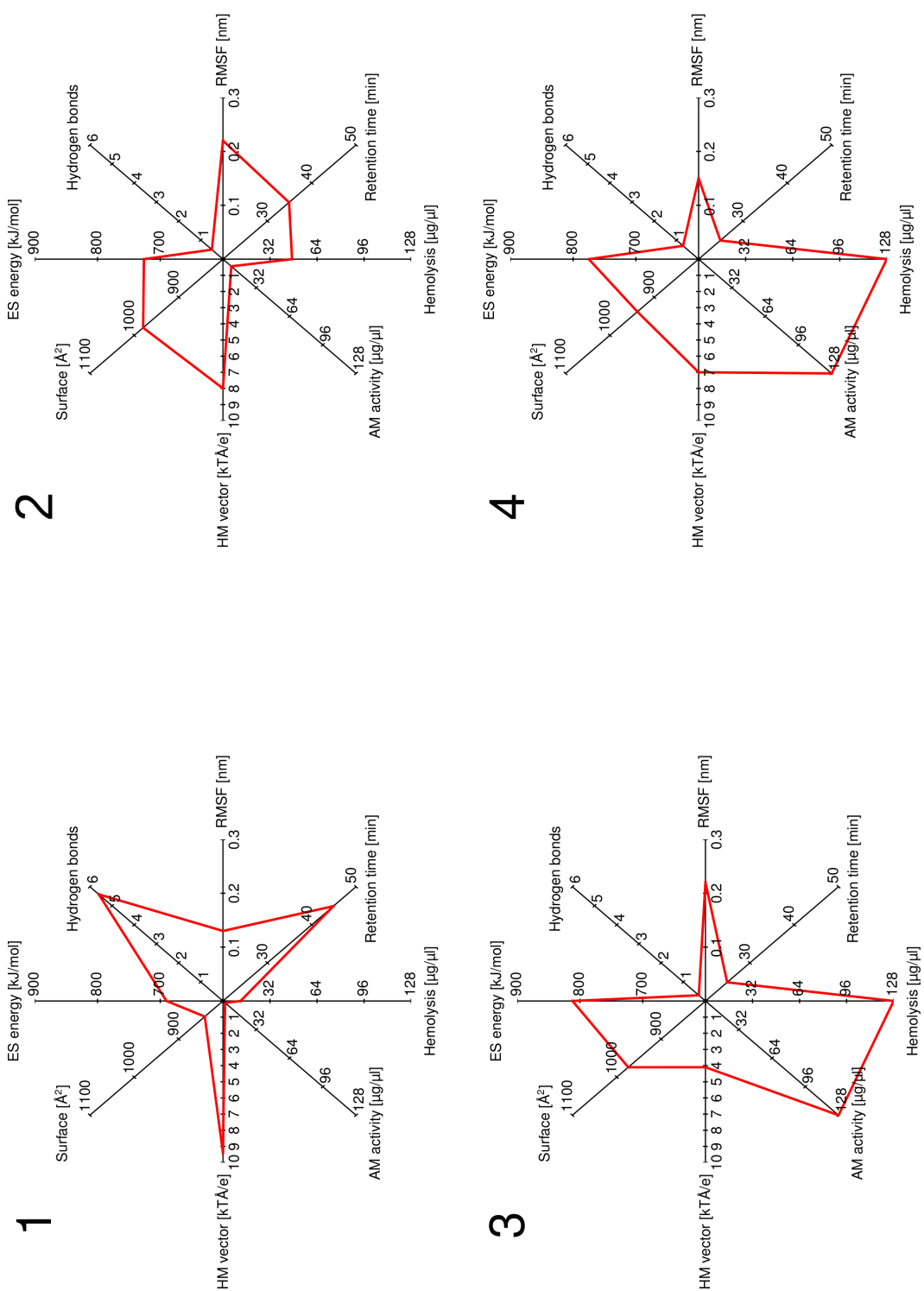
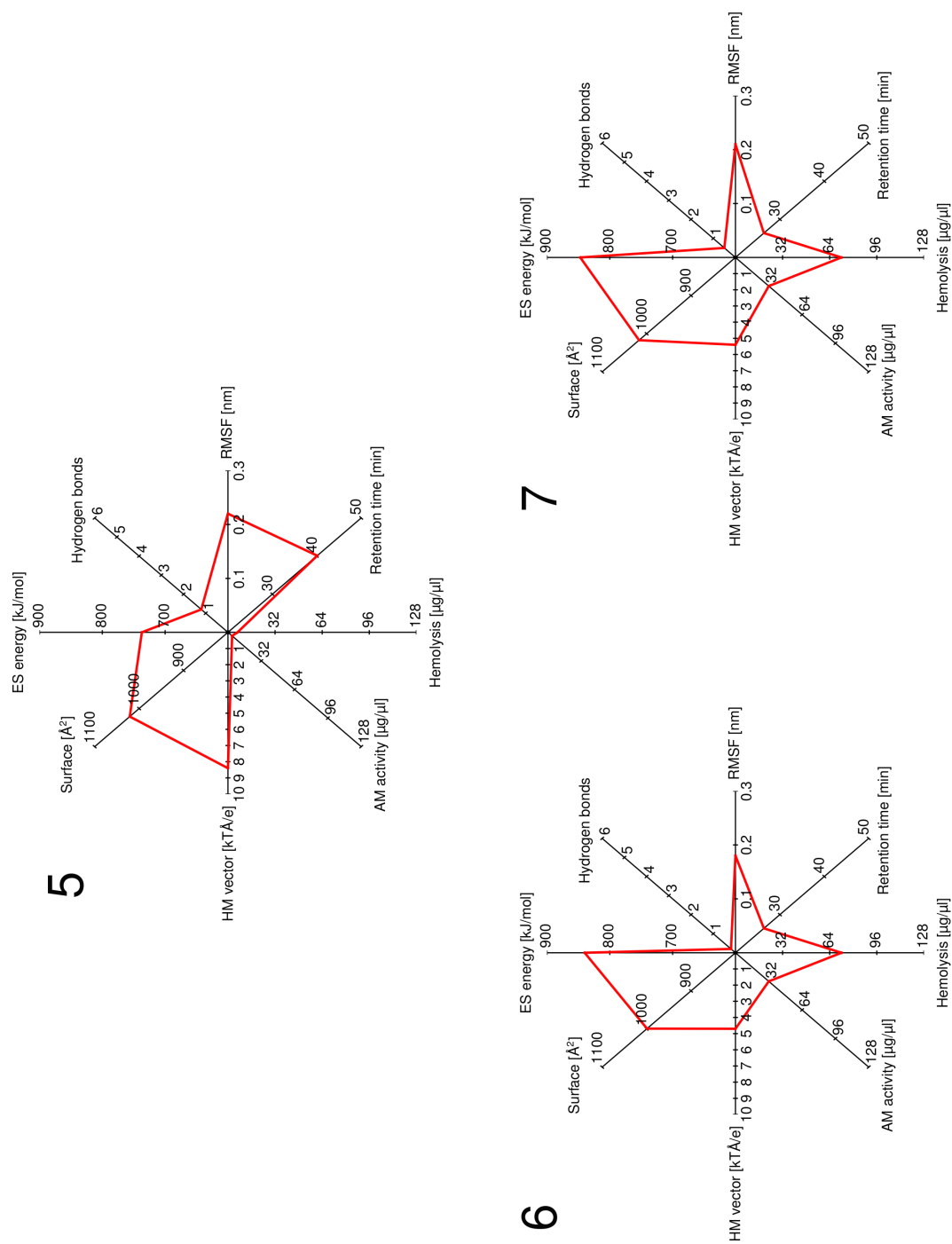


Figure 6.16: 1: GS, 2: LF\_SWO, 3: LF\_SC1, 4: LF\_SC2. Data for antimicrobial (AM) activity against *Staphylococcus aureus*, hemolysis and RP-HPLC retention times from [24]. AM activity is measured as minimal inhibitory concentration (MIC), hemolysis as 50% lysis of human erythrocytes. Low values indicate high activity. In RP-HPLC, more polar molecules elute more readily than less polar molecules, leading to shorter retention times.

Figure 6.17: 5: FP\_SWO, 6: FP\_SC1, 7: FP\_SC2. Data for antimicrobial activity against *S. aureus*, hemolysis and RP-HPLC retention times from [24].

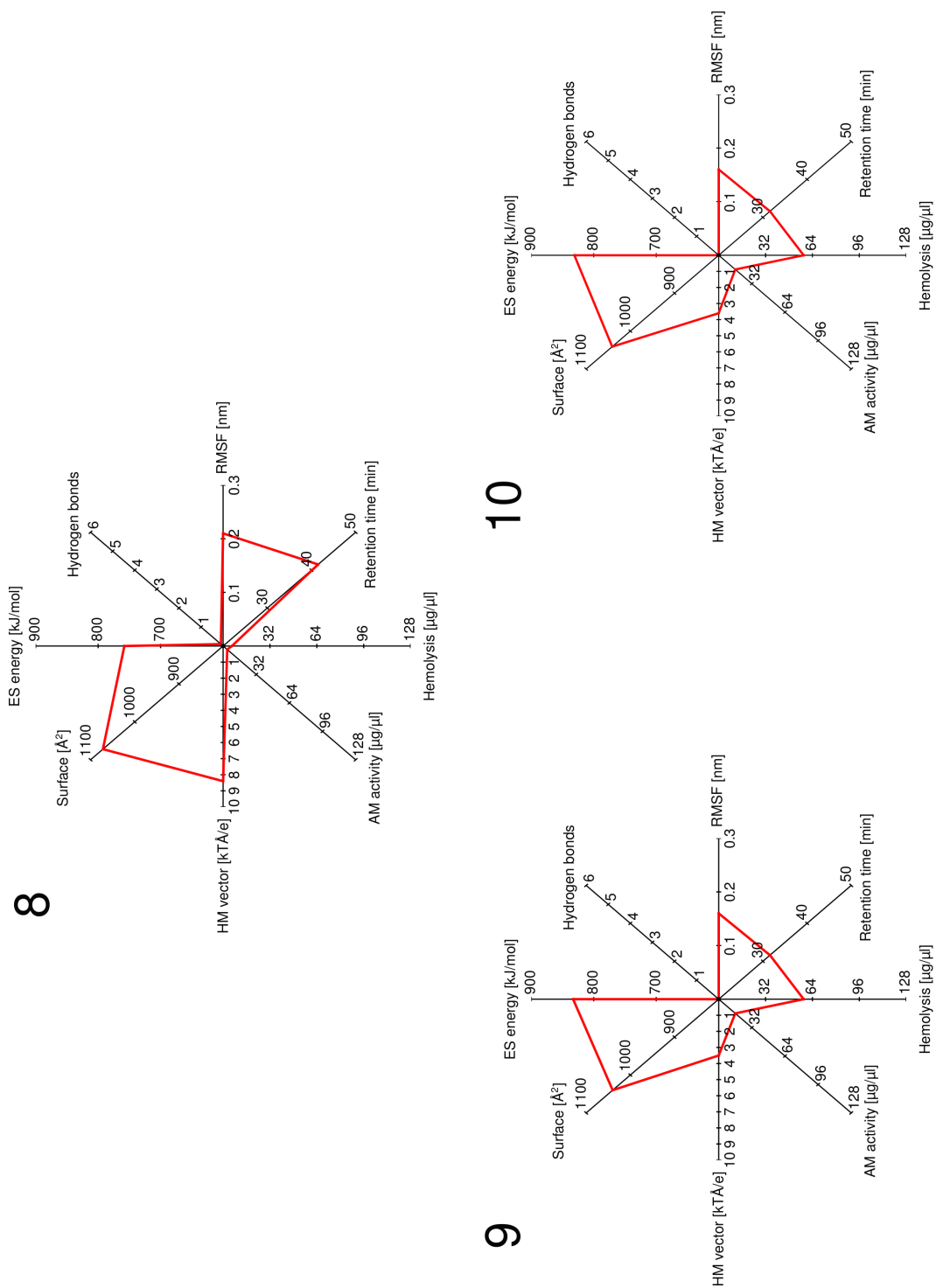


Figure 6.18: 8: PV\_SWO, 9: PV\_SC1, 10: PV\_SC2. Data for antimicrobial activity against *S. aureus*, hemolysis and RP-HPLC retention times from [24].

## 6.4 Discussion

Several properties of the molecules lead to their activity against bacterial and erythrocytal membranes. Most certainly, their ability to bind and insert into a membrane is one of them. GS and all analogs have two positive charges and are thus electrostatically attracted to the negatively charged membrane head groups of bacteria, respectively to the zwitterionically charged head groups of eucaryotic cells. Additionally, the hydrophobic parts of the molecules avoid the aqueous solution due to the hydrophobic effect. It is known that almost all antimicrobial peptides are amphiphilic, which allows them to orient themselves in a membrane in such a way that their hydrophobic side chains reach towards the membrane interior and their charged side chains reach towards the water phase, at least as monomers.

As a measure of the amphiphilicity we have calculated the hydrophobic moment vector in both MeOH and a DMPC membrane (section 6.3.1 and 6.3.2), which reflects the distribution of polar and unpolar patches on the molecular surface. The results in Figure 6.7 show, that already in the isotropic solution, GS has the longest vector and thus highest amphiphilicity. All analogs with the photoswitch in the 'open' form are more amphiphilic than the 'closed' ones. This happens, although the molecules in the MeOH solution are not forced to adapt to the anisotropic environment of the membrane. This 'intrinsic' amphiphilicity of the molecules might reflect their ability not only to bind but also to insert into the membrane.

Once bound to the membrane, the data in Figure 6.14 show that almost all analogs adapt to their environment and change their conformation in order to increase their amphiphilicity and as a consequence, their HM vector. In many cases, their amphiphilicity even exceeds that of GS, which can be explained by the increased flexibility due to missing H-bonds.

Interestingly, the H-bonds (which are a measure of structural similarity) and the HM vector are much more similar for all LF analogs in the bound state than in the solution. Despite their similarity, the LF peptidomimetics have the highest difference in the biological activity between 'open' and 'closed' analogs.

We suggest that the HM vector in MeOH can be interpreted as a binding affinity in HPLC, which explains the longer retention times for the 'open' analogs, because they bind stronger to the hydrophobic stationary phase. At the same time, the binding to cellular membranes should be increased, which is confirmed by the different activities measured in biological experiments.

Once the molecules are bound to the membrane, MD reflects, but could not

reveal what are the relevant properties to explain the biological activity. Nearly all evaluated properties show in MeOH a clear tendency in favor of either the 'open' or the 'closed' analogs. Therefore it is clearly necessary to consider the complex *in vivo* situation. Hypothetical models about pores stabilized by inter-molecular backbone H-bonds [79,80] might have to be reconsidered, since the analogs cannot form inter-molecular backbone H-bonds in the same way as GS, but clearly show biological activity.

Finally, more information is needed about the occurrence of the two 'closed' stereoisomers (SC1 and SC2). Based on the data from RP-HPLC, the two states can be quantified by evaluation of the peak intensity, but assignment of the R,R- or S,S-state to the peaks is yet impossible (Supporting Material in [24]). Clearly, the two states do not occur at a ratio of 1:1. Since the simulations showed considerable differences in the properties of the two stereo-isomers, information about their proportion would strongly help in the interpretation of the experimental data.

## 7. Calculation of structural parameters for fluorine labelled helical peptides<sup>1</sup>

### 7.1 Introduction

Fluorine labelled amino acids (<sup>19</sup>F labels) are an excellent tool to study the properties of antimicrobial peptides in SSNMR [26]. The high sensitivity and the absence of background signals in <sup>19</sup>F NMR allows the use of smaller amounts of peptides and shorter measurement times than with <sup>2</sup>H, <sup>15</sup>N or <sup>13</sup>C SSNMR. In the past, several fluorine labelled amino acids were incorporated into various peptides and extensively studied [19, 21, 26, 28, 29, 31, 52–54, 56, 78, 91, 99, 132, 142–148]. The major problem is the artificial character of the <sup>19</sup>F labels. Strict design principles and experimental verification are necessary to prove that these labels do not disturb the peptide structure or activity.

The orientational constraints obtained by the use of intact Ala-d<sub>3</sub> labelled peptides are very similar to those obtained by the use of CF<sub>3</sub>-Phg or CF<sub>3</sub>-Bpg labels [52, 99]. CF<sub>3</sub>-Phg and CF<sub>3</sub>-Bpg have so far been used to replace hydrophobic amino acids, mainly Ala, Leu, Ile, and Val. In order to use fluorine labelled amino acids as replacement for other amino acids, a range of <sup>19</sup>F labels has been designed, which are already existing or under current development. Here, a computational study is presented, where different existing or virtual <sup>19</sup>F labels and their configurational isomers are incorporated into the well-studied antimicrobial peptide PGLa [19, 32, 51–57, 82, 99, 100], at the positions which were studied also experimentally with CF<sub>3</sub>-Phg and CF<sub>3</sub>-Bpg [99].

The angles  $\beta$ ,  $\alpha$ ,  $\theta$  and the overall helicity of the peptides were obtained from energy-minimized structures and also from membrane simulations. These angles define the orientation of the C–CF<sub>3</sub> bond, the director, with respect to the helical axis ( $\beta$ ) and with respect to the corresponding C <sub>$\alpha$</sub>  atom in the projection onto the

---

<sup>1</sup>The simulations which were evaluated in this Chapter were partly performed by Patrick Mayer, former Bachelor student.

plane perpendicular to the helical axis ( $\alpha$  and  $\theta$ ). The exact definition can be found in Chapter 3.3. They are necessary for the fitting of NMR data to a helical model and for the calculation of the peptide orientation within the membrane. The helicity gives information about the overall perturbation of the helical structure by the different  $^{19}\text{F}$  labels.

## 7.2 Methods

### 7.2.1 Parametrization and model building

The fluorine labelled amino acids listed in Table 7.1 were constructed using the *xleap* tool from the AmberTools modelling package [98].

An acyl group was attached to the nitrogen, and an amide group to the carboxylate, to mimic a peptidic environment during the following quantum-mechanical charge calculation. Geometries were then optimized and atomic charges were calculated from the electrostatic potential (ESP) obtained with the Hartree-Fock method, using the basis set 6-31G\* [133] in the *Gaussian* quantum chemistry package [134]. Final charges were obtained with *antechamber* [98] using the restrained electrostatic potential (RESP) methodology [135]. The capping groups were then removed and the charges of the aminocarboxylate were set to the backbone charges used in the AMBER99SB force field. The excess charge was added to the  $\text{C}_\alpha$  carbon, to neutralise the fragment.

Each amino acid was incorporated into the antimicrobial peptide PGLa, by substituting the positions 9, 10, 13 and 14. In each peptide, only one position was replaced by a fluorine labelled amino acid. The peptides were built as ideal  $\alpha$ -helices with the backbone dihedral angles  $\Phi = -57^\circ$  (dihedral  $\text{C}_{i-1}, \text{N}_i, \text{C}_\alpha, \text{C}_i$ ) and  $\Psi = -47^\circ$  (dihedral  $\text{N}_i, \text{C}_\alpha, \text{C}_i, \text{N}_{i+1}$ ) [149], using the *xleap* tool.

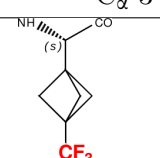
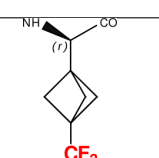
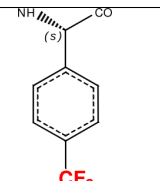
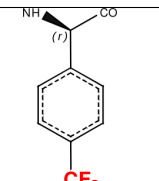
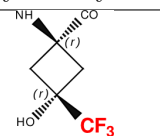
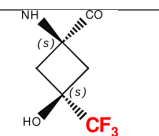
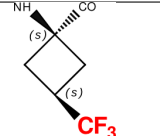
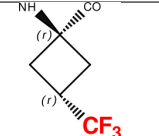
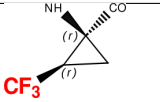
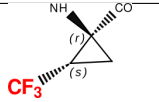
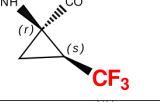
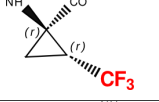
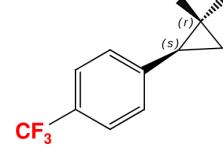
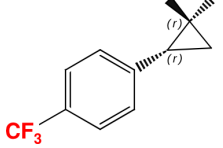
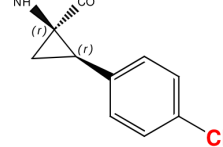
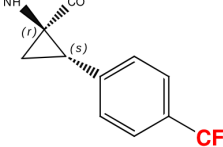
### 7.2.2 Simulations

All simulations were performed with the general settings and parameters described in Chapter 3.1.

#### Energy minimization

To optimize the geometries, each peptide was put into an empty box with side lengths of 5 nm. The potential energy was minimized using a *steepest descent* integrator with a step size of 0.001 nm, until the maximum force on an atom was  $<100 \text{ kJ}/(\text{mol nm})$  or the maximum number of 500 steps was reached.

Table 7.1: Fluorine amino acids. The director is equivalent to the direction of the C–CF<sub>3</sub> bond.

3-letter code <sup>a</sup>	structural formula	3-letter code <sup>a</sup>	structural formula
<b>C<sub>α</sub>-3-substitutes</b>			
BGS <sup>b</sup>		BGR	
PGS <sup>c</sup>		PGR	
<b>Cyclobutyl-based C<sub>α</sub>-4-substitutes</b>			
HSS		HSR	
CBS		CBR	
<b>Cyclopropyl-based C<sub>α</sub>-4-substitutes</b>			
CPS		CPR	
CRS		CRR	
PFR		PFS	
PRR		PRS	

<sup>a</sup>The full names are given in the abbreviation list.<sup>b</sup>Also known as CF<sub>3</sub>-Bpg.<sup>c</sup>Also known as CF<sub>3</sub>-Phg.

## Simulations in a membrane

Simulations were conducted in a DMPC bilayer consisting of 128 lipid molecules with ~4600 TIP3P water molecules [96]. The membrane insertion protocol is described in Chapter 3.1. After the insertion, the systems were simulated without any restraints at 303 K for 200 ns in the NPT ensemble.

Snapshots were saved every 50 ps, and the last 150 ns of the simulations were used for statistical analysis.

### 7.2.3 Helicity calculation

Chapter 3.2 describes the calculation of the helicity per residue.

## 7.3 Results

### 7.3.1 Energy minimization

From the energy-minimized structures, the angles  $\beta$ ,  $\alpha$  and  $\theta$ , defined in Chapter 3.3, have been calculated for each  $^{19}\text{F}$  labelled residue. In the calculations, the region from position 3-17 was taken as a reference to define the helical axis (exact definition in Equation 3.6). In Appendix Table D.1, the angles  $\alpha$ ,  $\beta$  and  $\theta$  of the fluorine labelled residue at position  $i$  and of the neighboring side chains are listed. The neighbors were defined as the two adjacent residues in the sequence (positions  $i - 1$  and  $i + 1$ ), and the spatially closest residues along the helical axis, positions  $i + 4$  and  $i - 4$ . For the helix pitch angle  $\theta$ , the values towards the adjacent residues  $i - 1$  and  $i + 1$  are shown. In Table 7.2, the average values of the angles  $\alpha$ ,  $\beta$  and  $\theta$  at the positions of the labels are listed, averaged over the 4 substituted positions 9, 10, 13 and 14.

#### Angle $\beta$

For the  $\text{C}_\alpha$ -3-substituted amino acids, the director is co-aligned with the  $\text{C}_\alpha$ - $\text{C}_\beta$ -bond. For the interpretation of SSNMR data, the angle  $\beta$  between the director and the helical axis was assumed to have a value of  $110^\circ$  [99] or  $121^\circ$  [52]. For all  $\text{C}_\alpha$ -4-substituted amino acids, the director is not co-aligned with the  $\text{C}_\alpha$ - $\text{C}_\beta$ -bond.

The peptides with the  $\text{C}_\alpha$ -3-substituted amino acids BGS and PGS have  $\beta$  angles between the values mentioned above, on average,  $\beta = 114^\circ$ . Their isomers BGR and PGR point towards the opposite end of the helical axis, as expected, with an average value of  $\beta = 70^\circ$ .

Table 7.2: The angles  $\beta_i$ ,  $\alpha_i$ ,  $\theta_{i-1,i}$ , calculated for the substituted  $^{19}\text{F}$  labels as averages over the for substituted positions 9, 10, 13, 14, with respect to the helical axis defined between positions 3 and 17. FAA stands for fluorine amino acid.

<b>FAA</b>	$\beta_i$	$\alpha_i$	$\theta_{i-1,i}$	$\theta_{i,i+1}$
BGS	114.0 $\pm 1.0$	32.0 $\pm 3.2$	97.7 $\pm 4.8$	99.3 $\pm 4.4$
BGR	70.0 $\pm 4.2$	-46.3 $\pm 4.7$	95.2 $\pm 3.4$	94.8 $\pm 3.0$
PGS	114.4 $\pm 1.0$	41.8 $\pm 3.3$	95.8 $\pm 4.7$	96.4 $\pm 2.4$
PGR	69.8 $\pm 2.8$	-37.9 $\pm 5.1$	99.1 $\pm 3.7$	96.2 $\pm 3.9$
HSS	134.5 $\pm 2.4$	-57.6 $\pm 5.2$	98.0 $\pm 5.0$	97.1 $\pm 4.1$
HSR	75.3 $\pm 1.9$	13.6 $\pm 3.2$	98.0 $\pm 4.7$	97.2 $\pm 3.6$
CBS	133.6 $\pm 2.5$	-53.7 $\pm 5.3$	98.4 $\pm 4.9$	97.0 $\pm 3.9$
CBR	79.1 $\pm 0.6$	8.9 $\pm 3.6$	97.6 $\pm 4.8$	96.8 $\pm 3.4$
CPS	155.5 $\pm 4.2$	-14.9 $\pm 9.1$	99.3 $\pm 4.9$	97.7 $\pm 5.2$
CPR	76.5 $\pm 1.0$	61.9 $\pm 3.9$	98.6 $\pm 4.9$	97.7 $\pm 3.8$
CRS	110.3 $\pm 1.7$	-70.7 $\pm 2.5$	100.6 $\pm 5.0$	99.9 $\pm 6.1$
CRR	46.1 $\pm 7.5$	4.4 $\pm 11.0$	101.1 $\pm 4.2$	97.7 $\pm 5.2$
PFR	156.7 $\pm 6.7$	24.0 $\pm 6.9$	99.1 $\pm 4.5$	97.4 $\pm 5.9$
PFS	79.0 $\pm 1.6$	66.4 $\pm 2.6$	99.6 $\pm 4.7$	99.0 $\pm 5.0$
PRR	117.8 $\pm 2.0$	-71.4 $\pm 4.6$	100.6 $\pm 5.4$	100.2 $\pm 5.3$
PRS	17.4 $\pm 1.8$	-12.0 $\pm 5.1$	98.0 $\pm 4.7$	101.7 $\pm 6.1$

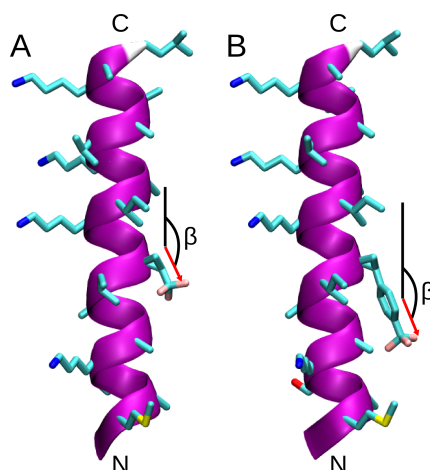


Figure 7.1: Energy-minimized structures of PGLa with  $^{19}\text{F}$  labels substituted at position 10. N indicates the amino, C the carboxy-terminus.  $\beta$  is the angle between the helical axis and the director (red arrow), which is equivalent to C–CF<sub>3</sub> bond. *A*: Position and orientation of CPS. *B*: Position and orientation of PFR. The color code is *cyan* for carbons, *blue* for nitrogen, *red* for oxygen, *yellow* for sulphur and *pink* for fluorine.

The cyclobutyl-based  $^{19}\text{F}$  labels HSS and CBS are oriented at an average angle of  $\beta = 134^\circ$  with respect to the helical axis, while their isomers HSR and CBR again point towards the opposite end, at an average angle of  $\beta = 77^\circ$ .

For the peptides with cyclopropyl-based  $^{19}\text{F}$  labels, CPS and PFR have the same orientation, with an average angle of  $\beta = 156^\circ$ . As it can be seen in Figure 7.1, the director is almost parallel to the helical axis for these labels. This is expected, since PFR has a similar structure as CPS. For PFR, the director, which is equivalent to the C–CF<sub>3</sub> bond, is prolonged by an additional aromatic ring, compared to CPS. The same relationship is given for CPR and PFS, CRS and PRR, and CRR and PRS. The stereo-isomers to CPS and PFR, CPR and PFS are oriented at an average angle of  $\beta = 78^\circ$ . CRS and PRR are oriented on average with  $\beta = 114^\circ$ . Only for their isomers CRR and PRS, which should also have a similar orientation with respect to the helical axis,  $\beta$  is quite different, with  $\beta = 46^\circ$  for CRR and  $\beta = 17^\circ$  for PRS.

$\beta$  is typically independent of the substituted position, which can be seen by the low standard deviations. The structures with CRR have the highest deviations between the different positions with a standard deviation of  $7.5^\circ$ .

For all  $^{19}\text{F}$  labelled peptides, the  $\beta$  angles for the neighboring residues are generally not influenced and close to the ideal value of  $121^\circ$ .

### Angle $\alpha$

The  $\alpha$ -angle is the angle between the vector from the center of the helix to the C $_{\alpha}$ -atom and the director, projected onto the plane perpendicular to the helical axis.

For canonical amino acids, where the  $C_\alpha$ - $C_\beta$ -bond is considered as the director,  $\alpha$  is  $\sim 40^\circ$  (Chapter 4.3).

For nearly all  $^{19}\text{F}$  labels, this angle is clearly different. For the  $C_\alpha$ -3 substitutes PGS and BGS, the conversion to the R-stereo-isomers BGR and PGR changes the sign of  $\alpha$ , as expected. When looking from the N-terminus down the helical axis, the directors of these two side chains point counter-clockwise away from the axis, at an average angle of  $\sim -42^\circ$ . For the S-stereoisomers BGS and PGS,  $\alpha$  is close to the value calculated in Chapter 4.3 ( $40^\circ$ ), with  $\alpha = 32^\circ$  for BGS and  $\alpha = 42^\circ$  for PGS.

The cyclobutyl-containing building blocks HSS and CBS and their stereoisomers HSR and CBR have pairwise almost the same orientation. HSS and CBS are orientated counter-clockwise with an average  $\alpha$  angle of  $-56^\circ$ . HSR and CBR have small positive angles, their average is  $11^\circ$ .

The fluorine amino acids which are based on a cyclopropyl ring, have very different orientations, depending on the position where the  $\text{CF}_3$  group is attached. The peptides with substituted CPS and CRS both have negative  $\alpha$  angles. For both these peptides  $\beta > 90^\circ$ , so the director points towards the N-terminus. For CPR and CRR, the situation is reversed. The director points more towards the C-terminus and  $\alpha$  is positive.

The distribution of  $\alpha$  for the amino acids based on a cyclopropyl and an additional aromatic ring is different. PFS and PFR both have positive values, while the angles for PRR and PRS are both negative. PRS and PFR, which are both pointing almost parallel to the helical axis in opposite directions, both have small  $\alpha$  angles ( $24^\circ$  for PFR and  $-12^\circ$  for PRS). Figure 7.2 shows the orientation of the four labels PFR, PFS, PRR and PRS, and CPR, CPS, CRR and CRS with respect to each other and the helical axis.

The variation of  $\alpha$  between the different substituted positions is again low with standard deviations of  $\leq 7^\circ$ , but there are two exceptions: for CPS, the standard deviation is  $9^\circ$ , and for CRR  $11^\circ$ .

### Angle $\theta$

The helix pitch angles  $\theta_{i-1,i}$  between the labelled residue and the previous residue, and  $\theta_{i,i+1}$  between the labelled residue and the subsequent residue are generally close to  $100^\circ$ . For most fluorine labels, the two angles are slightly lower, by  $\geq 5^\circ$ . Their standard deviations, however, are also in the range of  $\sim 5^\circ$ .

From the three groups –  $C_\alpha$ -3-substitutes, cyclobutyl-based substitutes and cyclo-

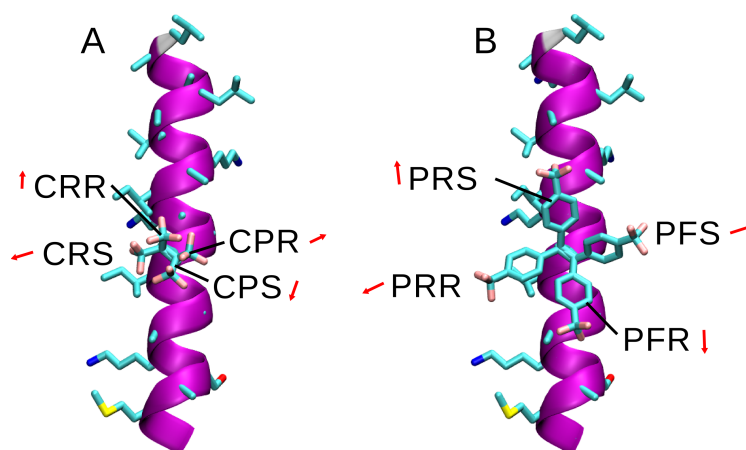


Figure 7.2: *A*: Orientation of the fluorine amino acids PFS, PFR, PRR and PRS, substituted at position 10 in PGLa, with respect to the helical axis. *B*: Orientation of the fluorine amino acids CPS, CPR, CRS, and CRR substituted at position 10 in PGLa, with respect to the helical axis. The red arrows show the approximate direction of the director.

propyl-based substitutes –, the cyclopropyl-based labels generally have values closest to the ideal value of  $100^\circ$ .

### 7.3.2 Membrane simulations

The peptides with 10 out of the 16  $^{19}\text{F}$  labels have been simulated for 200 ns in a DMPC membrane: BGS, PGS, HSS, HSR, CBS, CBR, CPS, CPR, PFR and PFS. The simulations show, that the substitution of single positions with fluorine labelled amino acids influences the overall helicity of PGLa. In Figure 7.3, the helicities, measured over the last 150 ns of the simulations, are shown.

#### Helicity

In Chapter 4.3 was shown, that the natural PGLa is helical from positions 2-17 (Figure 4.1).

When comparing the  $C_\alpha$ -3-substituted peptides with the others, the helicity is less disturbed. For BGS at positions 9, 10 and 14, the helicity at the position of the label gets disturbed towards the end of the simulation, so this does not appear to be an artefact from the setup. For position 13, however, there is a disturbance at position 8, which is there initially and which vanishes during the course of the simulation. For PGS, the helicity is nearly perfectly conserved, when substituted at positions 9, 10 and 13. For the substituted position 14, the helicity breaks down at position 19 after  $\sim 90$  ns.

The labels with cyclobutyl-rings cause no relevant disturbance of the helical struc-

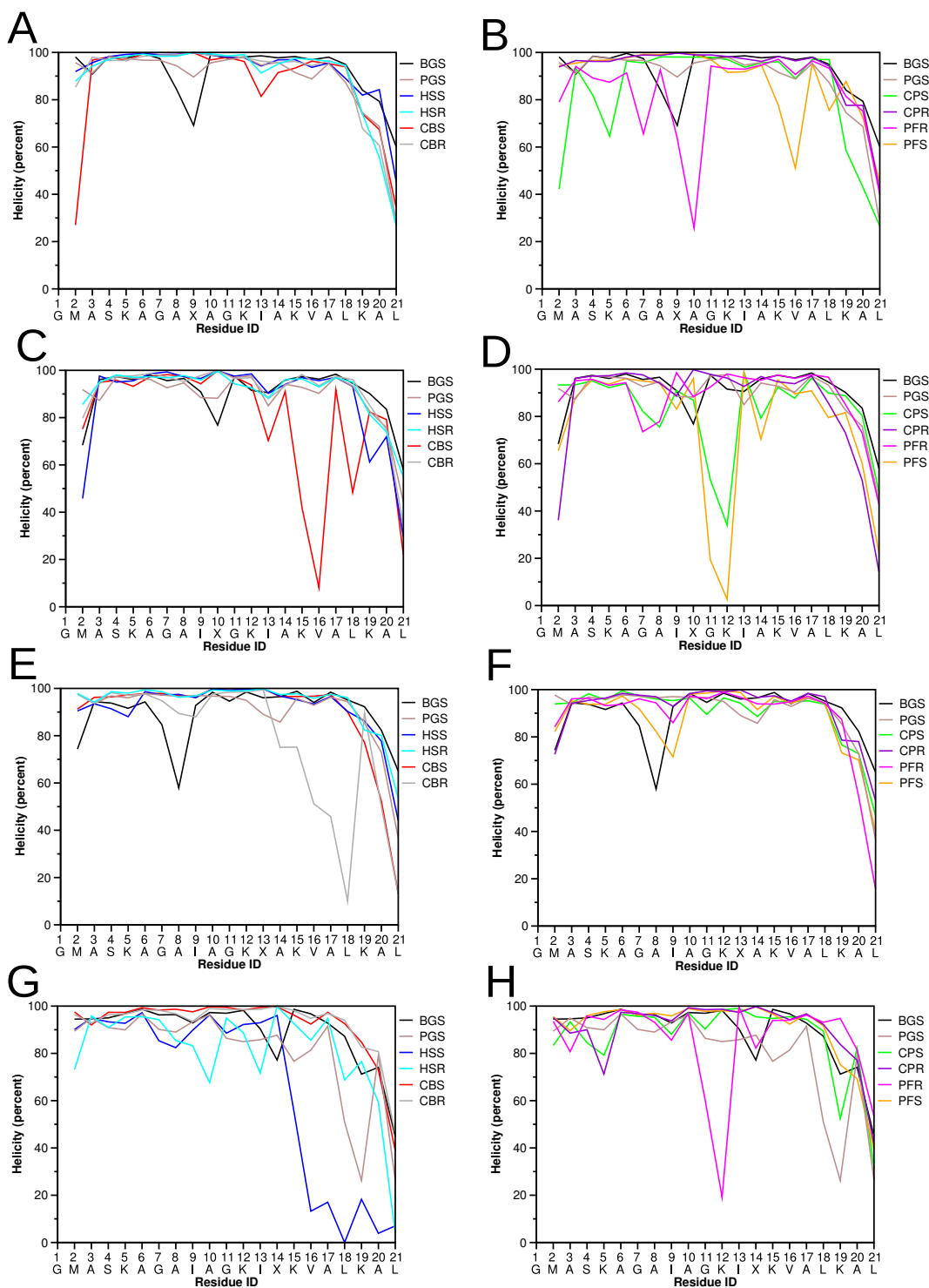


Figure 7.3: Helicity for PGLa with different fluorine labels at different positions. *A* and *B*: position 9, *C* and *D*: position 10; *E* and *F*: position 13, *G* and *H*: position 14. The helicities for BGS and PGS are shown redundantly for better comparison.

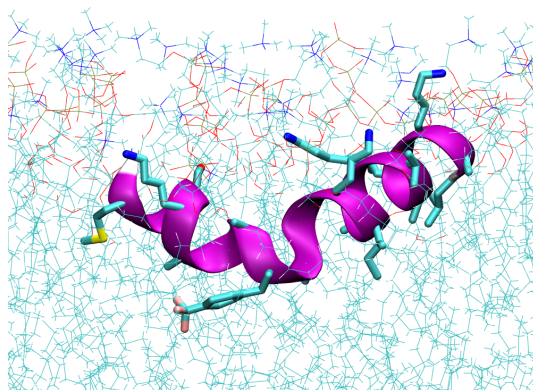


Figure 7.4: Snapshot from the end of the simulation of PGLa with the substituted fluorine amino acid PFR at position 9.

ture when substituted at position 9. For CBS at position 10, the hydrogen bond between position 15 and 19 breaks early in the simulation, which explains the drop of helicity. When CBR is substituted at position 13, the breakage of the hydrogen bond between the residues 14 and 18 is responsible for the disturbance of the helical structure between position 15 and 18. For the HSR-substituted peptide at position 14, the disturbance at position 10 goes away during the course of the simulation, while the drop of helicity at position 13, close to the replaced residue, is forming towards the end of the simulation. For HSS at position 14, the C-terminus starting from residue 15 next to the replaced position is already unraveled at the start of the evaluated time interval at 50 ns and stays unstructured for the rest of the simulation.

From the amino acids which are based on a cyclopropyl ring, CPR shows almost no disturbance of the helical structure at all four positions. For CPS at position 10, the helix is disturbed at its center in the beginning, but the hydrogen bonds reform and restore the helical structure in the last 50 ns. PFS behaves in a similar way, except that the disturbance at position 12 endures throughout the whole simulation. In the simulation of PGLa with a substituted PFR at position 9, a kink forms at position 10, which explains the loss of helicity here. A snapshot of the kinked peptide in the membrane environment is shown in Figure 7.4. When PFR is substituted at position 14, the helicity drops at position 12. However, this local instability rarely affects the overall structure and does not result in a strong kink as for the latter.

In Table 7.3, the average helicities, averaged over positions 3-17, are listed. Standard deviations of  $>7$  generally mean that there is at least one residue which causes a disturbance during the course of the simulations. From these values, PGS and CPR seem to be the least helix disturbing fluorine amino acids, followed closely by HSR. PFS and PFR have the lowest overall helicities and also the highest fluctuations.

Table 7.3: Helicities for all fluorine amino acids averaged over residues 3-17. The small numbers with a  $\pm$  sign are the standard deviations.

pos.	BGS	PGS	HSS	HSR	CBS	CBR	CPS	CPR	PFR	PFS	PGLa <sup>a</sup>
9	95 $\pm 8$	95 $\pm 3$	98 $\pm 2$	97 $\pm 2$	96 $\pm 4$	97 $\pm 1$	93 $\pm 9$	98 $\pm 1$	85 $\pm 19$	92 $\pm 12$	96 $\pm 3$
10	94 $\pm 5$	93 $\pm 4$	97 $\pm 2$	96 $\pm 3$	84 $\pm 25$	96 $\pm 3$	83 $\pm 17$	96 $\pm 3$	93 $\pm 7$	81 $\pm 28$	
13	92 $\pm 10$	95 $\pm 3$	96 $\pm 3$	98 $\pm 2$	98 $\pm 1$	87 $\pm 17$	95 $\pm 3$	97 $\pm 2$	95 $\pm 3$	93 $\pm 7$	
14	95 $\pm 5$	89 $\pm 5$	79 $\pm 27$	89 $\pm 9$	98 $\pm 2$	97 $\pm 2$	93 $\pm 5$	94 $\pm 7$	86 $\pm 20$	97 $\pm 2$	

<sup>a</sup>Helicity averaged over residues 3-17, from the PGLa membrane simulation in Chapter 4, calculated for the last 800 ns.

Generally, the helicity of the  $^{19}\text{F}$  labelled PGLa is more disturbed when labelled at positions 10 and 14, which are the Ala residues in the natural PGLa, than at positions 9 and 13, where Ile residues were substituted.

However, the helicity measurements should not be overestimated, due to the short simulation time.

### Angles $\tau$ and $\rho$

In Table 7.4, the tilt angle  $\tau$  and the azimuthal rotation angle  $\rho$  are listed. They have been calculated for the region between position 3 and 17. For the unlabelled PGLa, the angles where  $\tau = 99^\circ$  and  $\rho = 109^\circ$ , averaged over 400 ns, where the peptide was in a surface-aligned state (Table 4.1). The fluorine-labelled peptides are all in a surface-aligned state during the whole simulation time. They have tilt angles  $\tau$  between  $89^\circ$  and  $103^\circ$ . The azimuthal rotation angles  $\rho$ , however, which are in general wider spread, have values ranging from  $91^\circ$  up to  $138^\circ$ .

For position 9,  $\rho$  is generally close to or below  $109^\circ$ , except for CBR, CPR and PFR. This means that the label is located on the side of the peptide, pointing neither clearly towards the aqueous phase nor to the membrane interior. For position 10,  $\rho$  is generally between  $109^\circ$  and  $126^\circ$ , which means that position 10 is pointing clearly towards the membrane core. The simulations with the labelled position 13 show the largest spread in  $\rho$ . HSR is located at the side of the peptide with a  $\rho$  angle of  $91^\circ$ , similar to position 9, while CBS and PFR clearly tend to bury deep inside the membrane core, with  $\rho$  values of  $137^\circ$ . For position 14, HSS has the largest  $\rho$  value of  $134^\circ$  and is thus pointing towards the bilayer at an intermediate position.

The labels with C $_{\alpha}$ -3-substitutes, PGS and BGS, have the smallest spread in the

Table 7.4:  $\tau$  and  $\rho$  for all FAAs averaged over residues 3-17.

FAA	9		10		13		14	
	$\tau$	$\rho$	$\tau$	$\rho$	$\tau$	$\rho$	$\tau$	$\rho$
BGS	94 $\pm 5$	102 $\pm 18$	93 $\pm 6$	112 $\pm 20$	96 $\pm 5$	102 $\pm 34$	101 $\pm 7$	101 $\pm 19$
PGS	94 $\pm 7$	113 $\pm 17$	91 $\pm 7$	102 $\pm 18$	92 $\pm 8$	118 $\pm 17$	96 $\pm 5$	114 $\pm 19$
HSS	90 $\pm 7$	107 $\pm 18$	96 $\pm 7$	125 $\pm 15$	95 $\pm 7$	100 $\pm 19$	89 $\pm 8$	134 $\pm 28$
HSR	100 $\pm 7$	96 $\pm 13$	96 $\pm 7$	93 $\pm 16$	89 $\pm 7$	91 $\pm 16$	98 $\pm 6$	128 $\pm 32$
CBS	92 $\pm 7$	107 $\pm 19$	87 $\pm 8$	114 $\pm 16$	100 $\pm 8$	137 $\pm 14$	97 $\pm 6$	109 $\pm 15$
CBR	102 $\pm 9$	122 $\pm 14$	92 $\pm 6$	112 $\pm 16$	98 $\pm 9$	105 $\pm 21$	98 $\pm 7$	120 $\pm 15$
CPS	102 $\pm 6$	105 $\pm 21$	97 $\pm 6$	124 $\pm 28$	94 $\pm 7$	98 $\pm 17$	99 $\pm 7$	111 $\pm 23$
CPR	97 $\pm 6$	111 $\pm 14$	96 $\pm 7$	122 $\pm 16$	89 $\pm 6$	104 $\pm 19$	94 $\pm 6$	111 $\pm 20$
PFR	89 $\pm 7$	137 $\pm 42$	91 $\pm 8$	117 $\pm 33$	103 $\pm 6$	138 $\pm 22$	100 $\pm 6$	114 $\pm 28$
PFS	89 $\pm 6$	105 $\pm 19$	95 $\pm 6$	126 $\pm 29$	97 $\pm 6$	126 $\pm 19$	97 $\pm 6$	109 $\pm 21$

$\rho$  angles. Interestingly, in both cases the substituted position 10 has a remarkably different  $\rho$  angle from the other positions.

Also here, the exact  $\rho$  angles should not be overestimated, due to the short simulation time. Compared to  $\tau$ , they have high standard deviations and it was shown in Chapter 4, that  $\rho$  can vary strongly within a microsecond of simulation time.

### Angles $\beta$ , $\alpha$ , and $\theta$

The angles  $\beta$ ,  $\alpha$  and  $\theta$  have been calculated with respect to the helical axis from position 3-17 and are listed in Appendix Table D.2. The angle  $\beta$  between the director and the helical axis is almost unchanged (difference  $<6^\circ$ ) for all building blocks, when compared to the energy-minimized structures.

For the  $\alpha$  angles at the positions of the labels BGS, PGS, CPR and PFS, the differences between the angles obtained from the simulations and from the energy-minimized structures is also very low and  $\leq 6^\circ$ . In the simulations where residues were substituted by the cyclobutyl-based amino acids HSS, HSR, CBS, and CBR,  $\alpha$  was on average  $\sim 16^\circ$  higher than for the energy-minimized structures. HSR and CBR are oriented in a very similar way, they both have  $\beta$  angle of  $\sim 73^\circ$  and an  $\alpha$  angle of  $\sim 28^\circ$ . Also HSS and CBS have a very similar orientation, their average  $\beta$  is  $\sim 136^\circ$ , and the average  $\alpha$  is  $\sim -40^\circ$ .

For the cyclopropyl-based labels, CPS and PFR both have high standard deviations and an  $\alpha$  angle which is on average  $12^\circ$  lower than in the energy-minimized structures. For CPS, the standard deviation for  $\alpha$  is highest when substituted at position 10, and for PFR, when substituted at position 9. For both these peptides, the helical structure was disturbed in the center of the peptides (Figure 7.3).

The helix pitch angle  $\theta$  between the position of the label and the adjacent positions  $i - 1$  and  $i + 1$  has changed in all cases, when comparing the results from the energy-minimized structures with the data from the simulations. In most cases, the change is  $\leq 6^\circ$  for both angles. For BGS, the angle  $\theta_{i-1,i}$  is reduced by  $13^\circ$ . The deviation is caused mainly by substitutions at positions 9 and 10, which confirms the observation, that the fluorine label, substituted at these positions, disturbs the helicity directly at its location. For PFS, the average  $\theta_{i,i+1}$  is reduced by  $11^\circ$ , which is caused mainly by position 10. This position also showed a drop in the helicity at the peptide center (Figure 7.3). For CPS, both angles are reduced by an average amount of  $12^\circ$ . This reduction happens nearly uniformly at all positions. The highest deviation from the ideal helix pitch angle of  $100^\circ$  is measured for PFR. Here,  $\theta_{i-1,i}$  is on average reduced by  $31^\circ$ , and  $\theta_{i,i+1}$  by  $16^\circ$ . In all four simulations, visual

inspection revealed a kink in the peptide at the position of this label. This kink is largest for position 9 (Figure 7.4).

## 7.4 Discussion

In the energy-minimized structures, the orientations of the directors with respect to the helical axis are generally independent of the inserted position. Only for the cyclopropyl-based CPS, CRR and PFR labels, the standard deviations of  $\alpha$  were higher, in the range from 6 – 11°. For  $\beta$ , CRR and PFR had standard deviations of 6 – 8°. Therefore, the side chains in close proximity to the labels at positions 9, 10, 13 and 14 do not seem to play an important role for the orientations of the fluorine amino acids.

However, the membrane simulations revealed disturbances in the secondary structure of the peptides. For nearly all fluorine labeled peptides, the substitution leads to a reduced helicity in at least one of the four labeled peptides (Figure 7.3 and Table 7.3). Hereby, some disturbances appeared in the beginning of the simulations and the peptides re-established their helicity towards the end. In others, however, the peptide was completely helical for the first part and partly unraveled towards the end of the simulation. For PFR, a kink not directly at the labelled site was observed in the simulations of all four substituted positions. The disturbance is localised at the center of the peptide, while the amino-terminal and the carboxy-terminal ends of the peptide are still helical. As has been shown in Chapter 4, longer simulations are necessary to obtain a more reliable picture. Nevertheless, unlabeled PGLa under the same simulation conditions is completely helical in the region from position 3-17.

The calculation of the orientational angles  $\tau$  and  $\rho$  showed qualitatively the same tilt as in unlabeled PGLa. The  $\rho$  angle, however, exhibited a large spread of up to 40° (equivalent to two positions on the helical wheel) per  $^{19}\text{F}$  label.

The MD simulations could show that the fluorine labels may cause disturbances in the helical structure. The wide distribution of possible  $\rho$  angles and the decrease of helicity, which is in some cases distant to the substituted site, leads to the assumption, that some labels 'hook' into the membrane core, thereby creating tensions in the rest of the peptide. These tensions can lead to the breaking of hydrogen bonds and thus local loss of helicity.

However, the severity of these problems can only be quantified in longer simulations and in comparison with experiments.

## 8. Summary

In this work, several computational approaches have been used to study membrane-active peptides.

In Chapter 4, unrestrained MD simulations of  $\alpha$ -helical peptides in DMPC membranes were performed to evaluate the membrane-inserted orientations and structures, and to compare these results with those from SSNMR experiments. The simulations can qualitatively reproduce the SSNMR results at low peptide:lipid concentrations. The tilt angles  $\tau$  of the helical axis against the membrane normal agree well with the peptide orientations obtained from NMR splittings. For the peptides with amidated carboxy-terminus, PGLa, MSI-103 and KIA14, the azimuthal rotation angle  $\rho$  showed a systematic shift compared to the NMR data. The mobility factor  $S_{\text{mol}}$  goes down with longer simulation times. In most cases, it was still higher than in the NMR experiments. The helicity of the peptides was generally well reproduced, but underestimated in some cases. Important structural parameters, which define the orientation of the side chains with respect to the helical axis, have been calculated. These parameters are necessary for the interpretation of SSNMR data. In order to improve the simulations, longer simulation timescales are necessary, which is likely to become possible in the near future. Force field improvements are needed to correct for the systematic  $\rho$  shift.

In Chapter 5, a new 3D hydrophobic moment (HM) vector is defined. With this method, the electrostatic potential on the molecular surface is evaluated, resulting in a vector which points away from the polar parts of the surface, towards the hydrophobic side. This vector can predict the orientation of amphiphilic peptides in a membrane. For the helical peptides PGLa, TempA and BP100, the HM vector qualitatively predicts the states where the peptides are not surface-aligned but tilted towards the opposite leaflet, and which have been observed in the simulations. Since other states are still frequently observed in both NMR experiments and simulations, it is assumed that specific interactions with lipid head groups and/or other factors prevent the peptide from instantly assuming the tilted orientation. For the cyclic decapeptide GS, however, the experimentally observed surface-aligned state is also

the one which is predicted from the HM vector. Possibly, this implies a different mechanism of action for the short and nearly globular GS.

In Chapter 6, a simulation study on photoswitchable analogs of GS is presented. The photoswitch fragments have been parametrized and incorporated into GS at different positions. The structures of these analogs were elucidated both in an isotropic solution and when bound to a phospholipid membrane. It could be shown that the incorporation of the photoswitch leads to a strong reduction of the intra-molecular hydrogen bonds. Different physico-chemical properties of the molecules were calculated and compared to the experimental data. It could be demonstrated, that there is a general correlation between the biological activity and the HM vector of these peptidomimetics. Hereby, the absolute value of the HM vector is interpreted as a binding affinity to hydrophobic surfaces.

Chapter 7 shows a study on fluorine amino acids, which are used or planned to be used in  $^{19}\text{F}$  SSNMR experiments. The  $^{19}\text{F}$  labels have been incorporated into PGLa, by replacing the residues at positions 9, 10, 13 and 14. Like in Chapter 4, structural parameters have been calculated from both energy-minimized and membrane-bound structures, which characterise the orientation of these  $^{19}\text{F}$  labels with respect to the helical axis, and which are necessary for the interpretation of  $^{19}\text{F}$  SSNMR data and for the design of new labels. Additionally, the potential disturbance of helical structure, caused by  $^{19}\text{F}$  labels, has been evaluated.

## Bibliography

- [1] J. P. Swann. The search for synthetic penicillin during World War II. *The British Journal for the History of Science*, 16:154–190, 1983.
- [2] A. Fleming. On the antibacterial action of cultures of a penicillium, with special reference to their use in the isolation of B. Influenzae. *British Journal of Experimental Pathology*, 10:226–236, 1929.
- [3] D. C. Hodgkin. X-ray analysis of the structure of penicillin. *Advancement of Science*, 6:85–9, 1949.
- [4] D. J. Tipper and J. L. Strominger. Mechanism of action of penicillins: a proposal based on their structural similarity to acyl-D-alanyl-D-alanine. *Proceedings of the National Academy of Sciences, USA*, 54(4):1133–41, 1965.
- [5] R. R. Yocum, D. J. Waxman, J. R. Rasmussen, and J. L. Strominger. Mechanism of penicillin action: penicillin and substrate bind covalently to the same active site serine in two bacterial D-alanine carboxypeptidases. *Proceedings of the National Academy of Sciences, USA*, 76(6):2730–4, 1979.
- [6] E. P. Abraham and E. Chain. An enzyme from bacteria able to destroy penicillin. *Nature*, (3713):837, 1940.
- [7] J. Davies and D. Davies. Origins and evolution of antibiotic resistance. *Microbiology and Molecular Biology Reviews*, 74(3):417–33, 2010.
- [8] R. Hakenbeck. Mosaic genes and their role in penicillin-resistant *Streptococcus pneumoniae*. *Electrophoresis*, 19(4):597–601, 1998.
- [9] M. C. Roberts. Update on macrolide-lincosamide-streptogramin, ketolide, and oxazolidinone resistance genes. *FEMS Microbiology Letters*, 282(2):147–59, 2008.
- [10] H. W. Smith. Antibiotics in animal husbandry. *British Medical Journal*, 1(5078):1062, 1958.

- 
- [11] WHO. WHO | Antimicrobial resistance: global report on surveillance 2014, 2014.
- [12] A. A. Bahar and D. Ren. Antimicrobial peptides. *Pharmaceuticals*, 6(12):1543–75, 2013.
- [13] R. J. Dubos and R. D. Hotchkiss. The production of bactericidal substances by aerobic sporulating bacilli. *The Journal of Experimental Medicine*, 73(5):629–40, 1941.
- [14] J. M. Conlon and A. Sonnevend. Antimicrobial peptides in frog skin secretions. *Methods in Molecular Biology*, 618:3–14, 2010.
- [15] Y. Ma, C. Liu, X. Liu, J. Wu, H. Yang, Y. Wang, J. Li, H. Yu, and R. Lai. Peptidomics and genomics analysis of novel antimicrobial peptides from the frog, *Rana nigrovittata*. *Genomics*, 95(1):66–71, 2010.
- [16] E. Strandberg and A. S. Ulrich. NMR methods for studying membrane-active antimicrobial peptides. *Concepts in Magnetic Resonance Series A*, 23A(2):89–120, 2004.
- [17] W. W. Wilson, M. M. Wade, S. C. Holman, and F. R. Champlin. Status of methods for assessing bacterial cell surface charge properties based on zeta potential measurements. *Journal of Microbiological Methods*, 43(3):153–64, 2001.
- [18] H. v. Jenssen, P. Hamill, and R. E. W. Hancock. Peptide antimicrobial agents. *Clinical Microbiology Reviews*, 19(3):491–511, 2006.
- [19] R. W. Glaser, C. Sachse, U. H. N. Dürr, S. Afonin, P. Wadhvani, E. Strandberg, and A. S. Ulrich. Concentration-dependent realignment of the antimicrobial peptide PGLa in lipid membranes observed by solid-state  $^{19}\text{F}$ -NMR. *Biophysical Journal*, 88(5):3392–3397, 2005.
- [20] E. Strandberg, S. Esteban-Martín, J. Salgado, and A. S. Ulrich. Orientation and dynamics of peptides in membranes calculated from  $^2\text{H}$ -NMR data. *Biophysical Journal*, 96(8):3223–3232, 2009.
- [21] P. Wadhvani, E. Strandberg, J. van den Berg, C. Mink, J. Büreck, R. A. M. Ciriello, and A. S. Ulrich. Dynamical structure of the short multifunctional peptide BP100 in membranes. *Biochimica et Biophysica Acta*, 1838(3):940–9, 2014.

- [22] G. Saberwal and R. Nagaraj. Cell-lytic and antibacterial peptides that act by perturbing the barrier function of membranes: facets of their conformational features, structure-function correlations and membrane-perturbing abilities. *Biochimica et Biophysica Acta*, 1197(2):109–131, 1994.
- [23] E. Badosa, R. Ferre, M. Planas, L. Feliu, E. Besalú, J. Cabrefiga, E. Bardají, and E. Montesinos. A library of linear undecapeptides with bactericidal activity against phytopathogenic bacteria. *Peptides*, 28(12):2276–85, 2007.
- [24] O. Babii, S. Afonin, M. Berditsch, S. Reißer, P. K. Mykhailiuk, V. S. Kubyshkin, T. Steinbrecher, A. S. Ulrich, and I. V. Komarov. Controlling biological activity with light: diarylethene-containing cyclic peptidomimetics. *Angewandte Chemie (International ed. in English)*, 2014.
- [25] M. Berditsch, S. Afonin, T. Vladimirova, P. Wadhvani, and A. S. Ulrich. Antimicrobial peptides can enhance the risk of persistent infections. *Frontiers in Immunology*, 3:222, 2012.
- [26] A. S. Ulrich. Solid state  $^{19}\text{F}$ -NMR methods for studying biomembranes. *Progress in Nuclear Magnetic Resonance Spectroscopy*, 46(1):1–21, 2005.
- [27] E. Strandberg, S. Özdirekcan, D. T. S. Rijkers, P. C. A. der Wel, R. E. I. Koeppe, R. M. J. Liskamp, and J. A. Killian. Tilt angles of transmembrane model peptides in oriented and non-oriented lipid bilayers as determined by  $^2\text{H}$  solid state NMR. *Biophysical Journal*, 86(6):3709–3721, 2004.
- [28] A. S. Ulrich. Solid state  $^{19}\text{F}$ -NMR analysis of oriented biomembranes. In G. A. Webb, editor, *Modern Magnetic Resonance*, volume 1, pages 261–267. Springer, Dordrecht, 2006.
- [29] P. Wadhvani and E. Strandberg. Structure analysis of membrane-active peptides using  $^{19}\text{F}$ -labeled amino acids and solid-state NMR. In I. Ojima, editor, *Fluorine in Medicinal Chemistry and Chemical Biology*, pages 463–493. Blackwell Publishing, London, 2009.
- [30] J. D. Gehman and F. Separovic. Solid-state NMR of membrane-active proteins and peptides. In G. A. Webb, editor, *Modern Magnetic Resonance*, volume 1, pages 305–311. Springer, Dordrecht, 2006.
- [31] E. Strandberg, N. Kanithasen, D. Tiltak, J. Bürck, P. Wadhvani, O. Zvermann, and A. S. Ulrich. Solid-state NMR analysis comparing the designer-

- made antibiotic MSI-103 with its parent peptide PGLa in lipid bilayers. *Biochemistry*, 47(8):2601–16, 2008.
- [32] J. Bürck, S. Roth, P. Wadhvani, S. Afonin, N. Kanithasen, E. Strandberg, and A. S. Ulrich. Conformation and membrane orientation of amphiphilic helical peptides by oriented circular dichroism. *Biophysical Journal*, 95(8):3872–3881, 2008.
- [33] G. A. Olah and H. W. Huang. Circular dichroism of oriented  $\alpha$ -helices. 1. Proof of the exciton theory. *Journal of Chemical Physics*, 89(4):2531–2538, 1988.
- [34] G. A. Olah and H. W. Huang. Circular dichroism of oriented  $\alpha$ -helices. 2. Electric field oriented polypeptides. *Journal of Chemical Physics*, 89(11):6956–6962, 1988.
- [35] Y. Wu, H. W. Huang, and G. A. Olah. Method of oriented circular dichroism. *Biophysical Journal*, 57(4):797–806, 1990.
- [36] O. V. Nolandt, T. H. Walther, S. Roth, J. Bürck, and A. S. Ulrich. Structure analysis of the membrane protein TatCd from the Tat system of *B. subtilis* by circular dichroism. *Biochimica et Biophysica Acta*, 1788(10):2238–2244, 2009.
- [37] R. Heinzmann, S. L. Grage, C. Schalck, J. Bürck, Z. Banoczi, O. Toke, and A. S. Ulrich. A kinked antimicrobial peptide from *Bombina maxima*. II. Behavior in phospholipid bilayers. *European Biophysics Journal*, 40(4):463–470, 2011.
- [38] S. Esteban-Martín, E. Strandberg, J. Salgado, and A. S. Ulrich. Solid state NMR analysis of peptides in membranes: influence of dynamics and labeling scheme. *Biochimica et Biophysica Acta*, 1798:252–257, 2010.
- [39] S. Esteban-Martín, E. Strandberg, G. Fuertes, A. S. Ulrich, and J. Salgado. Influence of whole-body dynamics on  $^{15}\text{N}$  PISEMA NMR spectra of membrane peptides: a theoretical analysis. *Biophysical Journal*, 96:3233–3241, 2009.
- [40] P. C. A. der Wel, E. Strandberg, J. A. Killian, and R. E. I. Koeppe. Geometry and intrinsic tilt of a tryptophan-anchored transmembrane  $\alpha$ -helix determined by  $^2\text{H}$  NMR. *Biophysical Journal*, 83(3):1479–1488, 2002.
- [41] E. Strandberg, P. Tremouilhac, P. Wadhvani, and A. S. Ulrich. Synergistic transmembrane insertion of the heterodimeric PGLa/magainin 2 complex studied by solid-state NMR. *Biochimica et Biophysica Acta*, 1788:1667–1679, 2009.

- [42] S. Özdirekcan, C. Etchebest, J. A. Killian, and P. F. Fuchs. On the orientation of a designed transmembrane peptide: toward the right tilt angle? *Journal of the American Chemical Society*, 129(49):15174–15181, 2007.
- [43] T. Steinbrecher, S. Prock, J. Reichert, P. Wadhvani, B. Zimpfer, J. Bürck, M. Berditsch, M. Elstner, and A. S. Ulrich. Peptide-lipid interactions of the stress-response peptide TisB that induces bacterial persistence. *Biophysical Journal*, 103(7):1460–1469, 2012.
- [44] L. Monticelli, S. K. Kandasamy, X. Periole, R. G. Larson, D. P. Tieleman, and S. J. Marrink. The MARTINI coarse-grained force field: Extension to proteins. *Journal of Chemical Theory and Computation*, 4(5):819–834, 2008.
- [45] J. C. Hsu and C. M. Yip. Molecular dynamics simulations of indolicidin association with model lipid bilayers. *Biophysical Journal*, 92(12):L100–2, 2007.
- [46] S. Esteban-Martín and J. Salgado. The dynamic orientation of membrane-bound peptides: bridging simulations and experiments. *Biophysical Journal*, 93(12):4278–4288, 2007.
- [47] Y. Wang, T. Zhao, D. Wei, E. Strandberg, A. S. Ulrich, and J. P. Ulmschneider. How reliable are molecular dynamics simulations of membrane active antimicrobial peptides? *Biochimica et Biophysica Acta*, 1838(9):2280–2288, 2014.
- [48] D. Andreu, H. Aschauer, G. Kreil, and R. B. Merrifield. Solid-phase synthesis of PYLa and isolation of its natural counterpart, PGLa [PYLa-(4-24)] from skin secretion of *Xenopus laevis*. *European Journal of Biochemistry*, 149(3):531–5, 1985.
- [49] A. da Silva and O. Teschke. Effects of the antimicrobial peptide PGLa on live *Escherichia coli*. *Biochimica et Biophysica Acta*, 1643(1-3):95–103, 2003.
- [50] M. Hartmann, M. Berditsch, J. Hawecker, M. F. Ardakani, D. Gerthsen, and A. S. Ulrich. Damage of the bacterial cell envelope by antimicrobial peptides gramicidin S and PGLa as revealed by transmission and scanning electron microscopy. *Antimicrobial Agents & Chemotherapy*, 54(8):3132–3142, 2010.
- [51] B. Bechinger, M. Zasloff, and S. J. Opella. Structure and dynamics of the antibiotic peptide PGLa in membranes by solution and solid-state nuclear magnetic resonance spectroscopy. *Biophysical Journal*, 74(2):981–987, 1998.

- [52] E. Strandberg, P. Wadhvani, P. Tremouilhac, U. H. N. Dürr, and A. S. Ulrich. Solid-state NMR analysis of the PGLa peptide orientation in DMPC bilayers: structural fidelity of  $^2\text{H}$ -labels versus high sensitivity of  $^{19}\text{F}$ -NMR. *Biophysical Journal*, 90(5):1676–1686, 2006.
- [53] M. Ieronimo, S. Afonin, K. Koch, M. Berditsch, P. Wadhvani, and A. S. Ulrich.  $^{19}\text{F}$  NMR analysis of the antimicrobial peptide PGLa bound to native cell membranes from bacterial protoplasts and human erythrocytes. *Journal of the American Chemical Society*, 132(26):8822–8824, 2010.
- [54] R. W. Glaser, C. Sachse, U. H. N. Dürr, P. Wadhvani, and A. S. Ulrich. Orientation of the antimicrobial peptide PGLa in lipid membranes determined from  $^{19}\text{F}$ -NMR dipolar couplings of 4- $\text{CF}_3$ -phenylglycine labels. *Journal of Magnetic Resonance*, 168(1):153–163, 2004.
- [55] P. Tremouilhac, E. Strandberg, P. Wadhvani, and A. S. Ulrich. Conditions affecting the re-alignment of the antimicrobial peptide PGLa in membranes as monitored by solid state  $^2\text{H}$ -NMR. *Biochimica et Biophysica Acta*, 1758(9):1330–1342, 2006.
- [56] S. Afonin, S. L. Grage, M. Ieronimo, P. Wadhvani, and A. S. Ulrich. Temperature-dependent transmembrane insertion of the amphiphilic peptide PGLa in lipid bilayers observed by solid state  $^{19}\text{F}$ -NMR spectroscopy. *Journal of the American Chemical Society*, 130(49):16512–16514, 2008.
- [57] P. Tremouilhac, E. Strandberg, P. Wadhvani, and A. S. Ulrich. Synergistic transmembrane alignment of the antimicrobial heterodimer PGLa/magainin. *Journal of Biological Chemistry*, 281(43):32089–32094, 2006.
- [58] E. S. Salnikov and B. Bechinger. Lipid-controlled peptide topology and interactions in bilayers: structural insights into the synergistic enhancement of the antimicrobial activities of PGLa and magainin 2. *Biophysical Journal*, 100(6):1473–80, 2011.
- [59] E. Strandberg, J. Zerweck, P. Wadhvani, and A. S. Ulrich. Synergistic insertion of antimicrobial magainin-family peptides in membranes depends on the lipid spontaneous curvature. *Biophysical Journal*, 104(6):L9–11, 2013.
- [60] J. P. Ulmschneider, J. C. Smith, M. B. Ulmschneider, A. S. Ulrich, and E. Strandberg. Reorientation and dimerization of the membrane-bound anti-

- crobial peptide PGLa from microsecond all-atom MD simulations. *Biophysical Journal*, 103(3):472–482, 2012.
- [61] M. Zasloff. Magainins, a class of antimicrobial peptides from *Xenopus* skin: isolation, characterization of two active forms, and partial cDNA sequence of a precursor. *Proceedings of the National Academy of Sciences, USA*, 84(15):5449–53, 1987.
- [62] I. Harjunpää, P. Kuusela, M. T. Smoluch, J. Silberring, H. Lankinen, and D. Wade. Comparison of synthesis and antibacterial activity of temporin A. *FEBS Letters*, 449(2-3):187–190, 1999.
- [63] O. Simonetti, O. Cirioni, G. Goteri, R. Ghiselli, W. Kamysz, E. Kamysz, C. Silvestri, F. Orlando, C. Barucca, A. Scalise, V. Saba, G. Scalise, A. Giacometti, and A. Offidani. Temporin A is effective in MRSA-infected wounds through bactericidal activity and acceleration of wound repair in a murine model. *Peptides*, 29(4):520–8, 2008.
- [64] A. Landa, L. Jiménez, K. Willms, L. F. Jiménez-García, R. Lara-Martínez, L. Robert, O. Cirioni, W. Barañska-Rybak, and W. Kamysz. Antimicrobial peptides (Temporin A and Iseganan IB-367): effect on the cysticerci of *Taenia crassiceps*. *Molecular and Biochemical Parasitology*, 164(2):126–30, 2009.
- [65] D. Tiltak. *Strukturelle und funktionelle Untersuchungen der antimikrobiellen Peptide MSI-103 und Temporin A*. PhD thesis, Karlsruher Institut für Technologie (KIT), Universitätsbereich, 2009.
- [66] G. F. Gause and M. G. Brazhnikova. Gramicidin S. Origin and mode of action. *Lancet*, 247:715–716, 1944.
- [67] G. G. Gause and M. G. Brazhnikova. Gramicidin S and its use in the treatment of infected wounds. *Nature*, 154:703, 1944.
- [68] T. Katsu, H. Kobayashi, and Y. Fujita. Mode of action of gramicidin S on *Escherichia coli* membrane. *Biochimica et Biophysica Acta*, 860(3):608–619, 1986.
- [69] Y. Tanimoto. Permeability of dormant spores of *Bacillus subtilis* to gramicidin S. *FEMS Microbiology Letters*, 136(2):151–156, 1996.

- [70] T. Katsu, C. Ninomiya, M. Kuroko, H. Kobayashi, T. Hirota, and Y. Fujita. Action mechanism of amphipathic peptides gramicidin S and melittin on erythrocyte membrane. *Biochimica et Biophysica Acta*, 939(1):57–63, 1988.
- [71] T. Katsu, M. Kuroko, T. Morikawa, K. Sanchika, Y. Fujita, H. Yamamura, and M. Uda. Mechanism of membrane damage induced by the amphipathic peptides gramicidin S and melittin. *Biochimica et Biophysica Acta*, 983(2):135–141, 1989.
- [72] R. Conden, A. H. Gordon, A. J. Martin, and R. L. M. Synge. Gramicidin S: the sequence of the amino-acid residues. *The Biochemical Journal*, 41(4):596–602, 1947.
- [73] D. C. Hodgkin and B. M. Oughton. Possible molecular models for gramicidin S and their relationship to present ideas of protein structure. *The Biochemical Journal*, 65(4):752–6, 1957.
- [74] Y. Xu, I. P. Sugar, and N. R. Krishna. A variable target intensity-restrained global optimization (VARTIGO) procedure for determining three-dimensional structures of polypeptides from NOESY data: application to gramicidin S. *Journal of Biomolecular NMR*, 5(1):37–48, 1995.
- [75] G. Nemethy and H. A. Scheraga. Hydrogen bonding involving the ornithine side chain of gramicidin S. *Biochemical and Biophysical Research Communications*, 118(2):643–647, 1984.
- [76] D. Mihailescu and J. C. Smith. Molecular dynamics simulation of the cyclic decapeptide antibiotic, gramicidin S, in dimethylsulfoxide solution. *Journal of Physical Chemistry B*, 103(9):1586–1594, 1999.
- [77] D. Mihailescu and J. C. Smith. Atomic detail peptide-membrane interactions: molecular dynamics simulation of gramicidin S in a DMPC bilayer. *Biophysical Journal*, 79(4):1718–30, 2000.
- [78] J. Salgado, S. L. Grage, L. H. Kondejewski, R. S. Hodges, R. N. McElhaney, and A. S. Ulrich. Membrane-bound structure and alignment of the antimicrobial  $\beta$ -sheet peptide gramicidin S derived from angular and distance constraints by solid state  $^{19}\text{F}$ -NMR. *Journal of Biomolecular NMR*, 21(3):191–208, 2001.
- [79] A. L. Llamas-Saiz, G. M. Grotenbreg, M. Overhand, and M. J. van Raaij. Double-stranded helical twisted  $\beta$ -sheet channels in crystals of gramicidin S

- grown in the presence of trifluoroacetic and hydrochloric acids. *Acta Crystallographica. Section D, Biological Crystallography*, 63(Pt 3):401–7, 2007.
- [80] S. Afonin, U. H. N. Dürr, P. Wadhvani, J. B. Salgado, and A. S. Ulrich. Solid state NMR structure analysis of the antimicrobial peptide gramicidin S in lipid membranes: concentration-dependent re-alignment and self-assembly as a  $\beta$ -barrel. *Topics in Current Chemistry*, 273:139–154, 2008.
- [81] C. S. Alves, M. N. Melo, H. G. Franquelim, R. Ferre, M. Planas, L. Feliu, E. Bardaji, W. Kowalczyk, D. Andreu, N. C. Santos, M. X. Fernandes, and M. A. Castanho. *Escherichia coli* cell surface perturbation and disruption induced by antimicrobial peptides BP100 and pepR. *Journal of Biological Chemistry*, 285(36):27536–27544, 2010.
- [82] E. Strandberg, D. Tiltak, M. Ieronimo, N. Kanithasen, P. Wadhvani, and A. S. Ulrich. Influence of C-terminal amidation on the antimicrobial and hemolytic activities of cationic  $\alpha$ -helical peptides. *Pure and Applied Chemistry*, 79(4):717–728, 2007.
- [83] J. P. M. Jämbeck and A. P. Lyubartsev. Derivation and systematic validation of a refined all-atom force field for phosphatidylcholine lipids. *Journal of Physical Chemistry B*, 116(10):3164–79, 2012.
- [84] S. Lifson. Consistent force field for calculations of conformations, vibrational spectra, and enthalpies of cycloalkane and n-alkane molecules. *The Journal of Chemical Physics*, 49(11):5116, 1968.
- [85] T. Darden, D. York, and L. Pedersen. Particle mesh Ewald: An N-log(N) method for Ewald sums in large systems. *The Journal of Chemical Physics*, 98(12):10089, 1993.
- [86] R. Hockney, S. Goel, and J. Eastwood. Quiet high-resolution computer models of a plasma. *Journal of Computational Physics*, 14(2):148–158, 1974.
- [87] D. van der Spoel, E. Lindahl, B. Hess, A. R. van Buuren, P. J. Apol, E. Meulenhoff, D. P. Tieleman, A. L. T. M. Sijbers, K. A. Feenstra, R. van Drunen, and H. J. C. Berendsen. Gromacs user manual version 4.5.4, [www.gromacs.org](http://www.gromacs.org) (2010).
- [88] M. H. Levitt. *Spin Dynamics - Basics of Nuclear Magnetic Resonance*. WILEY, 2009.

- [89] A. W. Hing, S. P. Adams, D. F. Silbert, and R. E. Norberg. Deuterium NMR of Val1...(2-<sup>2</sup>H)Ala3...gramicidin A in oriented DMPC bilayers. *Biochemistry*, 29(17):4144–56, 1990.
- [90] J. H. Davis. The description of membrane lipid conformation, order and dynamics by <sup>2</sup>H-NMR. *Biochimica et Biophysica Acta*, 737(1):117–171, 1983.
- [91] P. Wadhvani, E. Strandberg, N. Heidenreich, J. Bürck, S. Fanghänel, and A. S. Ulrich. Self-assembly of flexible  $\beta$ -strands into immobile amyloid-like  $\beta$ -sheets in membranes as revealed by solid-state <sup>19</sup>F NMR. *Journal of the American Chemical Society*, 134(15):6512–6515, 2012.
- [92] S. Pronk, S. Pall, R. Schulz, P. Larsson, P. Bjelkmar, R. Apostolov, M. R. Shirts, J. C. Smith, P. M. Kasson, D. van der Spoel, B. Hess, and E. Lindahl. GROMACS 4.5: a high-throughput and highly parallel open source molecular simulation toolkit. *Bioinformatics*, 29(7):845–854, 2013.
- [93] B. Hess, H. Bekker, H. J. C. Berendsen, and J. G. E. M. Fraaije. LINCS: A linear constraint solver for molecular simulations. *Journal of Computational Chemistry*, 18(12):1463–1472, 1997.
- [94] S. Nosé. A molecular dynamics method for simulations in the canonical ensemble. *Molecular Physics*, 52(2):255–268, 1984.
- [95] M. Parrinello and A. Rahman. Polymorphic transitions in single crystals: A new molecular dynamics method. *Journal of Applied Physics*, 52(12):7182, 1981.
- [96] W. L. Jorgensen, J. Chandrasekhar, J. D. Madura, R. W. Impey, and M. L. Klein. Comparison of simple potential functions for simulating liquid water. *The Journal of Chemical Physics*, 79(2):926–935, 1983.
- [97] K. Lindorff-Larsen, S. Piana, K. Palmo, P. Maragakis, J. L. Klepeis, R. O. Dror, and D. E. Shaw. Improved side-chain torsion potentials for the Amber ff99SB protein force field. *Proteins*, 78(8):1950–1958, 2010.
- [98] D. A. Case, T. A. Darden, T. E. Cheatham III, C. L. Simmerling, J. Wang, R. E. Duke, R. Luo, R. C. Walker, W. Zhang, K. M. Merz, B. Roberts, S. Hayik, A. Roitberg, G. Seabra, J. Swails, A. W. Goetz, I. Kolossváry, K. F. Wong, F. Paesani, J. Vanicek, R. M. Wolf, J. Liu, X. Wu, S. R. Brozell, T. Steinbrecher, H. Gohlke, Q. Cai, X. Ye, M.-J. Hsieh, G. Cui, D. R. Roe, D. H.

- Mathews, M. G. Seetin, R. Salomon-Ferrer, C. Sagui, V. Babin, T. Luchko, S. Gusarov, A. Kovalenko, and P. A. Kollman. AMBER 12, University of California, San Francisco, 2012.
- [99] S. Afonin, P. K. Mikhailiuk, I. V. Komarov, and A. S. Ulrich. Evaluating the amino acid CF<sub>3</sub>-bicyclopentylglycine as a new label for solid-state <sup>19</sup>F-NMR structure analysis of membrane-bound peptides. *Journal of Peptide Science*, 13:614–623, 2007.
- [100] E. Soravia, G. Martini, and M. Zasloff. Antimicrobial properties of peptides from *Xenopus* granular gland secretions. *FEBS Letters*, 228(2):337–340, 1988.
- [101] E. Strandberg, D. Tiltak, S. Ehni, P. Wadhvani, and A. S. Ulrich. Lipid shape is a key factor for membrane interactions of amphipathic helical peptides. *Biochimica et Biophysica Acta*, 1818:1764–1776, 2012.
- [102] J. P. Ulmschneider, J. P. F. Doux, J. A. Killian, J. C. Smith, and M. B. Ulmschneider. Peptide partitioning and folding into lipid bilayers. *Journal of Chemical Theory and Computation*, 5(9):2202–2205, 2009.
- [103] Y. Wang, D. E. Schlamadinger, J. E. Kim, and J. A. McCammon. Comparative molecular dynamics simulations of the antimicrobial peptide CM15 in model lipid bilayers. *Biochimica et Biophysica Acta*, 1818(5):1402–1409, 2012.
- [104] S. Toraya, N. Javkhlantugs, D. Mishima, K. Nishimura, K. Ueda, and A. Naito. Dynamic structure of bombolitin II bound to lipid bilayers as revealed by solid-state NMR and molecular-dynamics simulation. *Biophysical Journal*, 99(10):3282–3289, 2010.
- [105] S. K. Kandasamy and R. G. Larson. Effect of salt on the interactions of antimicrobial peptides with zwitterionic lipid bilayers. *Biochimica et Biophysica Acta*, 1758(9):1274–1284, 2006.
- [106] B. L. Kagan, H. Jang, R. Capone, F. Teran Arce, S. Ramachandran, R. Lal, and R. Nussinov. Antimicrobial properties of amyloid peptides. *Molecular Pharmaceutics*, 9(4):708–717, 2012.
- [107] M. Mihajlovic and T. Lazaridis. Antimicrobial peptides bind more strongly to membrane pores. *Biochimica et Biophysica Acta*, 1798(8):1494–1502, 2010.
- [108] M. B. Ulmschneider, J. P. Doux, J. A. Killian, J. C. Smith, and J. P. Ulmschneider. Mechanism and kinetics of peptide partitioning into membranes

- from all-atom simulations of thermostable peptides. *Journal of the American Chemical Society*, 132(10):3452–3460, 2010.
- [109] S. L. Grage, S. Afonin, and A. S. Ulrich. Dynamic transitions of membrane-active peptides. *Methods in Molecular Biology*, 618:183–207, 2010.
- [110] Q. Du, P. G. Mezey, and K. C. Chou. Heuristic molecular lipophilicity potential (HMLP): a 2D-QSAR study to LADH of molecular family pyrazole and derivatives. *Journal of Computational Chemistry*, 26(5):461–470, 2005.
- [111] R. G. Efremov, A. O. Chugunov, T. V. Pyrkov, J. P. Priestle, A. S. Arseniev, and E. Jacoby. Molecular lipophilicity in protein modeling and drug design. *Current Medicinal Chemistry*, 14(4):393–415, 2007.
- [112] W. C. Wimley, T. P. Creamer, and S. H. White. Solvation energies of amino acid side chains and backbone in a family of host-guest pentapeptides. *Biochemistry*, 35(16):5109–5124, 1996.
- [113] W. C. Wimley and S. H. White. Experimentally determined hydrophobicity scale for proteins at membrane interfaces. *Nature Structural Biology*, 3(10):842–848, 1996.
- [114] D. M. Engelman, T. A. Steitz, and A. Goldman. Identifying nonpolar transbilayer helices in amino acid sequences of membrane proteins. *Annual Review of Biophysics and Biophysical Chemistry*, 15:321–353, 1986.
- [115] J. Kyte and R. F. Doolittle. A simple method for displaying the hydrophobic character of a protein. *Journal of Molecular Biology*, 157(1):105–132, 1982.
- [116] S. A. Wildman and G. M. Crippen. Prediction of physicochemical parameters by atomic contributions. *Journal of Chemical Information and Computer Sciences*, 39(5):868–873, 1999.
- [117] C. Snider, S. Jayasinghe, K. Hristova, and S. H. White. MPEx: a tool for exploring membrane proteins. *Protein Science*, 18(12):2624–8, 2009.
- [118] D. Eisenberg, R. M. Weiss, and T. C. Terwilliger. The helical hydrophobic moment: a measure of the amphiphilicity of a helix. *Nature*, 299(5881):371–374, 1982.
- [119] D. Eisenberg, R. M. Weiss, T. C. Terwilliger, and W. Wilcox. Hydrophobic moments and protein structure. *Faraday Symposia of the Chemical Society*, (17):109–120, 1982.

- [120] T. Beuming and H. Weinstein. A knowledge-based scale for the analysis and prediction of buried and exposed faces of transmembrane domain proteins. *Bioinformatics*, 20(12):1822–1835, 2004.
- [121] S. B. Vik. The transmembrane helices of the L, M, and N subunits of Complex I from *E. coli* can be assigned on the basis of conservation and hydrophobic moment analysis. *FEBS Letters*, 585(8):1180–1184, 2011.
- [122] S. L. Grage, A. V. Suleymanova, S. Afonin, P. Wadhvani, and A. S. Ulrich. Solid state NMR analysis of the dipolar couplings within and between distant  $\text{CF}_3$ -groups in a membrane-bound peptide. *Journal of Magnetic Resonance*, 183(1):77–86, 2006.
- [123] A. D. Mackerell, M. Feig, and C. L. Brooks. Extending the treatment of backbone energetics in protein force fields: limitations of gas-phase quantum mechanics in reproducing protein conformational distributions in molecular dynamics simulations. *Journal of Computational Chemistry*, 25(11):1400–15, 2004.
- [124] J. B. Klauda, R. M. Venable, J. A. Freites, J. W. O'Connor, D. J. Tobias, C. Mondragon-Ramirez, I. Vorobyov, A. D. MacKerell, and R. W. Pastor. Update of the CHARMM all-atom additive force field for lipids: validation on six lipid types. *The Journal of Physical Chemistry B*, 114(23):7830–43, 2010.
- [125] H. J. C. Berendsen, J. P. M. Postma, W. F. van Gunsteren, A. DiNola, and J. R. Haak. Molecular dynamics with coupling to an external bath. *The Journal of Chemical Physics*, 81(8):3684, 1984.
- [126] D. Sitkoff, K. A. Sharp, and B. Honig. Accurate calculation of hydration free energies using macroscopic solvent models. *Journal of Physical Chemistry*, 98(7):1978–1988, 1994.
- [127] S. Decherchi and W. Rocchia. A general and robust ray-casting-based algorithm for triangulating surfaces at the nanoscale. *PLoS One*, 8(4), 2013.
- [128] D. Sept, N. Baker, M. Holst, and J. A. McCammon. Electrostatic contributions to the structure and dynamics of microtubules. *Biophysical Journal*, 80(1):99a–99a, 2001.
- [129] A. Latal, G. Degovics, R. F. Epanand, R. M. Epanand, and K. Lohner. Structural aspects of the interaction of peptidyl-glycylleucine-carboxamide, a highly po-

- tent antimicrobial peptide from frog skin, with lipids. *European Journal of Biochemistry*, 248(3):938–946, 1997.
- [130] E. Strandberg, S. Esteban-Martín, A. S. Ulrich, and J. Salgado. Hydrophobic mismatch of mobile transmembrane helices: merging theory and experiments. *Biochimica et Biophysica Acta*, 1818(5):1242–1249, 2012.
- [131] C. Muhle-Goll, S. Hoffmann, S. Afonin, S. L. Grage, A. A. Polyansky, D. Windisch, M. Zeitler, J. Bürck, and A. S. Ulrich. Hydrophobic matching controls the tilt and stability of the dimeric platelet-derived growth factor receptor (PDGFR) b transmembrane segment. *Journal of Biological Chemistry*, 287(31):26178–26186, 2012.
- [132] S. Afonin, R. W. Glaser, C. Sachse, J. Salgado, P. Wadhvani, and A. S. Ulrich. <sup>19</sup>f nmr screening of unrelated antimicrobial peptides shows that membrane interactions are largely governed by lipids. *Biochimica et Biophysica Acta*, 1838(9):2260–2268, 2014.
- [133] R. Ditchfield, W. J. Hehre, and J. A. Pople. Self-consistent molecular-orbital methods. ix. an extended gaussian-type basis for molecular-orbital studies of organic molecules. *The Journal of Chemical Physics*, 54(2):724–728, 1971.
- [134] M. J. Frisch, G. W. Trucks, H. B. Schlegel, G. E. Scuseria, M. A. Robb, J. R. Cheeseman, J. A. Montgomery, Jr., T. Vreven, K. N. Kudin, J. C. Burant, J. M. Millam, S. S. Iyengar, J. Tomasi, V. Barone, B. Mennucci, M. Cossi, G. Scalmani, N. Rega, G. A. Petersson, H. Nakatsuji, M. Hada, M. Ehara, K. Toyota, R. Fukuda, J. Hasegawa, M. Ishida, T. Nakajima, Y. Honda, O. Kitao, H. Nakai, M. Iene, X. Li, J. E. Knox, H. P. Hratchian, J. B. Cross, V. Bakken, C. Adamo, J. Jaramillo, R. Gomperts, R. E. Stratmann, O. Yazyev, A. J. Austin, R. Cammi, C. Pomelli, J. W. Ochterski, P. Y. Ayala, K. Morokuma, G. A. Voth, P. Salvador, J. J. Dannenberg, V. G. Zakrzewski, S. Dapprich, A. D. Daniels, M. C. Strain, O. Farkas, D. K. Malick, A. D. Rabuck, K. Raghavachari, J. B. Foresman, J. V. Ortiz, Q. Cui, A. G. Baboul, S. Clifford, J. Cioslowski, B. B. Stefanov, G. Liu, A. Liashenko, P. Piskorz, I. Komaromi, R. L. Martin, D. J. Fox, T. Keith, M. A. Al-Laham, C. Y. Peng, A. Nanayakkara, M. Challacombe, P. M. W. Gill, B. Johnson, W. Chen, M. W. Wong, C. Gonzalez, and J. A. Pople. Gaussian 03, Revision C.02. Gaussian, Inc., Wallingford, CT, 2004.

- [135] C. I. Bayly, P. Cieplak, W. Cornell, and P. A. Kollman. A well-behaved electrostatic potential based method using charge restraints for deriving atomic charges: the RESP model. *The Journal of Physical Chemistry*, 97(40):10269–10280, 1993.
- [136] J. Wang, R. M. Wolf, J. W. Caldwell, P. A. Kollman, and D. A. Case. Development and testing of a general amber force field. *Journal of Computational Chemistry*, 25(9):1157–74, 2004.
- [137] N. Homeyer, A. H. C. Horn, H. Lanig, and H. Sticht. AMBER force-field parameters for phosphorylated amino acids in different protonation states: phosphoserine, phosphothreonine, phosphotyrosine, and phosphohistidine. *Journal of Molecular Modeling*, 12(3):281–9, 2006.
- [138] G. Bussi, D. Donadio, and M. Parrinello. Canonical sampling through velocity rescaling. *The Journal of Chemical Physics*, 126(1):014101, 2007.
- [139] G. Ross. Algorithm as 15: Single linkage cluster analysis. *Journal of the Royal Statistical Society*, 18(1):106–110, 1969.
- [140] F. M. Richards. Areas, volumes, packing and protein structure. *Annual Review of Biophysics and Bioengineering*, 6:151–76, 1977.
- [141] S. Reißer, E. Strandberg, T. Steinbrecher, and A. Ulrich. 3D Hydrophobic moment vectors as a tool to characterize the surface polarity of amphiphilic peptides. *Biophysical Journal*, 106(11):2385–2394, 2014.
- [142] U. H. N. Dürr, S. L. Grage, R. Witter, and A. S. Ulrich. Solid state  $^{19}\text{F}$  NMR parameters of fluorine-labeled amino acids. Part I: Aromatic substituents. *Journal of Magnetic Resonance*, 191(1):7–15, 2008.
- [143] D. Maisch, P. Wadhvani, S. Afonin, C. Böttcher, B. Koksche, and A. S. Ulrich. Chemical labeling strategy with (R)- and (S)-trifluoromethylalanin for solid state  $^{19}\text{F}$  NMR analysis of peptaibols in membranes. *Journal of the American Chemical Society*, 131:15596–15597, 2009.
- [144] R. Witter, F. Nozirov, U. Sternberg, T. A. Cross, A. S. Ulrich, and R. Fu. Solid-state  $^{19}\text{F}$  NMR spectroscopy reveals that Trp41 participates in the gating mechanism of the M2 proton channel of influenza A virus. *Journal of the American Chemical Society*, 130(3):918–924, 2008.

- [145] S. L. Grage, U. H. N. Dürr, S. Afonin, P. K. Mikhailiuk, I. V. Komarov, and A. S. Ulrich. Solid state  $^{19}\text{F}$  NMR parameters of fluorine-labeled amino acids. Part II: aliphatic substituents. *Journal of Magnetic Resonance*, 191(1):16–23, 2008.
- [146] K. Koch, S. Afonin, M. Ieronimo, M. Berditsch, and A. S. Ulrich. Solid-state  $^{19}\text{F}$ -NMR of peptides in native membranes. *Topics in Current Chemistry*, 306:89–118, 2012.
- [147] P. Wadhvani, J. Bürck, E. Strandberg, C. Mink, S. Afonin, and A. S. Ulrich. Using a sterically restrictive amino acid as a  $^{19}\text{F}$ -NMR label to monitor and control peptide aggregation in membranes. *Journal of the American Chemical Society*, 130:16515–16517, 2008.
- [148] S. Afonin, U. H. N. Dürr, R. W. Glaser, and A. S. Ulrich. 'Boomerang'-like insertion of a fusogenic peptide in a lipid membrane revealed by solid-state  $^{19}\text{F}$  NMR. *Magnetic Resonance in Chemistry*, 42(2):195–203, 2004.
- [149] C. Branden and J. Tooze. *Introduction to protein structure*. Garland Publishing, Inc., 1999.

## A. Membrane simulations of helical peptides

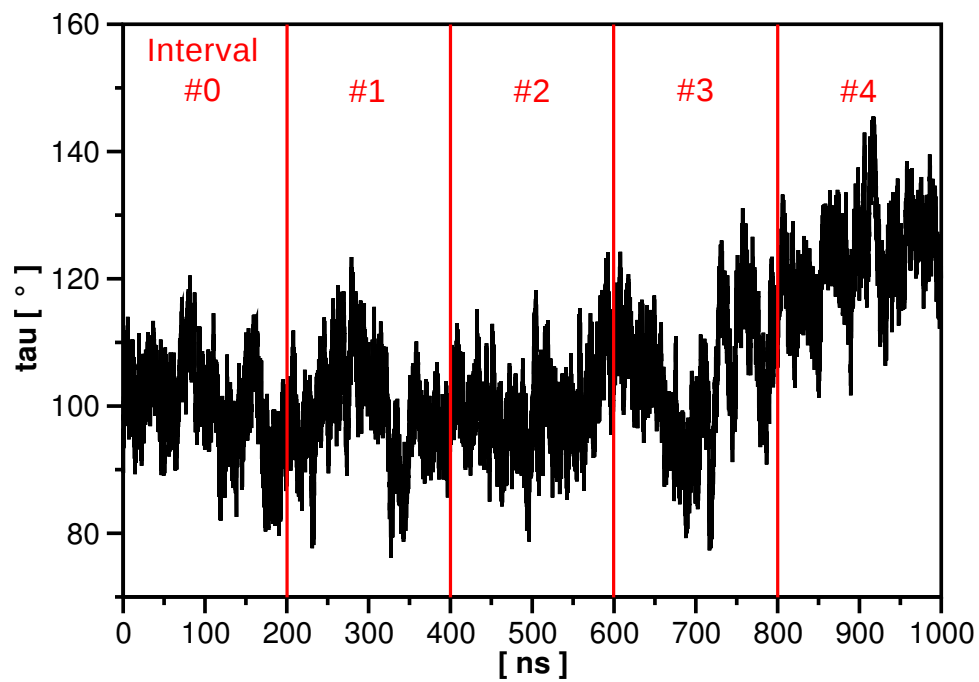


Figure A.1: The tilt angle  $\tau$  of PGLa, measured for the helical region from positions 2-17. The individually evaluated intervals are shown in red. Interval #0 is omitted in the evaluations, to ensure the system is well equilibrated.

Table A.1: Splittings  $\Delta\nu_q$  calculated from the simulations, averaged over intervals #1-4. Only the splittings from the helical part of the peptides are shown.

Position	PGLa <sup>a</sup>	PGLa <sup>b</sup>	MSI-103	KIA14	Mag2
2	-9.8 ± 21.4	-6.1 ± 19.0			
3	-26.5 ± 16.0	-21.6 ± 16.6	-33.3 ± 10.2	-31.4 ± 12.7	17.8 ± 22.6
4	51.2 ± 19.7	45.7 ± 19.6	56.7 ± 17.6	54.5 ± 18.9	-8.6 ± 22.3
5	-20.5 ± 19.3	-23.7 ± 15.2	-33.4 ± 10.2	-33.6 ± 9.9	24.5 ± 21.2
6	10.2 ± 24.0	22.2 ± 17.8	11.0 ± 21.6	24.8 ± 22.3	-31.3 ± 13.0
7	-19.9 ± 20.4	-26.1 ± 15.8	3.7 ± 25.8	-20.2 ± 20.7	46.6 ± 16.9
8	52.4 ± 21.6	49.6 ± 17.8	10.2 ± 27.7	31.6 ± 27.3	-34.6 ± 9.4
9	-30.5 ± 13.0	-30.2 ± 11.9	1.4 ± 23.5	-13.7 ± 23.1	28.4 ± 19.2
10	-12.9 ± 20.7	-2.3 ± 18.9	-28.9 ± 14.7	-13.1 ± 22.6	-15.2 ± 18.2
11	39.5 ± 22.9	33.0 ± 21.9	50.2 ± 18.7		14.2 ± 24.0
12	-1.9 ± 25.4	-8.1 ± 20.2	-33.3 ± 11.1		9.8 ± 20.8
13	7.1 ± 26.7	19.5 ± 18.8	30.9 ± 18.9		-26.6 ± 15.8
14	-35.6 ± 8.9	-36.0 ± 7.8	-24.9 ± 16.4		
15	58.7 ± 18.4	52.2 ± 15.3	28.5 ± 25.9		
16	-30.0 ± 14.7	-33.9 ± 10.5	-9.4 ± 24.9		
17	2.9 ± 29.9	21.7 ± 21.3	-8.5 ± 21.4		

<sup>a</sup> For PGLa, averaged over intervals #1-4.

<sup>b</sup> For PGLa, averaged over intervals #1-2.

Table A.2: Splittings and structural parameters obtained from the simulation of PGLa, for the four different intervals. The angles  $\beta$ ,  $\alpha$  and  $\theta$  have been calculated only for the helical part of the peptide from position 2-17.

residue	$\Delta\nu$				$\beta$				$\alpha$				$\theta_{i,i+1}$				$\Delta\delta_{i,i+1}$			
	200-400 ns	400-600 ns	600-800 ns	800-1000 ns	200-400 ns	400-600 ns	600-800 ns	800-1000 ns	200-400 ns	400-600 ns	600-800 ns	800-1000 ns	200-400 ns	400-600 ns	600-800 ns	800-1000 ns	200-400 ns	400-600 ns	600-800 ns	800-1000 ns
1 G	-26.8 $\pm 16.1$	-23.6 $\pm 16.7$	-27.2 $\pm 17.2$	-28.6 $\pm 17.1$	-	-	-	-	-	-	-	-	-	-	-	-	-	-	-	-
2 M	-2.9 $\pm 19.4$	-9.2 $\pm 18.1$	-2.0 $\pm 21.5$	-25.1 $\pm 18.0$	123.7 $\pm 8.4$	123.5 $\pm 8.0$	122.0 $\pm 8.7$	118.0 $\pm 11.7$	43.6 $\pm 15.8$	39.0 $\pm 16.7$	35.5 $\pm 20.7$	27.4 $\pm 18.0$	108.1 $\pm 22.1$	104.2 $\pm 18.5$	100.2 $\pm 26.2$	86.3 $\pm 20.9$	95.9 $\pm 13.6$	96.2 $\pm 13.3$	93.7 $\pm 14.5$	89.8 $\pm 16.6$
3 A	-23.8 $\pm 16.8$	-19.4 $\pm 16.2$	-30.2 $\pm 13.4$	-32.6 $\pm 13.7$	122.6 $\pm 7.8$	122.2 $\pm 7.5$	118.8 $\pm 8.4$	116.7 $\pm 9.1$	31.4 $\pm 9.5$	31.0 $\pm 8.9$	28.9 $\pm 9.3$	31.0 $\pm 8.0$	87.7 $\pm 10.5$	87.1 $\pm 9.6$	84.8 $\pm 13.8$	84.3 $\pm 7.9$	97.5 $\pm 13.1$	98.2 $\pm 12.9$	98.7 $\pm 16.0$	96.5 $\pm 13.0$
4 S	48.0 $\pm 20.2$	43.4 $\pm 18.8$	58.7 $\pm 17.6$	54.6 $\pm 18.6$	117.7 $\pm 7.1$	118.1 $\pm 6.1$	119.6 $\pm 7.4$	121.6 $\pm 7.0$	41.3 $\pm 8.0$	42.2 $\pm 7.4$	42.9 $\pm 8.5$	43.1 $\pm 7.8$	96.1 $\pm 5.8$	97.2 $\pm 5.4$	96.9 $\pm 8.5$	102.3 $\pm 8.7$	97.6 $\pm 12.0$	98.4 $\pm 12.3$	99.2 $\pm 14.8$	103.8 $\pm 13.7$
5 K	-25.7 $\pm 14.2$	-21.7 $\pm 15.8$	-29.5 $\pm 13.3$	-5.1 $\pm 22.7$	123.8 $\pm 6.8$	124.9 $\pm 6.6$	126.0 $\pm 10.2$	127.4 $\pm 6.7$	42.8 $\pm 7.0$	43.4 $\pm 7.5$	45.1 $\pm 7.8$	44.7 $\pm 7.7$	111.9 $\pm 6.8$	112.0 $\pm 6.1$	112.9 $\pm 12.8$	106.6 $\pm 7.4$	108.0 $\pm 11.2$	107.4 $\pm 11.2$	108.0 $\pm 12.7$	103.1 $\pm 11.7$
6 A	21.3 $\pm 19.3$	23.2 $\pm 16.2$	10.9 $\pm 21.3$	-14.5 $\pm 17.8$	123.8 $\pm 5.8$	122.7 $\pm 5.3$	121.6 $\pm 5.8$	118.8 $\pm 6.7$	38.8 $\pm 7.5$	38.9 $\pm 7.2$	40.3 $\pm 9.1$	41.1 $\pm 7.0$	98.5 $\pm 6.6$	99.2 $\pm 6.2$	98.9 $\pm 8.4$	103.8 $\pm 7.6$	105.3 $\pm 12.3$	104.6 $\pm 12.4$	102.8 $\pm 12.2$	103.2 $\pm 12.1$
7 G	-23.7 $\pm 16.8$	-28.6 $\pm 14.3$	-10.1 $\pm 24.9$	-17.3 $\pm 19.1$	120.7 $\pm 6.2$	120.6 $\pm 6.3$	119.0 $\pm 6.6$	121.8 $\pm 6.0$	45.7 $\pm 9.5$	44.2 $\pm 9.1$	44.2 $\pm 9.5$	40.6 $\pm 10.2$	97.5 $\pm 8.6$	97.9 $\pm 8.6$	100.8 $\pm 11.4$	98.0 $\pm 7.5$	91.4 $\pm 12.3$	92.5 $\pm 12.4$	92.5 $\pm 12.6$	96.3 $\pm 13.6$
8 A	48.2 $\pm 18.9$	51.0 $\pm 16.5$	42.7 $\pm 24.3$	67.8 $\pm 17.3$	123.0 $\pm 5.1$	124.2 $\pm 5.0$	125.1 $\pm 5.3$	126.8 $\pm 5.7$	39.5 $\pm 9.4$	38.8 $\pm 10.7$	35.8 $\pm 10.5$	38.8 $\pm 9.0$	100.5 $\pm 12.1$	97.8 $\pm 9.9$	94.2 $\pm 10.6$	87.6 $\pm 11.4$	98.3 $\pm 11.8$	98.1 $\pm 12.1$	98.3 $\pm 12.5$	91.6 $\pm 14.0$
9 I	-28.6 $\pm 12.8$	-31.9 $\pm 10.6$	-24.8 $\pm 16.7$	-36.8 $\pm 6.8$	122.0 $\pm 4.3$	122.7 $\pm 4.5$	122.7 $\pm 5.0$	119.5 $\pm 5.9$	37.3 $\pm 9.0$	39.2 $\pm 9.2$	40.0 $\pm 9.1$	42.8 $\pm 8.9$	99.3 $\pm 12.4$	99.5 $\pm 13.9$	95.3 $\pm 13.4$	103.9 $\pm 16.6$	104.5 $\pm 10.6$	104.2 $\pm 12.0$	102.4 $\pm 11.0$	105.1 $\pm 11.4$
10 A	-4.7 $\pm 19.5$	0.1 $\pm 18.0$	-17.2 $\pm 19.1$	-29.7 $\pm 10.4$	122.1 $\pm 4.2$	121.5 $\pm 4.5$	121.5 $\pm 4.5$	122.8 $\pm 4.1$	42.5 $\pm 9.0$	43.9 $\pm 10.4$	47.1 $\pm 10.6$	44.1 $\pm 10.3$	104.2 $\pm 11.4$	109.4 $\pm 20.9$	112.9 $\pm 16.1$	112.7 $\pm 13.2$	109.7 $\pm 12.2$	110.1 $\pm 13.2$	109.2 $\pm 12.6$	108.9 $\pm 12.4$
11 G	34.9 $\pm 22.3$	31.1 $\pm 21.3$	47.3 $\pm 22.1$	44.7 $\pm 21.6$	123.8 $\pm 5.4$	123.3 $\pm 5.4$	123.8 $\pm 5.6$	123.4 $\pm 5.8$	48.0 $\pm 9.9$	44.6 $\pm 12.5$	43.5 $\pm 11.9$	40.3 $\pm 10.0$	101.5 $\pm 10.2$	99.9 $\pm 11.9$	100.8 $\pm 12.7$	92.6 $\pm 8.8$	90.1 $\pm 12.4$	91.1 $\pm 12.1$	90.3 $\pm 12.4$	89.9 $\pm 11.8$

Table A.2: Splittings and structural parameters obtained from the simulation of PGLa, for the four different intervals. The angles  $\beta$ ,  $\alpha$  and  $\theta$  have been calculated only for the helical part of the peptide from position 2-17.

residue	$\Delta\nu$				$\beta$				$\alpha$				$\theta_{i,i+1}$				$\Delta\delta_{i,i+1}$			
	200-400 ns	400-600 ns	600-800 ns	800-1000 ns	200-400 ns	400-600 ns	600-800 ns	800-1000 ns	200-400 ns	400-600 ns	600-800 ns	800-1000 ns	200-400 ns	400-600 ns	600-800 ns	800-1000 ns	200-400 ns	400-600 ns	600-800 ns	800-1000 ns
12 K	-10.3 $\pm 19.8$	-5.8 $\pm 20.4$	-14.2 $\pm 20.7$	22.5 $\pm 22.8$	122.0 $\pm 4.8$	121.1 $\pm 6.2$	121.3 $\pm 5.5$	120.5 $\pm 4.8$	36.6 $\pm 8.4$	35.8 $\pm 8.3$	33.0 $\pm 9.6$	37.6 $\pm 6.7$	93.7 $\pm 8.3$	93.0 $\pm 8.1$	88.1 $\pm 9.7$	91.7 $\pm 7.1$	99.5 $\pm 10.6$	99.7 $\pm 10.4$	99.0 $\pm 11.7$	99.5 $\pm 10.3$
13 I	21.1 $\pm 18.5$	18.0 $\pm 19.0$	14.8 $\pm 23.1$	-25.6 $\pm 12.9$	120.1 $\pm 4.9$	120.4 $\pm 4.5$	119.2 $\pm 5.1$	120.9 $\pm 5.0$	42.5 $\pm 6.5$	42.5 $\pm 6.6$	43.8 $\pm 7.6$	45.4 $\pm 6.3$	101.2 $\pm 6.8$	102.7 $\pm 6.9$	103.2 $\pm 9.2$	109.9 $\pm 6.7$	95.5 $\pm 10.5$	98.2 $\pm 10.8$	98.5 $\pm 12.3$	101.3 $\pm 10.5$
14 A	-35.9 $\pm 8.5$	-36.1 $\pm 7.2$	-33.5 $\pm 11.6$	-36.8 $\pm 7.1$	123.3 $\pm 5.2$	123.7 $\pm 5.9$	124.8 $\pm 5.5$	125.0 $\pm 5.0$	36.8 $\pm 7.6$	38.0 $\pm 7.9$	39.1 $\pm 9.0$	36.8 $\pm 7.0$	104.3 $\pm 8.8$	103.8 $\pm 8.1$	106.8 $\pm 12.2$	99.3 $\pm 5.3$	107.5 $\pm 14.0$	106.9 $\pm 13.1$	110.5 $\pm 16.2$	103.9 $\pm 12.3$
15 K	50.7 $\pm 15.7$	53.7 $\pm 14.7$	54.0 $\pm 20.3$	76.5 $\pm 7.7$	125.4 $\pm 5.5$	124.4 $\pm 5.5$	122.4 $\pm 7.0$	120.8 $\pm 5.9$	40.0 $\pm 8.8$	41.1 $\pm 9.3$	42.9 $\pm 9.7$	41.4 $\pm 8.2$	85.2 $\pm 7.4$	86.3 $\pm 8.1$	88.7 $\pm 13.9$	89.7 $\pm 8.0$	90.2 $\pm 13.8$	90.1 $\pm 15.0$	93.1 $\pm 18.6$	85.8 $\pm 13.6$
16 V	-34.8 $\pm 10.2$	-33.0 $\pm 10.7$	-25.8 $\pm 20.0$	-26.5 $\pm 13.6$	110.8 $\pm 8.7$	109.5 $\pm 7.7$	107.4 $\pm 10.2$	111.9 $\pm 7.7$	44.9 $\pm 11.2$	44.9 $\pm 11.3$	47.4 $\pm 14.4$	37.5 $\pm 11.0$	115.8 $\pm 23.8$	119.9 $\pm 23.0$	129.3 $\pm 31.1$	111.5 $\pm 12.7$	101.6 $\pm 13.4$	99.6 $\pm 15.7$	96.0 $\pm 14.4$	105.5 $\pm 15.7$
17 A	22.0 $\pm 20.9$	21.4 $\pm 21.7$	-0.1 $\pm 26.4$	-31.8 $\pm 8.3$	121.0 $\pm 7.2$	121.2 $\pm 8.7$	122.7 $\pm 9.8$	129.9 $\pm 7.0$	30.7 $\pm 24.0$	24.6 $\pm 25.2$	14.1 $\pm 28.5$	31.4 $\pm 15.5$	-	-	-	-	-	-	-	-
18 L	-14.5 $\pm 21.1$	-19.9 $\pm 19.6$	-1.7 $\pm 29.8$	1.3 $\pm 22.1$	-	-	-	-	-	-	-	-	-	-	-	-	-	-	-	-
19 K	13.9 $\pm 25.3$	9.2 $\pm 27.0$	6.7 $\pm 37.7$	56.5 $\pm 17.1$	-	-	-	-	-	-	-	-	-	-	-	-	-	-	-	-
20 A	12.6 $\pm 26.8$	19.4 $\pm 28.5$	27.3 $\pm 36.0$	-36.1 $\pm 9.3$	-	-	-	-	-	-	-	-	-	-	-	-	-	-	-	-
21 L	-4.1 $\pm 29.7$	-0.4 $\pm 28.4$	-5.6 $\pm 34.7$	-36.0 $\pm 8.2$	-	-	-	-	-	-	-	-	-	-	-	-	-	-	-	-
Average residue 2-17																				
					121.6 $\pm 7.1$	121.5 $\pm 7.2$	121.1 $\pm 8.3$	121.6 $\pm 8.0$	40.1 $\pm 11.8$	39.5 $\pm 12.6$	39.0 $\pm 15.1$	39.0 $\pm 11.2$	100.4 $\pm 14.3$	100.7 $\pm 14.9$	100.9 $\pm 18.8$	98.7 $\pm 14.2$	99.5 $\pm 13.8$	99.7 $\pm 13.9$	99.5 $\pm 15.0$	99.0 $\pm 14.6$

Table A.3: Splittings and structural parameters obtained from the simulation of MSI-103, for the four different intervals. The angles  $\beta$ ,  $\alpha$  and  $\theta$  have been calculated only for the helical part of the peptide from position 3-17.

residue	$\Delta\nu$				$\beta$				$\alpha$				$\theta_{i,i+1}$				$\Delta\delta_{i,i+1}$			
	200-400 ns	400-600 ns	600-800 ns	800-1000 ns	200-400 ns	400-600 ns	600-800 ns	800-1000 ns	200-400 ns	400-600 ns	600-800 ns	800-1000 ns	200-400 ns	400-600 ns	600-800 ns	800-1000 ns	200-400 ns	400-600 ns	600-800 ns	800-1000 ns
1 K	-1.8 $\pm 34.4$	59.3 $\pm 16.6$	41.2 $\pm 32.6$	40.8 $\pm 29.1$	-	-	-	-	-	-	-	-	-	-	-	-	-	-	-	-
2 I	21.4 $\pm 24.3$	54.6 $\pm 17.3$	38.9 $\pm 26.8$	41.4 $\pm 23.0$	-	-	-	-	-	-	-	-	-	-	-	-	-	-	-	-
3 A	-32.8 $\pm 10.8$	-33.3 $\pm 9.7$	-35.3 $\pm 8.7$	-31.7 $\pm 11.0$	116.1 $\pm 9.2$	114.0 $\pm 11.6$	120.0 $\pm 9.8$	108.3 $\pm 13.2$	27.4 $\pm 13.2$	30.4 $\pm 11.9$	33.1 $\pm 11.4$	24.4 $\pm 15.1$	83.5 $\pm 15.3$	84.5 $\pm 14.1$	89.2 $\pm 15.7$	77.1 $\pm 20.4$	98.9 $\pm 13.8$	98.3 $\pm 12.7$	99.5 $\pm 15.4$	96.7 $\pm 14.9$
4 G	58.5 $\pm 15.8$	52.0 $\pm 18.2$	60.0 $\pm 17.5$	56.5 $\pm 17.4$	117.5 $\pm 8.2$	119.5 $\pm 7.9$	118.8 $\pm 7.7$	118.1 $\pm 9.8$	42.8 $\pm 8.8$	44.2 $\pm 8.7$	43.5 $\pm 8.8$	44.0 $\pm 8.9$	96.3 $\pm 8.9$	100.6 $\pm 10.2$	98.7 $\pm 9.8$	94.4 $\pm 16.6$	96.7 $\pm 13.5$	100.8 $\pm 15.0$	97.6 $\pm 14.8$	100.8 $\pm 18.8$
5 K	-36.6 $\pm 7.5$	-29.3 $\pm 12.1$	-33.9 $\pm 9.4$	-33.5 $\pm 9.9$	129.0 $\pm 8.5$	129.3 $\pm 8.6$	125.6 $\pm 8.0$	134.3 $\pm 13.8$	43.1 $\pm 8.5$	44.4 $\pm 9.5$	42.3 $\pm 8.0$	50.3 $\pm 19.5$	104.6 $\pm 7.8$	101.4 $\pm 7.2$	103.0 $\pm 6.8$	113.6 $\pm 22.3$	104.0 $\pm 12.8$	98.1 $\pm 14.2$	101.4 $\pm 13.3$	104.8 $\pm 19.9$
6 I	22.6 $\pm 20.4$	7.6 $\pm 20.3$	10.4 $\pm 19.2$	3.4 $\pm 21.7$	121.7 $\pm 6.4$	118.8 $\pm 6.8$	119.9 $\pm 6.5$	117.9 $\pm 7.3$	42.5 $\pm 7.1$	41.2 $\pm 7.0$	40.7 $\pm 7.3$	41.5 $\pm 7.1$	99.3 $\pm 5.6$	100.2 $\pm 5.4$	100.9 $\pm 5.6$	96.9 $\pm 10.1$	97.0 $\pm 10.9$	98.5 $\pm 12.0$	99.3 $\pm 11.1$	95.1 $\pm 12.1$
7 A	-16.1 $\pm 20.4$	13.0 $\pm 21.5$	3.0 $\pm 22.7$	15.0 $\pm 25.8$	117.6 $\pm 6.5$	119.1 $\pm 5.8$	119.5 $\pm 5.4$	113.0 $\pm 12.7$	40.2 $\pm 7.4$	39.5 $\pm 7.8$	39.1 $\pm 7.3$	39.7 $\pm 8.9$	106.8 $\pm 8.6$	105.0 $\pm 8.2$	104.3 $\pm 7.5$	113.7 $\pm 19.4$	98.9 $\pm 11.4$	99.7 $\pm 12.1$	100.0 $\pm 11.9$	99.4 $\pm 12.6$
8 K	27.3 $\pm 23.3$	-1.2 $\pm 23.0$	14.1 $\pm 29.0$	0.5 $\pm 24.8$	123.0 $\pm 6.2$	123.8 $\pm 6.2$	123.4 $\pm 5.4$	126.1 $\pm 7.2$	32.4 $\pm 9.7$	34.1 $\pm 9.6$	34.8 $\pm 9.0$	25.4 $\pm 19.9$	94.4 $\pm 10.2$	92.1 $\pm 9.7$	93.7 $\pm 8.4$	86.4 $\pm 11.8$	95.4 $\pm 13.3$	95.7 $\pm 14.1$	97.2 $\pm 13.5$	104.0 $\pm 23.1$
9 I	-13.3 $\pm 18.8$	11.4 $\pm 20.4$	0.3 $\pm 23.8$	7.2 $\pm 22.9$	120.7 $\pm 5.1$	120.8 $\pm 5.1$	120.9 $\pm 4.9$	123.0 $\pm 6.3$	33.4 $\pm 9.0$	37.8 $\pm 8.3$	38.2 $\pm 8.1$	43.0 $\pm 12.9$	91.2 $\pm 11.3$	92.4 $\pm 9.8$	94.7 $\pm 9.0$	81.1 $\pm 24.0$	107.1 $\pm 11.6$	102.7 $\pm 11.6$	103.3 $\pm 10.8$	93.9 $\pm 22.2$
10 A	-18.7 $\pm 17.9$	-33.9 $\pm 9.7$	-32.3 $\pm 10.5$	-30.4 $\pm 13.9$	122.5 $\pm 4.8$	123.2 $\pm 4.6$	123.4 $\pm 4.4$	118.3 $\pm 10.2$	49.4 $\pm 11.2$	48.2 $\pm 9.2$	46.9 $\pm 8.6$	55.7 $\pm 16.5$	115.3 $\pm 23.1$	110.8 $\pm 13.8$	109.9 $\pm 13.1$	138.8 $\pm 51.1$	112.0 $\pm 13.0$	108.6 $\pm 12.9$	108.6 $\pm 12.3$	117.6 $\pm 19.4$
11 G	48.4 $\pm 18.1$	51.9 $\pm 16.3$	55.4 $\pm 15.0$	45.1 $\pm 22.8$	122.7 $\pm 5.7$	123.6 $\pm 5.5$	123.1 $\pm 5.2$	123.6 $\pm 5.5$	46.1 $\pm 14.2$	46.0 $\pm 10.8$	45.6 $\pm 10.5$	34.5 $\pm 23.8$	107.7 $\pm 15.4$	103.3 $\pm 10.3$	102.9 $\pm 9.5$	88.6 $\pm 28.7$	93.5 $\pm 12.9$	90.8 $\pm 13.2$	91.8 $\pm 12.1$	86.1 $\pm 17.2$

Table A.3: Splittings and structural parameters obtained from the simulation of MSI-103, for the four different intervals. The angles  $\beta$ ,  $\alpha$  and  $\theta$  have been calculated only for the helical part of the peptide from position 3-17.

residue	$\Delta\nu$				$\beta$				$\alpha$				$\theta_{i,i+1}$				$\Delta\delta_{i,i+1}$			
	200-400 ns	400-600 ns	600-800 ns	800-1000 ns	200-400 ns	400-600 ns	600-800 ns	800-1000 ns	200-400 ns	400-600 ns	600-800 ns	800-1000 ns	200-400 ns	400-600 ns	600-800 ns	800-1000 ns	200-400 ns	400-600 ns	600-800 ns	800-1000 ns
12 K	-31.9 $\pm 12.2$	-35.7 $\pm 8.3$	-32.3 $\pm 11.2$	-33.2 $\pm 11.8$	118.7 $\pm 5.4$	119.6 $\pm 4.7$	120.3 $\pm 4.6$	114.0 $\pm 11.3$	31.9 $\pm 8.3$	33.4 $\pm 8.5$	34.5 $\pm 7.4$	31.8 $\pm 8.5$	91.0 $\pm 10.3$	91.2 $\pm 8.3$	91.8 $\pm 7.9$	86.8 $\pm 10.7$	97.8 $\pm 11.7$	98.1 $\pm 10.8$	96.4 $\pm 11.9$	94.4 $\pm 11.3$
13 I	35.3 $\pm 19.7$	31.6 $\pm 18.4$	27.4 $\pm 17.5$	29.3 $\pm 19.3$	118.1 $\pm 5.4$	119.3 $\pm 4.8$	118.7 $\pm 5.1$	119.2 $\pm 5.3$	38.6 $\pm 6.5$	40.3 $\pm 6.4$	39.2 $\pm 7.4$	39.4 $\pm 6.5$	101.0 $\pm 6.8$	101.3 $\pm 6.5$	102.1 $\pm 6.5$	103.5 $\pm 6.2$	100.5 $\pm 11.6$	100.8 $\pm 11.1$	102.5 $\pm 11.8$	104.8 $\pm 13.7$
14 A	-31.1 $\pm 12.4$	-22.9 $\pm 16.6$	-25.0 $\pm 15.8$	-20.8 $\pm 18.2$	126.2 $\pm 6.3$	125.8 $\pm 5.2$	125.5 $\pm 5.0$	131.3 $\pm 10.3$	38.1 $\pm 8.4$	39.8 $\pm 7.6$	39.5 $\pm 7.4$	40.7 $\pm 9.0$	103.5 $\pm 6.3$	103.3 $\pm 7.1$	102.9 $\pm 5.7$	100.9 $\pm 5.1$	108.9 $\pm 12.9$	104.7 $\pm 13.1$	104.3 $\pm 12.2$	106.3 $\pm 12.8$
15 K	31.4 $\pm 23.8$	26.2 $\pm 23.4$	35.4 $\pm 26.3$	20.7 $\pm 27.5$	124.0 $\pm 6.2$	122.7 $\pm 5.7$	123.1 $\pm 5.3$	120.4 $\pm 7.2$	43.5 $\pm 9.7$	41.2 $\pm 8.7$	41.0 $\pm 8.5$	46.1 $\pm 10.7$	91.2 $\pm 9.7$	93.8 $\pm 7.4$	93.2 $\pm 7.1$	90.5 $\pm 10.3$	92.5 $\pm 18.0$	96.5 $\pm 13.4$	94.7 $\pm 13.8$	88.5 $\pm 12.8$
16 I	-14.8 $\pm 22.5$	-2.9 $\pm 24.0$	-13.9 $\pm 24.4$	-5.9 $\pm 26.2$	110.9 $\pm 8.9$	114.2 $\pm 7.4$	114.9 $\pm 6.9$	110.0 $\pm 9.8$	44.8 $\pm 10.4$	43.8 $\pm 9.1$	42.5 $\pm 9.0$	44.0 $\pm 12.6$	120.4 $\pm 22.6$	113.6 $\pm 15.6$	111.9 $\pm 15.0$	122.7 $\pm 24.9$	99.7 $\pm 12.2$	96.2 $\pm 13.4$	98.5 $\pm 12.5$	95.6 $\pm 14.0$
17 A	-2.1 $\pm 23.0$	-10.1 $\pm 21.4$	-10.8 $\pm 18.6$	-10.9 $\pm 21.3$	122.3 $\pm 9.2$	122.7 $\pm 7.9$	123.4 $\pm 7.8$	127.6 $\pm 8.2$	24.1 $\pm 22.1$	26.4 $\pm 19.1$	29.1 $\pm 16.3$	16.9 $\pm 24.6$	-	-	-	-	-	-	-	-
18 G	25.4 $\pm 26.6$	32.8 $\pm 24.0$	35.3 $\pm 22.7$	35.4 $\pm 23.7$	-	-	-	-	-	-	-	-	-	-	-	-	-	-	-	-
19 K	-23.6 $\pm 22.0$	-27.7 $\pm 18.8$	-18.8 $\pm 22.1$	-29.3 $\pm 15.4$	-	-	-	-	-	-	-	-	-	-	-	-	-	-	-	-
20 I	36.7 $\pm 28.5$	39.1 $\pm 23.9$	28.7 $\pm 25.7$	41.3 $\pm 24.0$	-	-	-	-	-	-	-	-	-	-	-	-	-	-	-	-
21 A	-11.9 $\pm 32.3$	-16.7 $\pm 29.8$	-13.6 $\pm 33.8$	-14.0 $\pm 31.9$	-	-	-	-	-	-	-	-	-	-	-	-	-	-	-	-
Average residue 3-17																				
	120.7 $\pm 8.2$	121.1 $\pm 7.8$	121.4 $\pm 6.9$	120.3 $\pm 12.0$	38.5 $\pm 13.0$	39.4 $\pm 11.5$	39.3 $\pm 10.4$	38.5 $\pm 17.9$	100.4 $\pm 16.1$	99.5 $\pm 12.6$	99.9 $\pm 11.6$	99.7 $\pm 27.6$	100.2 $\pm 14.1$	99.2 $\pm 13.5$	99.7 $\pm 13.4$	99.1 $\pm 18.3$				



Table A.4: Splittings and structural parameters obtained from the simulation of KIA14, for the four different intervals. The angles  $\beta$ ,  $\alpha$  and  $\theta$  have been calculated only for the helical part of the peptide from position 3-10.

residue	$\Delta\nu$				$\beta$				$\alpha$				$\theta_{i,i+1}$				$\Delta\delta_{i,i+1}$																																																														
	200-400 ns	400-600 ns	600-800 ns	800-1000 ns	200-400 ns	400-600 ns	600-800 ns	800-1000 ns	200-400 ns	400-600 ns	600-800 ns	800-1000 ns	200-400 ns	400-600 ns	600-800 ns	800-1000 ns	200-400 ns	400-600 ns	600-800 ns	800-1000 ns																																																											
12 K	-31.6 $\pm 12.3$	-29.1 $\pm 16.6$	-18.3 $\pm 20.8$	13.9 $\pm 42.8$	-	-	-	-	-	-	-	-	-	-	-	-	-	-	-	-																																																											
13 I	26.9 $\pm 22.7$	42.7 $\pm 25.2$	22.8 $\pm 24.8$	47.4 $\pm 22.1$	-	-	-	-	-	-	-	-	-	-	-	-	-	-	-	-																																																											
14 A	-15.5 $\pm 33.8$	-14.1 $\pm 34.4$	-22.4 $\pm 27.8$	-9.8 $\pm 28.5$	-	-	-	-	-	-	-	-	-	-	-	-	-	-	-	-																																																											
Average residue 3-10																																																																															
122.0 $\pm 5.4$					121.4 $\pm 6.5$					121.8 $\pm 5.3$					121.5 $\pm 7.0$					39.7 $\pm 7.5$					39.0 $\pm 8.9$					39.5 $\pm 7.8$					37.5 $\pm 12.2$					98.5 $\pm 6.4$					98.4 $\pm 8.2$					98.6 $\pm 6.2$					98.3 $\pm 8.0$					99.6 $\pm 12.1$					99.2 $\pm 13.8$					99.8 $\pm 12.2$					97.7 $\pm 15.9$				

Table A.5: Splittings and structural parameters obtained from the simulation of Mag2, for the four different intervals. The angles  $\beta$ ,  $\alpha$  and  $\theta$  have been calculated only for the helical part of the peptide from position 3-13.

residue	$\Delta\nu$				$\beta$				$\alpha$				$\theta_{i,i+1}$				$\Delta\delta_{i,i+1}$			
	200-400 ns	400-600 ns	600-800 ns	800-1000 ns	200-400 ns	400-600 ns	600-800 ns	800-1000 ns	200-400 ns	400-600 ns	600-800 ns	800-1000 ns	200-400 ns	400-600 ns	600-800 ns	800-1000 ns	200-400 ns	400-600 ns	600-800 ns	800-1000 ns
1 G	-6.4 $\pm 39.7$	-13.5 $\pm 34.4$	-12.0 $\pm 33.5$	-18.6 $\pm 29.9$	-	-	-	-	-	-	-	-	-	-	-	-	-	-	-	-
2 I	33.5 $\pm 23.9$	43.1 $\pm 24.8$	44.1 $\pm 24.3$	37.3 $\pm 21.6$	-	-	-	-	-	-	-	-	-	-	-	-	-	-	-	-
3 G	5.9 $\pm 21.1$	16.9 $\pm 22.8$	24.8 $\pm 21.4$	23.6 $\pm 20.0$	128.1 $\pm 7.5$	127.1 $\pm 8.9$	123.4 $\pm 7.4$	125.8 $\pm 7.7$	64.9 $\pm 11.8$	67.4 $\pm 20.3$	59.6 $\pm 9.9$	61.8 $\pm 10.8$	131.8 $\pm 11.2$	135.5 $\pm 20.4$	127.8 $\pm 10.9$	131.3 $\pm 10.7$	94.8 $\pm 14.5$	96.1 $\pm 16.5$	96.6 $\pm 14.8$	98.7 $\pm 14.1$
4 K	-11.5 $\pm 21.5$	-4.1 $\pm 21.9$	-6.8 $\pm 23.8$	-12.0 $\pm 20.9$	121.2 $\pm 5.7$	121.6 $\pm 7.2$	123.0 $\pm 6.2$	123.2 $\pm 6.0$	27.8 $\pm 7.1$	28.0 $\pm 8.1$	28.4 $\pm 7.3$	29.2 $\pm 7.5$	91.4 $\pm 5.2$	89.2 $\pm 8.1$	90.6 $\pm 5.5$	90.6 $\pm 5.4$	98.3 $\pm 11.9$	95.6 $\pm 13.3$	98.3 $\pm 11.9$	95.4 $\pm 11.8$
5 F	35.4 $\pm 19.9$	18.5 $\pm 18.9$	19.5 $\pm 23.4$	24.8 $\pm 17.9$	117.1 $\pm 4.9$	116.5 $\pm 6.4$	118.8 $\pm 5.8$	117.0 $\pm 5.3$	34.7 $\pm 6.3$	34.4 $\pm 6.5$	36.1 $\pm 6.2$	34.0 $\pm 6.1$	86.4 $\pm 3.3$	86.3 $\pm 3.5$	85.2 $\pm 3.0$	86.7 $\pm 3.0$	93.9 $\pm 11.2$	92.3 $\pm 11.6$	91.5 $\pm 10.6$	94.7 $\pm 10.8$
6 L	-26.9 $\pm 15.6$	-29.4 $\pm 14.5$	-34.0 $\pm 9.5$	-35.0 $\pm 9.3$	123.0 $\pm 4.9$	123.8 $\pm 6.7$	123.1 $\pm 5.1$	123.3 $\pm 5.2$	42.2 $\pm 7.1$	40.4 $\pm 8.1$	42.3 $\pm 6.7$	42.0 $\pm 6.9$	106.8 $\pm 4.9$	106.4 $\pm 5.9$	106.2 $\pm 5.5$	107.0 $\pm 5.2$	108.6 $\pm 10.9$	111.0 $\pm 13.6$	108.4 $\pm 10.8$	107.5 $\pm 10.8$
7 H	33.4 $\pm 16.3$	49.1 $\pm 13.9$	52.2 $\pm 16.2$	51.6 $\pm 13.4$	127.5 $\pm 4.2$	127.6 $\pm 4.6$	126.5 $\pm 4.3$	127.0 $\pm 4.3$	44.0 $\pm 7.5$	45.0 $\pm 9.9$	44.6 $\pm 8.0$	42.5 $\pm 7.8$	103.8 $\pm 6.2$	102.3 $\pm 10.8$	106.2 $\pm 7.0$	105.5 $\pm 7.0$	100.9 $\pm 11.0$	100.0 $\pm 13.6$	101.3 $\pm 11.4$	104.1 $\pm 10.8$
8 S	-33.3 $\pm 11.0$	-35.6 $\pm 9.0$	-34.9 $\pm 8.2$	-34.7 $\pm 8.9$	118.0 $\pm 3.7$	116.4 $\pm 5.8$	117.4 $\pm 3.8$	117.3 $\pm 3.7$	41.1 $\pm 6.5$	42.7 $\pm 9.4$	39.7 $\pm 7.0$	41.0 $\pm 6.8$	99.0 $\pm 6.7$	107.7 $\pm 25.5$	100.5 $\pm 6.3$	100.8 $\pm 7.1$	95.4 $\pm 9.6$	99.8 $\pm 14.9$	95.4 $\pm 9.6$	95.5 $\pm 9.8$
9 A	41.2 $\pm 17.6$	27.2 $\pm 14.9$	22.0 $\pm 21.1$	23.1 $\pm 16.2$	119.4 $\pm 3.7$	118.8 $\pm 3.9$	120.1 $\pm 4.4$	118.9 $\pm 3.8$	37.5 $\pm 6.1$	34.7 $\pm 9.1$	34.5 $\pm 7.4$	35.8 $\pm 6.3$	104.6 $\pm 5.5$	102.4 $\pm 11.7$	102.0 $\pm 8.5$	105.6 $\pm 5.7$	99.2 $\pm 10.1$	99.3 $\pm 12.1$	103.3 $\pm 10.5$	103.4 $\pm 10.0$
10 K	-25.5 $\pm 15.0$	-16.8 $\pm 16.6$	-12.7 $\pm 17.3$	-5.8 $\pm 18.0$	125.8 $\pm 4.3$	123.8 $\pm 9.6$	126.9 $\pm 4.7$	126.3 $\pm 4.5$	32.1 $\pm 6.5$	31.6 $\pm 7.2$	35.8 $\pm 8.0$	33.6 $\pm 6.3$	92.3 $\pm 3.8$	91.3 $\pm 4.0$	90.6 $\pm 5.0$	91.3 $\pm 3.7$	106.0 $\pm 10.7$	104.2 $\pm 11.2$	100.5 $\pm 13.2$	101.7 $\pm 10.4$
11 K	6.5 $\pm 21.7$	16.6 $\pm 20.0$	21.7 $\pm 29.1$	12.2 $\pm 21.6$	126.6 $\pm 4.4$	127.6 $\pm 6.1$	125.5 $\pm 4.9$	125.6 $\pm 4.4$	45.7 $\pm 6.3$	44.5 $\pm 8.0$	45.8 $\pm 7.0$	44.0 $\pm 6.4$	88.6 $\pm 3.8$	88.3 $\pm 4.2$	93.9 $\pm 10.4$	90.6 $\pm 3.7$	98.7 $\pm 10.1$	100.1 $\pm 13.2$	108.6 $\pm 19.1$	103.2 $\pm 10.3$



Table A.5: Splittings and structural parameters obtained from the simulation of Mag2, for the four different intervals. The angles  $\beta$ ,  $\alpha$  and  $\theta$  have been calculated only for the helical part of the peptide from position 3-13.

residue	$\Delta\nu$				$\beta$				$\alpha$				$\theta_{i,i+1}$				$\Delta\delta_{i,i+1}$			
	200-400 ns	400-600 ns	600-800 ns	800-1000 ns	200-400 ns	400-600 ns	600-800 ns	800-1000 ns	200-400 ns	400-600 ns	600-800 ns	800-1000 ns	200-400 ns	400-600 ns	600-800 ns	800-1000 ns	200-400 ns	400-600 ns	600-800 ns	800-1000 ns
23 S	-29.7	-22.5	-4.4	-14.0	-	-	-	-	-	-	-	-	-	-	-	-	-	-	-	-
	$\pm 15.6$	$\pm 18.8$	$\pm 28.1$	$\pm 26.6$																
Average residue 3-13																				
					122.4	122.2	121.5	122.3	41.6	42.1	41.9	41.2	103.3	103.3	102.8	103.5	100.0	100.4	100.2	100.6
					$\pm 6.5$	$\pm 7.9$	$\pm 7.9$	$\pm 6.3$	$\pm 13.0$	$\pm 15.2$	$\pm 13.9$	$\pm 12.3$	$\pm 16.1$	$\pm 19.9$	$\pm 16.7$	$\pm 15.7$	$\pm 12.2$	$\pm 14.4$	$\pm 13.8$	$\pm 11.9$

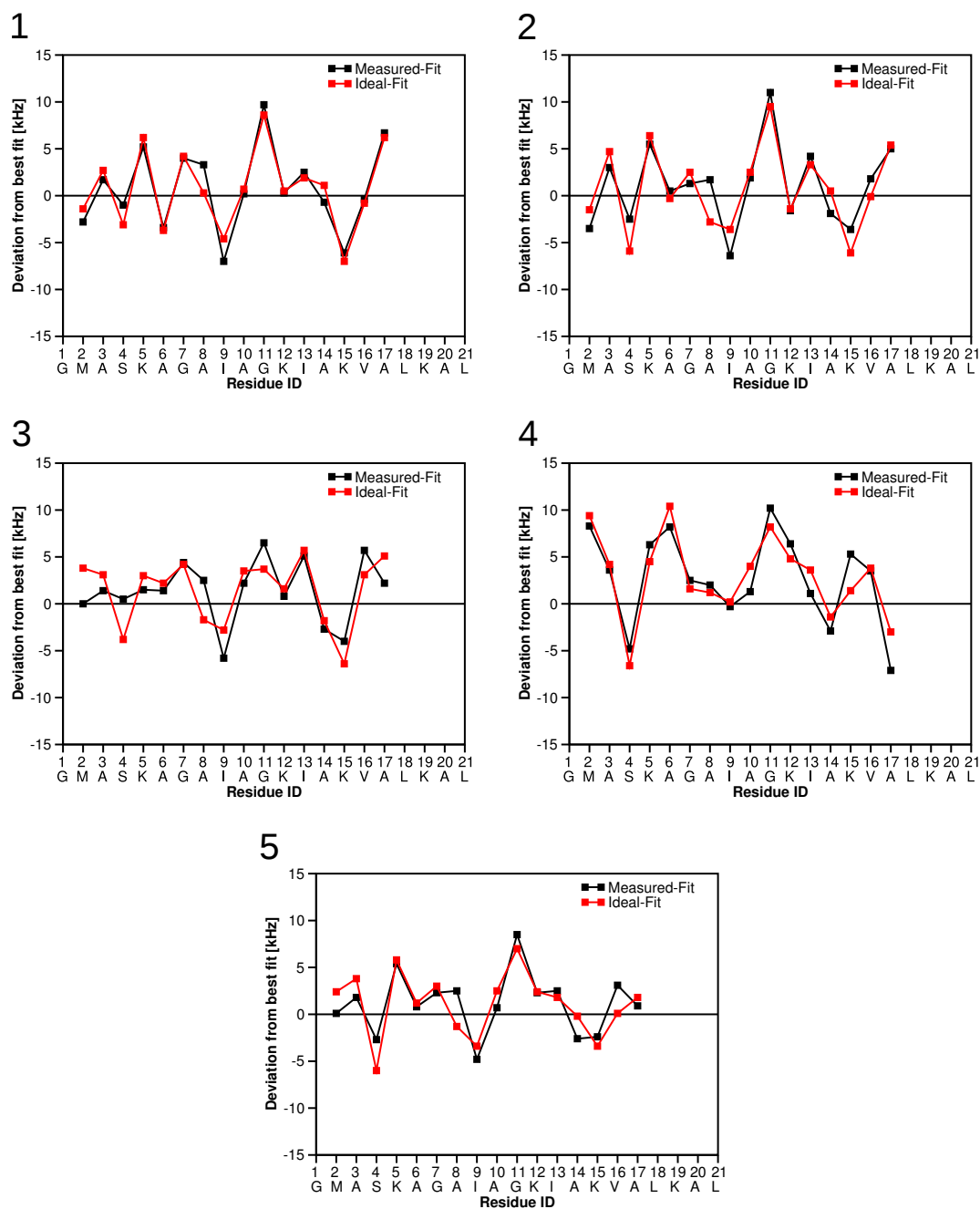


Figure A.2: PGLa, deviation of measured splittings and splittings calculated from simulation averages with respect to ideal splittings calculated via fit. 1-4 are the different intervals, each of 200 ns length, 5 are the values obtained for the complete evaluation period 200-1000 ns.

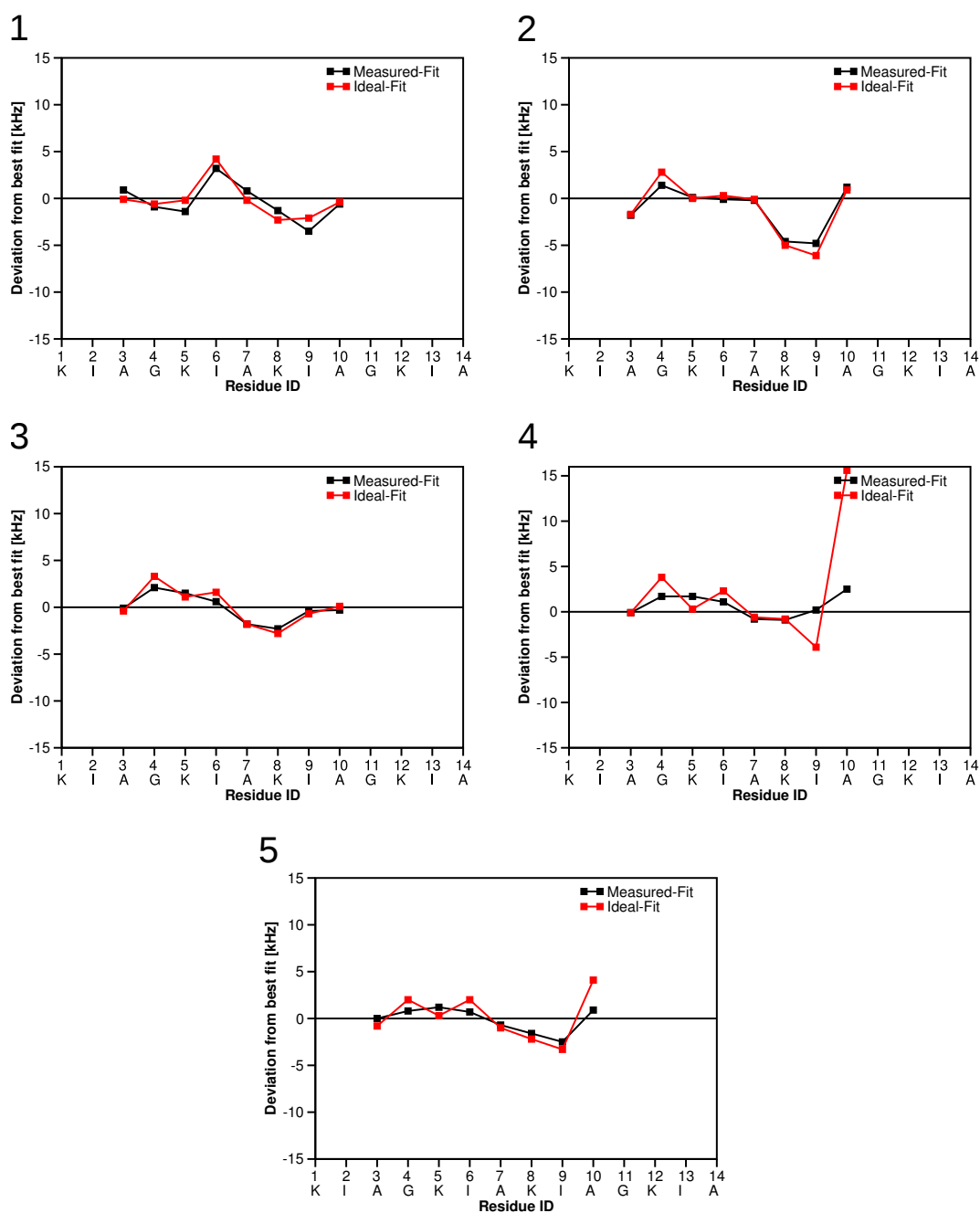


Figure A.3: KIA14, deviation of measured splittings and splittings calculated from simulation averages with respect to ideal splittings calculated via fit. 1-4 are the different intervals, each of 200 ns length, 5 are the values obtained for the complete evaluation period 200-1000 ns.

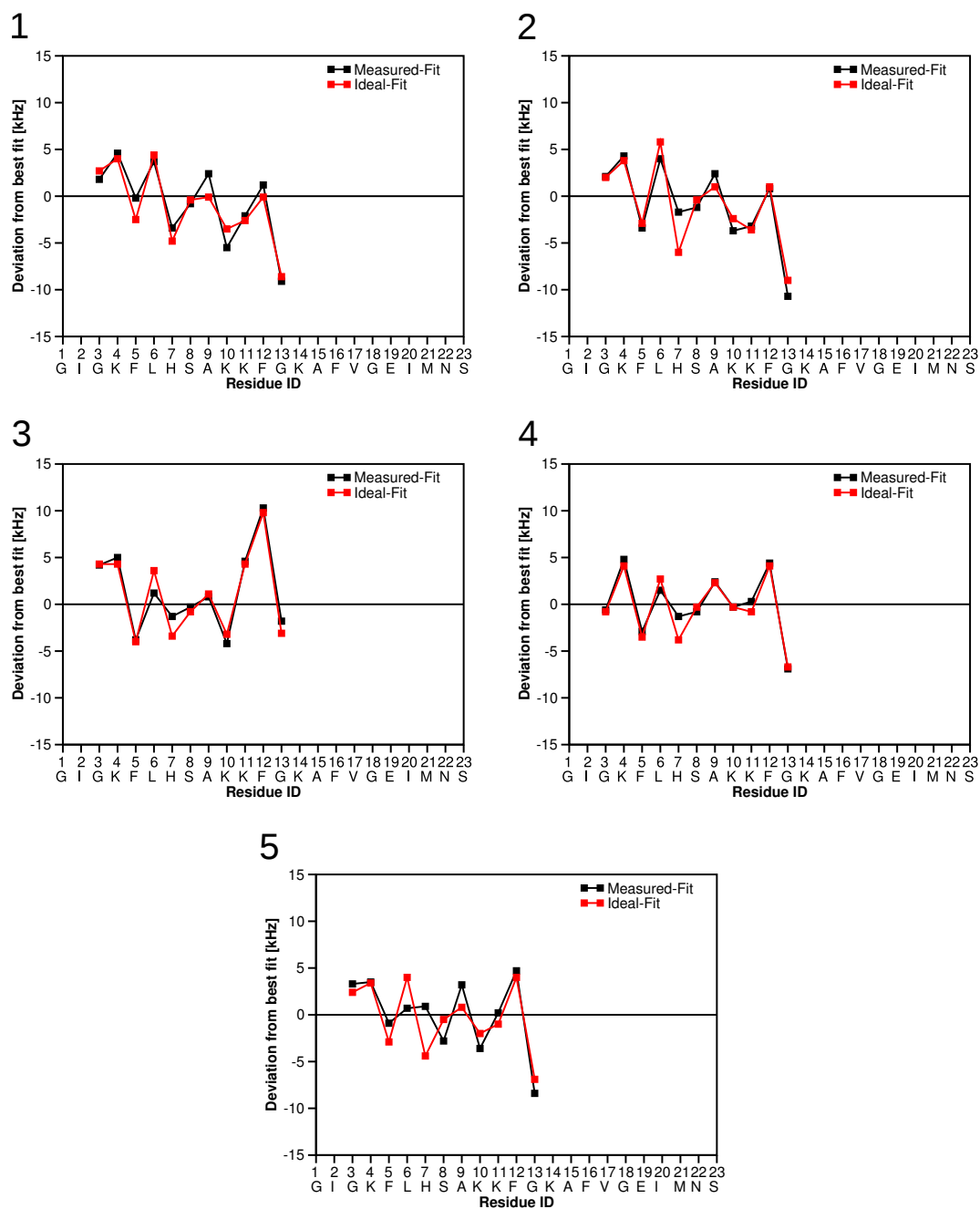


Figure A.4: Mag2, deviation of measured splittings and splittings calculated from simulation averages with respect to ideal splittings calculated via fit. 1-4 are the different intervals, each of 200 ns length, 5 are the values obtained for the complete evaluation period 200-1000 ns.

## B. 3D hydrophobic moment vectors

Table B.1: PGLa in DMPC control simulation rep2, showing a comparison between the average HM values obtained for different data sets. The simulation length used for the analysis entailed the last 100 or last 300 ns, and time steps between snapshots were either 50 ps or 1 ns.

<b>System</b>	<b>Average absolute HM vector (kTÅ/e)</b>	<b>Average angle variation from average HM vector (°)</b>	<b>Average angle between HM vector and membrane normal (°)</b>	<b>Angle between average HM vector and membrane normal (°)</b>
Last 300 ns, time step 50 ps - 6000 snapshots	$43.5 \pm 4.2$	$12.7 \pm 4.9$	$48.2 \pm 8.2$	48.1
Last 300 ns, time step 1 ns - 300 snapshots	$43.5 \pm 4.3$	$7.3 \pm 3.6$	$48.0 \pm 8.3$	47.9
Last 100 ns, time step 50 ps - 2000 snapshots	$43.0 \pm 4.1$	$6.2 \pm 3.2$	$48.9 \pm 7.3$	48.8
Last 100 ns, time step 1 ns - 100 snapshots	$42.9 \pm 4.1$	$4.7 \pm 2.7$	$48.3 \pm 7.4$	48.1

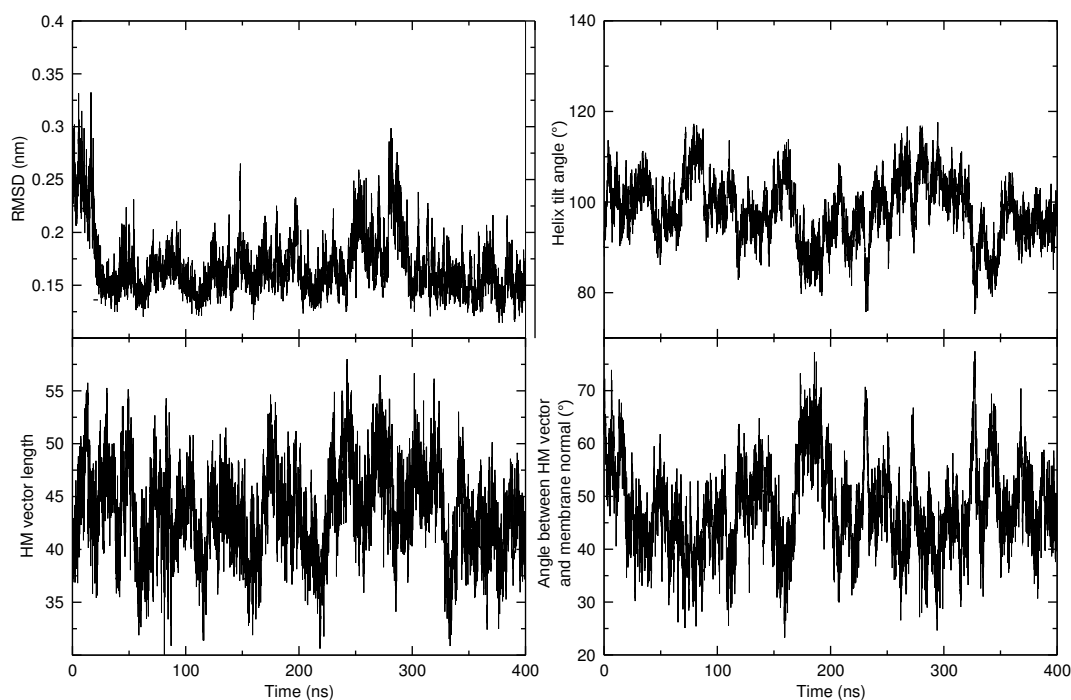


Figure B.1: Time evolution of relevant properties during one of the control simulations of PGLa, after high-temperature insertion and cooling to 303 K. *Top left*: All-atom RMSD for the peptide, compared to the energy-minimized starting structure before insertion. The graph begins after the high temperature insertion phase and cooling. The initial decrease shows that the structure of the peptide was more disturbed during the high temperature insertion and returns closer to the starting structure when embedded stably into the membrane. *Top right*: The orientation of the helical axis, measured by the tilt angle between the helix axis and the membrane normal. The peptide lies almost flat in the membrane at an angle of  $98^\circ \pm 7^\circ$ . *Bottom left*: The HM vector length fluctuates around a value of  $43^\circ \pm 4^\circ$ . *Bottom right*: The angle between the HM vector and the membrane normal fluctuates around  $48^\circ \pm 8^\circ$ .

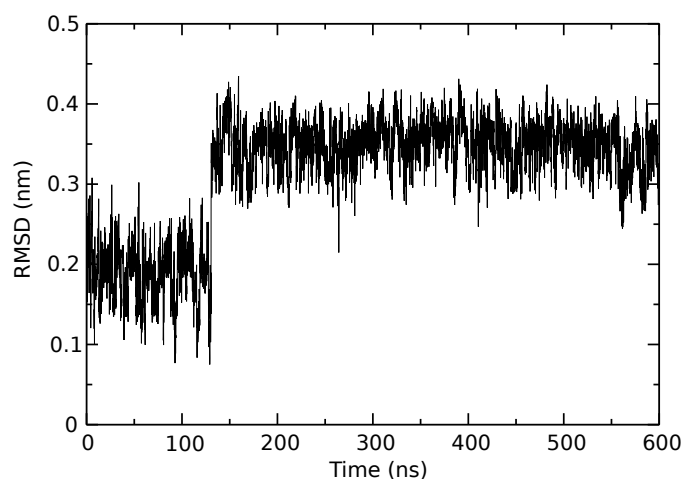


Figure B.2: All-atom RMSD of the Gramicidin S simulation in methanol compared to the NMR starting structure.

Table B.2: Average HM vector properties for all peptide-membrane simulations of PGLa and GS. The average values are averages over the last 100 ns of simulation, from snapshots taken at a time step of 1 ns. The simulations denoted as replica (rep) have a total length of 400 ns, while the original ones are 600 ns long for PGLa and 650 ns for GS.

System	Average absolute HM vector (kTÅ/e)	Average angle variation from average HM vector (°)	Average angle between HM vector and membrane normal (°)	Angle between average HM vector and membrane normal (°)
GS in DMPC	$15.2 \pm 2.0$	$17.9 \pm 9.5$	$28.8 \pm 17.1$	12.6
GS in DMPC rep1	$13.5 \pm 1.7$	$12.7 \pm 7.0$	$22.6 \pm 11.6$	4.9
GS in DMPC rep2	$12.7 \pm 1.7$	$14.1 \pm 7.2$	$27.5 \pm 11.2$	21.5
GS in DMPC rep2	$12.1 \pm 1.3$	$9.4 \pm 5.7$	$23.7 \pm 9.5$	9.6
PGLa in DMPC	$44.9 \pm 3.3$	$5.7 \pm 2.8$	$53.3 \pm 6.6$	53.2
PGLa in DMPC rep1	$39.9 \pm 5.0$	$7.7 \pm 4.2$	$50.6 \pm 9.3$	49.9
PGLa in DMPC rep2	$42.9 \pm 4.1$	$4.7 \pm 2.7$	$48.3 \pm 7.4$	48.1

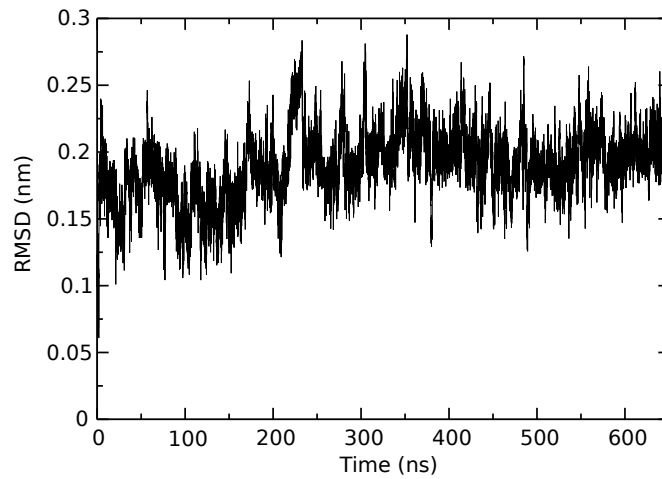


Figure B.3: All-atom RMSD of the Gramicidin S simulation in DMPC compared to the starting structure after high temperature insertion.

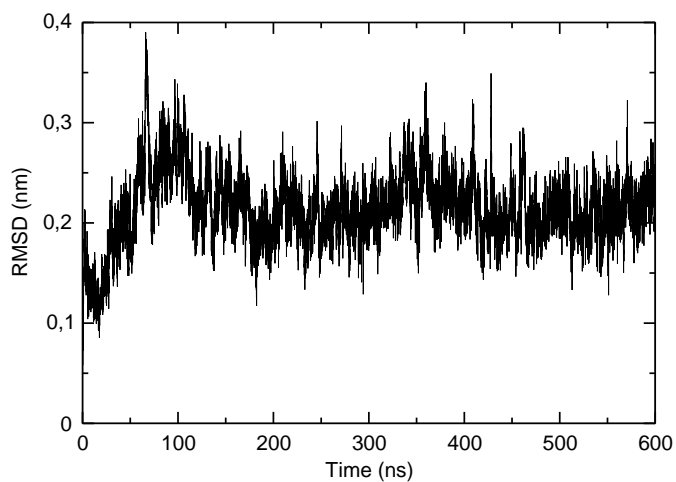


Figure B.4: All-atom RMSD of the PGLa simulation in DMPC compared to the starting structure of the unrestrained simulation after high temperature insertion.

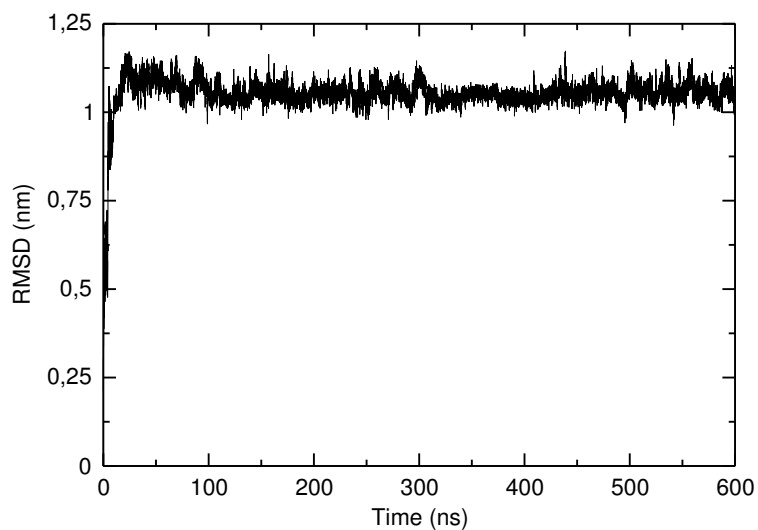


Figure B.5: All-atom RMSD of the PGLa simulation in water compared to the ideal  $\alpha$ -helical starting structure.

## C. Photoswitchable analogs of gramicidin S

Table C.1: Properties for the different molecules, measured over last 700 ns of 1  $\mu$ s simulation in MeOH. HM vector, electrostatic component of solvation free energy and molecular surface were calculated every ns, hydrogen bonds were evaluated every 50 ps.

Molecule	average RMSF (nm)	HM vector length (kT $\text{\AA}$ /e) <sup>a</sup>	El.statics of solvation (kJ/mol)	Molecular surface ( $\text{\AA}^2$ )	Hydrogen Bonds <sup>b</sup>
GS	0.13	9.4 $\pm$ 1.0	690 $\pm$ 38	841 $\pm$ 23	5.6
LF_SWO	0.22	8.0 $\pm$ 1.6	726 $\pm$ 34	980 $\pm$ 24	0.5
LF_SC1	0.22	4.1 $\pm$ 1.8	812 $\pm$ 34	974 $\pm$ 23	0.3
LF_SC2	0.15	7.0 $\pm$ 1.8	775 $\pm$ 49	938 $\pm$ 40	0.7
FP_SWO	0.22	8.4 $\pm$ 1.8	737 $\pm$ 42	1021 $\pm$ 25	1.2
FP_SC1	0.18	4.7 $\pm$ 2.2	840 $\pm$ 24	999 $\pm$ 24	0.2
FP_SC2	0.21	5.4 $\pm$ 2.0	847 $\pm$ 37	1017 $\pm$ 27	0.5
PV_SWO	0.21	8.4 $\pm$ 2.0	758 $\pm$ 42	1072 $\pm$ 36	0.1
PV_SC1	0.16	3.5 $\pm$ 1.6	833 $\pm$ 28	1040 $\pm$ 23	0.0
PV_SC2	0.16	3.6 $\pm$ 1.7	831 $\pm$ 30	1041 $\pm$ 24	0.0

<sup>a</sup>The average of the absolute values of all vectors calculated from the snapshots.

<sup>b</sup>Sum over all hydrogen bonds as defined by the criterion in equation 6.3.

Table C.2: Properties for the different molecules, measured over last 400 ns of 600 ns simulation in a DMPC membrane. HM vector, electrostatic component of solvation free energy and molecular surface were calculated every ns, hydrogen bonds and insertion depths were evaluated every 50 ps.

<sup>a</sup>The average of the absolute values of all 100 vectors calculated from the snapshots.

<sup>b</sup>Sum over all hydrogen bonds as defined by the criterion in equation 6.3.

<sup>c</sup>MID (membrane insertion depth) is distance between the average z-coordinate of the phosphorus atoms of the lipids and the average z-coordinate of the peptide resp. the switch

Mol.	Sim.	Average RMSF (nm)	HM vector length (kTÅ/e) <sup>a</sup>	Electrostatics of solvation (kJ/mol)	Molecular surface (Å <sup>2</sup> )	Hydrogen Bonds <sup>b</sup>	MID of the peptidic part (Å) <sup>c</sup>	MID of the switch part (Å)	MID of complete molecule (Å)
GS	1	0.13	14.0 ± 1.5	689 ± 689	841 ± 841	5.4	-	-	9.7 ± 1.7
	2	0.13	13.9 ± 1.4	678 ± 678	826 ± 826	5.7	-	-	10.0 ± 1.5
	3	0.14	14.3 ± 1.9	692 ± 692	844 ± 844	5.4	-	-	9.9 ± 1.4
	4	0.13	13.7 ± 1.6	695 ± 695	848 ± 848	5.3	-	-	10.3 ± 2.0
LF_SWO	1	0.15	13.5 ± 2.8	749 ± 49	912 ± 38	1.9	7.6 ± 2.9	9.2 ± 2.6	8.1 ± 2.6
	2	0.13	14.3 ± 2.2	752 ± 43	918 ± 22	2.2	8.0 ± 2.1	7.9 ± 2.2	8.0 ± 2.0
	3	0.14	14.9 ± 2.4	727 ± 47	908 ± 30	2.5	7.9 ± 2.1	8.8 ± 2.5	8.1 ± 2.0
	4	0.14	14.5 ± 2.0	788 ± 33	968 ± 28	0.7	6.9 ± 1.8	9.6 ± 2.4	7.7 ± 1.9
LF_SC1	1	0.13	14.3 ± 3.4	766 ± 41	859 ± 18	3.4	6.4 ± 2.7	8.3 ± 2.3	6.9 ± 2.4
	2	0.09	17.2 ± 1.9	824 ± 15	862 ± 11	2.5	7.7 ± 1.8	6.9 ± 2.1	7.5 ± 1.8
	3	0.13	14.2 ± 2.0	724 ± 29	907 ± 19	3.0	8.6 ± 2.1	7.1 ± 3.6	8.2 ± 2.3
	4	0.12	16.2 ± 2.6	816 ± 16	882 ± 22	1.4	4.6 ± 2.8	7.5 ± 2.2	5.4 ± 2.5
LF_SC2	1	0.11	8.8 ± 2.6	796 ± 21	920 ± 13	1.0	1.4 ± 2.3	6.5 ± 2.5	2.8 ± 2.3
	2	0.10	16.0 ± 1.5	711 ± 14	938 ± 11	2.2	6.6 ± 1.8	1.6 ± 2.5	5.2 ± 1.9
	3	0.17	10.0 ± 3.0	806 ± 23	937 ± 20	0.6	5.5 ± 2.4	6.0 ± 2.2	5.6 ± 2.1
	4	0.16	14.8 ± 2.4	763 ± 41	898 ± 19	1.7	7.8 ± 2.1	9.2 ± 2.5	8.2 ± 2.0
FP_SWO	1	0.18	9.4 ± 3.3	769 ± 27	965 ± 28	0.6	4.9 ± 2.2	4.6 ± 4.2	4.8 ± 2.6
	2	0.13	17.4 ± 1.8	806 ± 22	952 ± 16	0.4	5.8 ± 2.0	11.2 ± 2.1	7.3 ± 2.0
	3	0.14	14.2 ± 2.1	798 ± 24	958 ± 18	0.6	2.5 ± 1.9	8.1 ± 2.2	4.0 ± 1.9

Mol.	Sim.	Av. RMSF (nm)	HM vector length (kTÅ/e)	ES comp. of solv. free energy (kJ/mol)	Molecular surface (Å <sup>2</sup> )	Hydrogen Bonds	MID peptidic part (Å)	MID switch (Å)	MID complete molecule (Å)
	4	0.11	7.2 ± 1.8	708 ± 24	1012 ± 11	0.9	5.2 ± 2.6	6.8 ± 2.4	5.6 ± 2.2
	1	0.13	11.1 ± 2.4	849 ± 20	980 ± 16	0.2	1.8 ± 2.0	8.8 ± 2.1	3.7 ± 2.0
FP_SC1	2	0.17	11.7 ± 2.8	827 ± 19	958 ± 39	0.9	4.1 ± 2.5	10.3 ± 2.3	5.8 ± 2.4
	3	0.13	12.4 ± 2.1	823 ± 20	1023 ± 20	0.7	6.8 ± 2.1	6.9 ± 2.4	6.9 ± 2.0
	4	0.14	11.4 ± 2.6	810 ± 20	990 ± 19	0.6	5.9 ± 1.9	8.6 ± 1.9	6.7 ± 1.8
	1	0.16	12.7 ± 2.4	810 ± 25	968 ± 27	0.0	6.4 ± 2.3	11.1 ± 2.6	7.7 ± 2.3
FP_SC2	2	0.13	7.3 ± 2.2	843 ± 18	1007 ± 15	0.6	3.5 ± 2.0	10.2 ± 2.0	5.4 ± 2.0
	3	0.14	14.0 ± 2.3	808 ± 18	1009 ± 27	0.4	6.4 ± 1.6	8.2 ± 2.2	6.9 ± 1.7
	4	0.13	11.6 ± 1.9	804 ± 20	996 ± 16	0.9	6.8 ± 1.8	9.2 ± 1.8	7.4 ± 1.7
	1	0.15	14.2 ± 1.9	772 ± 39	1043 ± 31	0.3	7.3 ± 1.9	1.2 ± 1.9	5.7 ± 1.9
PV_SWO	2	0.17	15.7 ± 1.8	798 ± 20	1007 ± 24	0.1	7.2 ± 1.9	9.6 ± 2.2	7.8 ± 1.9
	3	0.17	17.1 ± 1.6	746 ± 29	1027 ± 25	0.7	8.7 ± 2.0	6.5 ± 2.4	8.1 ± 2.1
	4	0.12	17.7 ± 1.6	772 ± 28	962 ± 20	0.5	9.1 ± 2.0	8.4 ± 2.2	8.9 ± 2.0
	1	0.15	13.6 ± 3.1	761 ± 31	990 ± 20	1.1	7.2 ± 1.9	0.7 ± 1.8	5.5 ± 1.8
PV_SC1	2	0.11	20.1 ± 1.9	826 ± 18	938 ± 16	2.9	6.3 ± 1.8	-0.3 ± 1.8	4.6 ± 1.8
	3	0.16	12.0 ± 3.2	813 ± 22	1016 ± 21	0.0	6.1 ± 2.1	10.0 ± 2.1	7.2 ± 2.0
	4	0.13	20.2 ± 2.5	806 ± 21	956 ± 19	2.7	8.0 ± 1.9	2.0 ± 2.2	6.4 ± 2.0
	1	0.15	13.2 ± 2.6	829 ± 23	986 ± 19	0.2	-2.5 ± 2.0	-4.9 ± 2.4	-3.1 ± 2.0
PV_SC2	2	0.15	14.9 ± 2.2	797 ± 31	1057 ± 38	0.5	7.1 ± 2.3	11.1 ± 2.0	8.2 ± 2.1
	3	0.13	18.3 ± 2.1	827 ± 20	986 ± 15	1.8	8.0 ± 2.0	11.7 ± 2.2	9.0 ± 2.0
	4	0.15	14.4 ± 1.9	798 ± 32	1053 ± 37	0.5	9.7 ± 1.8	8.6 ± 2.1	9.4 ± 1.7

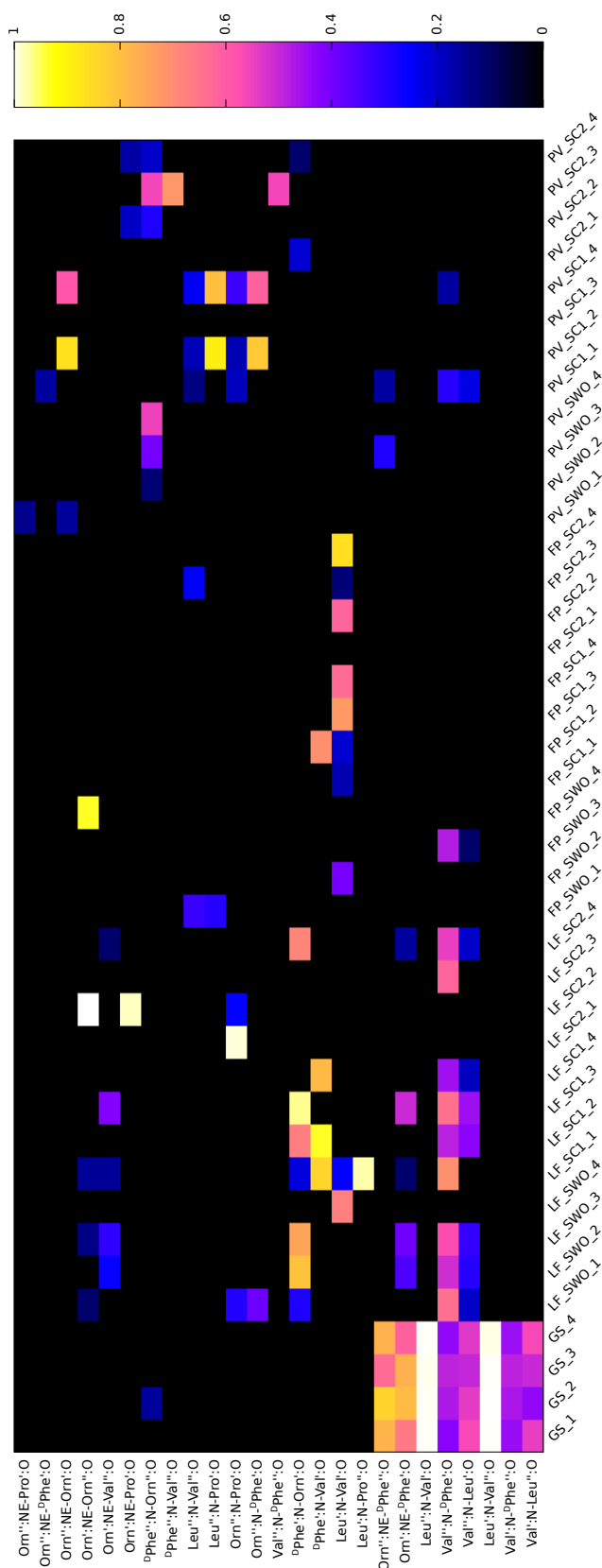


Figure C.1: Hydrogen bonds for gramicidin S and its analogues from all simulations in a DMPC membrane. The y-axis denotes the hydrogen bond pair, nomenclature is analog to Figure 6.1. O and N are backbone oxygens/nitrogens, NE is the nitrogen of the ornithine side chains.

## D. Fluorine amino acids

Table D.1: Structural parameters calculated for the fluorine amino acids, from the energy-minimized conformations of PGLa with fluorine substituted amino acid at the denoted position. The angles are defined in Chapter 3.

<b>FAA</b>	<b>pos.</b>	$\beta_{i-4}$	$\beta_{i-1}$	$\beta_i$	$\beta_{i+1}$	$\beta_{i+4}$	$\alpha_{i-4}$	$\alpha_{i-1}$	$\alpha_i$	$\alpha_{i+1}$	$\alpha_{i+4}$	$\theta_{i-1,i}$	$\theta_{i,i+1}$
BGS	9	115.8	120.6	113.3	127.2	119.6	39.2	40.2	34.6	34.3	33.3	90.4	105.7
BGS	10	123.1	116.4	113.0	120.8	122.5	34.3	41.3	26.8	46.7	43.7	103.8	99.6
BGS	13	118.4	121.4	114.1	118.0	122.7	44.2	44.9	34.6	47.3	54.5	97.3	98.4
BGS	14	124.4	119.4	115.6	118.6	121.4	33.2	37.5	32.1	47.8	47.1	99.1	93.4
Average		120.4 $\pm 3.5$	119.4 $\pm 1.9$	114.0 $\pm 1.0$	121.2 $\pm 3.6$	121.6 $\pm 1.2$	37.7 $\pm 4.4$	41.0 $\pm 2.7$	32.0 $\pm 3.2$	44.0 $\pm 5.6$	44.6 $\pm 7.6$	97.7 $\pm 4.8$	99.3 $\pm 4.4$
BGR	9	121.0	120.8	74.3	128.0	121.7	38.8	40.0	-40.7	41.8	31.6	90.2	99.7
BGR	10	128.0	118.6	71.3	119.6	125.7	33.4	35.4	-45.1	51.9	36.8	98.6	91.5
BGR	13	119.4	122.0	71.1	120.0	125.7	39.7	39.9	-45.6	51.5	41.9	94.0	94.3
BGR	14	127.6	117.1	63.1	122.7	123.7	29.2	33.5	-53.8	45.1	35.0	98.0	93.5
Average		124.0 $\pm 3.8$	119.6 $\pm 1.9$	70.0 $\pm 4.2$	122.6 $\pm 3.4$	124.2 $\pm 1.7$	35.3 $\pm 4.3$	37.2 $\pm 2.8$	-46.3 $\pm 4.7$	47.6 $\pm 4.3$	36.3 $\pm 3.7$	95.2 $\pm 3.4$	94.8 $\pm 3.0$
PGR	9	117.7	120.3	73.9	126.2	120.4	39.3	42.4	-29.2	35.6	34.5	93.5	102.6
PGR	10	124.3	118.8	69.9	121.5	123.3	34.6	41.0	-39.7	47.4	42.9	103.3	95.8
PGR	13	119.0	121.5	66.1	119.0	124.3	42.8	41.6	-41.3	49.2	52.6	98.4	94.0
PGR	14	125.9	119.5	69.4	120.1	121.2	32.4	35.1	-41.5	45.6	43.9	101.3	92.3
Average		121.7 $\pm 3.5$	120.0 $\pm 1.0$	69.8 $\pm 2.8$	121.7 $\pm 2.7$	122.3 $\pm 1.6$	37.3 $\pm 4.0$	40.0 $\pm 2.9$	-37.9 $\pm 5.1$	44.4 $\pm 5.3$	43.5 $\pm 6.4$	99.1 $\pm 3.7$	96.2 $\pm 3.9$
PGS	9	118.9	122.0	113.6	128.9	120.1	40.4	32.6	44.4	39.5	33.7	88.4	100.1
PGS	10	126.4	118.8	115.0	122.6	122.9	33.7	38.5	40.0	50.1	42.5	101.3	96.0
PGS	13	119.1	121.7	113.2	122.1	122.8	42.8	38.8	45.4	48.6	49.9	95.4	96.3
PGS	14	127.3	119.2	115.7	124.1	121.2	29.7	31.7	37.3	44.4	38.3	97.9	93.4

Table D.1: Structural parameters calculated for the fluorine amino acids, from the energy-minimized conformations of PGLa with fluorine substituted amino acid at the denoted position. The angles are defined in Chapter 3.

<b>FAA</b>	<b>pos.</b>	$\beta_{i-4}$	$\beta_{i-1}$	$\beta_i$	$\beta_{i+1}$	$\beta_{i+4}$	$\alpha_{i-4}$	$\alpha_{i-1}$	$\alpha_i$	$\alpha_{i+1}$	$\alpha_{i+4}$	$\theta_{i-1,i}$	$\theta_{i,i+1}$
Average		122.9 $\pm 3.9$	120.4 $\pm 1.4$	114.4 $\pm 1.0$	124.4 $\pm 2.7$	121.8 $\pm 1.2$	36.6 $\pm 5.2$	35.4 $\pm 3.3$	41.8 $\pm 3.3$	45.6 $\pm 4.1$	41.1 $\pm 6.0$	95.8 $\pm 4.7$	96.4 $\pm 2.4$
HSS	9	117.9	121.5	136.2	127.1	120.1	38.7	39.6	-51.8	36.3	33.8	90.4	104.0
HSS	10	124.4	117.4	130.4	120.0	123.5	35.2	36.6	-59.8	48.2	43.2	104.3	95.2
HSS	13	119.0	121.8	134.8	119.2	123.7	42.3	41.0	-65.0	48.5	51.6	97.6	95.9
HSS	14	125.7	118.7	136.5	120.8	120.9	32.7	32.8	-53.9	45.9	43.2	99.7	93.4
Average		121.8 $\pm 3.4$	119.8 $\pm 1.9$	134.5 $\pm 2.4$	121.8 $\pm 3.1$	122.1 $\pm 1.6$	37.2 $\pm 3.6$	37.5 $\pm 3.1$	-57.6 $\pm 5.2$	44.7 $\pm 5.0$	43.0 $\pm 6.3$	98.0 $\pm 5.0$	97.1 $\pm 4.1$
HSR	9	117.4	120.7	72.3	126.7	120.0	39.7	40.1	18.5	36.7	33.6	90.9	103.2
HSR	10	124.6	117.7	75.8	119.6	123.5	33.6	40.0	9.6	47.7	42.6	104.1	95.8
HSR	13	118.4	121.6	77.4	118.7	123.7	42.9	42.8	14.2	48.5	51.9	97.7	96.2
HSR	14	126.0	118.7	75.7	120.5	121.2	31.5	35.0	12.3	45.6	43.1	99.4	93.6
Average		121.6 $\pm 3.7$	119.7 $\pm 1.5$	75.3 $\pm 1.9$	121.4 $\pm 3.1$	122.1 $\pm 1.6$	36.9 $\pm 4.6$	39.5 $\pm 2.8$	13.6 $\pm 3.2$	44.6 $\pm 4.7$	42.8 $\pm 6.5$	98.0 $\pm 4.7$	97.2 $\pm 3.6$
CBS	9	118.1	121.0	134.0	126.9	120.0	39.6	39.9	-46.7	35.8	34.0	91.1	103.6
CBS	10	124.5	118.2	129.5	119.7	123.5	34.5	39.0	-57.6	47.3	43.0	104.8	95.6
CBS	13	118.9	122.2	134.5	119.2	123.7	42.9	41.0	-59.8	48.2	52.1	97.8	95.7
CBS	14	125.5	119.1	136.3	120.4	120.9	32.6	34.0	-50.5	45.8	43.9	100.1	93.2
Average		121.8 $\pm 3.3$	120.1 $\pm 1.6$	133.6 $\pm 2.5$	121.6 $\pm 3.1$	122.0 $\pm 1.6$	37.4 $\pm 4.1$	38.5 $\pm 2.7$	-53.7 $\pm 5.3$	44.3 $\pm 5.0$	43.2 $\pm 6.4$	98.4 $\pm 4.9$	97.0 $\pm 3.9$
CBR	9	119.3	121.6	78.0	127.6	120.4	39.1	38.8	14.3	37.6	33.8	90.4	102.5
CBR	10	126.1	117.9	79.3	120.4	123.4	33.2	40.0	4.4	48.9	42.3	103.5	95.0
CBR	13	119.7	121.7	79.3	120.1	123.3	42.3	41.2	9.4	48.4	51.0	96.9	96.0

Table D.1: Structural parameters calculated for the fluorine amino acids, from the energy-minimized conformations of PGLa with fluorine substituted amino acid at the denoted position. The angles are defined in Chapter 3.

<b>FAA</b>	<b>pos.</b>	$\beta_{i-4}$	$\beta_{i-1}$	$\beta_i$	$\beta_{i+1}$	$\beta_{i+4}$	$\alpha_{i-4}$	$\alpha_{i-1}$	$\alpha_i$	$\alpha_{i+1}$	$\alpha_{i+4}$	$\theta_{i-1,i}$	$\theta_{i,i+1}$
CBR	14	126.7	118.6	79.6	121.9	121.1	30.3	35.4	7.6	44.8	40.6	99.7	93.6
Average		122.9 $\pm 3.5$	119.9 $\pm 1.7$	79.1 $\pm 0.6$	122.5 $\pm 3.0$	122.1 $\pm 1.3$	36.2 $\pm 4.7$	38.9 $\pm 2.2$	8.9 $\pm 3.6$	44.9 $\pm 4.5$	41.9 $\pm 6.1$	97.6 $\pm 4.8$	96.8 $\pm 3.4$
CPS	9	114.7	120.3	152.6	126.1	120.0	39.6	40.2	-9.4	32.3	33.7	92.2	105.8
CPS	10	120.7	115.7	151.5	119.3	123.0	36.8	39.1	-21.2	44.7	44.5	105.9	97.2
CPS	13	116.8	121.5	155.6	116.8	123.2	44.3	43.2	-25.9	47.0	55.5	99.2	96.3
CPS	14	124.2	118.4	162.3	118.1	121.5	35.7	32.9	-3.1	47.0	48.7	100.1	91.3
Average		119.1 $\pm 3.6$	119.0 $\pm 2.2$	155.5 $\pm 4.2$	120.1 $\pm 3.6$	121.9 $\pm 1.3$	39.1 $\pm 3.3$	38.9 $\pm 3.7$	-14.9 $\pm 9.1$	42.8 $\pm 6.1$	45.6 $\pm 7.9$	99.3 $\pm 4.9$	97.7 $\pm 5.2$
CPR	9	117.9	121.5	75.2	127.0	120.2	39.5	40.3	67.6	36.6	34.3	91.2	103.6
CPR	10	125.3	118.4	77.9	120.7	122.8	33.1	42.9	56.5	47.7	43.5	104.6	97.1
CPR	13	119.0	121.9	76.5	119.8	123.5	42.7	43.3	61.4	48.0	52.7	98.0	97.1
CPR	14	126.4	119.3	76.5	120.5	121.3	31.1	35.6	62.2	45.4	43.2	100.5	93.1
Average		122.2 $\pm 3.7$	120.3 $\pm 1.5$	76.5 $\pm 1.0$	122.0 $\pm 2.9$	122.0 $\pm 1.3$	36.6 $\pm 4.7$	40.5 $\pm 3.1$	61.9 $\pm 3.9$	44.4 $\pm 4.6$	43.4 $\pm 6.5$	98.6 $\pm 4.9$	97.7 $\pm 3.8$
CRS	9	114.7	119.6	110.3	126.2	119.7	37.6	47.3	-66.6	30.5	32.6	93.2	109.1
CRS	10	121.6	118.0	107.5	118.5	122.8	35.0	45.9	-72.0	43.1	43.8	107.2	100.4
CRS	13	117.6	121.9	111.9	115.5	123.8	44.4	48.3	-73.0	47.7	56.5	100.0	97.6
CRS	14	125.2	120.3	111.3	116.4	121.9	35.3	37.5	-71.2	47.0	50.0	102.0	92.4
Average		119.8 $\pm 4.0$	120.0 $\pm 1.4$	110.3 $\pm 1.7$	119.2 $\pm 4.2$	122.1 $\pm 1.5$	38.1 $\pm 3.8$	44.8 $\pm 4.3$	-70.7 $\pm 2.5$	42.1 $\pm 6.9$	45.7 $\pm 8.8$	100.6 $\pm 5.0$	99.9 $\pm 6.1$
CRR	9	114.6	120.3	36.0	125.0	121.3	38.4	45.5	5.9	32.1	32.9	95.0	105.4
CRR	10	122.6	117.3	56.3	119.8	123.3	33.2	47.4	19.3	43.3	45.1	106.9	98.7
CRR	13	117.6	121.2	49.3	115.6	126.1	43.8	48.5	-11.6	48.8	54.8	101.0	95.3

Table D.1: Structural parameters calculated for the fluorine amino acids, from the energy-minimized conformations of PGLa with fluorine substituted amino acid at the denoted position. The angles are defined in Chapter 3.

<b>FAA</b>	<b>pos.</b>	$\beta_{i-4}$	$\beta_{i-1}$	$\beta_i$	$\beta_{i+1}$	$\beta_{i+4}$	$\alpha_{i-4}$	$\alpha_{i-1}$	$\alpha_i$	$\alpha_{i+1}$	$\alpha_{i+4}$	$\theta_{i-1,i}$	$\theta_{i,i+1}$
CRR	14	125.4	119.8	43.0	117.1	122.8	32.9	39.9	3.8	47.7	49.4	101.4	91.2
Average		120.0 $\pm 4.2$	119.7 $\pm 1.4$	46.1 $\pm 7.5$	119.4 $\pm 3.6$	123.4 $\pm 1.7$	37.1 $\pm 4.5$	45.3 $\pm 3.3$	4.4 $\pm 11.0$	43.0 $\pm 6.6$	45.6 $\pm 8.1$	101.1 $\pm 4.2$	97.7 $\pm 5.2$
PFS	9	116.3	121.0	79.3	127.1	120.0	38.5	43.6	70.1	34.2	32.8	92.7	106.6
PFS	10	123.2	117.9	77.8	119.2	122.9	33.2	47.6	63.8	44.7	43.8	105.5	99.2
PFS	13	118.2	121.6	77.5	117.2	123.6	43.8	47.3	67.6	47.9	55.1	98.8	97.6
PFS	14	125.4	119.9	81.5	118.5	121.4	32.5	40.3	64.0	47.7	48.0	101.5	92.7
Average		120.8 $\pm 3.7$	120.1 $\pm 1.4$	79.0 $\pm 1.6$	120.5 $\pm 3.9$	122.0 $\pm 1.4$	37.0 $\pm 4.6$	44.7 $\pm 3.0$	66.4 $\pm 2.6$	43.6 $\pm 5.6$	44.9 $\pm 8.1$	99.6 $\pm 4.7$	99.0 $\pm 5.0$
PFR	9	119.0	120.7	157.6	128.0	119.7	29.9	42.5	30.9	30.2	33.5	92.4	106.3
PFR	10	121.0	115.9	159.9	120.0	122.5	28.3	42.4	13.9	45.2	44.0	104.9	97.6
PFR	13	122.5	121.3	145.6	118.9	124.0	41.7	44.0	29.8	47.7	55.2	98.4	96.0
PFR	14	124.3	118.1	163.5	117.4	121.2	28.3	35.1	21.3	48.4	49.6	100.7	89.8
Average		121.7 $\pm 1.9$	119.0 $\pm 2.2$	156.7 $\pm 6.7$	121.1 $\pm 4.1$	121.8 $\pm 1.6$	32.1 $\pm 5.6$	41.0 $\pm 3.5$	24.0 $\pm 6.9$	42.9 $\pm 7.4$	45.6 $\pm 8.0$	99.1 $\pm 4.5$	97.4 $\pm 5.9$
PRS	9	115.1	121.3	16.0	125.4	118.9	37.8	44.0	-7.3	27.4	36.2	91.4	110.4
PRS	10	122.7	117.0	15.2	122.9	121.0	32.3	48.0	-20.3	40.6	52.4	104.0	103.1
PRS	13	118.4	121.6	19.1	119.1	122.4	43.2	46.8	-12.2	45.5	63.9	96.2	99.7
PRS	14	125.6	119.6	19.4	117.1	120.3	32.9	39.4	-8.4	45.2	52.3	100.2	93.5
Average		120.5 $\pm 4.0$	119.9 $\pm 1.8$	17.4 $\pm 1.8$	121.1 $\pm 3.2$	120.7 $\pm 1.3$	36.5 $\pm 4.4$	44.6 $\pm 3.3$	-12.0 $\pm 5.1$	39.7 $\pm 7.3$	51.2 $\pm 9.9$	98.0 $\pm 4.7$	101.7 $\pm 6.1$
PRR	9	114.3	118.9	117.8	125.0	120.2	39.0	47.5	-68.8	31.3	34.0	92.7	107.6
PRR	10	122.4	119.0	114.9	119.0	123.0	33.3	47.4	-75.0	43.2	43.9	107.4	101.5
PRR	13	118.4	120.9	120.6	116.0	123.4	45.2	46.7	-65.1	46.4	56.7	99.4	98.9

Table D.1: Structural parameters calculated for the fluorine amino acids, from the energy-minimized conformations of PGLa with fluorine substituted amino acid at the denoted position. The angles are defined in Chapter 3.

<b>FAA</b>	<b>pos.</b>	$\beta_{i-4}$	$\beta_{i-1}$	$\beta_i$	$\beta_{i+1}$	$\beta_{i+4}$	$\alpha_{i-4}$	$\alpha_{i-1}$	$\alpha_i$	$\alpha_{i+1}$	$\alpha_{i+4}$	$\theta_{i-1,i}$	$\theta_{i,i+1}$
PRR	14	125.3	121.6	117.8	116.8	121.6	33.6	39.4	-76.6	47.1	50.7	102.9	92.8
Average		120.1 $\pm 4.1$	120.1 $\pm 1.2$	117.8 $\pm 2.0$	119.2 $\pm 3.5$	122.1 $\pm 1.3$	37.8 $\pm 4.8$	45.3 $\pm 3.4$	-71.4 $\pm 4.6$	42.0 $\pm 6.4$	46.3 $\pm 8.4$	100.6 $\pm 5.4$	100.2 $\pm 5.3$

Table D.2: Structural parameters of the fluorine amino acids, obtained from the last 150 ns of the membrane simulations. The angles were calculated with respect to the helical axis, defined from residue 3-17.

<b>FAA</b>	<b>pos.</b>	$\beta_{i-4}$	$\beta_{i-1}$	$\beta_i$	$\beta_{i+1}$	$\beta_{i+4}$	$\alpha_{i-4}$	$\alpha_{i-1}$	$\alpha_i$	$\alpha_{i+1}$	$\alpha_{i+4}$	$\theta_{i-1,i}$	$\theta_{i,i+1}$
BGS	9	117.7 $\pm 9.1$	125.2 $\pm 6.6$	109.1 $\pm 9.0$	126.8 $\pm 4.3$	123.9 $\pm 8.0$	32.6 $\pm 7.1$	39.0 $\pm 12.8$	42.6 $\pm 17.2$	37.1 $\pm 21.5$	38.8 $\pm 8.9$	74.4 $\pm 17.2$	121.8 $\pm 46.5$
BGS	10	133.5 $\pm 6.8$	122.1 $\pm 6.6$	115.6 $\pm 7.4$	125.6 $\pm 5.7$	125.0 $\pm 8.1$	45.0 $\pm 10.5$	20.8 $\pm 9.7$	39.9 $\pm 13.7$	62.7 $\pm 13.9$	36.6 $\pm 7.5$	76.9 $\pm 13.7$	95.6 $\pm 17.4$
BGS	13	116.8 $\pm 7.6$	132.0 $\pm 7.1$	109.8 $\pm 7.3$	116.2 $\pm 7.3$	115.6 $\pm 9.4$	8.6 $\pm 20.7$	42.7 $\pm 11.1$	38.4 $\pm 8.7$	40.8 $\pm 6.9$	66.3 $\pm 19.5$	95.6 $\pm 12.1$	92.4 $\pm 8.9$
BGS	14	128.1 $\pm 4.5$	114.1 $\pm 5.3$	113.6 $\pm 6.7$	130.9 $\pm 5.4$	128.2 $\pm 12.4$	39.2 $\pm 9.8$	27.4 $\pm 7.0$	28.0 $\pm 9.4$	44.5 $\pm 9.5$	8.4 $\pm 21.6$	90.8 $\pm 7.8$	98.8 $\pm 10.4$
Average		124.0 $\pm 7.0$	123.3 $\pm 6.4$	112.0 $\pm 2.7$	124.9 $\pm 5.4$	123.2 $\pm 4.6$	31.3 $\pm 13.8$	32.5 $\pm 8.8$	37.2 $\pm 5.5$	46.3 $\pm 9.8$	37.5 $\pm 20.5$	84.4 $\pm 9.0$	102.1 $\pm 11.6$
PGS	9	120.9 $\pm 7.1$	119.7 $\pm 5.5$	119.4 $\pm 9.0$	124.6 $\pm 5.5$	114.4 $\pm 5.6$	34.2 $\pm 6.8$	32.2 $\pm 9.3$	29.2 $\pm 9.2$	48.5 $\pm 10.3$	32.9 $\pm 7.5$	92.5 $\pm 10.5$	93.6 $\pm 11.9$
PGS	10	131.0 $\pm 7.4$	120.4 $\pm 5.7$	114.5 $\pm 8.4$	126.0 $\pm 5.5$	130.1 $\pm 5.9$	44.6 $\pm 8.0$	21.6 $\pm 8.4$	45.8 $\pm 10.8$	59.4 $\pm 13.8$	38.1 $\pm 7.4$	77.3 $\pm 11.4$	103.4 $\pm 16.8$
PGS	13	121.3 $\pm 6.7$	121.6 $\pm 5.4$	120.1 $\pm 12.3$	123.6 $\pm 7.2$	122.0 $\pm 7.2$	31.2 $\pm 10.2$	30.4 $\pm 9.6$	40.1 $\pm 8.8$	43.0 $\pm 9.7$	30.7 $\pm 26.9$	87.0 $\pm 14.4$	95.0 $\pm 8.3$
PGS	14	125.1 $\pm 5.7$	111.8 $\pm 5.8$	119.0 $\pm 11.0$	125.9 $\pm 7.9$	124.5 $\pm 10.9$	37.4 $\pm 11.0$	30.7 $\pm 7.6$	28.7 $\pm 9.6$	38.7 $\pm 11.1$	26.1 $\pm 26.7$	100.5 $\pm 10.5$	96.8 $\pm 7.0$
Average		124.6 $\pm 4.1$	118.4 $\pm 3.9$	118.2 $\pm 2.2$	125.0 $\pm 1.0$	122.8 $\pm 5.6$	36.9 $\pm 5.0$	28.7 $\pm 4.2$	35.9 $\pm 7.3$	47.4 $\pm 7.8$	32.0 $\pm 4.3$	89.3 $\pm 8.4$	97.2 $\pm 3.8$
HSS	9	122.2 $\pm 5.8$	120.8 $\pm 4.7$	132.3 $\pm 6.8$	125.1 $\pm 4.6$	116.5 $\pm 6.4$	37.5 $\pm 6.5$	30.9 $\pm 7.9$	-37.6 $\pm 16.8$	48.0 $\pm 9.1$	32.2 $\pm 6.9$	90.2 $\pm 7.0$	90.5 $\pm 9.5$

Table D.2: Structural parameters of the fluorine amino acids, obtained from the last 150 ns of the membrane simulations. The angles were calculated with respect to the helical axis, defined from residue 3-17.

<b>FAA</b>	<b>pos.</b>	$\beta_{i-4}$	$\beta_{i-1}$	$\beta_i$	$\beta_{i+1}$	$\beta_{i+4}$	$\alpha_{i-4}$	$\alpha_{i-1}$	$\alpha_i$	$\alpha_{i+1}$	$\alpha_{i+4}$	$\theta_{i-1,i}$	$\theta_{i,i+1}$
HSS	10	123.4 $\pm 6.2$	116.6 $\pm 5.1$	136.4 $\pm 6.0$	121.0 $\pm 5.5$	125.9 $\pm 5.0$	42.6 $\pm 6.5$	28.3 $\pm 8.9$	-42.8 $\pm 14.9$	54.3 $\pm 10.0$	40.1 $\pm 7.0$	97.0 $\pm 9.0$	92.7 $\pm 9.7$
HSS	13	118.9 $\pm 4.1$	121.6 $\pm 4.5$	135.1 $\pm 5.9$	124.1 $\pm 4.6$	122.5 $\pm 6.1$	30.4 $\pm 7.8$	34.7 $\pm 6.8$	-39.2 $\pm 14.3$	43.2 $\pm 7.4$	40.6 $\pm 14.3$	88.5 $\pm 7.3$	94.7 $\pm 6.2$
HSS	14	122.2 $\pm 10.3$	110.0 $\pm 9.7$	126.7 $\pm 10.7$	127.3 $\pm 9.0$	92.8 $\pm 28.5$	43.6 $\pm 11.7$	34.1 $\pm 7.9$	-49.3 $\pm 14.8$	45.2 $\pm 14.1$	-15.0 $\pm 43.4$	108.5 $\pm 9.2$	88.1 $\pm 8.0$
Average		121.7 $\pm 1.7$	117.2 $\pm 4.6$	132.6 $\pm 3.7$	124.4 $\pm 2.3$	114.4 $\pm 12.9$	38.5 $\pm 5.2$	32.0 $\pm 2.6$	-42.2 $\pm 4.5$	47.7 $\pm 4.2$	24.5 $\pm 23.0$	96.0 $\pm 7.9$	91.5 $\pm 2.5$
HSR	9	122.6 $\pm 6.1$	120.7 $\pm 4.6$	62.1 $\pm 7.1$	125.3 $\pm 4.2$	113.2 $\pm 4.0$	36.5 $\pm 6.6$	30.5 $\pm 7.7$	38.0 $\pm 10.1$	48.0 $\pm 8.1$	29.7 $\pm 5.9$	90.9 $\pm 6.7$	93.1 $\pm 8.6$
HSR	10	128.8 $\pm 6.4$	114.0 $\pm 6.0$	77.0 $\pm 8.1$	119.7 $\pm 6.1$	122.7 $\pm 6.8$	37.0 $\pm 7.5$	29.1 $\pm 9.2$	21.1 $\pm 11.2$	51.6 $\pm 11.2$	39.5 $\pm 7.0$	104.2 $\pm 15.5$	91.7 $\pm 14.4$
HSR	13	121.0 $\pm 5.0$	121.2 $\pm 4.5$	65.6 $\pm 9.4$	121.7 $\pm 5.3$	121.8 $\pm 5.6$	35.0 $\pm 9.1$	35.8 $\pm 7.2$	31.7 $\pm 11.6$	42.5 $\pm 6.8$	47.6 $\pm 12.3$	95.2 $\pm 7.8$	95.4 $\pm 5.9$
HSR	14	112.6 $\pm 11.5$	109.4 $\pm 8.2$	88.8 $\pm 9.6$	113.8 $\pm 7.1$	141.0 $\pm 9.1$	69.7 $\pm 13.2$	33.4 $\pm 6.8$	25.7 $\pm 8.8$	64.2 $\pm 10.3$	57.8 $\pm 17.9$	107.9 $\pm 6.5$	86.8 $\pm 6.4$
Average		121.2 $\pm 5.8$	116.3 $\pm 4.9$	73.4 $\pm 10.5$	120.1 $\pm 4.2$	124.7 $\pm 10.1$	44.5 $\pm 14.5$	32.2 $\pm 2.6$	29.1 $\pm 6.4$	51.6 $\pm 8.0$	43.7 $\pm 10.3$	99.6 $\pm 6.8$	91.8 $\pm 3.1$
CBS	9	122.7 $\pm 6.7$	119.6 $\pm 5.1$	131.6 $\pm 6.9$	123.2 $\pm 5.6$	111.1 $\pm 5.4$	34.5 $\pm 6.8$	26.1 $\pm 10.0$	-40.4 $\pm 16.7$	53.5 $\pm 10.4$	30.6 $\pm 6.5$	91.2 $\pm 7.8$	83.0 $\pm 11.3$
CBS	10	125.1 $\pm 7.8$	117.1 $\pm 5.7$	132.6 $\pm 7.6$	123.5 $\pm 5.4$	130.1 $\pm 6.1$	43.2 $\pm 6.9$	28.6 $\pm 8.5$	-30.9 $\pm 19.1$	44.7 $\pm 12.9$	34.4 $\pm 8.4$	92.7 $\pm 11.2$	107.5 $\pm 19.5$

Table D.2: Structural parameters of the fluorine amino acids, obtained from the last 150 ns of the membrane simulations. The angles were calculated with respect to the helical axis, defined from residue 3-17.

<b>FAA</b>	<b>pos.</b>	$\beta_{i-4}$	$\beta_{i-1}$	$\beta_i$	$\beta_{i+1}$	$\beta_{i+4}$	$\alpha_{i-4}$	$\alpha_{i-1}$	$\alpha_i$	$\alpha_{i+1}$	$\alpha_{i+4}$	$\theta_{i-1,i}$	$\theta_{i,i+1}$
CBS	13	120.3 $\pm 4.5$	120.6 $\pm 4.5$	132.5 $\pm 7.1$	123.4 $\pm 4.8$	121.3 $\pm 5.8$	33.1 $\pm 8.1$	32.5 $\pm 6.9$	-35.3 $\pm 15.3$	42.6 $\pm 6.8$	41.8 $\pm 12.2$	91.5 $\pm 6.6$	94.3 $\pm 5.6$
CBS	14	125.1 $\pm 4.1$	119.5 $\pm 4.4$	130.4 $\pm 7.3$	125.6 $\pm 4.9$	126.0 $\pm 7.8$	40.1 $\pm 7.9$	34.4 $\pm 5.9$	-45.3 $\pm 16.4$	45.5 $\pm 7.8$	28.0 $\pm 14.4$	99.7 $\pm 5.2$	91.8 $\pm 4.6$
Average		123.3 $\pm 2.0$	119.2 $\pm 1.3$	131.8 $\pm 0.9$	123.9 $\pm 1.0$	122.1 $\pm 7.1$	37.7 $\pm 4.1$	30.4 $\pm 3.2$	-38.0 $\pm 5.4$	46.6 $\pm 4.1$	33.7 $\pm 5.2$	93.8 $\pm 3.5$	94.2 $\pm 8.8$
CBR	9	123.9 $\pm 6.7$	120.7 $\pm 4.8$	68.5 $\pm 9.4$	126.1 $\pm 4.5$	117.5 $\pm 5.7$	36.1 $\pm 7.9$	30.8 $\pm 7.8$	31.6 $\pm 11.3$	46.8 $\pm 8.4$	33.3 $\pm 7.5$	90.5 $\pm 8.3$	90.1 $\pm 8.3$
CBR	10	129.5 $\pm 6.4$	115.8 $\pm 4.7$	77.8 $\pm 10.1$	121.2 $\pm 5.8$	124.6 $\pm 6.7$	41.9 $\pm 7.5$	22.9 $\pm 9.4$	24.8 $\pm 11.3$	54.5 $\pm 11.0$	38.7 $\pm 6.9$	93.5 $\pm 9.5$	93.1 $\pm 14.4$
CBR	13	117.8 $\pm 5.4$	124.0 $\pm 6.4$	70.5 $\pm 11.6$	119.9 $\pm 6.6$	116.5 $\pm 15.0$	25.9 $\pm 12.3$	28.6 $\pm 9.7$	29.8 $\pm 12.9$	47.5 $\pm 12.6$	13.2 $\pm 41.1$	86.2 $\pm 10.2$	92.3 $\pm 13.5$
CBR	14	126.9 $\pm 4.4$	113.5 $\pm 5.8$	74.7 $\pm 10.3$	126.5 $\pm 5.6$	130.1 $\pm 7.5$	42.0 $\pm 8.5$	30.0 $\pm 7.0$	22.2 $\pm 10.4$	45.0 $\pm 8.2$	24.8 $\pm 15.1$	100.6 $\pm 6.3$	93.1 $\pm 4.7$
Average		124.5 $\pm 4.4$	118.5 $\pm 4.1$	72.9 $\pm 3.6$	123.4 $\pm 2.9$	122.2 $\pm 5.5$	36.5 $\pm 6.6$	28.1 $\pm 3.1$	27.1 $\pm 3.8$	48.5 $\pm 3.6$	27.5 $\pm 9.6$	92.7 $\pm 5.2$	92.2 $\pm 1.2$
CPS	9	111.6 $\pm 15.7$	121.6 $\pm 5.6$	155.5 $\pm 7.2$	126.5 $\pm 5.8$	118.7 $\pm 6.7$	36.4 $\pm 7.3$	31.7 $\pm 8.4$	-15.6 $\pm 22.7$	49.1 $\pm 8.8$	35.2 $\pm 9.2$	87.3 $\pm 11.2$	94.3 $\pm 10.8$
CPS	10	132.9 $\pm 8.8$	113.4 $\pm 9.1$	155.2 $\pm 7.5$	126.8 $\pm 7.1$	100.7 $\pm 15.8$	47.3 $\pm 9.6$	7.5 $\pm 17.5$	-47.7 $\pm 27.9$	68.5 $\pm 15.5$	35.8 $\pm 6.5$	82.0 $\pm 15.0$	69.1 $\pm 15.5$
CPS	13	120.9 $\pm 5.0$	121.8 $\pm 4.9$	153.3 $\pm 6.5$	123.2 $\pm 6.9$	116.9 $\pm 8.5$	29.3 $\pm 9.7$	28.4 $\pm 10.4$	-7.6 $\pm 19.1$	43.8 $\pm 8.6$	38.7 $\pm 26.3$	84.7 $\pm 9.8$	90.8 $\pm 9.1$

Table D.2: Structural parameters of the fluorine amino acids, obtained from the last 150 ns of the membrane simulations. The angles were calculated with respect to the helical axis, defined from residue 3-17.

<b>FAA</b>	<b>pos.</b>	$\beta_{i-4}$	$\beta_{i-1}$	$\beta_i$	$\beta_{i+1}$	$\beta_{i+4}$	$\alpha_{i-4}$	$\alpha_{i-1}$	$\alpha_i$	$\alpha_{i+1}$	$\alpha_{i+4}$	$\theta_{i-1,i}$	$\theta_{i,i+1}$
CPS	14	126.2 $\pm 4.8$	113.5 $\pm 8.4$	149.2 $\pm 7.9$	132.8 $\pm 7.3$	133.0 $\pm 10.0$	47.2 $\pm 9.2$	28.3 $\pm 7.3$	-31.7 $\pm 16.3$	50.4 $\pm 12.1$	8.1 $\pm 20.0$	92.2 $\pm 5.7$	92.1 $\pm 5.8$
Average		122.9 $\pm 7.8$	117.6 $\pm 4.1$	153.3 $\pm 2.5$	127.3 $\pm 3.5$	117.3 $\pm 11.4$	40.0 $\pm 7.6$	24.0 $\pm 9.6$	-25.7 $\pm 15.4$	52.9 $\pm 9.3$	29.4 $\pm 12.4$	86.5 $\pm 3.8$	86.6 $\pm 10.2$
CPR	9	120.9 $\pm 6.2$	119.5 $\pm 4.9$	79.9 $\pm 5.2$	125.7 $\pm 4.6$	117.3 $\pm 5.2$	34.0 $\pm 6.5$	34.1 $\pm 7.8$	67.5 $\pm 7.5$	44.7 $\pm 8.2$	32.5 $\pm 7.3$	95.2 $\pm 8.9$	93.4 $\pm 8.5$
CPR	10	123.3 $\pm 8.0$	114.9 $\pm 4.8$	80.1 $\pm 5.7$	121.5 $\pm 5.5$	126.8 $\pm 5.1$	42.4 $\pm 6.4$	28.6 $\pm 8.0$	72.1 $\pm 9.2$	48.8 $\pm 10.4$	41.2 $\pm 7.1$	94.7 $\pm 9.5$	104.1 $\pm 12.7$
CPR	13	119.0 $\pm 5.3$	120.6 $\pm 4.5$	78.0 $\pm 5.7$	122.2 $\pm 5.2$	122.0 $\pm 6.2$	30.1 $\pm 7.9$	35.3 $\pm 7.5$	68.8 $\pm 7.2$	41.4 $\pm 6.8$	45.2 $\pm 13.3$	95.6 $\pm 8.5$	96.3 $\pm 6.2$
CPR	14	124.8 $\pm 4.3$	118.8 $\pm 5.7$	80.6 $\pm 6.3$	122.3 $\pm 5.4$	127.4 $\pm 8.2$	39.6 $\pm 10.6$	34.8 $\pm 7.3$	64.2 $\pm 6.7$	44.2 $\pm 8.5$	32.3 $\pm 15.7$	103.7 $\pm 7.3$	92.5 $\pm 5.3$
Average		122.0 $\pm 2.2$	118.5 $\pm 2.1$	79.7 $\pm 1.0$	122.9 $\pm 1.6$	123.4 $\pm 4.1$	36.5 $\pm 4.8$	33.2 $\pm 2.7$	68.1 $\pm 2.8$	44.8 $\pm 2.6$	37.8 $\pm 5.6$	97.3 $\pm 3.7$	96.6 $\pm 4.6$
PFR	9	145.2 $\pm 19.7$	128.0 $\pm 11.7$	165.5 $\pm 8.4$	110.9 $\pm 9.9$	109.6 $\pm 7.8$	42.7 $\pm 26.1$	-6.3 $\pm 23.4$	69.5 $\pm 77.2$	73.9 $\pm 18.5$	31.2 $\pm 6.0$	64.0 $\pm 22.2$	47.8 $\pm 20.1$
PFR	10	135.9 $\pm 9.6$	120.7 $\pm 8.1$	156.2 $\pm 7.5$	128.6 $\pm 6.9$	124.6 $\pm 8.7$	53.5 $\pm 19.7$	15.4 $\pm 15.6$	-14.7 $\pm 28.1$	71.5 $\pm 20.0$	35.5 $\pm 7.2$	65.7 $\pm 14.4$	82.8 $\pm 19.5$
PFR	13	121.4 $\pm 5.1$	117.0 $\pm 5.5$	145.9 $\pm 7.2$	133.7 $\pm 7.1$	125.6 $\pm 7.8$	29.8 $\pm 7.5$	25.6 $\pm 7.1$	4.4 $\pm 16.6$	44.1 $\pm 8.9$	10.6 $\pm 18.1$	74.5 $\pm 8.7$	98.4 $\pm 7.0$
PFR	14	131.4 $\pm 4.7$	123.9 $\pm 6.7$	150.6 $\pm 6.9$	131.4 $\pm 7.3$	116.0 $\pm 10.2$	25.2 $\pm 10.7$	27.3 $\pm 7.8$	-9.9 $\pm 19.9$	39.1 $\pm 12.5$	19.5 $\pm 43.0$	69.4 $\pm 10.1$	97.2 $\pm 6.7$

Table D.2: Structural parameters of the fluorine amino acids, obtained from the last 150 ns of the membrane simulations. The angles were calculated with respect to the helical axis, defined from residue 3-17.

<b>FAA</b>	<b>pos.</b>	$\beta_{i-4}$	$\beta_{i-1}$	$\beta_i$	$\beta_{i+1}$	$\beta_{i+4}$	$\alpha_{i-4}$	$\alpha_{i-1}$	$\alpha_i$	$\alpha_{i+1}$	$\alpha_{i+4}$	$\theta_{i-1,i}$	$\theta_{i,i+1}$
Average		133.5 $\pm 8.6$	122.4 $\pm 4.1$	154.6 $\pm 7.3$	126.2 $\pm 9.0$	118.9 $\pm 6.6$	37.8 $\pm 11.1$	15.5 $\pm 13.4$	12.3 $\pm 33.7$	57.1 $\pm 15.7$	24.2 $\pm 9.8$	68.4 $\pm 4.0$	81.5 $\pm 20.4$
PFS	9	121.1 $\pm 6.7$	120.6 $\pm 5.3$	72.8 $\pm 9.1$	124.3 $\pm 4.4$	119.0 $\pm 4.8$	35.0 $\pm 6.7$	34.5 $\pm 8.7$	73.0 $\pm 11.7$	42.7 $\pm 10.2$	38.5 $\pm 6.8$	92.8 $\pm 9.8$	96.6 $\pm 12.6$
PFS	10	122.5 $\pm 7.9$	103.0 $\pm 5.4$	94.5 $\pm 8.2$	125.5 $\pm 5.9$	98.4 $\pm 6.8$	39.7 $\pm 7.8$	28.4 $\pm 10.9$	46.7 $\pm 9.7$	57.5 $\pm 11.4$	36.1 $\pm 5.9$	117.8 $\pm 17.0$	72.3 $\pm 8.2$
PFS	13	114.3 $\pm 7.1$	120.9 $\pm 4.8$	80.2 $\pm 10.0$	119.4 $\pm 6.3$	120.8 $\pm 6.7$	33.3 $\pm 12.3$	35.0 $\pm 7.4$	66.3 $\pm 9.0$	43.2 $\pm 7.0$	47.7 $\pm 12.9$	98.0 $\pm 9.5$	93.1 $\pm 7.8$
PFS	14	124.9 $\pm 4.3$	117.3 $\pm 6.8$	78.5 $\pm 9.2$	124.4 $\pm 5.5$	130.7 $\pm 8.5$	41.9 $\pm 10.2$	34.5 $\pm 7.0$	64.6 $\pm 7.9$	45.6 $\pm 8.8$	32.4 $\pm 16.2$	101.5 $\pm 6.7$	93.6 $\pm 5.4$
Average		120.7 $\pm 3.9$	115.5 $\pm 7.3$	81.5 $\pm 8.0$	123.4 $\pm 2.4$	117.2 $\pm 11.7$	37.5 $\pm 3.5$	33.1 $\pm 2.7$	62.6 $\pm 9.7$	47.2 $\pm 6.0$	38.7 $\pm 5.6$	102.5 $\pm 9.3$	88.9 $\pm 9.7$

Table D.3: Helicities for all fluorine amino acids averaged over all residues. The small numbers with a  $\pm$  sign are the standard deviations.

pos.	BGS	PGS	HSS	HSR	CBS	CBR	CPS	CPR	PFR	PFS	PGLa <sup>a</sup>
9	92 $\pm 11$	89 $\pm 16$	93 $\pm 12$	90 $\pm 18$	87 $\pm 21$	90 $\pm 18$	83 $\pm 22$	93 $\pm 13$	82 $\pm 19$	88 $\pm 15$	88 $\pm 18$
10	90 $\pm 11$	89 $\pm 12$	88 $\pm 19$	91 $\pm 10$	79 $\pm 26$	91 $\pm 14$	83 $\pm 17$	85 $\pm 23$	89 $\pm 13$	76 $\pm 28$	
13	90 $\pm 11$	91 $\pm 14$	92 $\pm 12$	94 $\pm 11$	89 $\pm 20$	78 $\pm 28$	91 $\pm 12$	92 $\pm 12$	88 $\pm 19$	88 $\pm 14$	
14	90 $\pm 13$	80 $\pm 20$	65 $\pm 37$	81 $\pm 21$	92 $\pm 14$	93 $\pm 12$	87 $\pm 16$	90 $\pm 13$	85 $\pm 19$	91 $\pm 14$	

<sup>a</sup>Helicity from the PGLa membrane simulation in Chapter 4, calculated for the last 800 ns.